Colour and Cloud Structure in the Atmospheres of the Giant Planets

Ashwin Sharma Braude
St Cross College
University of Oxford

A thesis submitted for the degree of
Doctor of Philosophy
Hilary 2019

Acknowledgements

It takes a Physics department to raise a DPhil student, and I would like to thank all the people here that I believe contributed in some way or another either directly to the creation of this thesis or to my personal development throughout my three and a half years at AOPP.

The overwhelming bulk of my gratitude, of course, goes to **Patrick Irwin**, for his supervision and diligent guidance throughout, as well as the Science and Technology Facilities Council (**STFC**) for providing me with the financial means to get through my DPhil. I am also grateful to my transfer and confirmation examiners **Simon Calcutt, Neil Bowles** and **Peter Read,** together with my external viva examiner **Santiago Pérez-Hoyos,** for allowing me to progress in my DPhil and for giving constructive advice on my work, as well as **David Marshall** and my college advisor **Helen Johnson** for ensuring that my DPhil never strayed too far off course in the first place.

I would also like to use this space to include people in the broader academic community who contributed to the science in my DPhil project, some of whose material has even appeared in this thesis (with their permission). These include **Mark Loeffler** for his absorption spectra of NH_4SH, **Cheng Li** and **Steven Levin** for directing me to preliminary retrievals of ammonia from the Juno/MWR instrument, **Matthew Wittal** for his guidance in the calibration of HST/WFC3 data that enabled me to properly calibrate my own MUSE data, and **Patrick Fry** and **Tyler Wilson** who attempted to assist me in the calibration of Cassini/VIMS spectra (unfortunately in vain, hence their absence from this thesis). My closest academic collaborators would however be **Glenn Orton** and **Leigh Fletcher,** who I am indebted to for their guidance and their willingness to wade through my draft paper and give constructive criticism, and to give me broader perspectives on my work and induct me into the planetary science community. I am particularly thankful to Glenn for his ability to write highly complimentary job references at very short notice!

There are also some people I would like to mention whose valuable contribution to the work conducted in AOPP (including my own) often gets overlooked. These include **Sarah Harrington, Catherine Morris, Lucy Liu** and **Andrea Simpson,** who ensured that I could focus my full attention on science instead of trudging through soul-destroying bureaucracy and completing expense forms, as well as **Man-Suen Chan** and **Elena Valenti**, who respectively addressed my very frequent IT issues and MUSE calibration issues with great patience and professionalism.

Finally, I would like to thank all my close colleagues in the department who provided immense moral support, sitting through my frequent rants about DPhil life with great understanding and without much conspicuous eye-rolling. These included both my actual officemates **Rohini Giles, Charlotte Marriner** and **Rowan Curtis** and my honorary officemate **Ryan Garland** for putting up with some idiosyncratic and conflicting views on personal space on my part; my fellow first year contemporaries **Christopher MacMackin** and **Susan Wright**; and all the remaining members of my research group (namely **Daniel Toledo Carrasco, Jean-Loup Baudino, Sophie Bauduin, Jake Taylor, Juan Alday Parejo**, **Joshua Krissansen-Totton** and **Victor Trees**).

Abstract

For decades, the origin of colour-carrying compounds ('chromophores') in Jupiter and Saturn's atmospheres has remained elusive. Changes in colour are often associated with cyclical meteorological events ('upheavals') on Jupiter. Multiple datasets were obtained from the VLT/MUSE instrument between 2014 and 2018, each containing spatially-resolved spectra of Jupiter and Saturn between 0.48µm and 0.93µm. We describe the analysis of these datasets to characterise Jovian and Saturnian chromophores and to retrieve abundance profiles of aerosol and gaseous ammonia. Through limb-darkening analysis of Jupiter's NEB, we retrieved chromophore optical constants similar to the laboratory chromophore of (Carlson et al. [2016] Icarus 274, 106-115). These also provided a good fit to spectra of the Great Red Spot, but not to spectra of Jupiter's zones. We applied these chromophore optical constants to other regions of Jupiter, and found that red haze in the NTBs was initially associated with elevated aerosol abundances, but remained in the atmosphere long after upwelling had subsided. We verified previous findings of colour and haze structure changes relating to the shrinkage of the Great Red Spot, where we retrieved the altitude of the chromophore layer at the tropopause. We found no evidence of changes to the cloud structure of Oval BA to explain its fade in colour in 2018. An equivalent retrieval of chromophore optical constants from Saturn's NEB resulted in an absorption spectrum similar to the laboratory chromophore of (Noy et al. [1981] JGR: Oceans 86, 11985-11988), which we located just above Saturn's tropospheric haze. However, we found considerable variability in Saturn spectra that was not entirely consistent with a single chromophore compound. We believe that this work provides a significant contribution to our understanding of both colour and tropospheric aerosol structure on Jupiter and Saturn, and sheds light on the origin of spatial and temporal changes in the visible appearance of the two planets.

Contents

Nomenclature

0.89μm Shorthand for the strongest and broadest methane absorption feature in the MUSE wavelength range, sensitive to aerosol around 0.1-0.2μm.

Abundance When relating to aerosol, the local specific density (in particles cm^2/gram of atmosphere) of particles in the atmosphere. When referring to gas, the volume mixing ratio.

Angular triplet A unique set of three angular values that defines how sunlight is reflected from a given location on the planet to an observer. This consists of a) the angle of incidence of solar radiation with respect to nadir (also known as the 'solar zenith angle'), b) the angle of reflection with respect to nadir (also known as the 'emission angle' or 'viewing zenith angle') and c) an azimuthal angle between the solar and viewing zenith angles. The angle between incident and reflected radiation is known as the 'phase angle'.

Blue wavelengths The region of the spectrum between 0.45 and 0.495μm.

Blue-absorption gradient The degree of the slope that is usually present in the spectra of Jupiter and Saturn between 0.4μm and 0.6μm, a quantitative measure of the local redness of the atmosphere.

Chromophore The generic term for a coloured, usually red or yellow, compound (or functional group of a molecule that is responsible for the molecule being coloured) that is present in the atmospheres of Jupiter and Saturn to varying degrees. This is usually distinguished in this thesis from cloud or haze, which is assumed to be white or colourless.

Cloud A dense region of aerosol, usually at lower altitudes and with a larger particle mean radius, and formed from the condensation of upwelling gases from the interior. In this thesis, it it often used as a short-hand for the thick layer of aerosol that marks the deepest level that MUSE can observe, usually around 1 bar, and is explicitly distinguished from chromophore.

Deep Troposphere The region of the atmosphere below the visible cloud layers ($>$ around 3 bars on Jupiter and $>$ around 1 bar on Saturn) that can only be remotely sensed at microwave/radio wavelengths.

Discrete Feature Any visible feature in the atmosphere (such as a vortex or storm feature) that is distinct from the general zone-belt structure of Jupiter or Saturn.

Haze A sparse region of aerosol, usually at higher altitudes and with a very small particle mean radius. The constituents of haze are generally thought to be the products of photochemistry, but the presence of condensibles could also have some contribution. In this thesis, it it often used as a short-hand for aerosol layers above the main cloud level around 1 bar, and is usually distinguished from chromophore.

Jovian Of, or relating to, Jupiter.

Kronian Of, or relating to, Saturn. In this work we prefer to use the word 'Saturnian'.

Opacity A measurement of the thickness of an aerosol layer and its impenetrability to electromagnetic radiation. Technically, this is calculated as the particle density (in particles/cm^3) multiplied by the thickness of a specific atmospheric layer (in cm) and then divided by the extinction cross-section of the particles (in cm^2) at a given wavelength.

Science In the context of calibration and reduction, we refer to the observation of Jupiter and Saturn itself as a 'science observation' or simply a 'science', in order to distinguish it from calibration data.

Standard In the context of calibration and reduction, a 'standard' is a reference star whose spectrum is known a priori. Generally, this spectrum contains as few stellar absorption lines as possible, and which are easily interpolated over.

Tropopause A cold trap region that separates the troposphere and the stratosphere, located at around 0.1 bars on both Jupiter and Saturn.

Upper Troposphere The region of the atmosphere just below the tropopause (around 0.1-0.5 bars), home to some sort of haze layer on both Jupiter and Saturn.

Chapter 1

Introduction

1.1 Overview and thesis structure

Jupiter and Saturn have a lot to teach us about the nature of planetary atmospheres. Being, to first approximation, balls of gas makes them ideal laboratories to test the behaviour of fluid, chemical and radiative processes under conditions that cannot be replicated on Earth. This allows for their atmospheres to be used as analogues for extrasolar gas giant atmospheres, which are more difficult to observe from the Earth and whose spectra are less constrained. They also have simpler atmospheres to model than the Earth, since biological processes and interactions with rocky surfaces or oceans do not need to be taken into account. Moreover, since radiative damping on the gas giants is much smaller than on Earth, the effects of solar forcing can be more easily observed [Squyres, 2011, Simon-Miller et al., 2007]. This therefore provides a first-order template onto which other more complex processes can be added to accurately model the atmosphere of our own planet. However, there is also some added complexity due to the fact that the atmospheres of the gas giants extend deep into the interior and are not simply confined to a shallow layer as on the Earth.

Since the dawn of the space age, most spacecraft intending to gain enough propulsion to reach the outer solar system have done so by harnessing Jupiter's gravitational field. For this reason, we know substantially more about the nature of Jupiter's atmosphere than we do about Saturn's. The first spacecraft to visit Jupiter were Pioneers 10 and 11 [Gehrels, 1976, Fimmel, 1977] in 1972 and 1973 respectively (the latter reaching Saturn in 1979), followed by additional flybys from Voyagers 1 and 2 (1979) that also reached Saturn in 1980 and 1981 respectively [Tomasko et al., 1984]. The next great leaps in our knowledge of Jupiter's atmosphere came from the Galileo spacecraft, which orbited Jupiter continuously between 1995 and 2003. Galileo also discharged a probe into a hotspot region of Jupiter's atmosphere [Niemann et al., 1998, von Zahn et al., 1998, Ragent et al., 1998], which recorded in situ measurements of Jupiter's atmospheric composition and aerosol structure. Jupiter's composition is hence much better constrained than that of Saturn, for which we only have measurements obtained through remote sensing. Galileo was then followed by an additional spacecraft, Cassini-Huygens [Porco et al., 2003], that observed Jupiter during a brief flyby in 2000/2001 before it reached its intended destination of Saturn, where it remained in orbit between 2004 (southern summer) and 2017 (northern summer). Despite 45 years of spacecraft observations, however, we still know very little about why the giant planets look the way they do to the human observer.

Here, we investigate two core properties of the atmospheres of the giant planets that contribute to their visual appearance, and to temporal changes thereof. One is the origin of the deep red colours seen in certain latitudinal bands and discrete features on Jupiter, but which are more thinly and evenly spread over the summer atmosphere of Saturn. These are thought to be due to the presence of red colour-carrying compounds ('chromophores') in their atmospheres, whose properties are still completely unknown. The other core property we wish to characterise about Jupiter and Saturn is their tropospheric cloud structures, and how they relate to changes in activity in the planets' interiors. Both of these properties act as tracers of interior dynamics and moist convection, and can also be used to infer changes in temperature at deep altitudes, where they are difficult to observe directly through remote sensing alone. This is particularly valuable for Jupiter, since Jupiter's low obliquity should imply a lack of seasonal variation over the course of the Jovian year, equal to approximately 12 Earth years, but which does show quasi-regular cycles in its cloud structure and colour that can only be initiated by similar cycles in its interior. In the case of Jupiter, we will also look at changes in the concentration of ammonia gas around the level of the deepest visible cloud layers, serving both as an additional probe of the dynamics of the interior and as a constraint on the composition of the cloud layers themselves.

Historically, most scientific studies of Jovian and Saturnian colour have relied on observations using a restricted number of wavelength filters (eg. Owen and Terrile [1981], Thompson [1990], Simon-Miller et al. [2001a], Strycker et al. [2011], Ordóñez-Etxeberria et al. [2016]). Usually, these studies involved principal component or cluster analyses, a set of techniques we will explore further in section 6.7, in order to qualitatively analyse spatial variations in colour. Although the spectral absorption peak responsible for red colour on Jupiter and Saturn is generally very broad and featureless, variations in chromophore composition, altitude and size distribution can all have minor effects on the shape of the absorption. These variations, however, require much greater spectral resolution to observe and decouple from each other than filter imaging can provide. The last comprehensive sets of hyperspectral data of Jupiter and Saturn in the visible wavelength range come from the Cassini/VIMS-V instrument [Brown et al., 2004], which observed Jupiter and Saturn at wavelengths between 0.35µm and 1.1µm. Sromovsky et al. [2017] used these data to propose the idea of a 'universal chromophore' for Jupiter, in which all red colour on Jupiter originated from the same source compound and reaction process. However, the Cassini flyby of Jupiter was too brief to fully observe Jovian atmospheric cycles over their full duration, and Jupiter's largest storm features (the 'Great Red Spot' and 'Oval BA' respectively), have undergone changes in colour and structure since the Cassini flyby.

The NASA/Juno spacecraft arrived in orbit around Jupiter in July 2016, where it has remained ever since, with a number of instruments on board intended to characterise Jupiter's deep interior structure. However, while the Juno spacecraft can observe Jupiter at a much greater spatial resolution, and down to much greater depths, than any ground-based instrument ever could, it also lacks both spatial coverage to provide global context to its observations, and wavelength coverage in the visible and near-infrared to adequately characterise colour and cloud structure (barring JunoCam, a simple camera intended mainly for public outreach and which has a signal-to-noise ratio too low to be used for science). For this reason, additional ground-based observations (known as Juno's 'ground support') are required to 'plug the gap' in both wavelength and spatial coverage left by Juno, in order to further constrain giant planet cloud structure and colour, as well as to continue where Cassini left off.

In this thesis, we analyse multiple sets of global spectral image cubes of both Jupiter and Saturn from the Multi Unit Spectroscopic Explorer (MUSE) instrument at the Very Large Telescope (VLT), covering a wavelength range of between 0.476 and 0.933µm [Bacon et al., 2010], and obtained over a four year period between 2014 and 2018. Our analysis consists of detailed, simultaneous spectral retrievals of cloud structure, chromophore and, in the case of Jupiter, ammonia gas abundance. We aim in particular to answer the following questions from the data:

1. To what extent can aerosol density be decoupled from particle size and real refractive index, and to what extent can these degeneracies (a result of the limited phase angle range covered by ground-based observations) be neglected to retrieve reliable cloud and chromophore profiles?
2. Are hypothetical chromophore spectra obtained under laboratory conditions compatible with

observed MUSE spectra of the giant planets? If not, can a reliable chromophore spectrum be retrieved directly from the MUSE data?

3. Can spatial variations in colour on Jupiter and Saturn be explained by one single chromophore compound (a ‘universal chromophore’), or is more than one chromophore compound necessary?
4. Can the most likely altitude of the chromophore be reliably constrained?
5. What is the source of the discrepancy in the most likely altitudes of the thick cloud layers on Jupiter between those predicted by Equilibrium Cloud Condensation Models (ECCMs) and observations made at different wavelengths? Hence, can the most likely composition of the uppermost cloud layer be deduced?
6. How does the concentration of ammonia gas vary with latitude and time on Jupiter, and to what extent does it match with deep observations of ammonia gas by Juno/MWR?
7. Can reliable latitudinal variations in ammonia abundance be obtained from MUSE observations of Saturn?
8. Can the NTBs and EZ revival events, the shrinking and reddening of the Great Red Spot (GRS), and the change in colour of Oval BA be related to changes in cloud structure and ammonia gas?

We will use the rest of this chapter to provide a more detailed introduction to giant planet cloud structure and the ‘chromophore problem’, as well as some of the changes observed in Jupiter’s visual appearance between 2014 and 2018. Chapter 2 gives a brief overview of both MUSE and the instruments from Juno that are most relevant to the work presented here, and then explains how the MUSE data was calibrated and reduced, with some detail about the issues encountered using the standard calibration pipeline and how they were accounted for. Chapter 3 then explains the physics behind a typical giant planet spectrum within the MUSE wavelength range, and how that spectrum can be modelled and inverted using the NEMESIS radiative transfer and retrieval algorithm to obtain vertical cloud and chromophore profiles, as well as gaseous ammonia concentration. In Chapter 4, we then select a single set of Jupiter MUSE data, which we use to perfect a reliable and comprehensive cloud model, and from which we retrieve a universal chromophore. This model and chromophore is then applied in chapter 5 to all sets of Jupiter MUSE data to shed light on the changes observed between 2014 and 2018 in Jupiter’s visual appearance, particularly with regards to the NTBs revival cycle and the changes in morphology of the GRS and Oval BA. Chapter 6 then applies the same method detailed in chapter 4 to design a comprehensive cloud model and retrieve a chromophore spectrum from Saturn MUSE spectra. The main findings of chapters 4 to 6 are then all brought together in chapter 7 to answer our original scientific aims, and suggestions for future work proposed. Chapters 1 and 3 mostly consist of a review of the literature, for which the author of this thesis has no personal contribution (apart from section 3.8, which is entirely the work of the author). For the remainder of this thesis, a description of the author's personal contribution is given in an overview at the beginning of each chapter.

1.2 Basic vertical and latitudinal structure of the giant planets

The classical view of Jupiter and Saturn's vertical and meridional atmospheric circulation, dating back to the Voyager era, is of each hemisphere divided into a series of multiple, adjacent latitudinal convection cells [Gierasch et al., 1986]. These are akin to the three cells per hemisphere found on Earth (ie the Hadley, Ferrell and Polar cells), but the atmospheres of Jupiter and Saturn rotate much faster than that of the Earth and so are subdivided into a much larger number of individual cells. Each of these cells is further divided into a cold upwelling region (a 'zone'), which contains a greater abundance of condensibles and therefore thick, elevated cloud, and a downwelling region (a 'belt') in which the opposite is the case. Each zone is bounded by an eastward jet on the poleward side and a westward jet on the equatorward side [Ingersoll et al., 2004]. Jupiter's individual zone-belt regions are very discernible at visible wavelengths, the zones generally appearing white (indicating chromophore depletion or suppression) due to thick cloud, and the belts appearing a dark red-brown (indicating chromophore enrichment), though the zone-belt structure starts to break down towards the poles, as one can see in figure 1.2.1. By contrast, Saturn's zone-belt colour contrast, while still visible, is more muted than that of Jupiter due to the presence of a thick, overlying yellow haze, as we will describe further in sections 1.3 and 1.4.

Given the rough composition and temperature-pressure profiles of the atmospheres of Jupiter and Saturn, as shown in figure 1.2.2, one can estimate the altitude and composition of each of the main cloud layers using what is known as an Equilibrium Cloud Condensation Model (ECCM). This was first done on the gas giant atmospheres by Lewis [1969] and Weidenschilling and Lewis [1973], with some minor modifications by Rossow [1978], Atreya and Romani [1985], Carlson et al. [1988] and

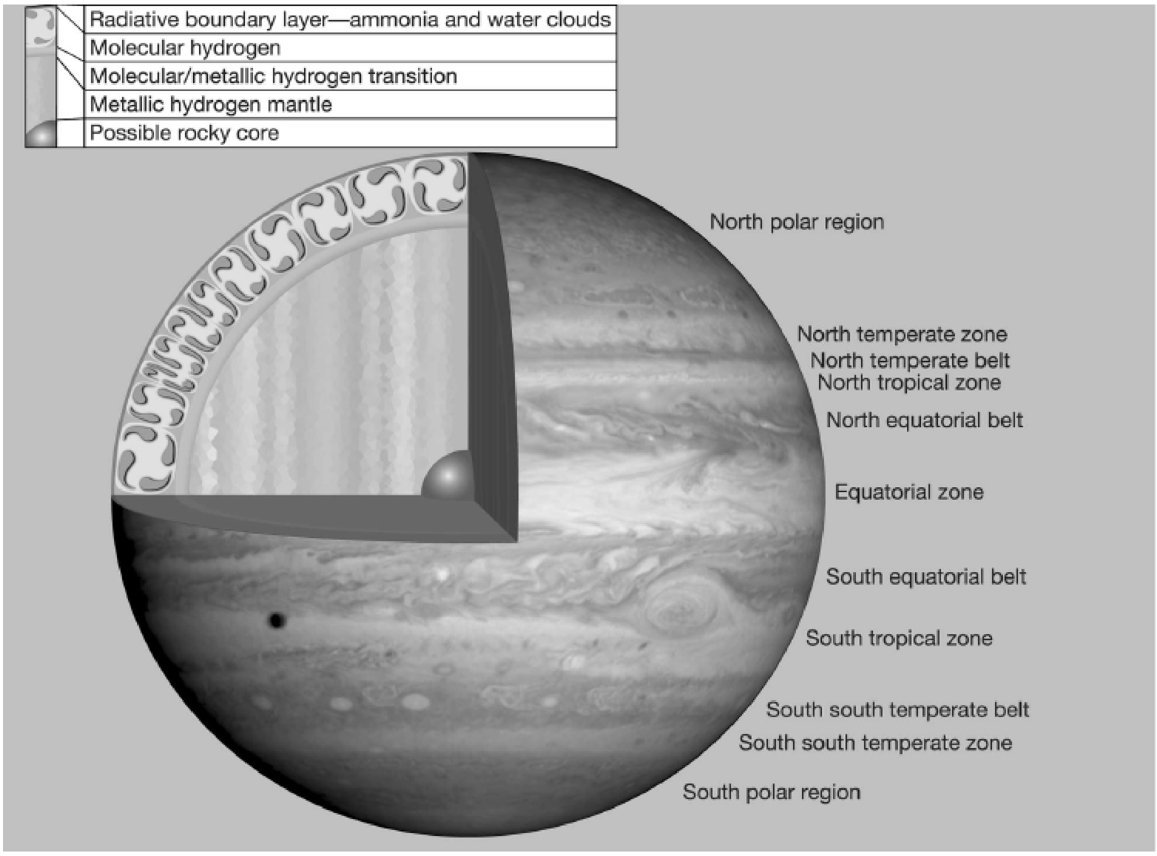

Figure 1.2.1: Key to nomenclature used in this thesis to refer to the specific zones and belts of Jupiter. This image was transposed directly from Figure 1.3 in Bagenal et al. [2007], and shows the state of Jupiter's atmosphere as observed by Cassini in November 2000. Although Jupiter's atmosphere has evolved since that time, the general zone-belt structure has remained roughly the same, with only a few exceptions as highlighted in section 1.4. This diagram also shows a model of the cross-section of Jupiter's interior; for a more detailed discussion of Jupiter's deep structure before the Juno era the reader is referred to Guillot et al. [2004], while preliminary results on the interior structure from Juno are summarised by Fortney [2018]. We refer the reader to figure 6.1.1 for an equivalent key for Saturn.

Atreya et al. [1999]. In all cases, however, ECCMs predict the atmospheres of Jupiter and Saturn to consist of three main cloud layers, as shown in figure 1.2.3: at the bottom, a cloud of aqueous ammonia (NH_3-H_2O) immediately below a cloud of water ice (with a base pressure of 5.7-7.2 bars on Jupiter and 12-21 bars on Saturn, all values quoted from Atreya et al. [1999]), and at the top, a cloud of ammonia ice (NH_3) at base altitude 0.7-0.85 bars on Jupiter and 1.5-1.8 bars on Saturn. Between these two layers is predicted to be another cloud layer, produced from the reaction chemistry of hydrogen sulphide (H_2S) and ammonia, at 2.2-2.6 bars on Jupiter and 4.5-5.75 bars on Saturn. The main component of this cloud layer is usually quoted as being ammonium hydrosulphide (NH_4SH), but a lack of reaction rate data has made the composition of this cloud layer difficult to constrain, with alternative constituents such as ammonium sulphide ($(NH_4)_2S$) also having been proposed (eg.

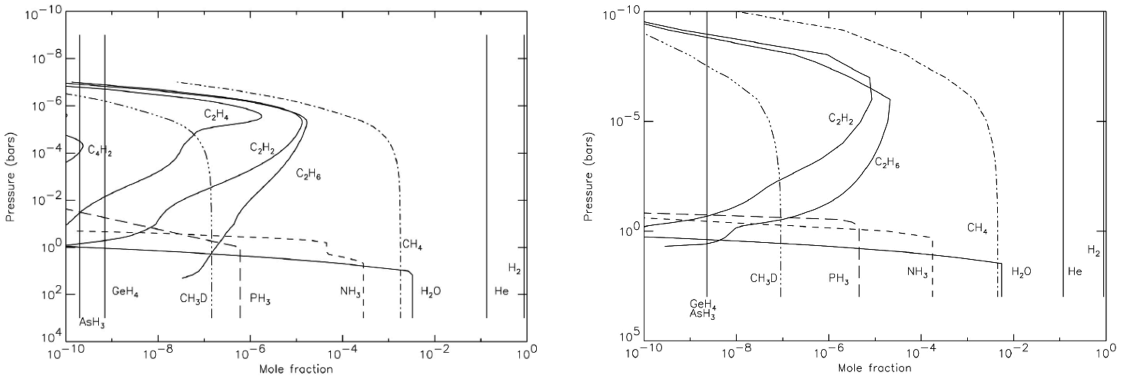

Figure 1.2.2: Estimated vertical composition profiles of (*left*) Jupiter and (*right*) Saturn [Irwin, 2008]. Hydrogen, Helium and Methane are all considered well-mixed in the troposphere.

Lewis and Prinn [1970], Wong et al. [2011]).

When it is attempted to validate these cloud layers observationally, however, the results appear to be inconsistent between observations from reflected sunlight (visible and near-infrared) and observations from thermal emission (mid-infrared), for both Jupiter and Saturn. The Galileo Probe Nephelometer experiment [Ragent et al., 1998] only found one substantial cloud layer at 1.3 bars during its descent through the atmosphere of Jupiter at the Probe Entry Site (PES), while the predicted ammonia cloud layer, at 0.5-0.6 bars, was very feeble and incoherent, and the water ice cloud barely detectable. This was mainly assumed to be due to the anomalous characteristics of the PES, a 'hotspot' region of extreme downwelling with unusually low abundances of condensibles compared with the rest of Jupiter [Atreya et al., 1999]. Banfield et al. [1998b] and Simon-Miller et al. [2001a] claimed to retrieve a thick cloud layer on Jupiter around 0.7 bars from Galileo/SSI, which would be consistent with a cloud layer made up primarily of ammonia ice. However, a large number of observations also appeared to show that the same thick cloud layer was required at a substantially lower altitude, where ammonia would surely sublimate. Irwin et al. [1998, 2001] showed using NIMS data at 1-2µm that a thick cloud layer was present around 1.5 bars, while Giles et al. [2015] constrained an EZ cloud at around 1.1 bars. Usually this cloud layer is quoted as being formed primarily of NH_4SH, despite being located at a higher altitude than one would expect an NH_4SH cloud base, and is actually closer to the altitude that Wong et al. [2011] would require ($(NH_4)_2S$) to form. Sato et al. [2013] derived a real refractive index value of the main cloud layer from Cassini/ISS of 1.85, which corresponds to the estimated PES value of the 1.3 bar cloud layer of around 1.7-1.8, and is close to the real refractive index of NH_4SH [Howett et al., 2007]. Matcheva et al. [2005] on the other

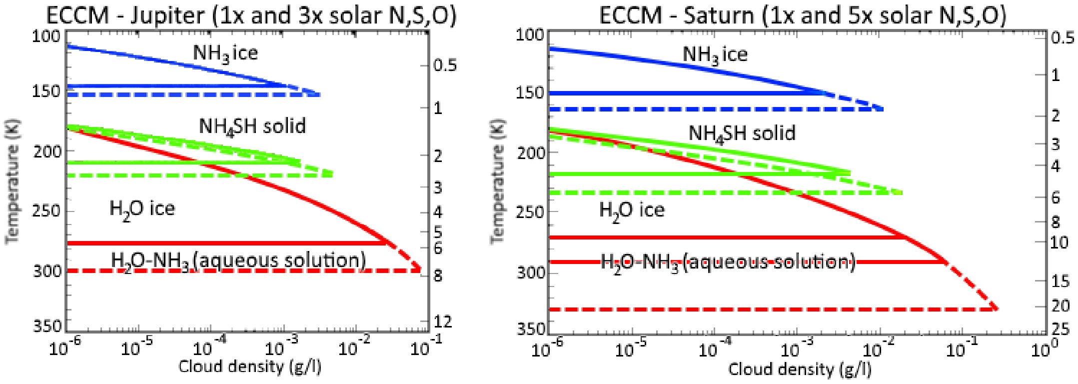

Figure 1.2.3: Theoretical cloud models of (*left*) Jupiter and (*right*) Saturn, adapted from Atreya et al. [1999]. Thick lines indicate solar abundances of nitrogen, sulphur and oxygen, with dashed lines indicating increased abundances relative to the Sun. Each cloud layer is colour-coded according to composition.

hand retrieved a cloud layer at 0.9 bars from Cassini/CIRS in the thermal infrared, which would indicate a mixture of NH_3 and NH_4SH.

A possible explanation for these discrepancies is either that the NH_3 and $NH_4SH/(NH_4)_2S$ cloud layers are contiguous with each other, or that the ammonia ice cloud is simply semitransparent in the thermal infrared [Drossart et al., 1998]. This would also explain observational discrepancies on Saturn, where observations from Cassini/ISS [Roman et al., 2013] indicate a thick cloud layer around 1.75 bars, while Fletcher et al. [2011a] retrieve a cloud layer around 2.5-2.8 bars from Cassini/VIMS-IR. Spectroscopic confirmation of an ammonia ice cloud layer is made even more difficult by the lack of characteristic ammonia ice absorption features in the infrared, apart from in very small regions of young cloud and substantial upwelling on Jupiter [Brooke et al., 1998, Baines et al., 2002, Sromovsky and Fry, 2018] and during Saturn's Great White Spot event of 2010-2011 [Sromovsky et al., 2013] (see section 1.4). This general lack of Spectrally Identifiable Ammonia Clouds (SIACs) could be a result of the deposition of photochemical compounds onto cloud particles which mask their ammonia ice signatures [Atreya et al., 2005].

Above these cloud layers, we also observationally constrain two distinct photochemical haze layers separated by the tropopause at around 0.1 bars (eg. Macy [1977], Tomasko et al. [1984], Banfield et al. [1998a], Zhang et al. [2013]), which we show for Jupiter in figure 1.2.4. The upper tropospheric haze is bounded below by the radiative-convective boundary around 0.5 bars [Banfield et al., 1998b]. On Jupiter this haze forms a zone-belt structure that, to a greater or lesser degree, overlaps with the meridional aerosol structure of the cloud layers below it. However, the haze is thickest around a band close to the equator, which has been known to shift in latitude in the past [Lii et al., 2010] and currently sits above the northern EZ, as well as over discrete features such as the GRS. The dominant process that is thought to form this haze layer on Jupiter is the photolysis of ammonia gas by solar UV radiation, which results in hydrazine (N_2H_4) condensate [Atreya et al., 1999], though this has yet to be confirmed spectroscopically. Other processes, such as phosphine (PH_3) photolysis which is particularly enhanced around the equator [Fletcher et al., 2009], may also contribute to upper tropospheric haze production. By contrast, Saturn's upper tropospheric haze layer is much denser and more spatially uniform than Jupiter's upper tropospheric haze. Although the aerosols in this layer are too sparse to be considered 'cloud' as opposed to 'haze' [Karkoschka and Tomasko, 2005], it nonetheless obscures most of the tropospheric cloud structure below it, since a combination of a lower gravitational acceleration (and hence a larger pressure scale height) and deeper cloud layers results in estimated haze column abundances that are five times greater than on Jupiter [Smith et al., 1982]. At these altitudes, ammonia is substantially depleted on Saturn, and so hydrazine cannot be the main component of this haze. Phosphine photolysis is thought to be a more likely haze formation process, the main product of which is diphosphine (P_2H_4) [Kaye and Strobel, 1984, Fouchet et al., 2009]. Again, however, P_2H_4 is poorly-constrained spectroscopically on the giant planets. The composition of the upper tropospheric and lower stratospheric haze layers therefore still remains unknown, although it most likely consists of a combination of the products of phosphine and methane photochemistry which have sedimented down from the upper stratosphere [Moses et al., 2000].

Methane gas is photolysed at very high altitudes in the atmosphere, estimated at the µbar level just below the homopause. This results in the production of hydrocarbon compounds that are further photolysed at deeper altitudes in the stratosphere [Moses et al., 2004], through very complex chemical reaction schemes that are beyond the scope of this thesis. This forms a stratospheric haze that is relatively uniform, with major concentrations around polar latitudes of Jupiter associated with aurora-induced hydrocarbon chemistry [Hord et al., 1979], forming a 'polar hood' above 0.01 bar [Banfield et al., 1998a, Zhang et al., 2013], as well as around the equator of Saturn just above the tropopause. Many of these stratospheric haze compounds then coagulate and sediment down to lower altitudes where they may also mix and react with compounds in the upper tropospheric haze [Friedson et al., 2002], potentially descending down all the way to the visible cloud tops. Not only could these compounds be responsible for the absence of SIACs on Jupiter, but they may also be responsible for the production of chromophore, as we will see in the next section.

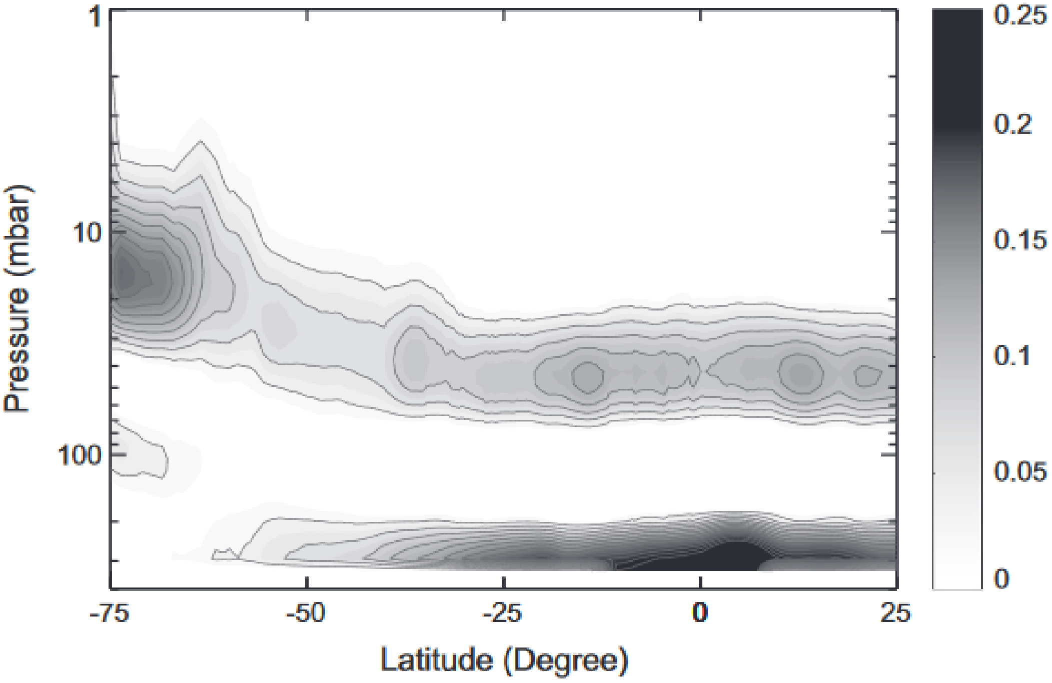

Figure 1.2.4: Retrieved stratospheric and upper tropospheric haze profiles on Jupiter retrieved from Cassini/ISS, taken from Figure 3 in Zhang et al. [2013]. Note the gap in haze around the tropopause (100 mbar) the elevated stratospheric haze at high latitudes around 10-20 mbar (the ‘polar hood’) and the thick haze in the upper troposphere around the equator.

1.3 Giant planet chromophore - Origin and location

Jupiter and, to a lesser extent, Saturn, both exhibit a wide range of colours in their atmospheres. In some areas, particularly in cyclonic regions where cloud is thought to be depleted, one can occasionally witness shades of grey or blue [Rogers, 1995], however the most common colours, which we will be focussing on in this thesis, range somewhere on a spectrum from white to yellow to red to dark brown. These colours are due to varying degrees of absorption of shorter-wavelength solar radiation relative to longer-wavelength radiation in the giant planet atmospheres. Sánchez-Lavega et al. [2013] created a quantitative measure of colour in giant planet atmospheres (a so-called ‘colour index’), defined as the gradient in the spectral slope as measured between two wavelength filters (usually centred around 0.410µm and 0.673µm respectively). Using the same logic applied to MUSE data, we prefer to define colour as the spectral slope between approximately 0.475µm and 0.600µm (the approximate longward extent of the blue-absorption feature in giant planet spectra), and we loosely and qualitatively refer to a spectrum as ‘red’ if the slope is large and ‘white’ if it is comparatively small. A detailed discussion of how colour defined this way relates to actual colours as they are perceived by the human eye is provided by Ordóñez-Etxeberria et al. [2016] and is mostly beyond the scope of this thesis, although we should note that a human observer in close proximity to Jupiter would perceive the planet as mostly white, with much less exaggerated colour variation than is perceived by astronomical instrumentation.

As previously mentioned, red colour on Jupiter is usually concentrated in the belts and in discrete anticyclonic features such as the GRS, while zones tend to be characterised by whiter colours, though there are numerous exceptions to this rule as will be mentioned elsewhere in this thesis. Saturn, on the other hand, has a more uniform distribution of yellow colour across its summer hemisphere, though subtle zone-belt differences in colour can still be discerned. From what we currently know about the composition of the giant planets, however, regions such as the belts with relatively sparse and deep cloud should actually appear slightly *blue,* since Rayleigh scattering from gas molecules would cause greater reflection of short-wavelength radiation to the observer than long-wavelength radiation, as on Uranus and Neptune, or indeed on the winter hemisphere of Saturn. While the presence of conservatively-scattering aerosol can, and does, moderate the discrepancy between the reflection of shortwave and longwave radiation, depending on the size of the aerosol distribution and thus its scattering regime, it cannot fully explain the degree of redness seen in Jupiter and Saturn. One therefore has to invoke the presence of an additional blue-absorbing substance, which we refer to as a *chromophore*.

Despite more than 50 years of conjecture, the origin and composition of giant planet chromophore remains elusive to this day. Cracking the so-called 'chromophore problem' has been made especially difficult by the absence of any characteristic absorption peaks in Jovian spectra, other than just a smooth gradient in absorption as one moves towards shorter wavelengths, that would disambiguate the various candidate compounds from each other. While simple electronic transitions in atoms usually result in absorption in the ultraviolet, far outside MUSE's wavelength range, certain functional groups can be both *bathochromic*, shifting the wavelength of absorption longward, and *auxochromic*, intensifying the absorption. If enough of these functional groups, or *auxochromes*, are added onto the molecule, in a process known as *conjugation*, the resulting bathochromic shift can be enough to see substantial absorption at visible wavelengths. This is thought to be the main mechanism that causes chromophores in giant planets to be so brightly-coloured. Generally, these auxochromes contain a combination of double-bonds and lone pairs of electrons, with the primary source of absorption due to the excitation of the double bond itself ($\pi \rightarrow \pi^*$), plus occasionally a secondary, separate longward peak due to the excitation of the lone pair of electrons into the double bond ($n \rightarrow \pi^*$). The reader is referred to Nassau [1983] for a more detailed review of the mechanisms behind colour production at the molecular level. However, since large numbers of these auxochromes may need to be conjugated together to produce the necessary bathochromic shift, this also means that chromophores which absorb visible light may be more likely to be mixtures of many different large and complex molecular structures than one single molecular endmember. Hence, when we talk about a universal chromophore, we do not necessarily imply that there is only one single chromophore compound in the whole of Jupiter and Saturn, but rather that there is a uniform chromophore production mechanism that results in the same general mixture of coloured compounds throughout the planets' visible area.

A review of different candidate chromophores is provided in West et al. [2004] and Simon-Miller et al. [2001b]. Generally, these chromophores can be divided into three main categories. The first is that of compounds resulting from sulphur chemistry, usually either sulphur allotropes (eg. Lewis and Prinn [1970]), or ionic compounds in the form of hydrogen polysulphides (H_2S_x) [Lewis and Prinn, 1970] or ammonium polysulphides ($(NH_4)_2S_x$) (eg. Sill [1976]). These are thought to be formed at or below the visible cloud layers due to the reaction of H_2S gas with NH_3, and as mentioned in the previous section, may even be the principal component of the visible cloud layers. The most serious laboratory experiments to test this hypothesis were made by Lebofsky and Fegley [1976], and more recently by Loeffler et al. [2015, 2016] and Loeffler and Hudson [2018]. These involved irradiating NH_4SH ice using high-energy protons to simulate cosmic radiation, resulting in a substance that was seen to strongly absorb short-wavelength radiation. A more detailed discussion of the results of this experiment will be described in section 4.5.2.

The second group of compounds pertains to the products of phosphine photochemistry in the upper tropospheric haze layers, specifically phosphorus allotropes such as P_4 (eg. Prinn and Owen [1976]). This is thought to be a probable chromophore formation mechanism in Saturn's atmosphere [Fouchet et al., 2009, Fletcher et al., 2015], where ammonia is predicted to be too scarce at visible altitudes to be involved in any substantial chromophore production. However, it has also been proposed in past decades as the chromophore responsible for the colour of the GRS, and other regions where vertical upwelling of phosphine from very deep altitudes is particularly strong [Noy et al., 1981]. We will revisit the possibility of a phosphine chromophore on Jupiter in section 4.5 and on Saturn in section 6.3.

The final group consists of organic compounds, usually resulting from the products of methane photochemistry reacting with the products of ammonia photochemistry in the upper troposphere. This will be the main focus of the work in this thesis. Particular attention has been paid to reactions involving the colourless molecule Hydrogen Cyanide (HCN), which spontaneously forms coloured polymers following condensation at low temperatures in the presence of ammonia gas. These polymers are heavily studied not only due to their astrobiological significance as prebiotics [Matthews, 1991] but also because their colour make them ideal giant planet chromophores, as first suggested by Woeller and Ponnamperuma [1969]. HCN was tentatively detected in the upper atmospheres both of Jupiter [Tokunaga et al., 1980] and Saturn [Weisstein and Serabyn, 1996]. While suggestions have been made for the production of HCN in the deep troposphere [Lewis and Fegley, 1984], the most commonly-studied production method in the laboratory involves the reaction between ammonia and acetylene (C_2H_2) under UV irradiation [Kaye and Strobel, 1983, Ferris and Ishikawa, 1987, 1988], the latter being a common product of methane photochemistry in the stratosphere.

Carlson et al. [2016] (hereon referred to as CR16) most recently measured the optical constants between 0.4 and 0.75µm of the residue resulting from the reaction between ammonia and acetylene following ultraviolet irradiation over a week. While the detection of HCN was inconclusive among the numerous aliphatic hydrocarbon compounds present in the residue, which we will refer to hereon as 'Carlson chromophore', it was seen to provide a good fit to the blue-absorption gradient of a sample GRS spectrum from Cassini/VIMS-V. The main drawback with Carlson chromophore, however, is that it requires an explanation for elevated abundances of acetylene in the troposphere; since any that diffused from higher altitudes would degrade in the lower stratosphere before it got to the upper troposphere [Moses et al., 2010]. One hypothesis by Baines et al. [2019] is that lightning locally elevates acetylene abundances sufficiently for a product like Carlson chromophore to form, but this is speculative given the lack of lightning observed in the GRS by Juno/MWR [Brown et al., 2018]. Nonetheless, Carlson chromophore provides a good starting point for the investigation of Jovian chromophore, as will be shown in chapter 4.

1.4 Temporal changes in visible appearance

1.4.1 Seasonal changes on Saturn

By convention in this thesis, when we talk about a change being 'seasonal', we imply a change in climate that is strictly the result of regular, cyclical variations in solar insolation over a planet's orbital period. Saturn's large obliquity of 26.7^o leads to very substantial seasonal changes over its 29-year orbit. Since the winter hemisphere of Saturn is difficult to observe from the Earth close to solstice, the most comprehensive knowledge of Saturn's seasonal changes comes from the Cassini-Huygens mission, which entered orbit around Saturn at southern summer solstice in 2004, and continued observing Saturn through equinox in 2009 before it ended its mission in 2017 at northern summer solstice. Over this time, it observed and confirmed substantial hemispheric asymmetries in both temperature, composition and aerosol structure.

One noticeable difference in appearance between the summer and winter hemispheres is its colour, a result of the different concentrations of overlying haze. This is shown clearly in figure 1.4.1. The winter hemisphere is characterised by thinner haze, but this does not result in the clear discernment of the tropospheric cloud bands as on Jupiter. The visible spectrum of Saturn's winter hemisphere is therefore dominated instead by Rayleigh scattering of methane gas molecules, as on Uranus and Neptune, which lends it a shade of blue [Edgington et al., 2012]. Saturn's summer hemisphere, on the other hand, is characterised by a yellow colour that most people would associate with the planet, which is due to chromophore produced in the haze layers.

Not all temporal changes in Saturn's visible appearance can be explained by seasonal variation alone, however. Large eruptions known as 'Great White Spots' (GWS) are typically observed once every Saturnian year that lead to substantial upheavals around northern mid-latitudes [Sánchez-Lavega et al., 2016]. The most recent one occurred in 2010-2011, which was earlier in the Saturnian year than predicted given past GWS events. Evidence suggests that this has disrupted the usual stratospheric temperature and circulation patterns relative to the last northern summer in the late 80s [Fletcher et al., 2017a], and hence would also lead to corresponding disruption in the upper troposphere at the haze-tops that should still be detectable in MUSE data. Aside from the GWS event, short-term variations in the brightness and colour of individual latitudinal bands have also been observed, particularly around equatorial and polar latitudes, which are thought to be a consequence of variations in the properties of the chromophore particles in the tropospheric haze [Pérez-Hoyos et al., 2006].

1.4.2 Planetary-scale cyclical changes on Jupiter

As Jupiter has an obliquity of just 3^o, it experiences only negligible seasonal variations over its orbital period, particularly in the troposphere where differences in temperature are more pronounced between zones and belts than between the equator and the poles. Curiously though, we still do see cyclical changes in Jupiter's atmospheric structure, usually with a period of the order of a few years to half a Jovian orbital period. The most famous cyclical phenomenon occurs in the stratosphere, and is analogous to the Quasi-Biennial Oscillation (QBO) on Earth, but instead has an average period of around four years and hence is known as the Quasi-Quadrennial Oscillation (QQO) [Leovy

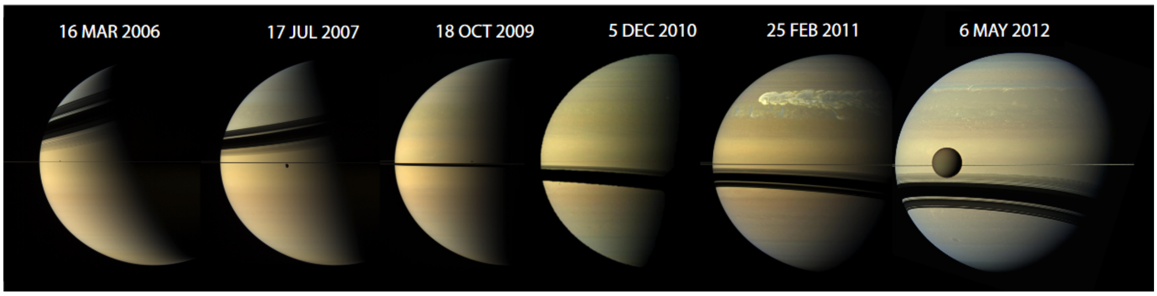

Figure 1.4.1: An illustration of seasonal changes in Saturn's visible appearance from late southern summer to early northern summer, as obtained from the Cassini orbiter. This image is Figure 10.1 in Fletcher et al. [2015]. Note the hemispherical asymmetry in colour particularly in 2006 and 2007, as well as the white streak in the northern mid-latitudes in 2011, a result of a Great White Spot event.

et al., 1991]. A similar phenomenon in the troposphere has also been observed around the equator [Simon-Miller et al., 2007]. However, Jupiter also exhibits a number of 'upheaval' events, in which one or more latitudinal bands drastically changes in appearance and colour, often accompanied by turbulent dynamic activity. The source of most of these upheaval events, and why they are quasi-cyclical, still remains a mystery however. A concise summary of the various cycles is provided by Fletcher [2017].

In this thesis, we focus on three upheaval events in particular that arose between 2014 and 2018. One is the expansion of a portion of the northern half of the NEB into the NTropZ in 2015, before it receded again temporarily in the first half of 2016. This is known as an 'NEB expansion' event, which occurs approximately every 3-5 years as summarised in Fletcher et al. [2017c]. In the middle of 2018, we also witnessed the beginning of an EZ colouration event, in which the northern half of the EZ turned red [Antuñano et al., 2018]. However, the most prominent event throughout our MUSE data is a cycle of disappearance and revival of the southern NTB (NTBs) over a 5 year period (an 'NTBs revival' or 'NTBs upheaval' event). This usually consists of a gradual fading of the red colour of the NTBs, before a dramatic set of outbreaks of convective plumes from the NTBs jet at 23.7N temporarily disrupts the typical zone-belt pattern of the region. This is then followed by the reappearance of a bright red band around the NTBs. This red NTBs band is distinct in appearance from other red belt regions in its spatial homogeneity and brightness, and in fact has more in common with the red colour of the GRS. It has therefore been conjectured by Fletcher [2017] that, if more than one chromophore is indeed present in Jupiter's atmosphere, the NTBs chromophore would have more in common with the GRS chromophore than the other belt chromophores. We provide a greater discussion and analysis of the NTBs upheaval in section 5.3.

1.4.3 Evolution of discrete features

Although discrete features on Jupiter generally do not show observable, quasi-regular cycles in their behaviour, they do often show substantial, unexplained changes in their appearance. In this thesis, we focus on two of these discrete features in particular. The GRS is the largest discrete feature in Jupiter's atmosphere, and has the reddest colour of any region of Jupiter. In recent years, however, it has been shown to shrink dramatically in longitudinal extent, a process that has been accompanied by a visible reddening [Simon et al., 2014, 2018]. The second-largest discrete feature is Oval BA, which since its formation 20 years ago has undergone dramatic changes in colour from white to red, and back to white again. We discuss these two features further in sections 5.5 and 5.6 respectively. Similar changes in smaller discrete features, while also substantial, are difficult to resolve spatially with MUSE, and so are generally excluded from these thesis. However, our MUSE data has also captured dramatic changes in appearance in another discrete feature in the northern hemisphere known as White Spot Z (WSZ). We propose the analysis of this feature as part of future work.

Chapter 2

Instrumentation and data calibration

2.1 Overview

In this chapter, we give a brief introduction to the MUSE instrument, describing how data from it was calibrated and reduced, and then identifying flaws in the calibration processes and how they were alleviated if at all. For reference, we will also present a brief overview in section 2.3 of the Juno probe, in order to provide a contextual overview of how atmospheric retrievals of Jupiter from MUSE can support and complement observations of Jupiter's interior from Juno.

Much of section 2.2, with regards to the instrumentation itself and the ESOREX pipeline, was extracted directly from the latest MUSE[1] and MUSE pipeline[2] user manuals respectively.All Jupiter MUSE observations from 2018 were the result of a proposal (101.C-0097) in which I was Principal Investigator (PI). I was therefore responsible for specifying the required time and longitude of observation in each case, as well as constraints on the observing conditions. However, these observations were conducted in 'Service Mode', where the observation and obtention of the science and calibration data was delegated to an anonymous on-site observer in Paranal, Chile. These were uploaded as raw, uncalibrated and unreduced data to an online repository[3], where I was able to download

---

[1] Document ESO-261650, version 8.12, available at https://www.eso.org/sci/facilities/paranal/instruments/muse/doc/ESO-261650_MUSE_User_Manual_8p12.pdf (accessed 22.02.2019)

[2] Document ESO-264503, version 0.15, available at ftp://ftp.eso.org/pub/dfs/pipelines/muse/muse-pipeline-manual-2.0.1.pdf (accessed 22.02.2019)

[3] http://archive.eso.org/eso/eso_archive_main.html (accessed 22.02.2019)

it myself. The same is true for the remaining MUSE data for which I was not PI, and for which I had no part in the planning of. Jupiter and Saturn observations from 2014, and AO observations of Saturn from 2017, were proposed as commissioning data by the MUSE team themselves, while Jupiter MUSE data from 2016 and 2017 were the result of four proposals (095.C-0149, 096.C-0173, 098.C-0035 and 099.C-0192) with Patrick Irwin as PI. The remaining Saturn data from April 2017, obtained in NOAO mode, was proposed by a different team with Enric Palle (IAC) as PI, under proposal number 298.C-5050. I of course had no contribution to anything presented in section 2.3.

ESOREX is the standard MUSE calibration pipeline, which I had no contribution in designing, and can generally be treated as a black box. However, one can tailor the pipeline to one's own data to some degree, which I did. The MUSE data itself were calibrated entirely by me from start to finish, albeit using other people's software at some stages, which I have specified. This includes the MUSE spectra presented in Irwin et al. [2018, 2019a] which were calibrated according to the procedure we detail in this chapter, although the remaining models and analysis presented in those works are entirely Patrick Irwin's own. IDL codes to project the MUSE data using ellipsoid limb fitting and derive navigational metadata, as well as codes to smooth the MUSE data to lower spectral resolution, were mostly the work of Patrick Irwin (personal communication), though I made substantial contributions, particularly with regards to ring masking of Saturn and more effective derotation of the raw data during projection, as well as the quantification of errors following smoothing. Everything presented in section 2.4.3 is entirely my work, aside from a contribution from Amy Simon of NASA/GSFC [Simon et al., 2015], who provided ready-calibrated and projected 360^o maps, in units of I/F, of the Jupiter and Saturn OPAL data on the MAST website[4].

2.2 An introduction to the MUSE instrument

The Multi-Unit Spectroscopic Explorer (MUSE), is an integral-field spectrograph, which began operation in January 2014 [Bacon et al., 2010]. Its spectral range nominally covers wavelengths from 0.48µm to 0.93µm (though in practice one can usually get reliable radiance values down to 0.476µm and up to 0.933µm), with radiance values sampled at 0.125µm intervals. Another instrument - the New mexico state university Acousto-optic Imaging Camera (NAIC) - has very similar instrumental specifications to MUSE for the most part, and also has a major role to play in Juno's ground support

---

[4] archive.stsci.edu/prepds/opal/ (accessed 22.02.2019)

(eg. Dahl et al. [2018]). However, it can only take individual images, obtained over several minutes, of the planet at a single wavelength at a time, resulting in substantial rotational offsets between the shortest and longest wavelengths. By contrast, MUSE can provide individual spectra over the whole visible hemispheres of Jupiter and Saturn at seeing-limited spatial resolution within an exposure time of a fraction of a second. We provide detailed instrumental specifications for MUSE in Table 2.2.1, and leave a description of the scientific interpretation of MUSE spectra to chapter 3. A major downside of MUSE is that it does not cover the whole visible spectrum down to 0.4µm. This makes it difficult to completely gauge the fit of laboratory chromophores to giant planet spectra over the entire visible range, even though the required data often exists. There is an option to conduct MUSE observations of Jupiter using an extended wavelength range down to 0.46µm. However, this extended wavelength mode is supposedly beset by second-order contamination across most of the near-infrared wavelength range, unlike in the nominal wavelength mode where it is only noticeable above around 0.905µm, as we will explain further in section 2.4.3. We have been granted time in mid-2019 for trial observations of Jupiter and Saturn using the extended wavelength mode, the analysis of which will be left to future work.

	WFM-NOAO-N	WFM-AO-N
Number of CCD modules	24	
Wavelength range	0.48-0.93µm	0.48-0.58µm, 0.60-0.93µm
Resolving Power $\frac{\lambda}{\Delta\lambda}$	1770 (0.48µm) - 3590 (0.93µm)	
Spectral Sampling	1.25Å/pixel	
Field of View	59.9” x 60.0”	
Spatial Sampling	0.2”/pixel	
Seeing-limited spatial resolution (FWHM)	0.3-0.4”	
Throughput (atmosphere + telescope + instrument)	18% (0.48µm) 33% (0.75µm) 14% (0.93µm)	

Table 2.2.1: Technical specifications of relevant MUSE observation modes, adapted from table 1 in the MUSE user manual[1].

Since the end of 2017, MUSE has also been able to make use of Adaptive Optics (AO) [Arsenault et al., 2010, Ströbele et al., 2012], which can correct for the effects of atmospheric seeing by beaming a sodium laser (a ‘Laser Guide Star’) into the sky. This can provide spectral images of planets that are guaranteed to be spatially resolved to within the instrumental constraints, regardless of seeing conditions. However, an observation block with AO takes around 50% longer to execute than one without. Competition for time on MUSE was unusually high in 2018 due to the novelty of MUSE’s AO facility, making it difficult to propose multiple, time-hungry observations of Jupiter. For this reason, all our Jupiter observations were made in the Wide Field Mode (WFM) without the use of adaptive optics and using the nominal wavelength range (WFM-NOAO-N). This turned out not to be too detrimental a decision, as our MUSE datasets from April 2018 were obtained at unusually good seeing conditions (see appendix A). We have, however, been granted time for a trial observation of Jupiter using AO in mid-2019, which we will leave for future work. One set of commissioning data of Saturn using adaptive optics (WFM-AO-N) has been made use of in this thesis; the remaining Saturn datasets were all obtained in mode WFM-NOAO-N as the MUSE AO facility was not available at the time. AO spectra also contain no reliable scientific information within the wavelength range covered by the laser guide star (in practice, between around 0.573μm and 0.604μm inclusive), but this matters little since giant planet spectra have no noticeably distinct features at those wavelengths.

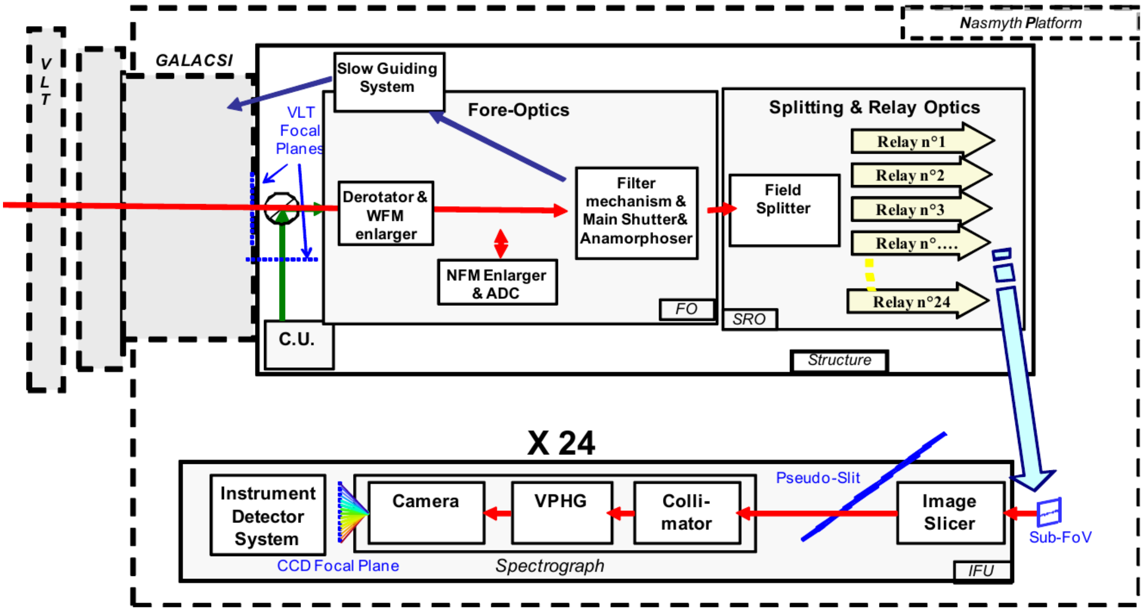

Figure 2.2.1: Schematic of MUSE (equivalent to figure 2 in MUSE user manual[1])

Figure 2.2.1 shows a schematic of the inner apparatus of MUSE in the NOAO mode. Incident radiation is first derotated and magnified in the horizontal direction by a factor of 0.5 in an anamorphoser, with a slow guiding system correcting for small motions by looking at reference background stars. The radiation is then split into 24 individual horizontal beams, each to be redirected into a spectrograph known as an *Integral Field Unit* (IFU) where the beams are analysed in parallel to maximise readout time. At these IFUs, the incident beams are further sliced into 48 one-dimensional ‘slits’, each of thickness 0.2” and width 15”, which are then arranged into a single line along the direction of the slit widths, in the order shown in figure 2.2.2, in front of a Charge-Coupled Device

(CCD). This allows a spectrum to be obtained by dispersing all 48 slits simultaneously perpendicular to the length of the line using a volume phase holographic grating. The CCD then records the voltage produced by the incident photons on each pixel, converting the voltage into a digital signal in units of ADU. This data can subsesquently be processed by a standard pipeline (see section 2.4) to produce a spectral image cube in units of radiance that can be viewed graphically.

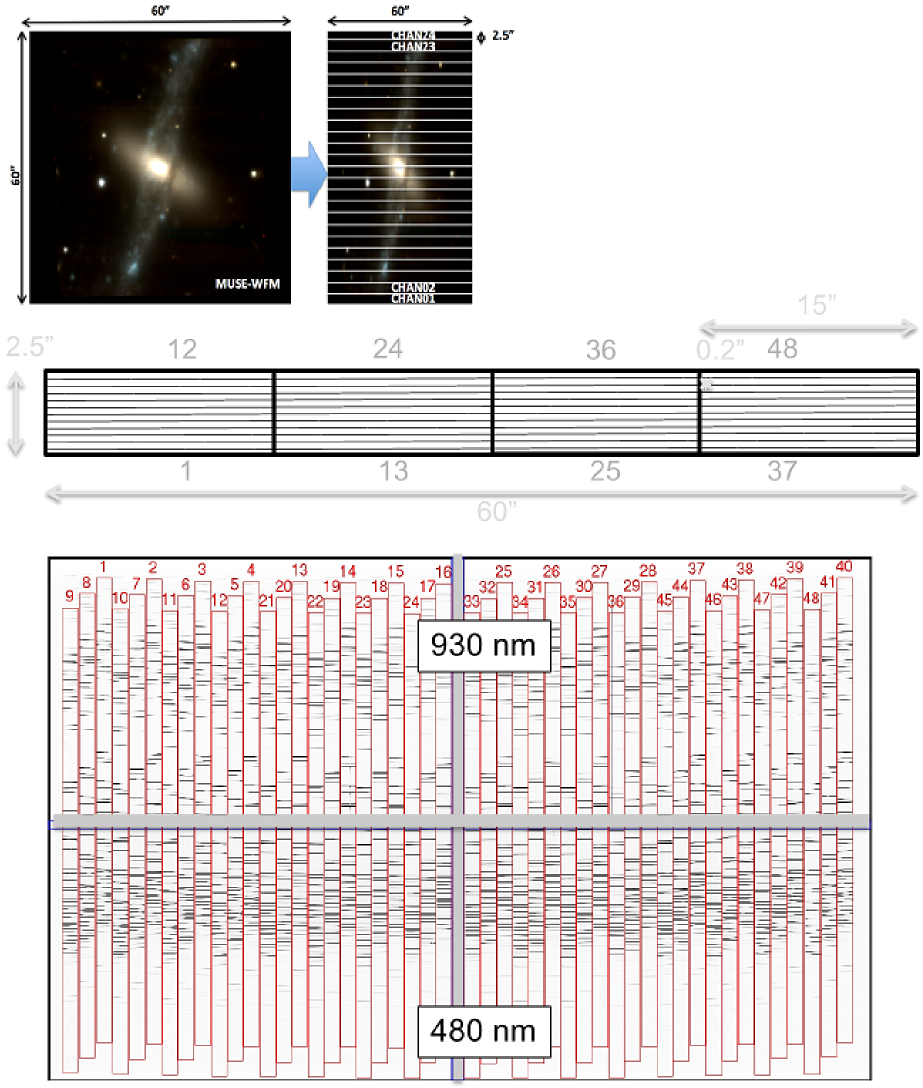

Figure 2.2.2: (*top*) splitting of a MUSE image into 24 horizontal beams, each to be directed to a different IFU, (*centre*) each beam is then split into 48 horizontal slits, which are then lined up horizontally as shown in the bottom diagram, and dispersed perpendicularly (taken from MUSE User Manual, link in overview section 2.1).

A number of sets of Jupiter MUSE data were obtained between 2014 and 2018, which are all listed in appendix A. The Jupiter commissioning data in 2014 consisted of 108 separate observations of Jupiter within a time period of just under 4 hours. Two further sets of observations were made in 2016: one between the 8th and 9th of March, consisting of three 20-minute observation blocks each containing seven individual observations of Jupiter, and another between the 31st of March and 2nd of April, consisting of four 20-minute observation blocks each containing five individual observations of Jupiter. In both of these cases, the observation blocks were designed to provide full longitudinal wavelength coverage in anticipation of the Juno mission that would arrive in orbit around Jupiter later that year. Several more sets of Jupiter observations were made in 2017 and 2018, which each consisted of a single 20-minute observation block of 7 individual observations. These sets of observations were intended to coincide as closely as possible, in both date and longitude, with Juno perijove passes. However, when scheduling the 2017 observations, it was assumed that Juno would increase its orbital period once it went into orbit around Jupiter, which it failed to do as will be explained in section 2.3. This means that the dates of the 2017 observations do not correspond well to the dates when Juno actually achieved its closest approaches to Jupiter.

Three sets of observations were available of Saturn during the same time period, which are also listed in appendix A. The first set of commissioning data was obtained without the use of AO, and consisted of 8 observations within a 20 minute time period on a single night in 2014. An additional commissioning dataset, this time making use of AO, was obtained in June 2017, and consisted of four individual observations. Finally, a set of 43 observations without AO, obtained over a period of an hour on a single night in April 2017, was made by a research team led by Enric Pallé as stated in overview section 2.1. These were originally proposed in order to model Saturn as an exoplanet, but ended up being unusable for that purpose. We make use of these observations with their permission.

2.3 MUSE as ground support for the Juno mission

NASA's JUpiter Near-polar Orbiter (Juno) arrived in orbit around Jupiter in July 2016. It exhibits a highly elliptical $90^{\underline{o}}$ polar orbit, with perijove at 1.06 Jupiter radii and apojove at 39 Jupiter radii, and a period of approximately 53 days. This maximises spatial resolution, coverage and solar illumination, while minimising external damage to the payload from Jupiter's radiation belts [Matousek, 2007, Bolton et al., 2017]. The Juno mission was originally intended to last for 37 orbits until around February 2018, at which point its instruments would be too degraded by radiation to continue science. However, a fault in the propulsion system meant that Juno was unable to decrease its orbital period from 53 days to 14 days as originally planned, in order to provide regular observations of Jupiter at perijove. On the flipside, it also means that Juno spends less time in Jupiter's radiation belts, and so is set to last until at least 2021.

Juno has two main aims that cannot be achieved using ground-based observations alone, both of which are mostly beyond the scope of this thesis and so will only be briefly summarised here. Its orbit is designed to make it the first spacecraft to look directly at Jupiter's polar regions, and hence better analyse auroral emission and the polar radiation field using a number of instruments such as the Jovian Energetic particle Detector Instrument (*JEDI*) [Mauk et al., 2017], the UltraViolet imaging Spectrograph (*UVS*) [Gladstone et al., 2008], a radio and plasma wave sensor (codenamed *Waves*) [Kurth et al., 2017] and a near-infrared image spectrometer known as the Jovian InfraRed Auroral Mapper (*JIRAM*) [Adriani et al., 2008]. The JunoCam instrument [Hansen et al., 2014], although mainly intended for public outreach, was also the first instrument to directly photograph Jupiter's poles at nadir, using three colour filters plus a methane band filter.

Juno's other aim is to map Jupiter's internal structure, and thereby to constrain how Jupiter originally formed at the dawn of the Solar System. To this end, Juno has three on-board instruments to probe different layers of the atmosphere: a *Gravity Science* radiometer [Asmar et al., 2017] to characterise the possible presence of a core, a *Magnetometer* [Connerney et al., 2017] to characterise its metallic hydrogen mantle, and a *Microwave Radiometer* (MWR) [Janssen et al., 2014], which probes the temperature and composition of the deep troposphere. Preliminary findings from the first two instruments were published in Fortney [2018]. The instrument that is most important for our purposes, however, is the MWR, as it is able to map Jupiter's deep ammonia profile from the cloud tops all the way down to around 1000 bars. Preliminary retrievals of deep ammonia abundances from MWR were made by Li et al. [2017], and will be discussed further in section 5.2 in which we relate deep ammonia abundances with those we retrieve at the cloud tops from MUSE.

However, as previously mentioned, Juno has two major setbacks. Firstly, it lacks global spatial coverage due to being in close proximity to Jupiter and having a small field-of-view. Secondly, it lacks completely comprehensive wavelength coverage in order to probe the whole of Jupiter's atmosphere and to hence provide full context to Juno observations. For this reason, further ground-based telescope observations are required, to observe Jupiter as close in date and longitude to each Juno perijove as observational and scheduling constraints will allow. MUSE, together with NAIC as previously mentioned, is able to plug both the gap in spatial coverage (it is able to view an entire hemisphere of Jupiter at a time) and spectral coverage (in the visible and near-IR, at 1nm resolution), so that Juno's observations of the deep ammonia gas profile can be correlated with higher aerosol structure and cloud-top ammonia gas abundances. We will mention some examples of other instruments that make up Juno's ground support in section 3.2. Conversely, UVS, JIRAM and MWR all probe wavelengths that are difficult to observe Jupiter at from the Earth, either due to telluric absorption (in the case of UVS and JIRAM) or synchrotron emission from Jupiter's radiation belt (in the case of MWR) [Berge and Gulkis, 1976].

2.4 Calibration

2.4.1 The ESOREX calibration pipeline - a summary

Each giant planet science observation is calibrated and reduced through a standard data reduction pipeline known as the ESO Recipe EXecution tool (ESOREX) [Ballester et al., 2006]. The steps taken by the ESOREX pipeline are as follows:

- A set of images, each of zero exposure time, are taken with the shutter closed, and averaged together. These are used to remove the read-out signal from the science observations, consisting of a zero level (the *overscan*), and pixel-to-pixel variations from the zero-level (the *bias*).

- A bright lamp is shone at the detector with the shutter closed, in order to obtain a set of 'flat-field' images which are then averaged together. This is used to correct the science observations for variations in the light sensitivity within the slices of each detector, as well as to detect the outline of each slice and any bad pixels.

- A set of three arc lamps (HgCd, Xe and Ne respectively) with known emission lines are then used to map the signal variation across each slice to corresponding wavelength values.

- An additional set of flat-field images of twilight sky is obtained, in order to correct the science observations for general variations in illumination and temperature across the field of view.

- A standard star with a known, smooth radiance spectrum, is observed close in time to the science observation. This is used to derive both the spectral response of the detector (the variation of the signal sensitivity with wavelength), and a telluric spectrum to correct for absorption lines present due to gases in Earth's atmosphere (mostly oxygen and water vapour, as shown in figure 2.4.7).

- The science observation is then corrected for atmospheric refraction, cosmic rays and the radial velocity of the observer, and then divided by the spectral response and the telluric spectrum derived from the standard. This results in a calibrated spectral image cube (with two spatial dimensions and one wavelength dimension), in units of radiance. Spectral uncertainties are also calculated automatically by the pipeline, with the biggest contributions due to telluric correction and interpolation over stellar lines in the standard spectrum, and smaller contributions from the calculation of spectral response and readout noise.

2.4.2 Post-processing and error quantification

Following calibration and reduction by the ESOREX pipeline, each spectral image cube is first projected using ellipsoid limb fitting, in order to calculate the necessary latitude and longitude metadata associated with the cube, as well as incident, viewing and azimuthal angle metadata, which are subsequently tacked on to the spectral image cube as additional extensions. This procedure involves a number of steps. Firstly, a set of ephemeris data for the planet at the time of observation is obtained from JPL/HORIZONS, namely the angle subtended by the planet over the sky (in arcsecs), its angular orientation with respect to the celestial north pole, and the sub-solar and sub-observer latitudes and longitudes. Using this data, and given that the MUSE spatial sampling is 0.2"x0.2" per spatial pixel, an ellipsoid is calculated that approximates the size and shape of the planet as viewed by the observer (we generally use an oblateness value of 0.062 for Jupiter and 0.098 for Saturn), with manual adjustments made to the ellipsoid so that the outer perimeter of the image of the planet fits just within the confines of the ellipsoid. These manual adjustments can be made difficult by the presence of mixing with the sky towards the perimeter (or 'terminator') of the planet due to limb darkening and low spatial resolution, which means that the terminator is not always well-defined and difficult to discern precisely by eye, thereby leading to small systematic errors in the resulting metadata. The metadata are then calculated for each spatial pixel from the intercept between the local vector of line of sight and the ellipsoid using spherical geometry.

Following projection, the spectral resolution of each cube is reduced from 0.125 nm to 1 nm resolution by smoothing it with a triangular function of HWHM = 1 nm (equivalent to the SpeX [Rayner et al., 2003] instrument function). This is done for two main reasons. One is to save computational time and memory, since one MUSE spectrum at native 0.125 nm resolution would contain just over 3600 individual wavelengths. A NEMESIS run on just a single spectrum at native resolution would therefore take several days to complete, given available computing power. The other is that neither solar spectrum data nor accurate methane band data exists at MUSE native resolution. We therefore assume that the majority of absorption lines less than 1 nm wide, particularly at wavelengths shorter than 0.6μm where most of these lines are found, are due to solar Fraunhofer lines. This could also mean, however, that we lose information about characteristic absorption lines of unknown compounds in Jupiter's atmosphere that are otherwise difficult to characterise in the infrared, including possible chromophore compounds. Such an analysis will have to wait until more precise solar and gas absorption data become available. In the meantime we simply assume that the only characteristic feature of chromophore is its single broad absorption band at blue wavelengths.

As a consequence of the central limit theorem, random error is reduced to very small values in the smoothing process, and is therefore neglected. However, the uncertainties produced by the ESOREX pipeline are predominantly systematic, and so cannot be reduced by smoothing. One therefore has to take two additional terms into account when computing the uncertainties of the smoothed spectrum. Firstly, we have to calculate the covariance between adjacent wavelengths induced by the smoothing process. Let us relate the unsmoothed radiance values R_r with the smoothed radiance values R_s using the following equation:

$$\begin{aligned} R_s(\lambda_i) &= \frac{\sum_j \left(1 - \frac{|\lambda_i - \lambda_j|}{2 \times 1nm}\right) R_r(\lambda_j)}{\sum_j \left(1 - \frac{|\lambda_i - \lambda_j|}{2 \times 1nm}\right)} \\ &= \frac{\sum_j W_{ij} R_r(\lambda_j)}{\sum_j W_{ij}} \end{aligned} \tag{2.4.1}$$

where $W_{ij}(\lambda_i, \lambda_j)$ is the SpeX instrument function. Let the variance on each value $R_s(\lambda_i)$ be expressed as a function $\sigma_i^2 + \epsilon_i^2 R_r^2(\lambda_i)$, where σ_i^2 represents random error and $\epsilon_i^2 R_r^2(\lambda_i)$ systematic error. It can therefore be shown that the covariance matrix $\mathbf{C}$ associated with $R_s(\lambda)$ is as follows:

$$\mathbf{C} = \begin{pmatrix} \sigma_1^2 + \epsilon_1^2 R_s^2(\lambda_1) & \epsilon_1\epsilon_2 R_s(\lambda_1)R_s(\lambda_2) & \cdots & \epsilon_1\epsilon_n R_s(\lambda_1)R_s(\lambda_n) \\ \epsilon_2\epsilon_1 R_s(\lambda_2)R_s(\lambda_1) & \sigma_2^2 + \epsilon_2^2 R_s^2(\lambda_2) & \cdots & \epsilon_2\epsilon_n R_s(\lambda_2)R_s(\lambda_n) \\ \vdots & \vdots & \ddots & \vdots \\ \epsilon_n\epsilon_1 R_s(\lambda_n)R_s(\lambda_1) & \epsilon_n\epsilon_2 R_s(\lambda_n)R_s(\lambda_2) & \cdots & \sigma_n^2 + \epsilon_n^2 R_s^2(\lambda_n) \end{pmatrix} \tag{2.4.2}$$

and hence, from standard propagation of errors, the total variance on each wavelength $V(\lambda_i)$ can be expressed as follows, substituting in equations 2.4.1 and 2.4.2:

$$\begin{aligned} V(\lambda_i) &= \sum_j \sum_k C_{jk} \frac{\partial(R_s(\lambda_i))}{\partial(R_r(\lambda_j))} \frac{\partial(R_s(\lambda_i))}{\partial(R_r(\lambda_k))} \\ &= \frac{\sum_j W_{ij}^2(\sigma_j^2 + \epsilon_j^2 R_r^2(\lambda_j))}{\left(\sum_j W_{ij}\right)^2} + \frac{\sum_j \sum_k W_{ij} W_{ik} \epsilon_j \epsilon_k R_r(\lambda_j) R_r(\lambda_k)}{\left(\sum_j W_{ij}\right)^2} \end{aligned} \tag{2.4.3}$$

In the limit where systematic errors are negligible relative to random error ($\epsilon_j^2 R_r^2(\lambda_j) << \sigma_j^2$), the right-hand term of equation 2.4.3 tends to 0, and we derive the standard random error propagation equation assuming no correlation between adjacent wavelengths.

Even when we take covariance into account, however, we find that the uncertainties generally still shrink to unrealistically low values following smoothing. This is because we have to consider what is known as the *bias-variance dilemma* [Geman et al., 1992]. A *bias* is a systematic error that occurs when a spectrum is smoothed to a resolution that is too low, resulting in underfitting. Conversely, if the spectrum is not smoothed to a low enough resolution, then the bias is low, but the variance remains high, resulting in overfitting. We illustrate both possible scenarios in figure 2.4.1. Here, we simply calculate the bias as the absolute difference between the smoothed and unsmoothed spectrum at a given wavelength, and add it to the variance calculated in equation 2.4.3 to give the total uncertainty $\Delta_s(\lambda)$ on $R_s(\lambda)$, neglecting random error:

$$\begin{aligned}\Delta_s(\lambda_i) &= \sqrt{(Bias)^2 + Variance} \\ &= \sqrt{(R_s(\lambda_i) - R_r(\lambda_i))^2 + \frac{\sum_j \left[W_{ij}^2 \epsilon_j^2 R_r^2(\lambda_j) + \sum_k W_{ij} W_{ik} \epsilon_j \epsilon_k R_r(\lambda_j) R_r(\lambda_k)\right]}{\left(\sum_j W_{ij}\right)^2}}\end{aligned} \tag{2.4.4}$$

Our calculation of $\Delta_s(\lambda)$ was seen to encompass most of the intrinsic systematic uncertainties in our spectra, with a few exceptions that we will highlight in section 2.4.3. A discussion on the quantification of uncertainties due to experimental methodology ('forward modelling error') will be provided in section 3.7.

2.4.3 Issues encountered following the standard calibration pipeline and post-processing

2.4.3.1 Systematic offsets in radiance

In order to validate the quality of the MUSE spectra, we use reference data from the Outer Planet Atmospheres Legacy (OPAL) [Simon et al., 2015] project. This involves annual observations, with 360 degree longitudinal coverage, of each of the giant planets using a select number of HST/WFC3 band filters from the UV to the infrared. The five relevant band filters that cover the MUSE wavelength range, named respectively after their central wavelength (in nm), are F502N, F631N and F658N, plus two filters F547M and FQ889N that were used to observe Jupiter and two filters FQ727N and F763M that were used to observe Saturn. However, OPAL observations of Jupiter only started in January 2015, while observations of Saturn only started in June 2018. Mendikoa et al. [2017] obtained meridional reflectivity profiles of Jupiter between 2012 and 2016 from the PlanetCam-UPV/EHU instrument [Mendikoa et al., 2016] (hereon referred to as PlanetCam). However, these published profiles were mostly obtained from filters just outside MUSE's wavelength range (both

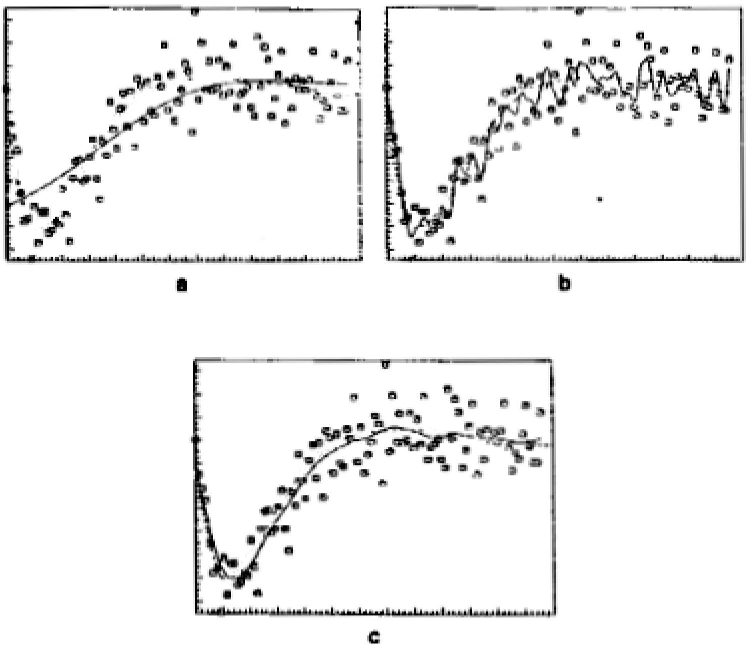

Figure 2.4.1: An illustration of the bias-variance dilemma, as taken from Wahba and Wold [1975], using an arbitrary distribution of variables (for instance, spectral radiances at MUSE native resolution). Figure (a) shows the underfit case, where the curve of best fit (in our case the smoothed spectrum) models the sample distribution poorly near the origin. Hence, the curve has a high *bias*, but a low *variance*. Figure (b) shows the opposite overfit case, where the curve of best fit fluctuates wildly to take outliers into account. This curve has a low *bias*, but a high *variance*. Figure (c) shows the ideal case, where a tradeoff has been made between bias and variance in order to minimise the total uncertainty of the fit. Our own smoothed spectra tend towards the underfit case, as we are limited by the resolution of the reference methane band and solar absorption data.

shortward and longward). In addition, their profiles assumed that the disc-averaged spectrum of Jupiter remained constant over the entire four year period, an assumption that was not valid for years in which Jupiter appeared unusually blue-absorbing as a result of major upheaval events (particularly in 2012). For the MUSE data obtained before the start of the OPAL program, we therefore use the earliest OPAL observations as a baseline for calibration, and use the PlanetCam profiles to qualitatively assess any discrepancies in Jupiter's atmospheric state during the intervening period.

To validate the calibration, we first integrate the MUSE datacubes with each of the aforementioned HST filter functions. We then correct the filtered images for limb darkening through a Minnaert correction, as had been done with the OPAL observations. We retrieve the Minnaert coefficients $k(\lambda)$ as a function of central wavelength λ empirically using the following equations:

$$\begin{aligned} B(\lambda) &= B_0(\lambda)\mu_0^{k(\lambda)}\mu^{k(\lambda)-1} \\ \Longrightarrow \ln(\mu B(\lambda)) &= \ln(B_0(\lambda)) + k(\lambda)\ln(\mu_0\mu) \end{aligned}$$

where B is the observed I/F, B_0 is the I/F where $\mu_0 = 1$ and $\mu = 1$, and $\{\mu_0, \mu\}$ are the cosines of the solar- and viewing zenith angles respectively. Here, the only unknown quantities are $B_0(\lambda)$ and $k(\lambda)$, which we obtain for each latitudinal band of 1 degree width through linear regression of $\ln(\mu B(\lambda))$ against $\ln(\mu_0\mu)$. For each wavelength, the value of $k(\lambda)$ is then averaged over all latitudinal bands within a planetocentric latitude range of $\{-15^o, 30^o\}$ in order to avoid having to take into account darkening towards the poles and discrete features in the southern hemisphere. Using these average values of $k(\lambda)$, we then invert the Minnaert equation to get a cube in values of $B_0(\lambda)$ instead of $B(\lambda)$.

We then extract a single meridional swath from of each of the filtered and corrected MUSE images, averaged within 10 degrees of the sub-observer longitude, and do the same with the corresponding HST images obtained closest in time. Figure 2.4.2 shows a plot of the percentage difference between the MUSE and HST I/F values in each case, with a particular focus on the Jupiter 2014 data in figure 2.4.3. In most cases, the observed I/F values around the equatorial regions and tropics are within approximately 5-10% of each other, with deviations particularly around the SEB mostly due to featural changes that have occurred between the obtention of the MUSE and HST data. Larger deviations as one moves towards mid-latitudes are most likely a result of the rapidly-decreasing spatial resolution, which is substantially smaller for MUSE than it is for HST/WFC3, as one moves away from the sub-observer latitude. In some cases, however, the MUSE I/F values are consistently offset higher, across all latitudes and filters, than their respective HST values. This is most noticeably the case in the 2014 and 2016 data, as well as in the later 2018 data. These offsets cannot be ignored in the 2014 and 2016 data, as they often lead to I/F values that are consistently much greater than 1 in the brightest regions of Jupiter (notably the STropZ), which is unphysical. The source of these offsets is unknown to us, and appears to have nothing to do with either the distance of Jupiter from the Earth or the observing conditions at the time. Variations of the MUSE spectral response, or the choice of standard, are also insufficient to explain such large discrepancies. In the case of the July and September 2018 data, the EZ colouration event should only affect I/F values close to the EZ, but not elsewhere on Jupiter.

For the 2016 data, we therefore choose to scale down I/F values systematically over all wavelengths by approximately 15%, in order to be within 5% of the HST values. Using the HST data alone, however, it is difficult to determine whether to scale the 2014 data according to radiance values in the EZ or the NTropZ, since the appropriate OPAL data was observed almost a year later. PlanetCam observations show the NTropZ gradually decreasing in brightness at continuum wavelengths, starting in 2014. We therefore assessed the MUSE/OPAL discrepancy at the EZ instead, and decided to systematically scale down the MUSE I/F values from 2014 by 20% across all wavelengths, before performing retrievals. In the case of the July and September 2018 observations, the scaling factor is more difficult to determine due to the EZ colouration event, but we find that a 15% downward scaling factor for the July observations and a 20% downward scaling factor for the September observations is sufficient to obtain reasonable I/F values in the STropZ.We observe that the percentage discrepancy between MUSE and HST/WFC3 in FQ889N I/F values is approximately double what it is in the other filters. One factor which partly contributes is the relatively low SNR of the FQ889N band, but this appears to be insufficient to be the sole cause of the discrepancy. The Minnaert correction performed on the OPAL data assumed no limb variation in the FQ889N band ($k = 1$), whereas we observe clear limb brightening ($k > 1$) in the MUSE data at those wavelengths. Again, however, this is insufficient to completely explain the discrepancy. Taking into account brute radiance offsets instead of relative percentage offsets in I/F makes the discrepancies even greater. We may therefore need to take into account the uncertainty in the FQ889N filter function itself. In any case, this will likely lead to some overestimation of retrieved high-altitude haze opacities from the MUSE data, although general meridional variations should still stand.

In Figure 2.4.4 we perform the same analysis using three observations of Saturn and comparing them with a single set of Saturn OPAL data obtained in 2018 at 5 separate wavelength filters. Here, we assume that equatorial I/F values remain roughly constant over the four-year period. We find that the average offset in I/F between MUSE and HST is consistenly within a 5% interval, even despite the temporal evolution of Saturn's brightness (although there does appear to be some discrepancy between AO and non-AO values). For this reason, we performed no scaling on the Saturn MUSE data. Curiously, the F763M filter is offset more than the other filters, perhaps due to uncertainties relating to telluric correction.

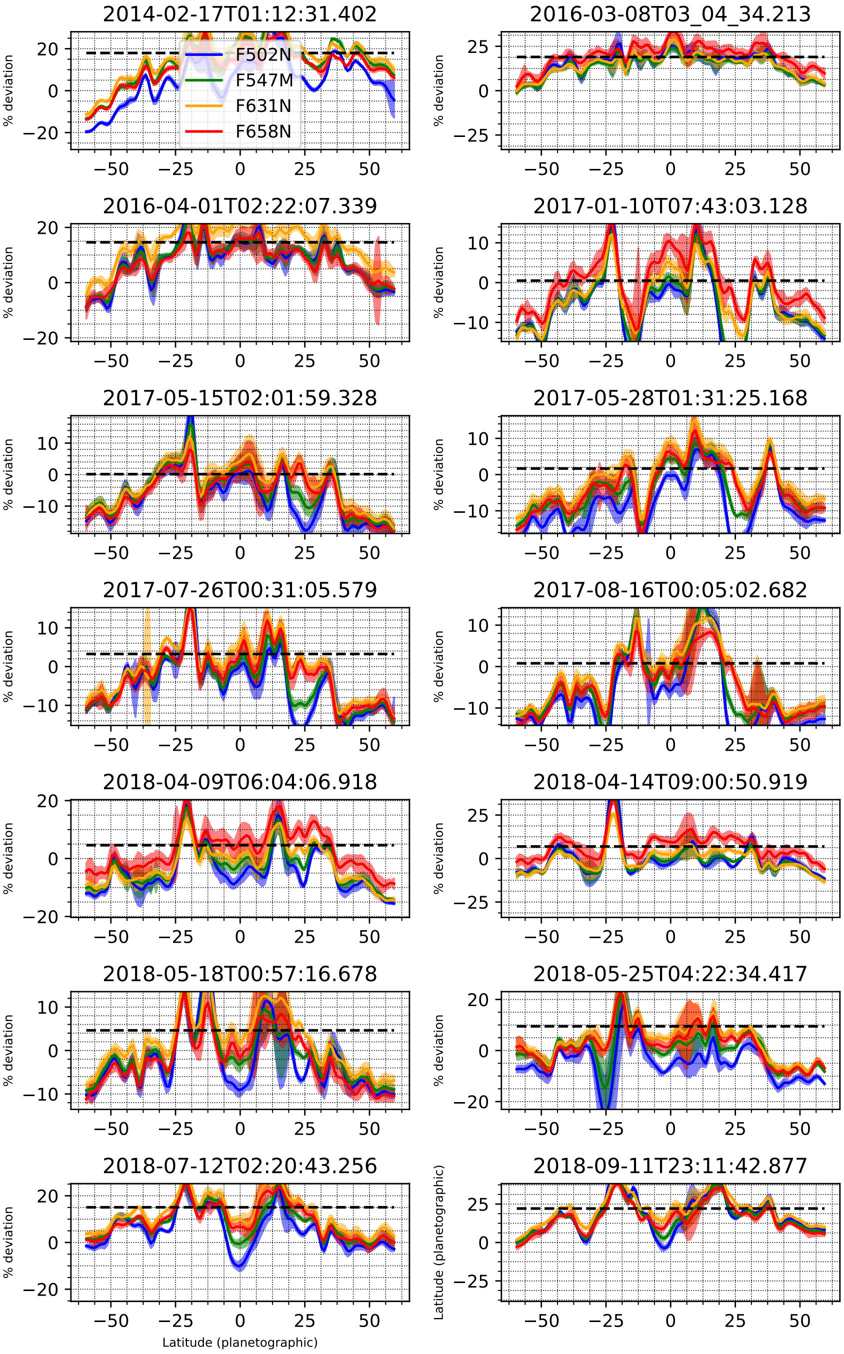

Figure 2.4.2: Percentage difference in latitude swaths: 100*(MUSE-OPAL)/OPAL, both averaged within 10 degrees of MUSE sub-observer longitude, for a number of sample Jupiter MUSE observations. Different colours correspond to different HST/WFC3 filters, as shown in the key in the top left diagram. The FQ889N filter is excluded here as the percentage differences associated with it are substantially larger than those of the other four filters. MUSE observation 2014-02-17T01:12:31.402 is compared with OPAL data from the 19th of January 2015, MUSE observations from 2016 with OPAL data from the 16th of February 2016, MUSE observations from 2017 with data from the 3rd of April 2017, and MUSE observations from 2018 with data from the 17th of April 2018. In each case, the black dashed line shows the percentage offset between the MUSE and OPAL I/F values averaged over all latitudes and wavelength filters except FQ889N.

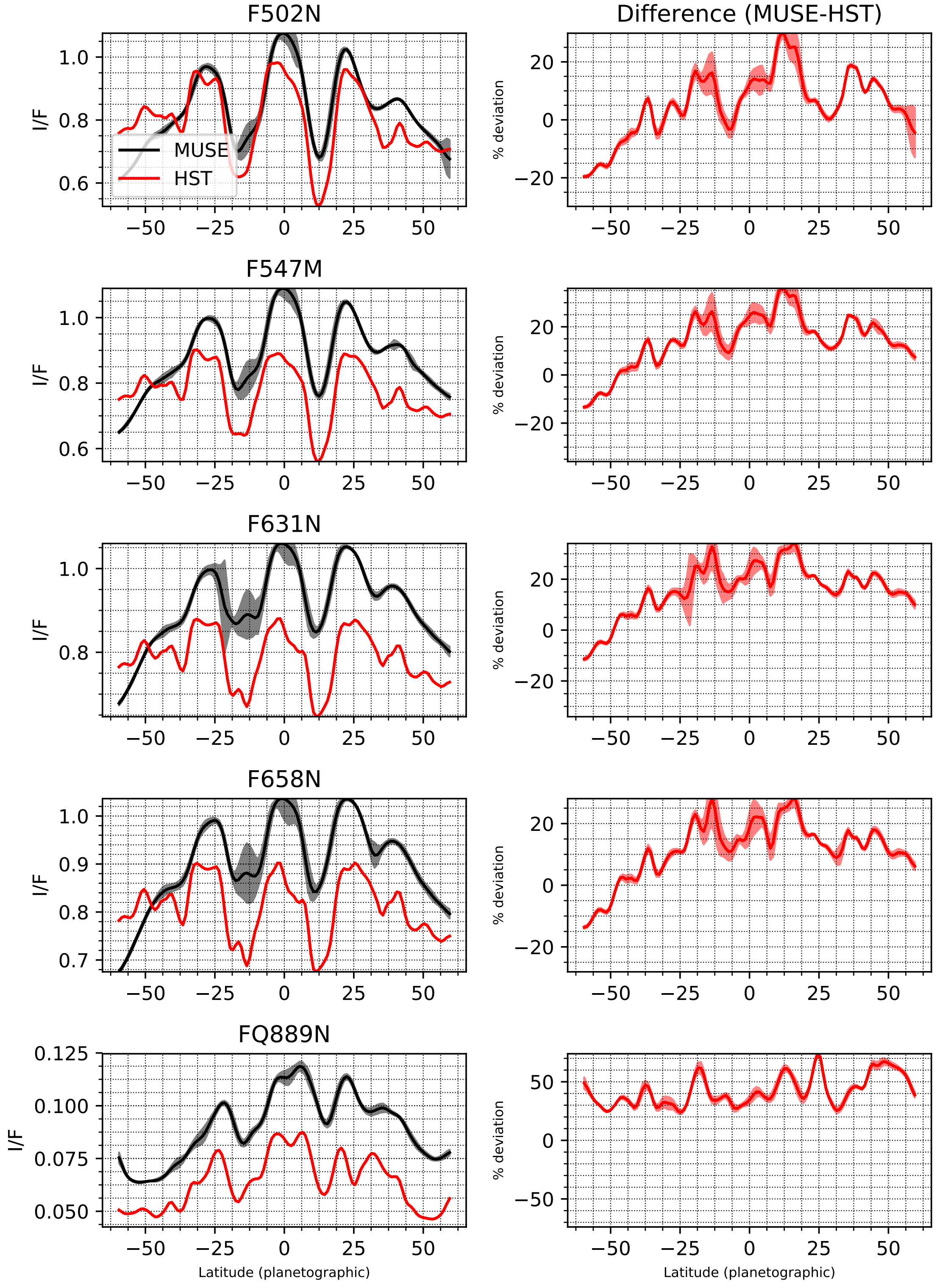

Figure 2.4.3: Left panels: Comparison of I/F values between MUSE observation 2014-02-17T01:12:31.402 and HST OPAL observations from the 19th of January 2015. Swaths correspond to within 10 degrees of 345.4^{o} System III longitude. Right panels show percentage difference 100*(MUSE-OPAL)/OPAL.

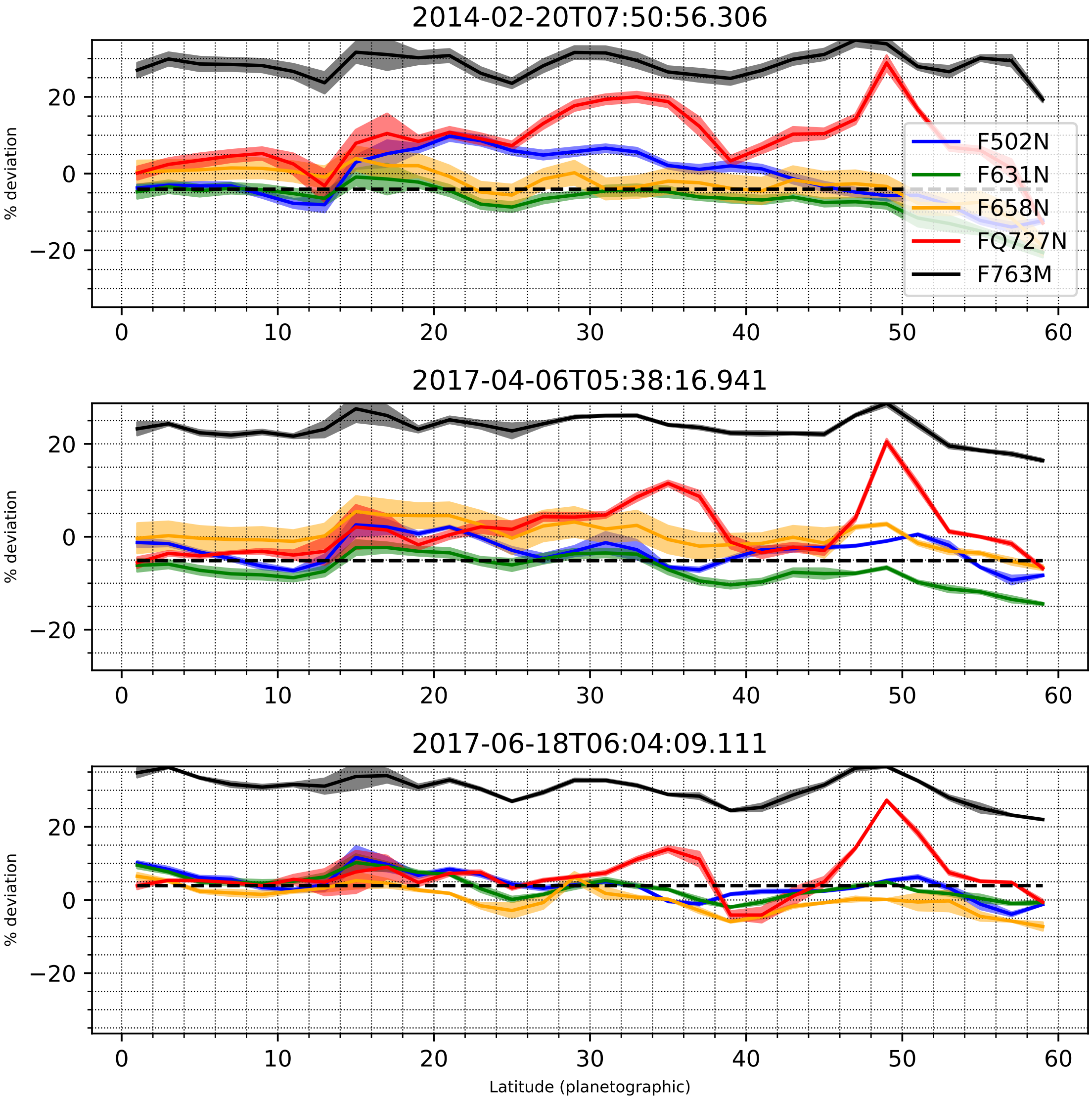

Figure 2.4.4: Percentage difference in latitude swaths: 100*(MUSE-OPAL)/OPAL, both averaged within 10 degrees of MUSE sub-observer longitude, for three sample Saturn MUSE observations. Different colours correspond to different HST/WFC3 filters, as shown in the key in the top diagram. OPAL data was obtained on the 10th of July 2018. In each case, the black dashed line shows the percentage offset between the MUSE and OPAL I/F values averaged over all latitudes and wavelength filters (except F763M).

2.4.3.2 Striping artefacts in commissioning data

A noticeable issue in the 2014 commissioning data is the presence of striping artefacts, where adjacent IFUs that make up the MUSE FOV meet. These are much less visible in later MUSE data and are therefore usually ignored due to their lack of detriment on local atmospheric retrievals (with the exception of dataset 2018-05-25T04:22:34.417, as we will touch on in section 5.5). 2014 observations of Saturn were obtained with the MUSE field of view at a 90° angle relative to the sky, so that the artefacts are aligned vertically with respect to Saturn. As Saturn generally exhibits little longitudinal variation in appearance, it is possible to mostly ignore the artefacts in the Saturn data by selecting longitudes where they are absent. By contrast, the stripes are aligned horizontally in the Jupiter commissioning data, often going straight through important features such as the GRS, and therefore affect retrievals, particularly of cloud and ammonia abundance. The widths of each of the individual IFUs are narrow enough that it is often impossible to select an observation where a large feature such as the GRS is not bisected by at least one of these artefacts. They are also present at all wavelengths, but their positions are not constant with wavelength, making it difficult to simply neglect individual spatial pixels in our analyses. Unfortunately, these commissioning data are the only set of MUSE data that are available from 2014, and since significant morphological changes were observed particularly in the GRS after 2014, they are simply too valuable to discard. It is therefore necessary to destripe these data as much as possible in order to ensure that they can be used for science.

It is unclear why these artefacts are only noticeable in 2014 data. One factor may be the lamp flat-fields themselves. All lamp flat-fields show vignetting around the edges of each IFU due to gaps in the field-splitter lenses, but this is usually taken into account in the calibration process and has not changed noticeably over time. The commissioning flat-fields do exhibit a larger number of striping artefacts themselves, due to the presence of dust in the instrumentation, than in subsequent flat-fields, but they are insufficient to completely explain the number of artefacts in the reduced data. Another factor may be due to the quality of geometric calibration, which may have inaccuracies in where to replace each IFU onto the MUSE field-of-view following calibration. This would also explain the tell-tale signal of the striping artefacts, usually consisting of a local horizontal trough adjacent to a local horizontal spike in radiance. Again, however, the geometric calibration process did not change substantially after 2014.

To destripe the commissioning data, we first linearly interpolated over any lines where there was a clear horizontal trough next to a horizontal spike, and then added on the resulting difference in radiance to the total spectral error as a bias term. However, abrupt changes in radiance between adjacent IFUs were still clearly visible after this. We therefore convolved each observation further with a Gaussian kernel $G(x, y)$:

$$G(x, y) = \frac{1}{2\pi\sigma^2} \exp\left(-\frac{x^2 + y^2}{2\sigma^2}\right)$$

where x and y are respectively the horizontal and vertical widths of the kernel, which are set so

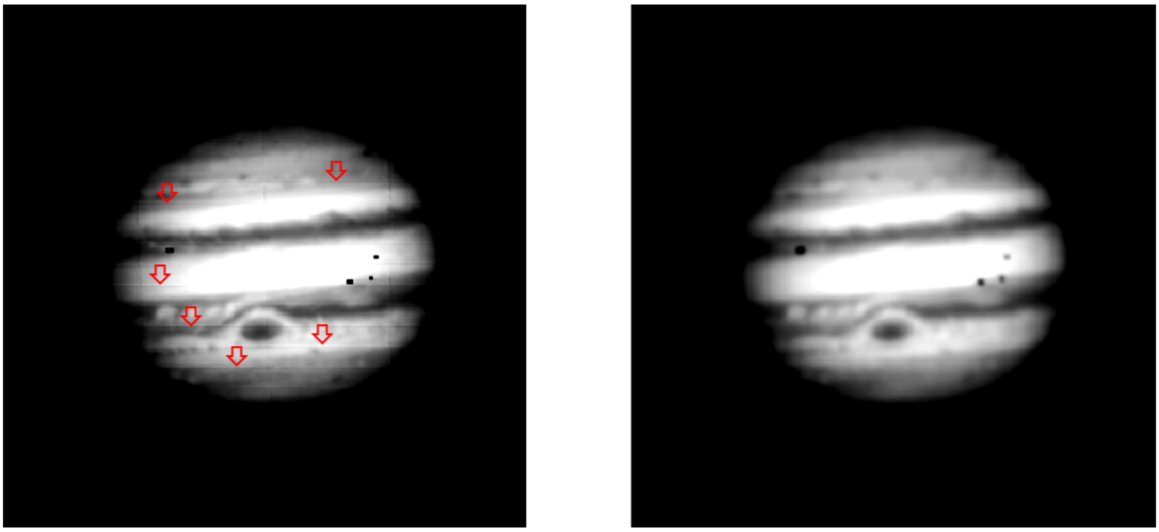

Figure 2.4.5: Image of Jupiter (2014-02-17T02:07:56.907) at 0.480µm, (left) before destriping, (right) after destriping. The most obvious stripes in the left image are indicated by the red arrows. Note the effect of the stripes in the left image particularly on the colour of the GRS. The contrast has been exaggerated in both of these images in order to make the striping clearer to the reader of the print version of this thesis.

that the kernel contains approximately three standard deviations in both dimensions. A value of $\sigma = 1.5$ was seen to smooth over the worst effects of the artefacts, as shown in figure 2.4.5, without excessively degrading the spatial resolution.

2.4.3.3 Second-order contamination

In all our MUSE data of Jupiter, we also observe very noticeable striping artefacts at the longest continuum wavelengths, starting to be discernable around 0.905µm but becoming stronger with increasing wavelength. A demonstration of these artefacts is shown in figure 2.4.6. These are a consequence of second-order contamination, an optical aberration caused by imperfect dispersion of light incident on the detectors, resulting in interference between secondary diffraction orders. The brighter and more extended the object, the more the effect is visible. This explains why the striping artefacts are much less apparent in spectra of Saturn, even when close to opposition. In our Saturn data obtained using AO, they are barely visible at all. We made no effort to correct for second-order contamination in either our Jupiter or Saturn data, however we still decided not to exclude wavelengths above 0.905µm in our retrievals, due to the information it contained on both ammonia abundances and deep cloud cover where Rayleigh scattering could be neglected. Spectral retrievals from locations where second-order contamination was particularly egregious (usually, but not exclusively, in regions of Jupiter far from the sub-observer point) usually resulted in poor fits at

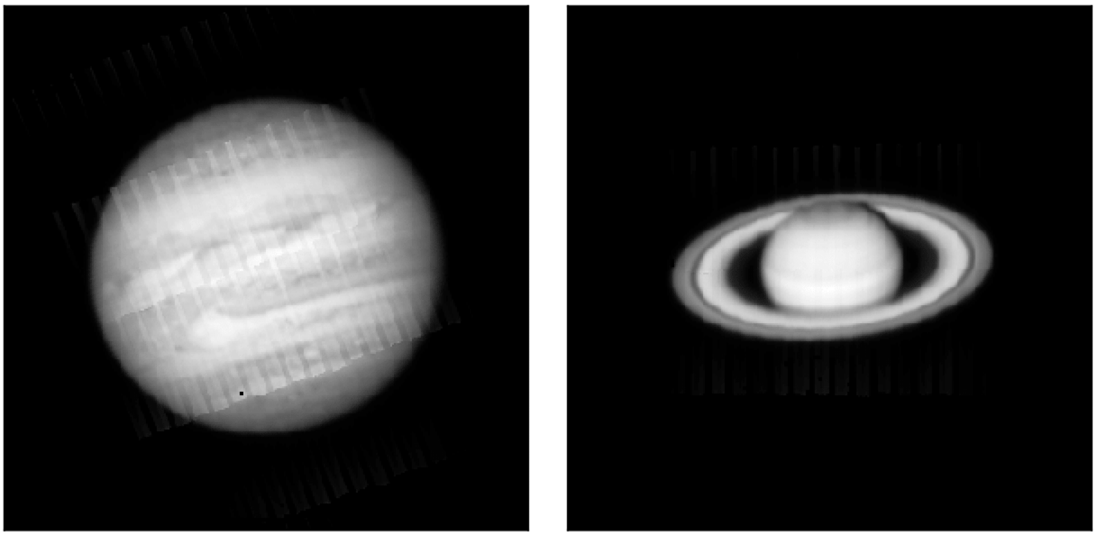

Figure 2.4.6: Images of (*left*) Jupiter from dataset 2018-04-09T06:04:06.918 and (*right*) Saturn from dataset 2017-04-06T05:38:16.941, both at a wavelength of 0.930µm where the presence of second-order contamination is most apparent. The resulting artefacts are visible in the Saturn image as vertical stripes. We note that the orientation of these striping artefacts are dependent on the orientation of the MUSE field-of-view and are therefore not necessarily aligned vertically with respect to the planet.

continuum wavelengths above 0.91µm but little noticeable deficiency to the fit at other wavelengths. Second-order contamination was therefore not seen to have a particularly strong detriment to the retrieval of any atmospheric variables, aside from in terms of χ^2/n.

2.4.3.4 Large airmass differences between standard and science

Although ESOREX theoretically corrects for airmass differences between the standard star and the science observation, it does so imperfectly particularly when the difference is large. This can have a major impact on the shape of the resulting MUSE spectra. The most noticeable sign of a large airmass difference is in the shape of the spectrum at wavelengths of high telluric absorption: if the airmass of the science is much larger than that of the standard, then the depths of telluric lines are overestimated and one obtains large spikes in I/F at those wavelengths. Conversely, if the airmass of the science is much smaller than that of the standard, the depths of telluric lines are underestimated and one obtains deep absorption peaks in I/F. These effects are clearly shown in figure 2.4.7. Generally, these wavelengths have a low signal-to-noise ratio and do not contain substantial scientific information that cannot also be found at other wavelengths unaffected by telluric absorption. Nonetheless, it is still important to know the effect of airmass differences on these wavelengths. In Irwin et al. [2018], the effect of ammonia absorption around 0.76µm was overestimated, as that wavelength region is also home to the largest telluric absorption feature in the MUSE wavelength range, as later clarified in Irwin et al. [2019a]. However, such airmass discrepancies can also have other effects on more important wavelengths. One is around the shallow, but broad, telluric ozone absorption feature at 0.6µm, which is usually taken into account by MUSE as part of the spectral response instead of as a telluric absorption feature. This means that if there are large airmass discrepancies between the standard and the science, the ozone absorption feature will not be properly accounted for. In addition, large airmass discrepancies could lead to a slight 'slant' in the spectrum, where I/F values at blue wavelengths are overestimated while I/F values in the near-infrared are underestimated, or vice versa, due to miscalculation of telluric Rayleigh scattering. This could mean that the forward model requires erroneous particle sizes to fit the spectrum, as well as unrealistic chromophore optical constants. It is for this reason that we chose to refine our forward model in Chapter 4 on one single observation of Jupiter: 2018-04-09T06:04:06.918, which had an airmass difference of less than 0.01 between the standard and science, both of which were observed at airmass values close to 1. Once the forward model was perfected on that observation, the analysis could be extended to the remaining Jupiter observations in chapter 5 where the quality of calibration was less reliable.

For a few datasets (as stated in appendix A), the quality of the standard provided by the observatory was so poor that it could not be used to derive the MUSE spectral response. In these cases, we calibrated the science using a sample spectral response curve provided with the ESOREX pipeline software, and then performed telluric correction using the supplied standard. This usually resulted in spectra of Jupiter that appeared reasonable to first order, except at wavelengths below 0.48µm which had to be discarded.

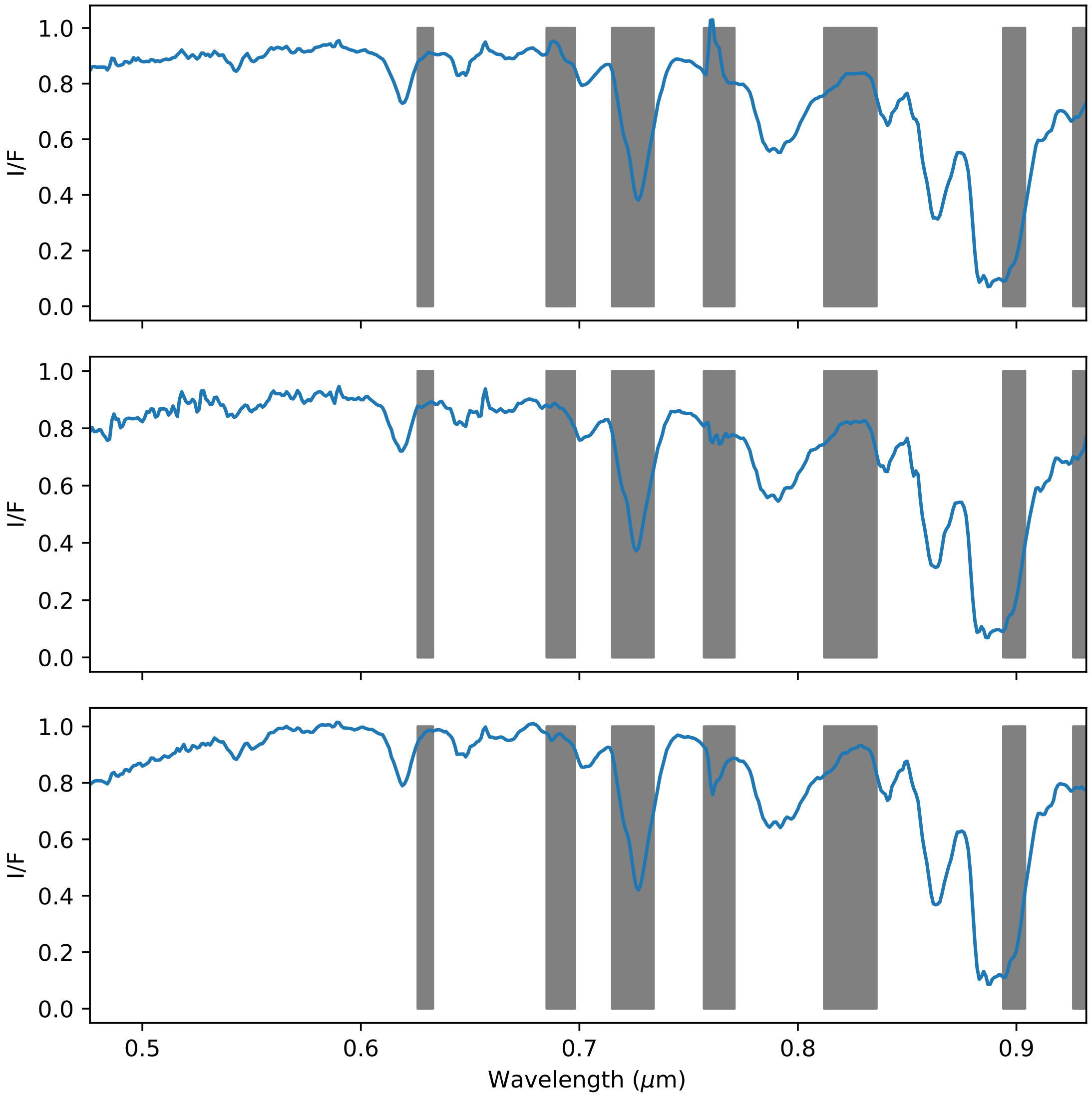

Figure 2.4.7: Examples of the effect of airmass discrepancies between an observation of Jupiter and its associated observatory standard on a MUSE spectrum. Grey bars indicate wavelength regions in which telluric absorption is significant. The largest telluric absorption features (around 0.63µm, 0.69µm and 0.76µm) are due to oxygen, the remaining features are due to water vapour. Top spectrum is from 2017-08-16T00:05:02.682, an example of an observation obtained at high airmass relative to the standard. Bottom spectrum is from 2018-07-12T02:20:43.256, an example where the standard was obtained at a high airmass relative to the science observation. Middle spectrum (from 2018-04-09T06:04:06.918) shows a near-optimal case.

Chapter 3

Using NEMESIS to model and retrieve atmospheric parameters

3.1 Introduction to NEMESIS

In this chapter, we will explain what information is contained in remotely-sensed giant planet spectra, and how it can be extracted from the spectra in order to obtain useful atmospheric data about the planet in question. This is performed using an algorithm known as the Non-linear optimal Estimator for MultivariatE Spectral analySIS (NEMESIS) [Irwin et al., 2008], which is multi-purpose and can be applied to a wide range of planetary atmospheres, be they terrestrial or gas giant, hot or cold, or scattering and non-scattering, as well as to a wide range of spectral wavelengths from the ultraviolet to the microwave.

There are two main stages of the NEMESIS algorithm. The first is that of the *forward model*, in which NEMESIS uses a set of initial, or *prior*, estimates of the various parameters that one wishes to obtain (the *state vector*), together with a fixed reference atmosphere consisting of estimates of other atmospheric parameters that one cannot obtain from the spectrum (such as, in the case of MUSE spectra, a vertical pressure-temperature profile), and then uses physics to model an initial spectrum. The theory behind how one models a spectrum from a set of state vector values is explained in sections 3.3-3.6. The second is that of the *retrieval*, in which the state vector, and hence the resulting model spectrum, is iteratively re-computed through a process known as *spectral inversion,* until the model spectrum converges to a solution which, if the retrieval goes well, should

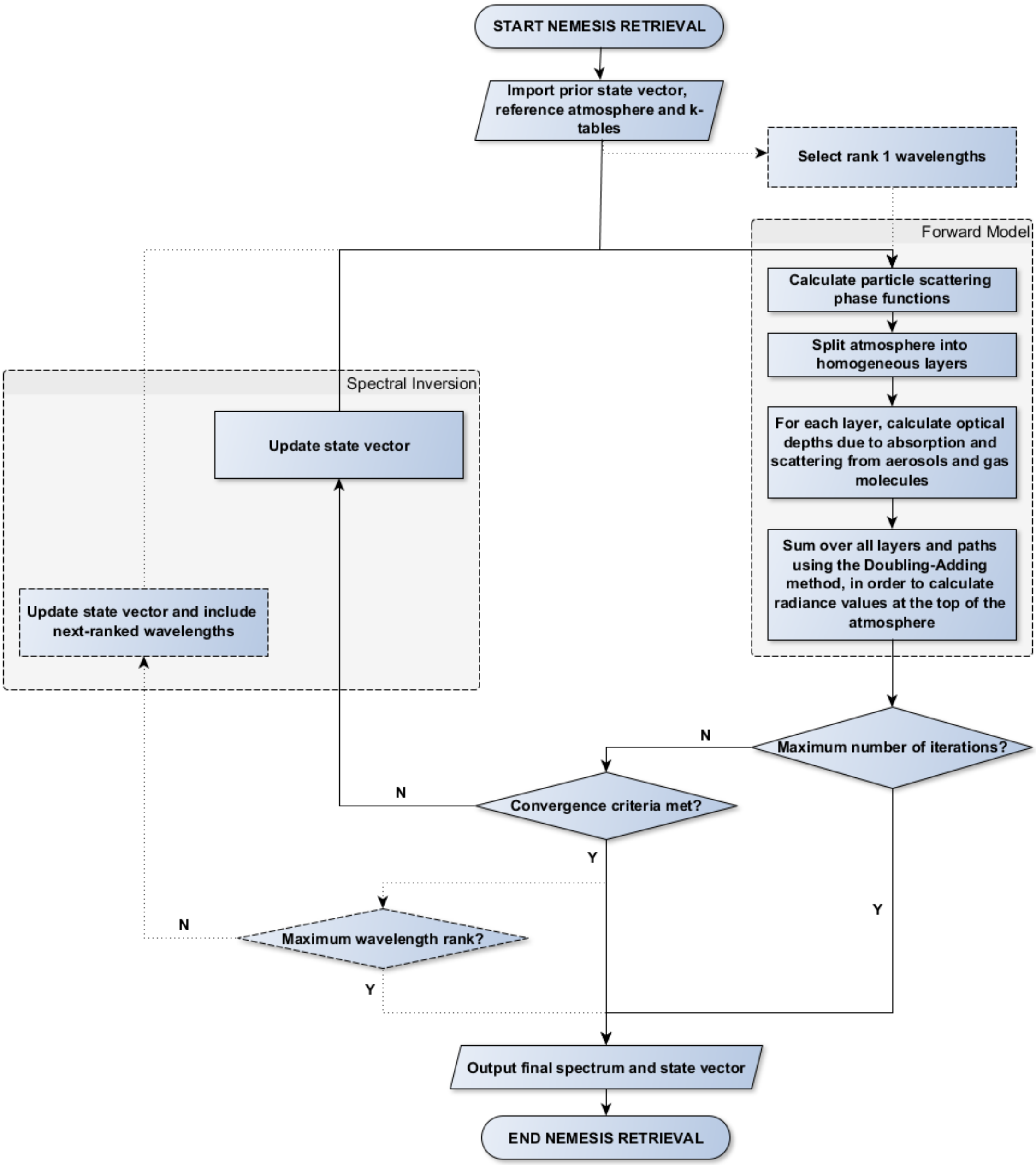

Figure 3.1.1: NEMESIS flow chart, adapted from Barstow [2012]. Dotted arrows indicate steps that only apply when using a reduced wavelength scheme.

match, or *fit*, the observed giant planet spectrum as closely as possible. This stage is detailed in section 3.7. NEMESIS can, however, take a very long time to converge to a solution if there is too much spectral data or if the amount of information to retrieve from the spectrum is too great. Section 3.8 therefore details how the retrievals were optimised to save as much time while retaining as much accuracy as possible. A full diagram of the NEMESIS algorithm is given in figure 3.1.1.

3.2 Giant planet spectra from ultraviolet to radio wavelengths

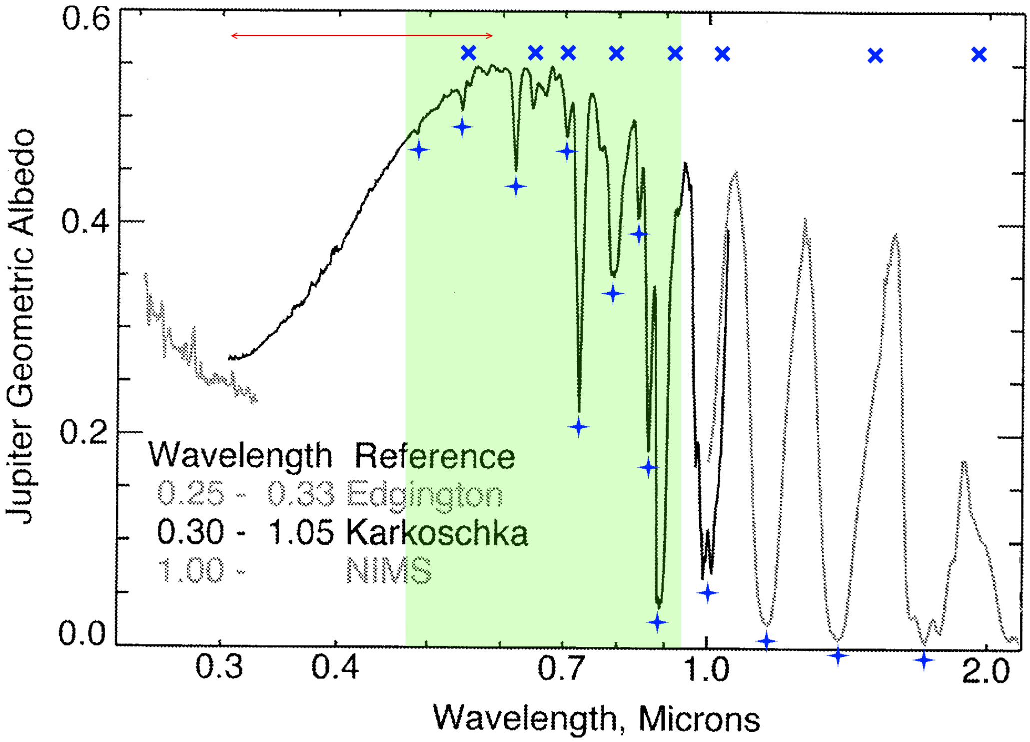

Figure 3.2.1: Sample disc-averaged spectra of Jupiter from the near-UV to the near-IR, adapted from figure A1.1 in Spencer et al. [2004]. References given in the legend are Edgington et al. [1998, 1999], Karkoschka [1998] and for NIMS, Carlson et al. [1996]. The locations of the most important methane and ammonia absorption features have been highlighted using straight and diagonal blue crosses respectively, while the broad chromophore absorption feature has been highlighted using the red arrow. We highlight the MUSE wavelength range in green. The general shape of Saturn disc-averaged spectra is similar, but with larger methane and smaller ammonia absorption features respectively.

In this section, we will give a brief overview of the main processes that govern the shapes of giant planet spectra from the near-UV to the longwave, and hence describe the main aspects of the atmospheres of Jupiter and Saturn that can be retrieved from the different wavelength regimes through remote sensing. In each case, we will also provide some examples of instruments (either from Juno itself or its ground support) that currently observe or have observed in these regimes. Although this thesis mostly focuses only on the visible and near-infrared from 0.476µm to 0.933µm, we will refer regularly to findings of different atmospheric variables in the literature that we are not sensitive to in the MUSE wavelength range, in order to provide context to our own MUSE observations. This section is mostly adapted from Rogers [1995] and Irwin [2008], and we show the main features of Jovian spectra from the near-UV to the near-IR pictorially in figure 3.2.1. We will ignore wavelengths shorter than around 0.2µm, where solar radiation becomes ionising and therefore cannot penetrate far into the atmosphere.

- **Mid- and near-UV (0.2-0.4µm):** Spectra at these wavelengths are dominated by both Rayleigh scattering of sunlight and the photolysis of different gases (primarily methane, ammonia and acetylene) in the high atmosphere, both of which prevent incident radiation from penetrating far into the atmosphere. Sensitive mainly to stratospheric haze. E.g. Juno/UVS, HST/STIS, the lowest wavelength filters of HST/WFC3.
- **Visible (0.4-0.7µm):** The wavelength regime at which solar spectral irradiation peaks. Rayleigh scattering becomes less important with increasing wavelength, allowing deeper altitudes to be probed. Chromophore absorption dominates at shorter wavelengths, while weak absorption features of methane and ammonia are found towards longer wavelengths. Sensitive mainly to colour, with some sensitivity to cloud and ammonia gas. E.g. Cassini/VIMS-V, JunoCam, Cassini/ISS, some HST/WFC3 filters.
- **Near-IR (0.7-5µm):** Dominated both by the reflection of sunlight by aerosol particles and the absorption of sunlight by methane and ammonia gas. Generally, these gas absorption features become stronger with increasing wavelength, allowing vertical aerosol structure to be probed, as will be explained further in section 3.4. Thermal emission can still mostly be neglected due to the low brightness temperatures of Jupiter and Saturn. Sensitive mainly to tropospheric and stratospheric aerosol structure, as well as ammonia gas and, to a lesser extent, collision-induced absorption of H_2-H_2 and H_2-He. E.g. Cassini/VIMS-IR, IRTF/SpeX, Galileo/NIMS, Juno/JIRAM, the highest HST/WFC3 wavelength filters.
- **Mid- or thermal-IR (5-20µm):** At these wavelengths, reflected sunlight becomes less significant and thermal blackbody emission from the planet itself starts to dominate. This wavelength regime also contains absorption features of many different compounds such ammonia,

methane, water vapour, hydrocarbons (notably acetylene and ethane), disequilibrium species (such as phosphine) and H_2 and He through collision-induced absorption. Sensitive mainly to variations in temperature and composition with height. Some upper tropospheric aerosol structure can also be probed at longer wavelengths, but not to the same vertical precision as in the near-IR. In the region around 5μm (the so-called '5-micron window') [Gillett et al., 1969] , the atmosphere becomes particularly transparent to absorption and reflection, allowing deeper cloud structure to be probed. E.g. VLT/VISIR, Cassini/CIRS, IRTF/TEXES.

- **Far-IR, Microwave and Radio (20μm-):** The atmospheres of Jupiter and Saturn become very transparent to cloud structure at these wavelengths, but strong absorption features (particularly of ammonia gas) remain well into the radio regime. Sensitive to deep compositional structure, with little to no degeneracy with cloud. E.g. Juno/MWR, VLA.

3.3 Radiative Transfer theory

To model a giant planet spectrum in the visible-to-near-IR, one has to trace how solar photons are absorbed and reflected by the planetary atmosphere in question, to produce a given spectral radiance at the top of the atmosphere (TOA), which equals the spectral radiance observed from the Earth following correction for telluric absorption. The plane-parallel approximation is valid at all but the highest viewing zenith angles, as the thickness of the layer of atmosphere that is probed by MUSE is very small compared with the radii of the planets themselves, and pressures are sufficient for Local Thermodynamic Equilibrium (LTE) to hold. The derivations shown here are all taken from, and described more fully in, Irwin [2008] and Andrews [2010].

Consider a beam of spectral radiance L_ν incident at an angle θ_s from zenith and azimuth ϕ_s, passing through a discrete layer of atmosphere of thickness dz from an initial altitude z_0 to an altitude z, containing some absorbant molecules of mass density ρ_a. From the Beer-Lambert Law, and assuming a local source of radiance J_ν, the resulting change in radiance dL_ν through the layer is given by:

$$dL_\nu = -\frac{1}{\cos\theta_s} k_\nu(z)\rho_a(z)(L_\nu(z) - J_\nu(z))dz \tag{3.3.1}$$

where the term $k_\nu(z)$ is an *extinction coefficient* characteristic of the absorbing gas. The way this is calculated for MUSE spectra will be shown in more detail in section 3.4.

We then define a quantity τ_ν known as the *optical thickness*, and a quantity T known as the *transmission* which quantifies the fraction of incident radiation that is transmitted through a given layer of atmosphere:

$$T = \exp(-\tau_\nu(z)) = \exp(-\int_{z_0}^{z} k_\nu(z')\rho_a(z')dz') \tag{3.3.2}$$

and hence:

$$\cos\theta_s \frac{dL_\nu(\tau_\nu)}{d\tau_\nu} = L_\nu(\tau_\nu) - J_\nu \tag{3.3.3}$$

At the wavelengths MUSE is sensitive to, the principal source of radiance would be light scattered into the beam by aerosol particles present in the atmospheric layer. Let the effective extinction cross-section σ_{ext} of these aerosols be divided into an absorbing component σ_{abs} and a scattering component σ_{sca}. First, we define a parameter ω_0 known as the *single-scattering albedo,* which defines the likelihood of an aerosol particle to scatter a photon at a given wavelength λ instead of absorbing it:

$$\omega_0(\lambda) = \frac{\sigma_{sca}(\lambda)}{\sigma_{sca}(\lambda) + \sigma_{abs}(\lambda)} = \frac{\sigma_{sca}(\lambda)}{\sigma_{ext}(\lambda)} \tag{3.3.4}$$

An aerosol particle with $\omega_0(\lambda) = 1$ is known as a *conservative scatterer.*

We then expand J_ν to take into account the full solution for multiple scattering as derived by Hanel et al. [2003]. The resulting equation is known as the *Radiative Transfer Equation:*

$$\begin{aligned} \cos\theta_s \frac{dL_\nu(\tau_\nu, \cos\theta_s, \phi_s)}{d\tau_\nu} &= L_\nu(\tau_\nu, \cos\theta_s, \phi_s) \qquad (3.3.5) \\ &-\frac{\omega_0(\tau_\nu)}{4\pi}\left(\int_0^{2\pi}\int_{-1}^{1} P(\cos\theta_s, \phi, \cos\theta', \phi')L_\nu(\tau_\nu, \cos\theta', \phi')d\cos\theta' d\phi'\right) \end{aligned}$$

where θ' and ϕ' are the respective zenith and azimuth angles at which the aerosol particle scatters the incident radiation. The term P is an intrinsic property of the particle known as the *phase function*, which defines the probability that the particle scatters light at a given angle, and will be further described in section 3.5.

To solve this equation, NEMESIS splits the reference atmosphere vertically into 39 separate homogeneous layers according to a scheme which will be described in section 4.2. The atmospheric composition, temperature and density are all assumed invariant within each homogeneous layer.

NEMESIS then solves the radiative transfer equation for each homogeneous layer numerically using the Doubling-Adding method detailed by Plass et al. [1973], in each case starting from a single infinitesimally thin layer where single scattering applies. The integration over viewing zenith angle is performed using Gaussian-Lobatto quadrature, while the integration over azimuth is performed using Fourier decomposition. Solving the radiative transfer equation at a higher viewing zenith angle requires a larger number of Fourier azimuth components to compute, and so the further the location on the planet from the sub-observer point, the longer NEMESIS requires to model a spectrum from that location.

3.4 Gas absorption features in giant planet spectra

In the previous section, we explained how the radiative transfer equation could be solved if one knew the extinction coefficient of a gas molecule at a given wavelength. In this section, which mostly paraphrases Straughan [1976] and Irwin [2008], we will describe the different processes that would result in such molecular gas absorption.

As was explained in section 1.3, molecular absorption at short wavelengths as found in chromophore is most likely a result of electronic transitions either within an atom itself or a molecular bond. However, at longer wavelengths, two other energy absorption mechanisms dominate. One is that of a *vibrational* transition, in which a molecular bond, analogously to a spring, can absorb energy from a photon (usually through a change in the electric dipole moment) to bend and stretch at discrete frequency values following simple harmonic motion. Taking into account the number of different bonds that can be excited, this results in $3N$-6 degrees of freedom, where N is the number of atoms in a given non-linear molecule. Hence, the resulting fundamental frequencies of each vibrational degree of freedom, or *vibrational modes*, are labelled from ν_1 to ν_{3N-6} in ascending order of energy. The other is that of a *rotational* transition, in which a molecule can absorb energy by gaining angular momentum. The resulting number of additional degrees of freedom ranges from 1, for a spherical top (such as CH_4) with equal moments of inertia about all three principal axes, to 3 for asymmetric tops (such as H_2O) where each principal axis has a different moment of inertia.

Although purely rotational energy transitions are several orders of magnitude smaller than purely vibrational transitions, and therefore only occur in the far-infrared, they often coincide with vibrational transitions to form *vibration-rotation bands* that are present in the near- and mid-infrared. However, even these cannot occur at sufficient frequencies to form absorption features at MUSE wavelengths. One therefore needs to take into account both *overtones*, where a vibration is excited to frequencies above the fundamental mode (labelled $2\nu_1$, $3\nu_1$ etc.), and *combinations*, where two or more bonds are excited simultaneously (eg. $\nu_1 + \nu_2$). While these are more energetic than fundamental vibration-rotation transitions, they are also less likely to occur, and therefore form weaker absorption bands.

Jupiter and Saturn's atmospheres are composed mainly of H_2 and He gases. The latter is monatomic and therefore has no rotational or vibrational degrees of freedom to induce spectral features at these wavelengths. H_2 is a homonuclear diatomic molecule for which changes in the electric dipole moment cannot occur, but weak absorption bands can be formed through other means. Induced changes in the *quadrupole* moment of H_2 can lead to absorption features in the visible and near-IR, but these are very weak and will be neglected here. Temporary dipoles in H_2 molecules can also be induced through collisions either with other H_2 molecules or with helium atoms, and although the dipoles induced in this way are very small, the sheer number of H_2 and He molecules on Jupiter produces clear *collision-induced absorption* (CIA) bands. The largest absorption bands at MUSE wavelengths are however due to methane and ammonia gas, which are the next-most abundant compounds above the cloud tops. These absorption bands are tabulated in table 3.4.1. For comparison, we usually refer to wavelengths with little gas absorption or Rayleigh scattering (usually around 0.74-0.75µm, 0.81-0.82µm and longward of 0.91µm) as *continuum* wavelengths. While Saturn has a larger tropospheric methane concentration than Jupiter, with a volume mixing ratio of 4.7×10^{-3} [Fletcher et al., 2009] versus Jupiter's value of 1.8×10^{-3} [Niemann et al., 1998], the ammonia abundance at visible altitudes is observed to be far lower than on Jupiter due to its deeper altitude of condensation. Nonetheless, the strongest ammonia absorption features are still detectable in Saturn MUSE spectra, even though they are much smaller than in their equivalent Jupiter spectra.

In practice, the individual lines in these bands have finite spectral widths due to two main processes (excluding natural broadening, which is a result of the Heisenberg uncertainty principle, but only has a very small effect on the spectra). At high temperatures and pressures, *pressure broadening* dominates, in which the wavelengths of the photons absorbed and emitted by a gas molecule are affected by collisions with other gas molecules due to the uncertainty principle. The resulting line shape of the extinction coefficient k_ν as a function of wavenumber ν around the central wavenumber ν_0 is described by a Lorentzian line shape:

$$k_\nu(\nu) = \frac{S}{\pi\gamma_L}\left(\frac{1}{(\nu-\nu_0)^2+\gamma_L^2}\right) \tag{3.4.1}$$

where γ_L describes the Lorentz line-width as a function of temperature and pressure, starting

	Band	Approximate Centre (μm)
CH_4	$3\nu_1 + \nu_3$	**0.887**
	$2\nu_1 + 2\nu_3$	**0.861**
	$\nu_1 + 3\nu_3$	**0.841**
	$4\nu_3$	(0.828)
	$3\nu_1 + \nu_3 + \nu_4$	**0.784**
	$2\nu_1 + \nu_2 + 2\nu_3$	(0.746)
	$4\nu_1 + \nu_3$	**0.727**
	$3\nu_1 + 2\nu_3$	0.703
	$4\nu_1 + \nu_3 + \nu_2$ or $4\nu_1 + \nu_3 + \nu_4$	0.667
	$6\nu_1$ or $5\nu_1 + \nu_3$	**0.619**
	$4\nu_1 + 2\nu_3$	0.597
	$5\nu_1 + \nu_3 + \nu_2$ or $5\nu_1 + \nu_3 + \nu_4$	0.576
	$6\nu_1 + \nu_3$	0.543
	$5\nu_1 + 2\nu_3$	(0.521)
	$6\nu_1 + \nu_3 + \nu_2$ or $6\nu_1 + \nu_3 + \nu_4$	(0.509)
	$7\nu_1 + \nu_3$	0.486
NH_3	$3\nu_1 + \nu_2$?	**0.93 (approx.)**
	$3\nu_1 + \nu_4$	0.880
	$4\nu_1$	**0.793**
	$3\nu_1 + 2\nu_4$ or $4\nu_3$	0.755
	$4\nu_1 + \nu_2$	0.735
	$4\nu_1 + \nu_4$	0.702
	$5\nu_1$	**0.648**
	$4\nu_1 + \nu_3$	(0.623)
	$3\nu_1 + 2\nu_3$ or $5\nu_3$	0.606
	$4\nu_1 + \nu_2 + \nu_3$	(0.590)
	$5\nu_1 + \nu_4$	0.585
	$6\nu_1$	0.550
	$6\nu_1 + \nu_4$	(0.506)
H_2-H_2 CIA	$S_2(1) + Q_1(1)$	0.784
	$S_2(0) + Q_1(1)$	0.796
	$S_3(1)$	0.815
	$Q_3(1)$	0.850
H_2-He CIA	$S_3(1)$?	0.810
	$Q_3(1)$?	0.844

Table 3.4.1: Approximate locations of ammonia, methane and hydrogen absorption bands in MUSE giant planet spectra, with speculated overtone and combination assignments. The strongest bands in each case are highlighted in bold. Bands in brackets are so weak as to be barely detectable in MUSE spectra of either Jupiter or Saturn. Ammonia band assignments were taken from Herzberg [1945], McBride and Nicholls [1972], Bowles [2003] and Lucchesini and Gozzini [2009]. We were unable to find a band assignment in the literature for the ammonia absorption feature around 0.93µm despite its apparence in Jupiter spectra; we have estimated the most likely assignment based on the fundamental modes of vibration of ammonia. Methane band assignments were taken from Herzberg [1945], Giver [1978], Scherer et al. [1984] and Bowles [2003]. H_2-H_2 CIA band assignments were taken from Belton and Spinrad [1973] while corresponding data on H_2-He CIA was taken from Borysow and Frommhold [1989] although the band assignments in the latter case are our own. Notation of CIA band assignments is given in the form $S_x(y)$, corresponding to a transition from vibrational quantum numbers $0 \rightarrow x$ and rotational quantum numbers $y \rightarrow y + 2$, $Q_x(y)$ corresponds to an equivalent transition with no change in rotational quantum number. We have excluded CIA bands from third overtone transitions ($S_4(y)$ and $Q_4(y)$) from this table, as while they are predicted to be found between 0.62µm and 0.64µm, they are too weak to be visible in MUSE spectra, and we are not aware of any accurate CIA band models for this region in the literature.

from a reference value γ_{L0} at a reference temperature and pressure $\{P_0, T_0\}$:

$$\gamma_L(P,T) = \gamma_{L0}\left(\frac{P}{P_0}\right)\left(\frac{T_0}{T}\right)^n \tag{3.4.2}$$

where n is a coefficient usually equal to 0.5. The quantities γ_{L0} , ν_0 and $S = \int_0^\infty k_\nu(\nu)d\nu$ which describes the *line strength* are both found empirically from laboratory data.

The dominant line-broadening process at low pressures, on the other hand, is *Doppler broadening*, which results from the motion of the absorbing gas molecule inducing a Doppler shift on absorbed and emitted photons. This broadening is described with an analogous Gaussian line shape:

$$k_\nu(\nu) = \frac{S}{\sqrt{\pi}\gamma_D}\exp\left(-\frac{(\nu-\nu_0)^2}{\gamma_D^2}\right) \tag{3.4.3}$$

where the analogous Doppler line width γ_D is a function of temperature:

$$\gamma_D = \gamma_{D0}\sqrt{\frac{T}{T_0}} \tag{3.4.4}$$

In practice, both pressure and Doppler broadening need to be taken into account when modelling absorption band widths, most commonly using a *Voigt profile* which is solved numerically:

$$k_\nu(\nu) = \frac{S}{\pi^{3/2}}\left(\frac{\gamma_L}{\gamma_D^2}\right)\int_{-\infty}^{\infty}\frac{\gamma_D^2\exp(-t^2)}{(\nu-\nu_0-\gamma_D t)^2+\gamma_L^2}dt \tag{3.4.5}$$

Lastly, there is one more factor to take into account that affects the shape of the gas absorption peaks: that of the presence of aerosol. The higher and thicker the layer of aerosol, the shorter the optical path taken by a photon as it passes through the planet's atmosphere before it is reflected back to space, and hence the less likely it is to be absorbed in the atmosphere. This causes individual gas absorption peaks to appear much shallower than they would if there was no aerosol present. On the other hand, the weaker the gas absorption peak in the first place, the deeper into the atmosphere the photon can penetrate before it is sufficiently likely to be absorbed. Weaker absorption peaks are therefore more sensitive to aerosol deeper in the atmosphere, while stronger absorption peaks are more sensitive to high-altitude aerosol. This is demonstrated clearly in figure 3.4.1.

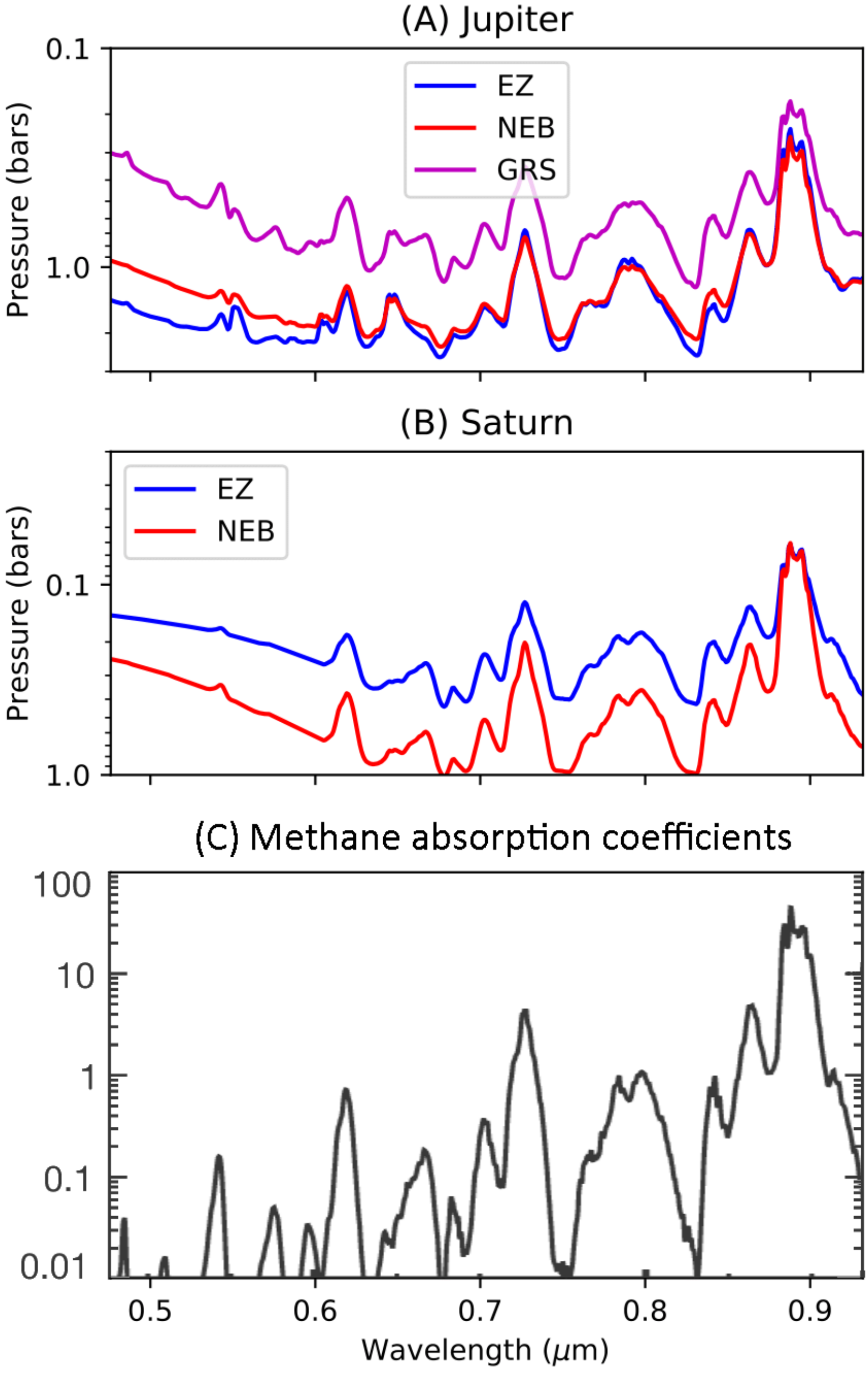

Figure 3.4.1: Approximate altitude of peak sensitivity as a function of wavelength, calculated according to an average weighted by retrieved Jacobians, for different locations on (A) Jupiter and (B) Saturn. The increase in altitude of peak sensitivity in the GRS and Saturn's EZ is due to the presence of haze. For comparison, we provide a plot of methane absorption coefficients in subfigure (C) for a cloud-free atmosphere, which was adapted from figure 5.3 in West et al. [2004], in units of (km-amagat)$^{-1}$. Note the general correspondence between methane absorption and altitude of peak sensitivity, except at short wavelengths where Rayleigh scattering and chromophore absorption dominate.

For this reason, the presence of aerosol can induce substantial degeneracies on retrievals of gaseous abundances. For instance, unusually shallow gaseous ammonia absorption peaks in a sample spectrum of Jupiter may either be a result of genuine ammonia depletion or the presence of an unusually thick or elevated cloud layer in the region. To break the degeneracy, we therefore require a gas in the atmosphere that absorbs in the wavelength range we are probing, but which is well-mixed in the atmosphere. In our case, that role is played by methane gas, as the atmospheres of Jupiter and Saturn are too warm for methane to condense, and methane photolysis occurs at altitudes far higher than those we can probe with MUSE. Thus, by taking measurements of methane abundance at one location in the atmosphere, one can infer the vertical abundance profile of methane over the whole atmosphere and hence retrieve accurate aerosol abundance profiles by analysing variations in the depths of individual methane absorption peaks. The methane abundance of Jupiter's atmosphere was constrained to within an uncertainty of 20% by the Galileo probe [Niemann et al., 1998]. On Saturn, the equivalent value is generally less well-constrained due to the lack of in situ measurements, instead we rely on retrievals from remote sensing in the thermal infrared where the degeneracy between methane and aerosol can be broken [Fouchet et al., 2009], as well as measurements of CIA. We will provide a discussion of the effect of this uncertainty on Saturnian aerosol profiles in section 6.6.

3.5 Modelling particle scattering phase functions

Gas molecules in the giant planets are small enough relative to MUSE wavelengths that their scattering phase functions $P(\theta)$ can be modelled as a function of scattering angle θ using the Rayleigh approximation :

$$P(\theta) = \frac{3}{4}\left(1 + \cos^2\theta\right) \tag{3.5.1}$$

However, the effective radii of aerosol particles in the upper troposphere are close in magnitude to the wavelength scales observed by MUSE, and so Mie scattering dominates. We need to know two main properties of the aerosol particles to model their phase functions. The first is their approximate size distribution, which is modelled using a Gamma distribution [Hansen, 1971]:

$$N(r) \sim \Gamma\left(\mu, \sigma^2\right) = r_0 r^{\frac{1-3\sigma^2}{\sigma^2}} \exp\left(-\frac{r}{\mu\sigma^2}\right) \tag{3.5.2}$$

where r is the particle radius with mean μ and variance σ^2, and r_0 is a normalisation constant. The second is the dependency of the complex refractive index of the particles with respect to wavelength $\bar{n}(\lambda) = n(\lambda) + ik(\lambda)$, consisting of a real component *n(λ)* which quantifies the velocity of electromagnetic radiation through the particle relative to the speed of light in a vacuum, and an imaginary part *k(λ)* which describes the absorptivity of the aerosol particle. The complex refractive index spectrum (also referred to as the *optical constants*) of an aerosol is defined primarily by its composition, and can be derived experimentally in the laboratory as a function of temperature and pressure. Conversely, this also means that, by retrieving the refractive index spectra of chromophore particles, one can shed some light on what they are made out of. It is sufficient to know just the full wavelength solution of k (from $-\infty$ to $+\infty$) and a single value of n at a reference wavelength *a priori*, and use Kramers-Kronig analysis (eg. Roessler [1965], Sheik-Bahae [2005]) to then compute the full wavelength solution of *n.* In practice, one usually only has prior knowledge of k over a limited wavelength range, and so empirical modifications of the Kramers-Kronig relations are needed (eg. Irwin et al. [2015]) so that one can still compute the approximate conjugate solution for n provided one does not deviate too far from the reference wavelength.

Knowing their particle size distributions and optical constants, the aerosol scattering phase functions are then derived numerically using a Mie scattering model for homogeneous spheres known as DMIE [Dave, 1968], together with their extinction efficiencies and single-scattering albedo spectra. We neglect inelastic (Raman) scattering of photons in our model, as it is not seen to have a major effect on gas giant spectra at these wavelengths [Karkoschka, 1994]. Technically, Mie theory can only be used for particles that are spherical, which is a valid assumption for liquid condensates, but as mentioned in section 1.2, most of the visible cloud particles present in giant planet atmospheres are thought to be made of ices, and are therefore highly non-spherical. However, a collection of randomly-oriented non-spherical particles can usually be modelled to first order by spheres of an equivalent size distribution. Features of the Mie phase function that are characteristic only of spherical particles, such as 'rainbow' and 'glory' [Straughan, 1976, West et al., 2009], are then smoothed over using the double Henyey-Greenstein approximation [Henyey and Greenstein, 1941]:

$$P(\theta) = \frac{1}{4\pi}\left[f\frac{1-g_1^2}{(1+g_1^2-2g_1\cos(\theta))^{\frac{3}{2}}} + (1-f)\,\frac{1-g_2^2}{(1+g_2^2-2g_2\cos(\theta))^{\frac{3}{2}}}\right] \tag{3.5.3}$$

where ϑ is the scattering angle, $\{g_1,g_2\}$ are asymmetry parameters which determine the degree of forward- and back-scattering, and f is a weighting constant, which determines the size of the forward-scattering peak relative to the back-scattering peak.

If the effective radii of the scattering particles are small relative to the wavelength scattered, the phase function tends towards the Rayleigh approximation in which radiation is equally likely to be either forward-scattered or back-scattered. The greater the particle size is increased, the more forward-scattering becomes dominant over back-scattering. However, even for a large particle, one can still increase the level of back-scattering by increasing the real part of its refractive index. This can make it difficult to decouple the size of cloud particles from their real refractive index, especially with remote sensing on the ground where one is not able to observe the particles' phase functions over a wide phase angle range, resulting in a major degeneracy as we show further in chapters 4 and 6.

3.6 The Correlated-k method

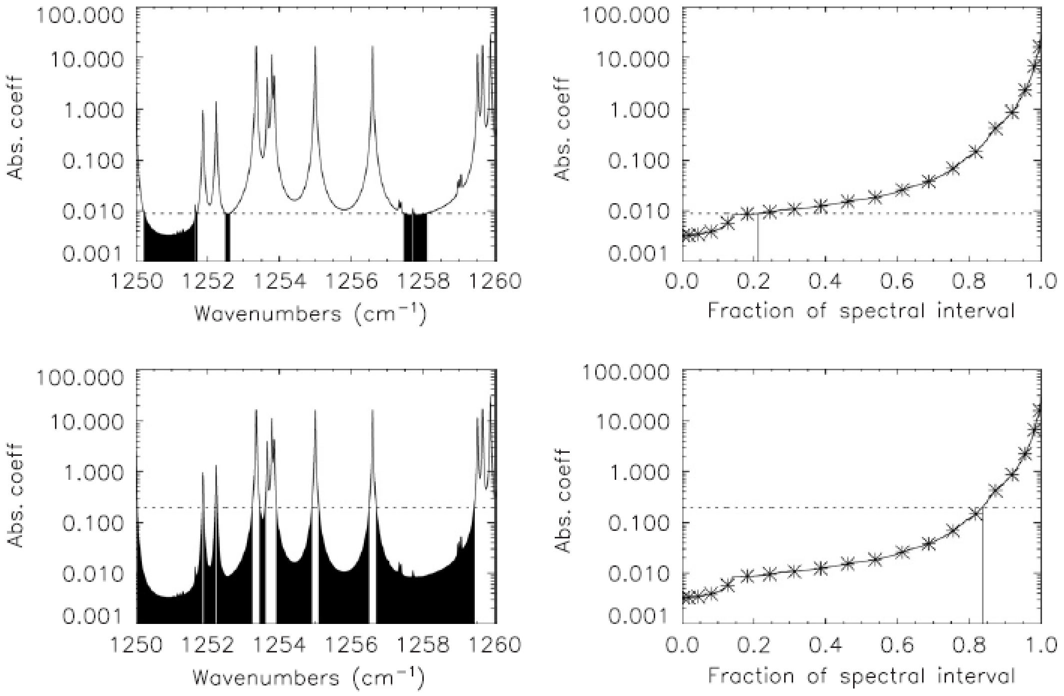

Figure 3.6.1: An illustration of the correlated-k method for *(left)* a sample spectrum of Saturn, where the portion of the spectrum below a given absorption coefficient is highlighted, and *(right)* the highlighted proportion of the spectrum mapped onto its equivalent k-distribution [Irwin et al., 2008].

To solve the radiative transfer equation, one has to calculate the contribution of all gas absorption features together with the optical depth of the atmosphere at a given wavelength. This is performed most accurately using the line-by-line method, in which the extinction coefficients are calculated by summing together individual molecular absorption lines for a given temperature and pressure within each small wavenumber step $\Delta\nu$ over the whole wavelength range. This is, however, slow and cumbersome, since the reference line data could be at a very high spectral resolution, and so calculating the optical depth of a layer of atmosphere could require the adding of thousands of individual lines together. NEMESIS therefore makes use of an approximation that is significantly faster and less computationally-intensive than the line-by-line method to calculate the transmission of an atmospheric layer.

Unlike in the line-by-line method, the correlated-k method [Goody et al., 1989] does not need to take into account exactly *where* in the wavenumber step $\Delta\nu$ certain absorption peaks lie, but instead quantitively analyses *how much* of that spectral interval can be assigned a given range of absorption values, as illustrated in figure 3.6.1. This means that the spectrum can be modelled as a cumulative absorption distribution, or *k-distribution*, which varies with respect to wavenumber interval both smoothly and monotonically. The k-distribution can thus be integrated over the frequency range using far fewer quadrature points than the original spectrum which was rapidly fluctuating with wavelength, thereby requiring fewer steps of integration than the line-by-line method. The correlated-k method makes use of look-up tables, or *k-tables*, that were precalculated using line or band data for specific gases at a range of temperatures and pressures.

In the line-by-line method, the mean transmittance $\bar{T_G}$ within a frequency interval $\{\nu_0, \nu_0 + \Delta\nu\}$ through an atmospheric layer of a single gas, of density ρ_G and extinction coefficient k_G, is calculated by averaging the effect of the gas absorption over the frequency interval:

$$\bar{T_G} = \frac{1}{\Delta\nu} \int_{\nu_0}^{\nu_0+\Delta\nu} \exp(-\rho_G k_G(\nu)) d\nu \tag{3.6.1}$$

However, using the correlated-k approximation, it can be assumed that, for a single gas, the fraction of the spectral range that has extinction coefficients within a given interval $\{k_G, k_G + \Delta k_G\}$ can be modelled by a function $f_G(k_G)$, hence equation 3.6.1 can be simplified to:

$$\bar{T_G} = \int_0^\infty f_G(k_G) \exp(-\rho_G k_G) dk_G \tag{3.6.2}$$

This can then be simplified further to define $\bar{T}$ in terms of a cumulative function $g = \int_0^{k_G} f_G(k_G) dk_G$:

$$\bar{T_G} = \int_0^1 \exp(-\rho_G k_G(g)) dg \tag{3.6.3}$$

and then approximating the integration as a discrete summation over the interval $g = \{0, 1\}$ so that:

$$\bar{T_G} = \sum_{n=1}^{N} \exp(-\rho_G k_{G(n)})\Delta g_{(n)} \tag{3.6.4}$$

Irwin et al. [2008] propose $N = 10 - 20$ quadrature points, which typically induces an error in the resulting forward model of less than 5%. Once the total transmission for each gas has been calculated over the entire atmosphere, the total transmission for all gases together can be calculated through the product of each of the individual gaseous transmissions according to the overlapping lines approximation [Lacis and Oinas, 1991].

3.7 Retrieval theory

In the previous subsections, we explained how an initial state vector could be used to forward model a synthetic spectrum. Here, we will now explain how the information provided by the forward model can be used to derive a state vector that minimises the difference between the observed and modelled spectrum. This process is commonly known as *spectral inversion.* The most rigorous way of doing this is using a Monte Carlo method such as *nested sampling* [Feroz and Hobson, 2008, Garland and Irwin, 2019], where one generates thousands of initial forward models with random state vector values, and then progressively eliminates state vector values that lead to poor fits to the observed spectra to leave behind the most likely atmospheric parameters. This works best for very underconstrained spectral retrievals of exoplanetary atmospheres, where observations only consist of a few noisy datapoints from which only a few atmospheric parameters can be retrieved. However, nested sampling was seen to be prohibitively slow for MUSE retrievals of the giant planets, whose spectra are far more constrained and therefore require the retrieval of a large number of spectral wavelengths and state vector variables with the use of a scattering model. We therefore use a process known as *optimal estimation* to constrain the state vector instead. This section is mostly adapted from Rodgers [2000] and Irwin et al. [2008].

In a perfectly linear problem, the equation of the forward model relating the observed spectrum $\mathbf{y}$ with the state vector $\mathbf{x}$ would be expressed as such:

$$\mathbf{y} = \mathbf{K}\mathbf{x} + \epsilon \tag{3.7.1}$$

where ϵ is a systematic error term on the observed spectral radiances and $\mathbf{K}$ is a *Jacobian* matrix (also known as the *weighting function)* which gives the derivative of the observed spectrum with respect to each of the state vector elements. $\mathbf{Kx}$ together would therefore give the forward modelled spectrum. Hence, to get $\mathbf{x}$ from $\mathbf{y}$, one would simply need to invert $\mathbf{K}$.

In practice, however, the relation between the state vector and the observed spectrum is non-linear. In addition, there can often be some degeneracy between different state vectors that would result in a given spectrum. Make the state vector uncertainties too high, or attempt to retrieve a vertical profile at too high a resolution, and a process called *ill-conditioning* may occur where a highly-fluctuating state vector is retrieved which, while providing a good fit to the observed spectrum, is not physical. One must therefore also use the prior state vector itself as a constraint on the final state vector solution. NEMESIS does this by minimising a *cost function* ϕ:

$$\phi = (\mathbf{y} - \mathbf{K_n x_n})^T \mathbf{S_y}^{-1} (\mathbf{y} - \mathbf{K_n x_n}) + (\mathbf{x_n} - \mathbf{x}_0)^T \mathbf{S_0}^{-1} (\mathbf{x_n} - \mathbf{x_0}) \tag{3.7.2}$$

where $\mathbf{K_n}$ and $\mathbf{x_n}$ are respectively the Jacobian and state vector following the nth iteration of the inversion, $\mathbf{x_0}$ is the prior state vector with an associated error covariance matrix $\mathbf{S_0}$, and $\mathbf{S_y}$ is a covariance matrix that encompasses all uncertainties associated with the fit to the observed spectrum.

The model is deemed to have converged to a solution when the percentage difference in ϕ between subsequent iterations is less than 0.1%, which usually occurs after around 10-15 iterations. The quality of the convergence is gauged by calculating the weighted sum of squared errors between the observed and modelled spectrum divided by the total number of wavelengths (χ^2/n). The lower the value of χ^2/n, the better the fit, although any value below around 1.0-1.5 is usually considered adequate. One can therefore retrieve a solution in the left-hand term of the cost function which minimises the least-squares difference between the observed and modelled spectrum, while at the same time providing a prior constraint in the right-hand term to ensure physicality. Changing the priors by an order of magnitude may however result in a drastically different retrieval using this method if the solution is underconstrained, and doing so can therefore act as a good test of the sensitivity of the observed spectrum to each of the atmospheric parameters in the state vector.

The state vector $\mathbf{x_n}$ itself is found using a Levenberg-Marquardt iteration scheme which acts to minimise ϕ:

$$\mathbf{x'_n} = \mathbf{x_0} + \mathbf{S_0 K^T_{n-1}} (\mathbf{K_{n-1} S_0 K^T_{n-1}} + \mathbf{S_y})^{\mathbf{-1}} (\mathbf{y} - \mathbf{K_{n-1} x_0}) \tag{3.7.3}$$

$$\mathbf{x_n} = \mathbf{x_{n-1}} + \frac{\mathbf{x'_n} - \mathbf{x_{n-1}}}{1+\lambda} \tag{3.7.4}$$

where λ is a *braking parameter* that is adjusted arbitrarily with each iteration to ensure the scheme does not converge to a solution that is unphysical. In optimal estimation, the covariance matrix $\mathbf{S_n}$ associated with the state vector $\mathbf{x_n}$ is usually given by:

$$\mathbf{S_n} = (\mathbf{S_0^{-1}} + \mathbf{K_n^T}\mathbf{S_y^{-1}}\mathbf{K_n})^{-1} \tag{3.7.5}$$

However, as we assume virtually no prior knowledge of the atmospheric variables to be retrieved, $\mathbf{S_0}$ in this case does not represent the actual quantified uncertainty values on the prior state vector, but is simply an arbitrary parameter that constrains the variability of the retrieval. Set $\mathbf{S_0}$ too low, and $\mathbf{x_n}$ will barely deviate from $\mathbf{x_0}$, but set $\mathbf{S_0}$ too high and $\mathbf{x_n}$ becomes ill-conditioned. This is problematic, since $\mathbf{S_n} \leq \mathbf{S_0}$ for all diagonal values (where $\mathbf{S_n} = \mathbf{S_0}$ represents the limit in which there is no information that can be derived about $\mathbf{x_n}$ from the spectrum), and so retrieval errors will appear unrealistically small if the prior error is set too low. We therefore perform an empirical correction on the diagonal values of $\mathbf{S_n}$ in order to derive more realistic constraints on the uncertainties $\Delta\mathbf{x_n}$ associated with the final state vector [Irwin et al., 2019b]:

$$\Delta x_{nii} = (S_{nii}^{-1} - S_{0ii}^{-1})^{-1} \tag{3.7.6}$$

Hence, for variable profiles where no information can be derived from the spectrum, $\mathbf{\Delta x_n} \rightarrow \infty$, as desired.

Diagonal values of $\mathbf{S_0}$ (S_{0ii}), representing the variance σ_{0i}^2 of each state vector term x_i, are found empirically for each variable in chapters 4 and 6 according to the extent to which we wish to vary them while also preventing ill-conditioning. The lower the retrieved value of $\frac{\sigma_{ni}}{x_{ni}}$ relative to $\frac{\sigma_{0i}}{x_{0i}}$, the more sensitive the spectrum to the value of x_{ni} over the value of x_{0i}. By default, the prior state vector values are assumed to be independent of each other ($S_{0ij} = 0, i \neq j$). The exception is with continuous profiles for which we wish to retrieve smooth variation with pressure in the case of a vertical aerosol profile, or wavelength in the case of a complex refractive index spectrum. In these cases, the non-diagonal values of $\mathbf{S_0}$ ($S_{0ij}, i \neq j$) are controlled by a parameter Λ known as the *correlation length*, whose value we specify explicitly in chapters 4 and 6:

$$S_{0ij} = \sqrt{S_{0ii}S_{0jj}}e^{-\left\|\frac{p_i - p_j}{\Lambda}\right\|}, i \neq j \tag{3.7.7}$$

where p_i is the pressure grid (in the case of aerosol profiles) or wavelength grid (in the case of complex refractive index) associated with each state vector term x_i.

The covariance term $\mathbf{S_y}$ consists of two components added together: a spectral error term and a forward modelling error term. The former, consisting of uncertainties resulting in the measurement and calibration of the observed spectrum, was described in section 2.4. The latter term, on the other hand, consists of systematic uncertainties that are the result of the spectral modelling itself. In the case of MUSE, the main factors would be a) a combination of experimental uncertainties in the measurement of the reference gas absorption data, b) uncertainties that result from the use of the correlated-k approximation instead of the line-by-line method, and c) uncertainties that result from other approximations made in the radiative transfer equation. However, these quantities are usually very difficult to measure. In practice, the forward modelling error is qualitively determined to ensure that χ^2/n values are consistently below 1 when fits to the spectrum are visibly adequate, without making retrieved atmospheric parameters too imprecise. We found empirically that a consistent 1% error on Jovian spectra and a 2.5% error on Saturn spectra (to account for the fact that Saturn is not as bright as Jupiter), on top of the spectral errors derived in the calibration process, was sufficient for this.

3.8 Balancing the speed and accuracy of a retrieval

Although optimal estimation is substantially faster than nested sampling, a NEMESIS retrieval of cloud structure, colour and ammonia from MUSE spectra at a single observing geometry requires taking multiple scattering into account, which is computationally intensive. Retrievals from a single geometry could therefore still take of the order of several hours to an entire day to complete, while limb darkening retrievals with multiple geometries would take far longer. For a small set of sample retrievals from Jupiter and Saturn, this may not pose a major issue. However, creating maps of aerosol and ammonia of entire discrete features would require hundreds or even thousands of retrievals corresponding to each individual MUSE pixel. While individual NEMESIS retrievals can be run simultaneously in parallel, there are only so many cores available on a single cluster, and that cluster is usually shared among several people each with their own computing needs. For this reason, one has to consider ways of making a NEMESIS retrieval more time-efficient without sacrificing too much in the way of accuracy. There are two simple ways of reducing the amount of time needed by the NEMESIS retrieval: either reduce the number of variables in the state vector, or reduce the number of wavelengths to be retrieved. The best way of doing the former is by using a more efficient forward model, which will be discussed in more detail in chapter 4. In this section, however, we will discuss how to reduce the number of wavelengths in the analysis of a MUSE spectrum without losing substantial information on the state of the atmosphere of Jupiter or Saturn.

A smoothed MUSE spectrum consists of 459 individual wavelengths. The amount of information contained in the spectrum, however, is not evenly distributed across all wavelengths: a single I/F value in the middle of a methane absorption band (such as at 0.727µm) will tell you more about the local cloud structure than an I/F value at 0.765µm which is dominated by telluric noise. A saving in time could therefore be made if one only selected the wavelengths that contained the most information on the state of the atmosphere and discarded the rest. An attempt was made to do this using a channel selection algorithm [Rodgers, 1996, Ventress and Dudhia, 2014], which sequentially selects wavelengths in descending order of information content. This is done by measuring the *degrees of freedom for signal* (d_s) for a single wavelength with respect to the total degrees of freedom of the entire spectrum (d_{stot}):

$$d_{stot} = Tr(\mathbf{I} - \mathbf{S_x S_0^{-1}}) \tag{3.8.1}$$

where $\boldsymbol{I}$ is the identity matrix of order equal to the total number of wavelengths n_λ, and $\mathbf{S_x}$ is the covariance matrix associated with the final retrieved state vector $\mathbf{x}$. The algorithm works as follows:

1. Let m be the number of iterations of the algorithm that have been performed and C_m be the the cumulative proportion of the total information content extracted from the spectrum after the mth iteration (by definition, $0 \leq C_m \leq 1$ and $C_m - C_{m-1} > 0$ for all values of m). Hence, initialise variables $\mathbf{S_{(m=0)}} = \mathbf{S_0}$ and $C_0 = 0.0$.

2. Do the following for each wavelength λ_i where $1 \leq i \leq n_\lambda$:

    (a) Let $\mathbf{k}$ be the row of the Jacobian matrix $\mathbf{K}$ and σ^2 the diagonal value of $\mathbf{S_y}$, both corresponding to wavelength λ_i.

    (b) By analogy with equations 3.7.5 and 3.8.1, calculate the degrees of freedom of signal for each wavelength:

$$\mathbf{s_{(m,i)}} = (\frac{\mathbf{1}}{\sigma^{\mathbf{2}}}(\mathbf{k^T k}) + \mathbf{S^{-1}_{(m-1)}})^{-1} \tag{3.8.2}$$

$$d_{s(m,i)} = Tr(\mathbf{I} - \mathbf{s_{(m,i)} S_0^{-1}}) \tag{3.8.3}$$

3. Select the index $i = imax$ which leads to the largest value of $d_{s(m,i)}$. Let λ_{imax} be the wavelength at which this occurs, that is, the wavelength with the greatest information content out of those wavelengths not already selected in previous iterations.

4. Calculate the proportion of the total information content at this wavelength $P(\lambda_{imax})$:

$$\mathbf{S_{(m-1)}} = \mathbf{s_{(m,imax)}} \tag{3.8.4}$$

$$C_m = d_{s(m,imax)} \tag{3.8.5}$$

$$P(\lambda_{imax}) = \frac{C_m - C_{m-1}}{d_{stot}} \tag{3.8.6}$$

5. Increment m and repeat steps 2-5 until the desired number of wavelengths or the desired proportion of the total information content has been selected. Individual wavelengths are never selected more than once by the algorithm.

The greatest prior unknowns in this analysis are $\mathbf{S_0}$, whose value is arbitrary and optimised solely to prevent ill-conditioning, and $\mathbf{K}$, which is calculated numerically by NEMESIS in the retrieval itself. The uncertainty in $\mathbf{S_0}$ matters little in this case, as it would simply create a uniform systematic error across all wavelengths. The uncertainty in $\mathbf{K}$, on the other hand, is more problematic, as it is the source of information on the effect of changing the I/F at each wavelength on the resulting state vector. One therefore has to run the algorithm on a set of ready-run retrievals, using all SpeX-resolved wavelengths, in order to see which wavelengths on average have the most information content. This creates a chicken-and-egg problem since, as shown in Chapter 4, you need to reduce the number of wavelengths in order to refine the forward model in the first place using limb darkening. The wavelengths selected by the algorithm can therefore only be used as an approximate guide to which wavelengths actually have the greatest information content, which means that retrievals that do not make use of the full set of wavelengths at some point in the retrieval process will be considered highly unreliable.

A way round this conundrum is that, while the final state vector solution should take all wavelengths into account, this does not mean that all wavelengths must be taken into account throughout the entire retrieval. Unless the prior state vector solution is already very close to the final state vector solution, a typical NEMESIS retrieval would need at least 5 iterations to come even remotely close to fitting the observed spectrum. It therefore makes very little sense to perform the first few iterations of a retrieval using the full set of wavelengths. We therefore constructed a *reduced wavelength scheme*, in order to change the number of wavelengths being fitted according to how many iterations of the retrieval have been performed. The scheme is summarised as follows (and in figure 3.1.1):

- Each wavelength in the full grid is assigned a ranking from 1 to a maximum ranking MAXRANK.
- NEMESIS then selects rank 1 wavelengths and attempts to fit them until the solution approximately converges as per the standard NEMESIS convergence criteria.
- NEMESIS then adds on rank 2 wavelengths, and feeds in the state vector retrieved using just the rank 1 wavelengths to perform further iterations using the combined rank 1 and 2 wavelengths until convergence is achieved in the same fashion.
- The process is repeated until all wavelengths from rank 1 to MAXRANK are included in the retrieval (or if convergence still hasn't been achieved 2 iterations before the maximum number of iterations, the final 2 iterations are performed using the full wavelength grid). Once convergence is achieved at this point, the retrieval ends.

Of course, using such a scheme also means that NEMESIS will require a larger number of iterations to converge to a solution than if the full set of wavelengths was used throughout. Nonetheless, if one selects the wavelength ranks and the forward model wisely, one can usually converge to a solution that is almost indistinguishable from the full wavelength solution in a substantially shorter time, despite the larger number of iterations needed. The aforementioned channel selection algorithm can be used as a tool to assign a rank to each wavelength, with wavelengths of high information content given the lowest rank, and wavelengths of little information content the highest rank.

A column of pixels from observation MUSE.2018-04-09T06:04:06.918 was selected, and a retrieval performed in each pixel within the planetocentric latitude range $\{-57°, 44°\}$ using a prior forward model with only minor differences in chromophore imaginary refractive index to the one retrieved in chapter 4. The resulting average information content distribution is presented in figure 3.8.1. The most commonly selected wavelengths are at the bluest wavelengths, which contain the most information on chromophore abundance and altitude, with another cluster around the 0.793µm ammonia absorption feature. The broad methane absorption feature around 0.784µm is also regularly selected, which is sensitive to aerosol around 0.7 bar, although curiously the algorithm mostly ignores the 0.619µm feature, which is sensitive to the lowest-altitude aerosol opacity, perhaps because the cloud layer at that altitude also has the greatest contribution to continuum I/F. In order to have a relative geometric progression in number of wavelengths over incremental rank, we generally chose to make wavelengths with over 0.5% of the total information content rank 1, wavelengths with between 0.3% and 0.5% of the total information content rank 2, wavelengths between 0.2% and 0.3% rank 3, and wavelengths with less than 0.2% rank 4.

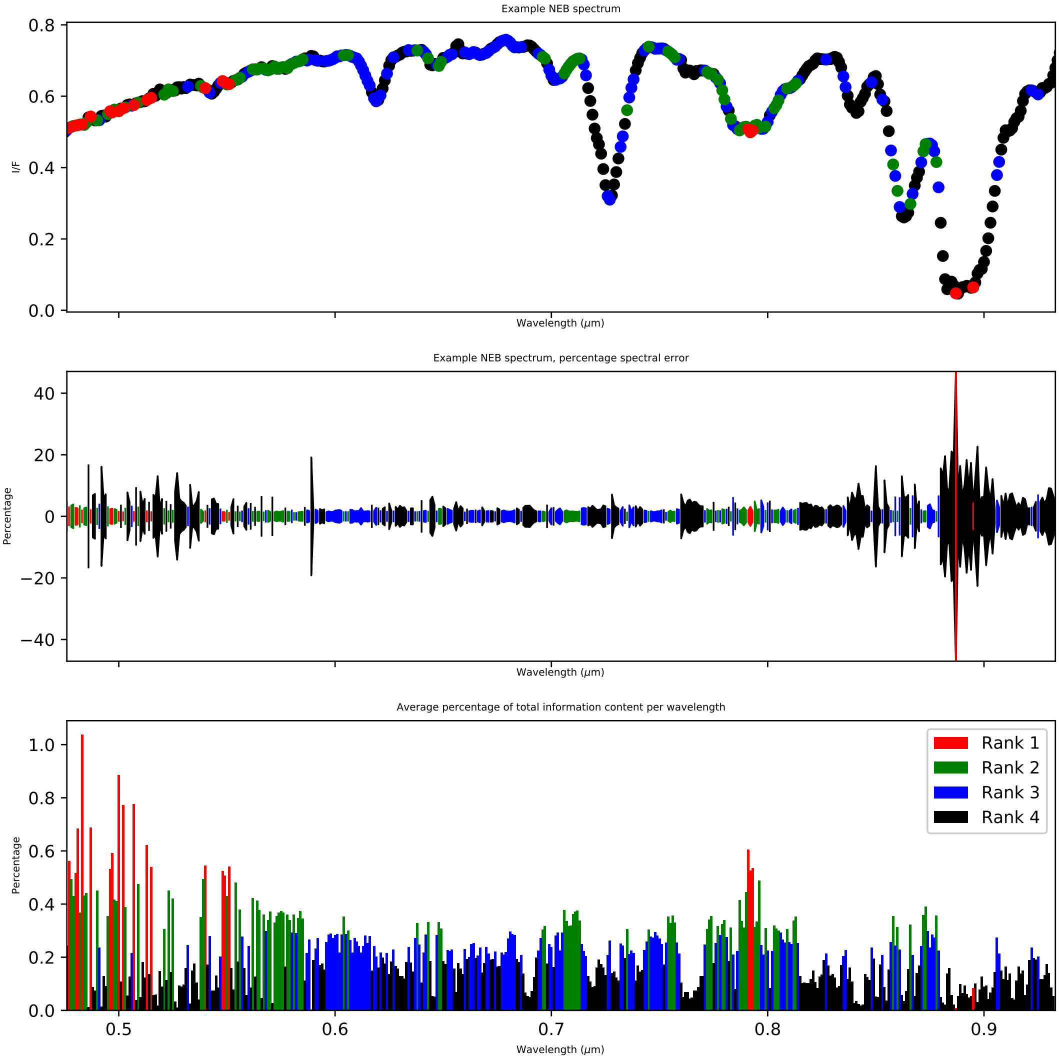

Figure 3.8.1: Results of channel selection algorithm implemented on 161 different locations along a single meridional swath of Jupiter (2018-04-09T06:04:06.918). Rank 1 wavelengths each contain more than 0.5% of the total information content; Rank 2 wavelengths between 0.3% and 0.5% of the total information content, Rank 3 wavelengths between 0.2% and 0.3% of the total information content and Rank 4 wavelengths below 0.2%. Top: Example NEB spectrum with each wavelength colour-coded by rank; associated percentage spectral error on the same spectrum is shown in the middle plot for comparison. Bottom: P(λ).

The most noticeable flaw in the selection algorithm, however, is that it assumes no spectral correlation between wavelengths. Since the individual wavelengths around the strong 0.89µm methane absorption feature have a low signal-to-noise ratio, they are perceived by the algorithm as having little information content, however when the overall shape of the methane absorption feature is taken into account, it holds substantial information content on high-altitude haze opacity. To account for this, we therefore made both 0.887µm, which has the strongest methane absorption in the broad feature, and 0.895µm which has a slightly lower signal-to-noise ratio, rank 1 wavelengths. We also included additional rank 1 wavelengths (0.618µm, 0.619µm, 0.750µm and 0.923µm) to further constrain the extent of methane absorption at 0.619µm with respect to continuum brightness early in the retrieval, in order to provide a better estimate of vertical aerosol distribution and particle size. Figure 3.8.2 shows very little difference in the retrieved cloud profiles and fit to spectrum with and without using a reduced wavelength scheme: the difference in χ^2/n is only 0.01 and all the state vector variables are identical to within a quarter of a sigma. However, the former retrieval takes around half the time to complete.

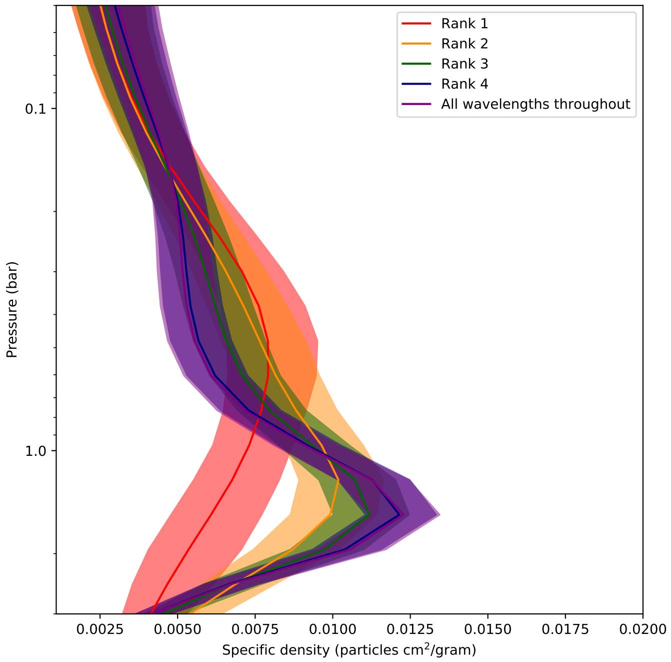

Figure 3.8.2: Retrieved aerosol profile, with errors, from a single spectrum in the EZ: *(purple)* without using a reduced wavelength scheme (458 wavelengths, $\chi^2/n = 0.77$), *(red)* reduced wavelength scheme using just rank 1 wavelengths (25 wavelengths in total, $\chi^2/n = 1.28$), *(yellow)* reduced wavelength scheme using ranks 1 and 2 (110 wavelengths, $\chi^2/n = 1.05$), *(green)* reduced wavelength scheme using ranks 1, 2 and 3 (236 wavelengths, $\chi^2/n = 0.93$), *(blue)* reduced wavelength scheme using all wavelengths ($\chi^2/n = 0.76$).

Chapter 4

Jupiter - Constraining a universal chromophore and cloud model

4.1 Overview

In this chapter, we explain how we tested and refined our retrieval model in order to maximise the amount of reliable information that could be extracted from our MUSE spectra. We did this using just one representative observation (2018-04-09T06:04:06.918) out of all the sets of MUSE data of Jupiter between 2014 and 2018, for reasons relating to calibration and seeing conditions that were already discussed in chapter 2. Unless otherwise stated, all of the spectra presented in this chapter therefore originate from the 2018-04-09T06:04:06.918 dataset, apart from spectra specifically of the NTBs, which were taken from the 2017-05-15T02:01:59.328 dataset, as the colour of the NTBs had already faded substantially by 2018. Analysis of the remaining Jupiter MUSE datasets will be presented in chapter 5. We should state that the paper of Baines et al. [2019], which elaborated on the findings of Sromovsky et al. [2017] comparing the so-called *'Crème Brûlée'* model with other possible chromophore models, as well as providing some greater physical constraints on chromophore production, was only published following initial submission of this thesis. Nonetheless, we have made additional references to this paper in this chapter where appropriate.

As a starting point, we first attempt to validate the results of Sromovsky et al. [2017] (hereafter SR17), who found that a so-called *'Crème Brûlée'* model with a single chromophore compound was able to provide a good fit to representative Cassini/VIMS-V spectra of different regions of Jupiter.

We show that the *Crème Brûlée* model is inadequate in accounting for vertical variations in aerosol concentration, and therefore try to fit representative MUSE spectra of Jupiter using our own cloud model, comparing the fit using Carlson chromophore with the fit using other laboratory chromophore optical constants. We then attempt to improve the spectral fit further than is possible with Carlson chromophore alone, by retrieving our own set of chromophore spectra, as a function of particle size, from limb darkening over a single latitudinal swath of the NEB. We then select the 'optimal' retrieved chromophore spectrum that can both produce a good fit to a GRS spectrum and result in vertical aerosol profiles that are physical. Finally, we fit our retrieved chromophore spectrum to other regions of Jupiter, gauging the reliability of the model through a sensitivity analysis, and thereby derive some preliminary conclusions about spatial differences in colour, cloud structure and ammonia abundance.

The design of the framework of NEMESIS was primarily implemented by my supervisor, Professor Patrick Irwin, based on the original Radtran code developed by Dr Simon Calcutt, though NEMESIS is a collaborative project and minor modifications to its functionality have been made by a large number of people, including myself. The *Crème Brûlée* model, although designed by SR17, was adapted for NEMESIS by me. Reference atmospheres, gas absorption data and scattering codes are given in each case as citations, to which I made little personal contribution. The parametrisation of a continuous cloud profile for NEMESIS with a limited number of sample altitudes, as first described in section 4.4, was a joint effort between me and Patrick Irwin, together with the homogeneous layer splitting. However, the customisation of the cloud model itself for its application to Jovian MUSE spectra was entirely my own work. All the remaining analysis and conclusions presented in this chapter, where citations are not provided, are, of course, entirely my own work.

4.2 Reference atmosphere and gas absorption data

In this section, we describe aspects of the reference atmosphere that remain unchanged throughout chapters 4 and 5 regardless of the other parameters of the forward model. Most of these are also described in, and are the same as in, Irwin et al. [2018, 2019a] and Giles [2016].

The reference atmosphere covers pressure values from a deep limit of 10 bars (90km below the 1 bar reference level) to a high-altitude limit of 1 mbar (150km above the 1 bar level); both altitudes lie far outside MUSE's sensitivity range. This atmosphere is split into 39 homogeneous layers, which are equally-spaced in log pressure in section 4.3, but the layer-splitting for the remaining sections is clarified further in section 4.4 and is shown graphically in figure 4.4.1. The temperature-pressure profile from the high stratosphere down to 0.8 bars is taken from Fletcher et al. [2009], and extrapolated to deeper altitudes using a dry adiabat. We neglect spatial variations in temperature, for which no information can be retrieved from visible and near-infrared spectra. This should not have a major effect on our retrievals, given that the temperature profile on Jupiter only varies between zones and belts by approximately ±5K at 0.1 bar [Fletcher et al., 2016]. All reference compositional abundance profiles are as shown in figure 1.2.2, apart from ammonia which is as in Fletcher et al. [2009]. Only the ammonia profile will be allowed to vary, as the other gases are either well-mixed in the troposphere (in the case of methane), are present in very low abundances above the cloud-tops (in the case of water vapour), or do not have spectral features in the MUSE wavelength range that would allow them to be retrieved directly (in the case of every other gas). Deep volume mixing ratios of H_2, He and CH_4 (primarily isotopologue 211 as specified in the HITRAN database [Rothman et al., 2013]), which are the gases that are present at the greatest concentration in the troposphere, are 0.86, 0.134 and 1.8×10^{-3} respectively [Niemann et al., 1998, von Zahn et al., 1998].

Methane absorption data was obtained from Karkoschka and Tomasko [2010], where each absorption band was approximated with a Goody-Voigt band model [Goody and Yung, 1995], due to the lack of accurate methane line lists at these wavelengths. Ammonia absorption data was obtained from the new Coles et al. [2018] line list, as was described in Irwin et al. [2019a]. Weak H_2 quadrupole absorption data was obtained from the line lists found in the HITRAN database [Rothman et al., 2013], although their contribution to MUSE spectra was barely observable. The methane, ammonia and H_2 absorption coefficients were converted into k-tables before running retrievals with them, in order to save computational time as previously discussed in section 3.6. Rayleigh scattering cross-section computation codes were obtained from Sromovsky (personal communication) and modelled using standard theory (eg. Goody and Yung [1995]). The reference extraterrestrial solar spectrum, used to convert radiance values into I/F, was obtained from Chance and Kurucz [2010].

H_2 - He and H_2 - H_2 CIA data was supposed to have been modelled according to Borysow and Frommhold [1989] and Borysow et al. [2000] respectively. However, there was a computational fault in our CIA look-up table which was only discovered shortly before submission of this thesis. This means that none of the retrievals presented here or in chapter 5 properly take CIA into account (the contribution of CIA to giant planet spectra was originally assumed to be as small as that of the pure quadrupole H_2 lines, while the resulting discrepancies in fit around 0.80µm-0.85µm were blamed instead on poor methane band data and telluric noise). Fortunately, the lack of CIA only induces small errors in a few of our retrieved parameters, which we will discuss in appendix B, and does not invalidate any of the results presented either here or in chapter 5.

4.3 The *Crème Brûlée* model

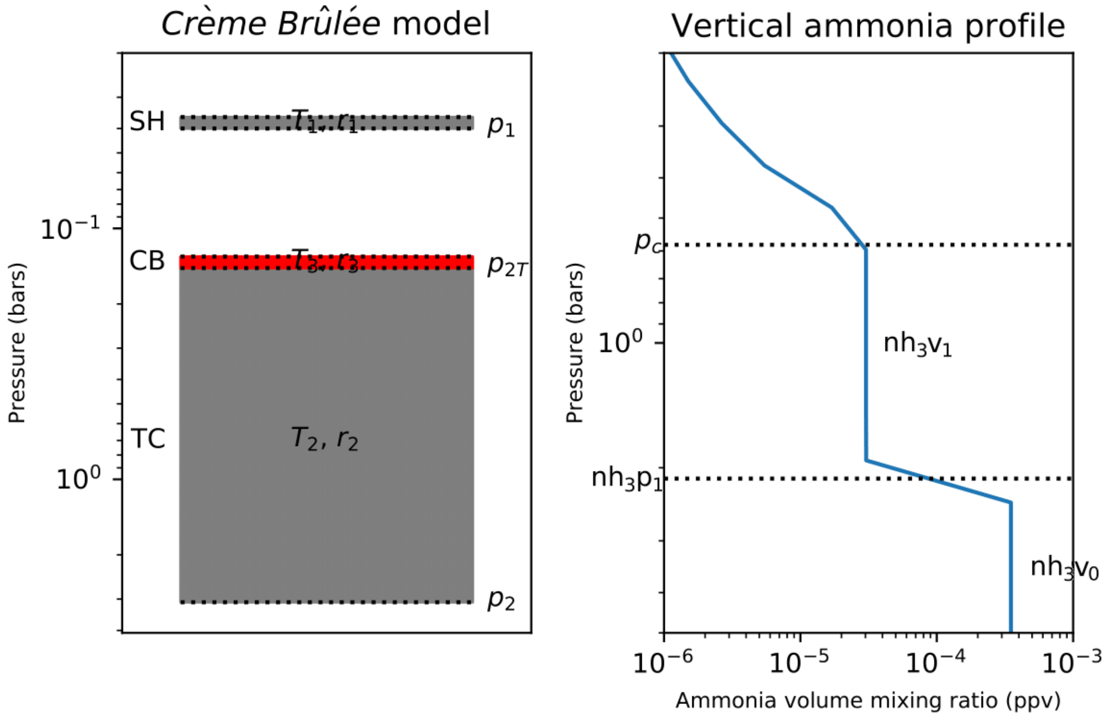

Figure 4.3.1: Ammonia VMR profile, assumed to be saturated above the condensation pressure level p_c, together with a diagram of the *Crème Brûlée* model on the left with free parameters labelled. The VMR around the knee pressure nh_3p_1 is modelled using a hyperbolic approximation $nh_3v(p) = \frac{1}{2}(nh_3v_0 - nh_3v_1)(1 + \tanh(20(p - nh_3p_1))) + nh_3v_1$ since the step function used in SR17 was seen to inadequately account for variation in the value of nh_3p_1.

We first attempt to validate the results of SR17 using a cloud model parametrisation that resembles that of the SR17 model as closely as possible, with parameters defined in Table 4.3.1. The decision to fix or vary each parameter is therefore, when possible, also the same as in SR17, even when the writer of this thesis disagrees on doing so. Their cloud model consisted of a very thin layer of chromophore fixed to the top of an extended tropospheric cloud layer, plus an additional detached sheet haze layer higher in the stratosphere, which they nicknamed the '*Crème Brûlée* model' due to its superficial resemblance to the eponymous dessert, as can be seen in figure 4.3.1. Baines et al. [2019] found that this model provided a superior fit to VIMS-V spectra of the GRS than either placing the chromophore in the stratosphere or as a thin coating around tropospheric cloud particles. The optical constants of the chromophore layer are fixed to Carlson chromophore values from CR16 (which we remind the reader refers to Carlson et al. [2016]), which are exponentially extrapolated to wavelengths above 0.75µm for which CR16 values do not exist (see figure 4.5.1). Although SR17 obtain their ammonia absorption data from Bowles et al. [2008], and ignore the shorter-wave ammonia absorption features, we have chosen here to use the new ammonia absorption data from Coles et al. [2018] anyway to provide a fair test of the *Crème Brûlée* model's suitability to Jovian visible and near-infrared spectra. SR17's vertical ammonia profile consists of a sudden step change in abundance at a given retrieved 'knee' pressure nh_3p_1. Below this step, the abundance is fixed to a 'deep' value nh_3v_0 obtained from radio observations [Showman and de Pater, 2005]. Above the step, the abundance nh_3v_1 is assumed constant with height up to the saturation level, and is retrieved directly from the data. We assume 100% saturation above the condensation level.

Particle size distributions are very difficult to constrain from spectra observed at just a single geometry. Often, the likelihood function of particle effective radius follows a bi- or multimodal distribution, especially when one assumes a constant particle size distribution over a wide range of altitudes. Two local maximum likelihood estimates of effective radius could provide indistinguishable fits to an observed spectrum, but result in drastically different vertical aerosol profiles. Optimal estimation functions poorly for solutions that do not follow an approximately Gaussian distribution, and so NEMESIS will usually choose one or the other maximum likelihood estimate entirely at random, even if the one it chooses actually gives a worse χ^2/n value than the other estimate. If one therefore attempts spectral retrievals of an entire meridional cross-section of Jupiter, the variation in the retrieval of particle size and density will oscillate wildly from pixel to pixel between the two estimates. A way of getting round this may be to decrease the prior errors on particle effective radius, but then one has to be careful to choose a prior value that is closer to the maximum likelihood estimate with the smaller χ^2/n value. This is difficult if, say, one maximum likelihood estimate gives a superior χ^2/n in the zones while the other gives a better χ^2/n in the belts. For this reason, we have chosen in this section only to look at a small sample of spectra, as SR17 did. The locations of the EZ, NEB and SEB spectra were chosen to match as closely as possible to those in SR17, while we chose the GRS spectrum with the largest I/F gradient at blue wavelengths. Additionally, we chose a spectrum of the NTBs from MUSE cube 2017-05-15T02:01:59.328 in order to test the *Crème Brûlée* model's applicability to a red region of Jupiter that was not modelled in SR17. A more general analysis of meridional and zonal variations in spectral fit and retrieved quantities will be given in section 4.7.

When we apply the *Crème Brûlée* model to our MUSE data (with results for specific regions of Jupiter presented in tables 4.3.2 and 4.3.3 and for a broader latitudinal range in figure 4.3.2), we find good consistencies between our retrieved opacity values τ_1 and τ_3 and those of SR17 in

Parameter	**Description**	**Fixed (F) or variable (V)?**	**Prior value with constraints**
p_1	Stratospheric Haze (SH) pressure	F	0.04 bars
r_1	Effective radius of SH particles	F	$0.1\mu m$
τ_1	SH opacity at $\lambda = 0.89\mu m$	V	(0.2 ± 0.1)
$\bar{n}_1(\lambda) = n_1 + ik_1$	Complex refractive index of SH particles	F	$1.4 \pm 0i$
p_2	Tropospheric Cloud (TC) base pressure	V	(2.5 ± 1.25) bars
p_{2T}	TC top pressure	V	(0.2 ± 0.1) bars
r_2	Mean radius of TC particles	V	(0.5 ± 0.05)µm or (5 ± 1) µm in the GRS
τ_2	TC opacity at $\lambda = 0.89\mu m$	V	(20 ± 10)
$\bar{n}_2(\lambda) = n_2 + ik_2$	Complex refractive index of TC particles	F	$1.4 \pm 0i$ or $1.85 \pm 0i$
p_3	Chromophore layer (CB) base pressure	V	Set as equal to p_{2T}
p_{3T}	CB top pressure	V	Set as equal to $0.9 \times p_{2T}$
r_3	Effective radius of CB particles	V	(0.18 ± 0.018) µm
τ_3	CB opacity at $\lambda = 0.89\mu m$	V	(0.2 ± 0.1)
$\bar{n}_3(\lambda) = n_3 + ik_3$	Complex refractive index of CB particles	F	$CR16$
b	Variance of particle size distribution (same for all layers)	F	0.1
H_c/H_g	TC particle/gas particle fractional scale height	F	1.0
nh_3p_1	Ammonia knee pressure	V	(1.5 ± 0.15) bars
nh_3v_0	Ammonia vmr ($p > nh_3p_1$)	F	0.0035 ppv
nh_3v_1	Ammonia vmr ($nh_3p_1 < p < p_c$)	V	$(1 \pm 0.5) \times 10^{-5}$ ppv

Table 4.3.1: Key to *Crème Brûlée* model parameters with default prior values. Cloud particle size distributions in each layer are described by a gamma distribution [Hansen and Travis, 1974]: $n(r) = n_0 r^{(1-3b)/b} \exp(-r/r_i b)$ where r_i is the effective radius of the particles in layer i. Parameter notation was chosen to be consistent with SR17.

the NEB and SEB, especially given that the cloud structure in those regions would have evolved considerably between 2000 and 2018. We also retrieve the same chromophore altitude p_{2T} in the NEB within error, while the small differences in the SEB could easily be attributed to longitudinal or temporal changes. In any case, both values are consistent with a chromophore located in the upper tropospheric haze just below the tropopause altitude. However, although we usually obtain χ^2/n values less than 1.5 in all our retrievals (apart from in the EZ), we can see a number of clear flaws in the *Crème Brûlée* model when applied to our MUSE data using NEMESIS, particularly in regions of thick haze. One issue is the difficulty of retrieving two particle size distributions on top of cloud opacities: although we were able to fit most of the spectra using prior values of r_2 similar to those in SR17, we had to choose a much larger prior r_2 value to have an even remotely good fit to the GRS. Elsewhere on Jupiter, we were unable to retrieve any physical variations in r_2 and r_3, as can clearly be seen in figure 4.3.2, due to their degeneracy with opacity, and so we derive no scientific return in

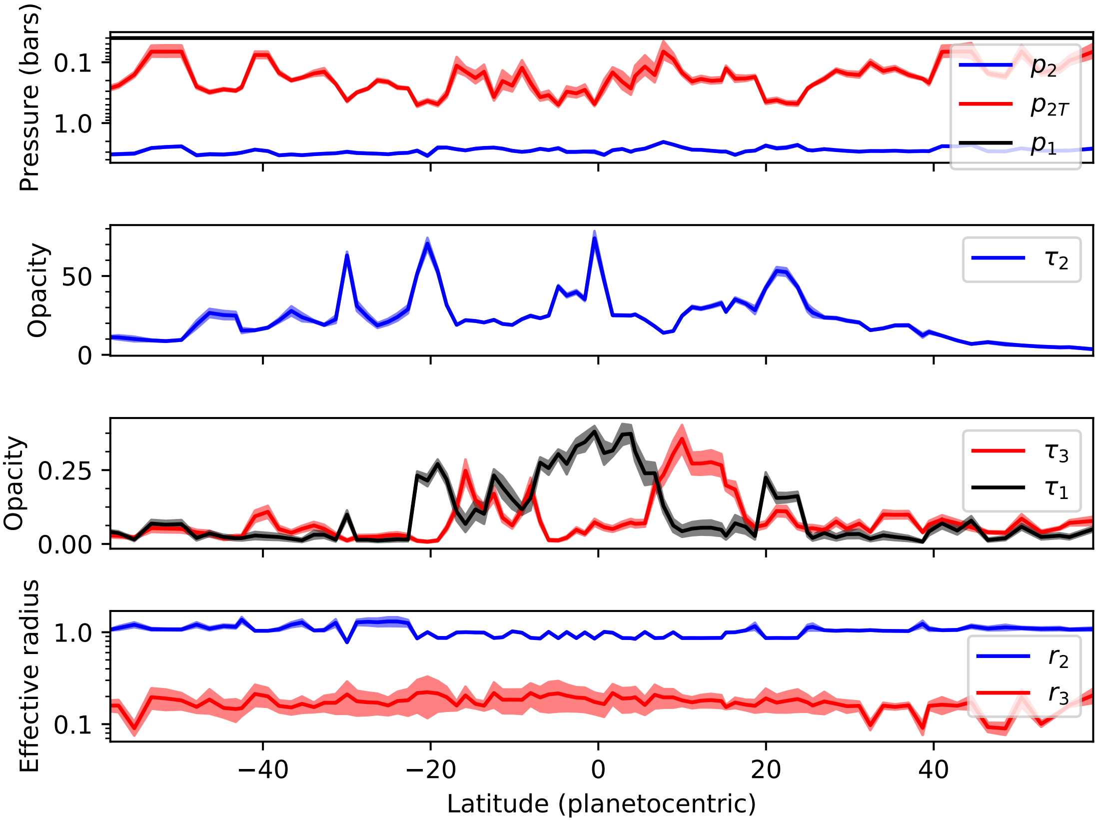

Figure 4.3.2: Retrieved parameters as a function of latitude along a single meridional swath of Jupiter (MUSE cube 2018-04-09T06:04:06.918); we refer to table 4.3.1 for a key to each of the variables in the plots.

allowing those parameters to vary in our model. In addition, we clearly cannot constrain ammonia abundances while also allowing nh_3p_1 to vary, which may be because we lack ammonia absorption data above 0.93µm that would allow us to retrieve vertical variations in ammonia abundances, even despite new ammonia line data which allows us to accurately model the 0.648µm absorption band.

Apart from the presence of degenerate variables, the biggest issue with the *Crème Brûlée* model is the wide pressure range covered by the tropospheric cloud layer. A uniform fractional scale height in cloud opacity is assumed from p_2, which is generally retrieved at an altitude that can only be sensed directly in the 5 micron window, to p_{2T}. This means that if the chromophore layer is placed at too low an altitude, the reflectance at 0.89µm, which is sensitive to haze around 0.1-0.2 bars, will be underestimated as the entire region between the chromophore layer and the stratospheric haze layer is assumed clear of aerosol, making it difficult to completely decouple real variations in chromophore altitude from differences in high-altitude haze opacity even if sufficient information is contained in the MUSE spectra to do so. The assumption of a constant fractional scale height also means that it is difficult to simultaneously provide a good fit to wavelengths sensitive to high-altitude haze (at 0.89µm) and wavelengths sensitive to deeper cloud (eg. at 0.619µm), which we show clearly in figure 4.3.3. The stratospheric haze layer is placed at too high an altitude for τ_1 to be adequately constrained, due to the absence of information close to 0.4µm that is present in the VIMS-V data. While it could be placed deeper in the atmosphere in order to account for 0.89µm reflectance, doing so was seen to interfere with the retrieval of p_{2T}.

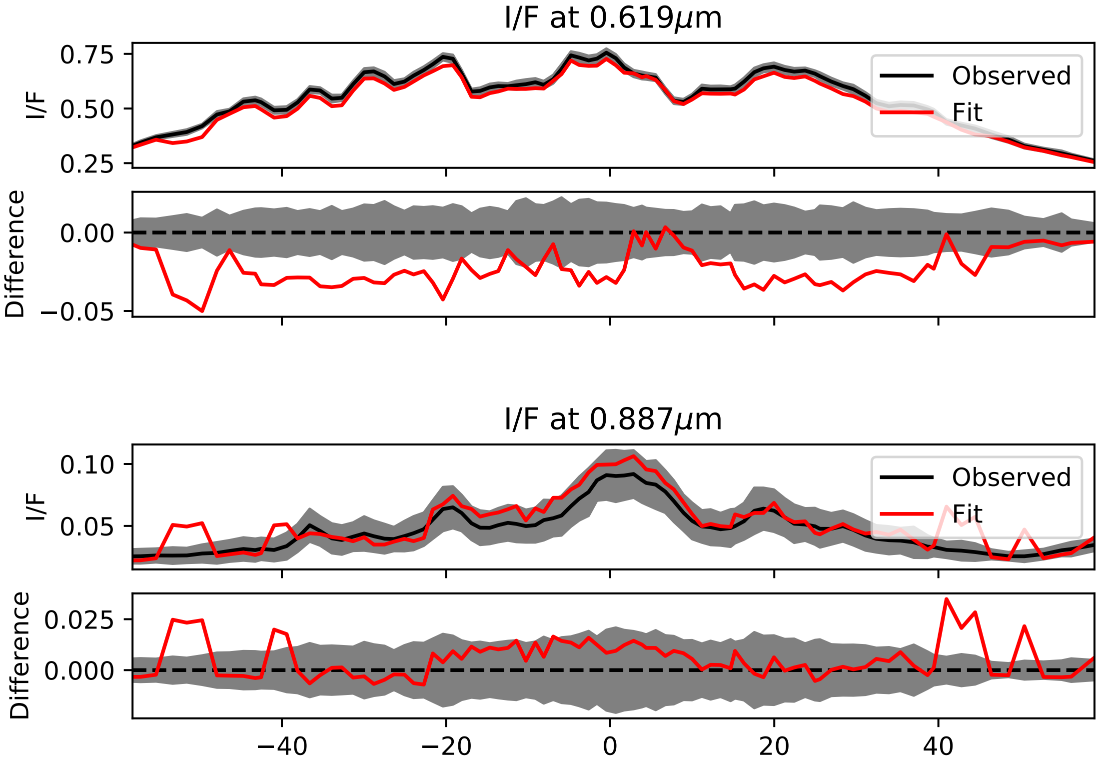

Figure 4.3.3: Meridional variation in the observed and fit I/F values at a wavelength sensitive to deep cloud (0.619µm) and a wavelength sensitive to high-altitude haze (0.887µm) using the *Crème Brûlée* model, showing the poor simultaneous fit to both wavelengths.

Although the *Crème Brûlée* model is seen to provide a good approximation to the cloud structure of most regions of Jupiter, its inadequacies in modelling MUSE spectra motivates us to use a different cloud model, where degenerate variables are kept to a minimum and where tropospheric cloud, high-altitude haze and chromophore altitude can all be decoupled and varied independently, while still keeping the number of state vector variables as low as possible. We will present such a model in section 4.4.

	EZ			**NEB**		**SEB**	
	MUSE (2.9°)	**SR17 (1.8°)**	$\mathbf{n_2}$	**MUSE (12.2°)**	**SR17 (12.6°)**	**MUSE (-12.5°)**	**SR17 (-12.9°)**
p_2 (bars)	2.67 ± 0.08	2.6 ± 0.3	1.4	2.85 ± 0.06	2.5 ± 0.2	2.28 ± 0.04	2.4 ± 0.2
			1.85	3.01 ± 0.02	2.6 ± 0.2		
p_{2T} (bars)	0.06 ± 0.04	0.08 ± 0.03	1.4	0.16 ± 0.02	0.22 ± 0.05	0.14 ± 0.03	0.33 ± 0.04
			1.85	0.17 ± 0.08	0.23 ± 0.3		
τ_2	14.4 ± 0.6	21 ± 4	1.4	16.8 ± 0.9	15 ± 2	9.3 ± 0.3	11 ± 2
			1.85	14.5 ± 0.6	6.8 ± 0.4		
τ_3	0.10 ± 0.02	0.154 ± 0.000	1.4	0.27 ± 0.03	0.33 ± 0.05	0.17 ± 0.03	0.15 ± 0.03
			1.85	0.23 ± 0.02	0.35 ± 0.03		
τ_1	0.26 ± 0.03	0.000 ± 0.000	1.4	0.05 ± 0.02	$0.01^{+0.07}_{-0.01}$	0.07 ± 0.05	0.03 ± 0.02
			1.85	0.05 ± 0.03	0.000 ± 0.000		
r_2 (µm)	0.31 ± 0.01	0.5 ± 0.1	1.4	0.32 ± 0.02	0.6 ± 0.1	0.253 ± 0.009	0.5 ± 0.1
			1.85	0.26 ± 0.02	0.33 ± 0.03		
r_3 (µm)	0.19 ± 0.05	0.18 ± 0.02	1.4	0.16 ± 0.01	0.18 ± 0.02	0.17 ± 0.02	0.15 ± 0.01
			1.85	0.15 ± 0.01	0.22 ± 0.01		
nh_3p_1 (bars)	1.15 ± 0.05	$1.4^{+1.2}_{-0.5}$	1.4	1.44 ± 0.08	1.5 ± 0.5	1.16 ± 0.04	1.4 ± 0.4
			1.85	1.49 ± 0.02	1.6 ± 0.5		
$nh_3v_1 \times 10^{-5}$	14 ± 21	11 ± 12	1.4	9 ± 1	4 ± 2	26 ± 35	4 ± 1
			1.85	10 ± 14	4 ± 2		
χ^2	831.7	93.13	1.4	491.4	96.04	470.3	100.3
			1.85	572.7	90.49		
χ^2/N	1.8	1.1	1.4	1.1	1.2	1.0	1.2
			1.85	1.3	1.1		

Table 4.3.2: Best-fit values retrieved by SR17 at low phase angle compared with MUSE retrievals at similar planetocentric latitude. Note that optical depths are taken at 0.89µm using MUSE data but at 1µm in SR17.

	NTBs	**GRS**	
	MUSE (-13.6°)	**MUSE (-20.1°)**	**SR17 (-20.4°)**
p_2 (bars)	2.94 ± 0.08	3.8 ± 0.1	2.9 ± 0.3
p_{2T} (bars)	0.34 ± 0.05	0.094 ± 0.004	0.33 ± 0.04
τ_2	24 ± 1	43 ± 2	11 ± 2
τ_3	0.074 ± 0.008	0.100 ± 0.002	0.14 ± 0.03
τ_1	0.13 ± 0.01	0.011 ± 0.003	$0.02^{+0.09}_{-0.02}$
r_2 (µm)	0.152 ± 0.004	5.11 ± 0.05	0.3 ± 0.1
r_3 (µm)	0.096 ± 0.007	0.042 ± 0.003	0.13 ± 0.02
nh_3p_1 (bars)	1.6 ± 0.9	1.59 ± 0.05	$1.6^{+1.2}_{-0.6}$
$nh_3v_1 \times 10^{-5}$	12 ± 1	3.6 ± 1.0	8 ± 3
χ^2	623.5	565.2	80.49
χ^2/N	1.4	1.3	0.98

Table 4.3.3: Same as table 4.3.2, but for the NTBs and GRS. The MUSE NTBs observation was taken from spectral image cube 2017-05-15T02:01:59:328. In this table we only include retrievals where $n_2 = 1.4$.

4.4 Continuous model with Carlson chromophore as a universal chromophore

Due to the inadequacies of the *Crème Brûlée* model in modelling upper tropospheric haze, we chose instead to use a model where variations in aerosol density with height could be determined to within greater vertical sensitivity. In Irwin et al. [2018], an example of such a model is presented, where a vertical profile of a single aerosol population, together with its imaginary refractive index spectrum, is retrieved continuously over the entire reference atmosphere. Such a retrieval is computationally expensive, as it requires the retrieval of a single cloud abundance value for each and every one of the 39 pressure levels specified in the reference atmosphere. Most of these retrievals are completely unnecessary, as firstly the pressure levels are spaced much more closely together than could possibly be resolved from the MUSE spectra, and secondly many of these pressure levels lie at altitudes where MUSE has very little sensitivity to cloud structure.

We therefore choose instead to model a continuous aerosol profile, where densities are only retrieved at a small number of selected pressure levels (spaced within half a pressure scale height apart in the region of peak MUSE sensitivity between 0.1-1.5 bar), and then interpolated over all 39 homogeneous layers in the model atmosphere between 1mbar and 10 bar using a cubic spline (Figure 4.4.1). The profile is set to vary smoothly with altitude according to a fixed correlation length $\Lambda_{\tau n}$ as previously described. This model has the advantage over the *Crème Brûlée* model of greater vertical resolution in the upper troposphere, yet is faster than a full layer-by-layer retrieval as in Irwin et al. [2018]. The biggest downside to such a parametrisation is that it makes vertical variations in particle size very difficult to model. Attempts to model variations in particle size with height usually result in smaller particle sizes as one moves away from the equator, due to the longer path length of light scattered by cloud and haze, and provide no noticeable improvement in fit compared to having a single particle size distribution. Specifying a gradual change in particle size with height is also very computationally expensive, since it requires the calculation of particle scattering phase functions for each of the 39 homogeneous layers in our reference atmosphere individually.

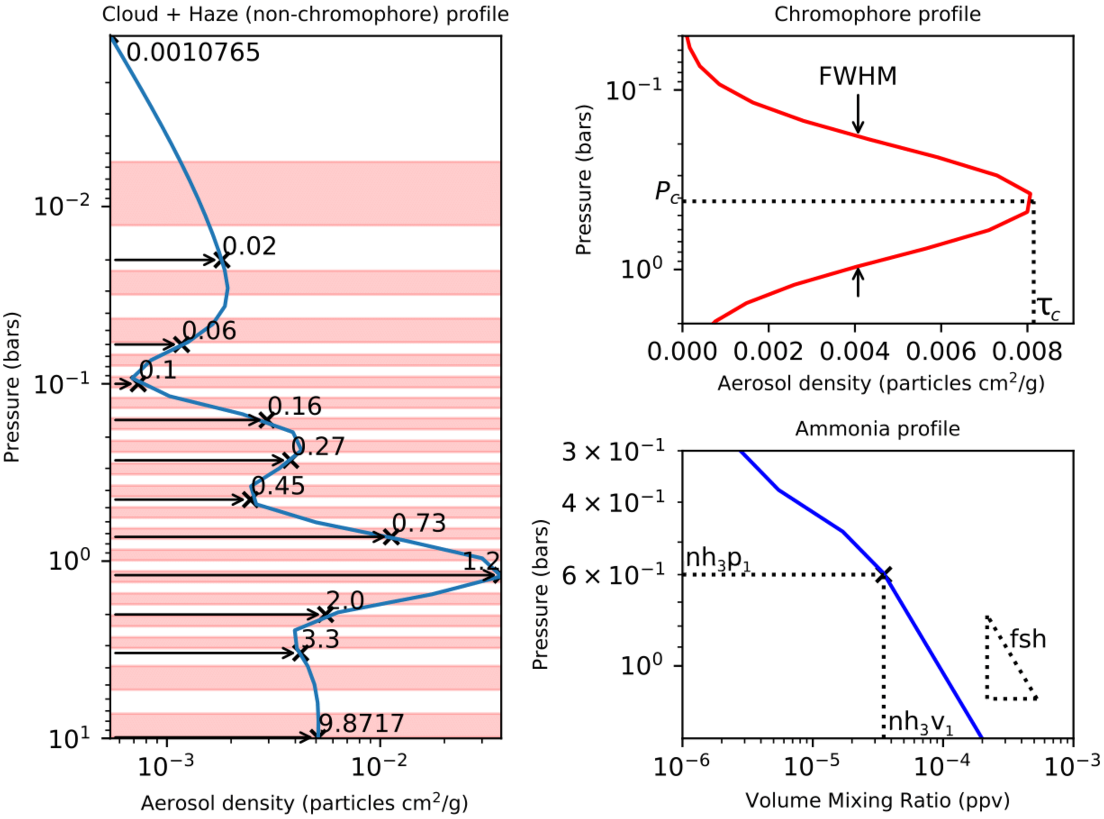

Figure 4.4.1: Graphs showing arbitrary (and unphysical) retrieved atmospheric parameters from a synthetic spectrum of Jupiter, chosen to best highlight all variable parametrisations in our model. Left is a continuous vertical profile of conservatively-scattering non-chromophore aerosol. Particle density values are retrieved at the altitudes marked with the black crosses (and with pressure values in bars stated next to each cross), and then interpolated over the whole atmosphere using a cubic spline. These altitudes are chosen to be more closely-spaced in regions of greater vertical sensitivity and further-spaced in regions of little sensitivity. Alternating red and white horizontal lines indicate the altitudes of the 39 homogeneous layers used in our reference atmosphere (which also apply to our other variable profiles), whose vertical spacing is chosen according to the same criteria. Top-right is a vertical chromophore profile, which we parametrise using a Gaussian of peak abundance τ_c centred around an altitude p_c, and with a full width half-maximum FWHM. Bottom-right is a vertical profile of gaseous ammonia. We retrieve a reference volume mixing ratio value nh_3v_1 at a reference pressure value nh_3p_1. We then extrapolate this value to all other pressure levels either using a scale height value fsh, which we require to be less than 1 in order for the ammonia abundance to decrease with ascending height, or by assuming 100% saturation (whichever value is lower).

In our model, we therefore assume a constant cloud particle size distribution with height. For this profile, the cloud particles are assumed to be conservatively-scattering, which is a safe assumption as the imaginary refractive index of ammonia ice is only of the order of 10^{-5} at these wavelengths [Martonchik et al., 1984]. We set the correlation length $\Lambda_{\tau n}$ of this profile to be 1.5, which was seen to be a good compromise between providing a reasonable fit to Jovian spectra while still providing realistic information on vertical variations of aerosol without ill-conditioning.

Another drawback of the model of Irwin et al. [2018] is that it does not decouple chromophores from other aerosol particles, instead assuming the same optical constants for all aerosols when in practice only a small fraction of the total aerosol content is likely to be blue-absorbing. This makes it very difficult to fit laboratory optical constants, which were obtained from much purer samples of chromophore, to Jovian spectra. We therefore retrieve two separate aerosol profiles simulaneously: one conservatively-scattering cloud profile as previously mentioned, plus an additional vertical profile of chromophore abundance with optical constants fixed to those listed in CR16. When doing preliminary modelling of a continuous chromophore profile, we found that the retrieval naturally converged to a solution where the chromophore profile would roughly resemble a Gaussian centred at an altitude of peak chromophore opacity. We therefore decided to model the chromophore profile as a Gaussian, of a retrievable pressure and peak opacity, and fixed FWHM of a pressure scale height. This was in order to a) save computational time, due to the fewer variables to be retrieved, and b) in order to properly decouple cloud and chromophore particles at altitudes where there is sensitivity to cloud but not to chromophore. We usually parametrise both our cloud and chromophore profiles in units of particles cm^2/gram of atmosphere (that is, the specific density in particles/gram multiplied by the extinction cross-section of the particles at 0.89µm), since this allows individual cloud layers to be better discerned than using more intuitive density units of particles/cm^3 of atmosphere, although in section 4.6 we will convert these values into units of g/l in order to compare them with theoretical and observational constraints in the literature. The ammonia gas profile was parametrised by a fractional scale height, with a single retrieved value at a fixed pressure level of 0.6 bars. This is somewhat above the altitude of peak ammonia sensitivity, but ensured sub-saturation above the predicted ammonia cloud condensation level. We set abundances to never exceed 100% saturation regardless of altitude. A full list of the forward model parameters used in this section, together with their prior values and constraints, is given in table 4.4.1.

Our new model now leaves us with three unconstrained parameters that are very difficult to retrieve directly using optimal estimation: the effective radii of both particle populations (r_n and r_c for the non-chromophore and chromophore particles respectively) and the most likely value for the real part of the refractive index of non-chromophore particles (n_n). We therefore perform several

Profile	**Variable definition**	**Variable symbol**	**Fixed (F) or variable (V)?**	**Prior values with uncertainties**
Combined cloud and haze	Specific aerosol densities of non-chromophore profile $\tau_n(P)$ (in units of aerosol particles cm^2/gram of atmosphere)as a function of a given pressure grid P (in bars)	$\tau_n(9.87)$	V	$(1.0 \pm 0.3) \times 10^{-3} \forall P$
		$\tau_n(3.30)$		
		$\tau_n(2.00)$		
		$\tau_n(1.20)$		
		$\tau_n(0.73)$		
		$\tau_n(0.45)$		
		$\tau_n(0.27)$		
		$\tau_n(0.16)$		
		$\tau_n(0.10)$		
		$\tau_n(0.06)$		
		$\tau_n(0.02)$		
		$\tau_n(0.001)$		
	Correlation length of aerosol profile	$\Lambda_{\tau n}$	F	1.5
	Effective particle radius (μm)	r_n		Found through χ^2/n analysis
	Variance of particle size distribution	σ_n		0.1
	Real refractive index at $\lambda = 0.7\mu m$	n_n		Found through χ^2/n analysis
	Imaginary part of complex refractive index spectrum as a function of wavelength λ	$k_n(\lambda)$		$10^{-9} \forall \lambda$
	Correlation length of refractive index spectrum	Λ_{kn}		0.1
Chromophore	Aerosol density at centre of Gaussian (particles cm^2/g)	τ_c	V	$(1.0 \pm 0.5) \times 10^{-3}$
	Altitude of centre of Gaussian (bars)	P_c		1.0 ± 0.5
	Gaussian FWHM (pressure scale height)	Δ_c	F	1
	Effective particle radius (μm)	r_c		Found through χ^2/n analysis
	Variance of particle size distribution	σ_c		0.1
	Real refractive index at $\lambda = 0.7\mu m$	n_c		1.4
	Imaginary part of complex refractive index spectrum as a function of wavelength λ	$k_c(\lambda)$		Carlson et al. [2016] extrapolated exponentially to wavelengths $\lambda > 0.75\mu m$
	Correlation length of refractive index spectrum	Λ_{kc}		0.1
Ammonia gas	Reference pressure level (bars)	nh_3p_1	F	0.6
	Reference volume mixing ratio (VMR) at a pressure level of 0.6 bars	nh_3v_1	V	$(1.0 \pm 0.5) \times 10^{-5}$, saturation-limited
	Fractional scale height	fsh	V	0.50 ± 0.25, decreasing with height and saturation-limited

Table 4.4.1: Explanation of variables used to parametrise the forward model in section 4.4, with prior values and constraints specified when applicable.

retrievals fixing each of these parameters to a range of different values, and then selecting those values that result in the lowest χ^2/n. We refer to this method as a 'χ^2/n analysis', and is similar to the method used by Sato et al. [2013] to find the most likely real refractive index value of the visible cloud layers of Jupiter from Cassini/ISS. We place a lower bound on n_n of 1.42, akin to the value of ammonia ice [Martonchik et al., 1984], and an upper bound of 1.8, close to the value found by Sato et al. [2013], while we fix the chromophore real refractive index n_c to 1.4 in line with CR16. The lower and upper bounds on r_n and r_c are more difficult to estimate. Ragent et al. [1998] estimate the effective radii of the 0.5 and 1.2 bar cloud layers found in the PES to be anything from 0.5 to 5 microns, but West et al. [2004] estimate stratospheric haze particle effective radii, to which MUSE spectra may be sensitive towards the poles, of below 0.2µm. These values are also similar to constraints provided by spectropolarimetric observations of Jupiter (e.g. Stoll [1980], McLean et al. [2017]). We therefore place the lower and upper bounds on r_n at 0.1µm and 7.5µm respectively. We have even less prior constraint on chromophore particle sizes, other than that they are most likely located above the visible cloud layers and are hence smaller than aerosols in the deepest visible cloud layer. The chosen lower and upper bounds on r_c respectively of 0.02µm and 1µm are therefore more arbitrary. We choose to perform our χ^2/n analysis using a grid of 8 different r_n values $\{0.1, 0.25, 0.5, 0.75, 1, 2.5, 5, 7.5\}$, 6 different r_c values $\{0.02, 0.05, 0.1, 0.2, 0.5, 1.0\}$ and 4 different n_n values $\{1.42, 1.5, 1.6, 1.8\}$, giving a total of 192 separate retrievals for a single spectrum. For our initial modelling test, we choose a spectrum from the centre of the GRS (-20.4^o planetocentric latitude, 146.5^o System III longitude), since this is both the reddest region of Jupiter and, as we found in section 4.3, the most difficult region of Jupiter to model using Carlson chromophore. We fix the variances of both particle size distributions to be 0.1 as in SR17; this is a relatively arbitrary value and we find that changing it to 0.05 as in eg. Irwin et al. [2018] does not provide a noticeable improvement in fit to MUSE spectra or provide a better constraint on particle effective radii.

Figure 4.4.2 shows the results of this χ^2/n analysis. As the blue-absorption slope of the GRS is so much steeper than that of the Carlson chromophore absorption spectrum, the retrieval has to make the blue-absorption slope as steep as possible by raising the value of r_n and n_n (to increase the scattering efficiency at red and near-infrared continuum wavelengths), while also decreasing r_c to very low values (to drive down scattering at very short wavelengths). The best fit to the GRS spectrum, achieved with $r_n = 5\mu m$, $r_c = 0.02\mu m$ and $n_n = 1.6$, is shown in figure 4.4.3. The overestimation of I/F around 0.82-0.83µm is partly due to poor modelling of CIA, as we explain in appendix B. In addition, CR16 did not publish data above 0.75µm, so our exponential extrapolation of the CR16

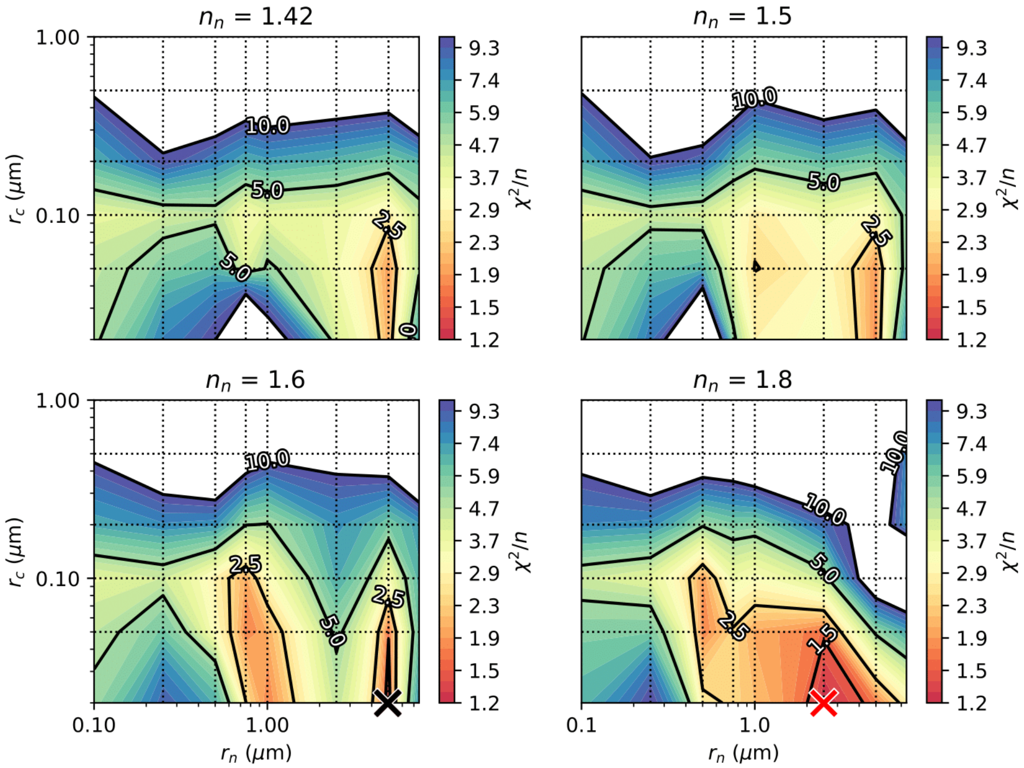

Figure 4.4.2: Results of χ^2/n analysis, when chromophore optical constants are fixed to CR16 values. Each retrieval is plotted against r_n on the x-axis and r_c on the y-axis, for a single value of n_n as given in the plot title. Intersections of dashed grid lines show the fixed r_n and r_c values of the retrievals themselves. The red cross shows the retrieval with the best convergence ($\chi^2/n = 1.18$), but the resulting cloud profile is unphysical. The black cross shows the retrieval with the second-best convergence ($\chi^2/n = 1.22$), and whose spectral fit is plotted in figure 4.4.3.

optical constants to near-infrared wavelengths could be incorrect. There are, however, two poorly-fit wavelength regions that lie within the range of tabulated values in CR17 and which clearly highlight flaws in the absorption spectrum of Carlson chromophore. One is the region around 0.63-0.70μm, whose reflectance is underestimated by Carlson chromophore, and the other is around 0.53-0.58μm, which is home to a weak methane and ammonia absorption feature. By contrast, the I/F below 0.5μm is underestimated, a result of having to make the value of r_c very small in order to improve the fit to the spectral slope at higher wavelengths. Expanding our parameter space down to lower values of r_c would only make the I/F values at these wavelengths even more greatly underestimated due to the lower scattering efficiency. Together, these discrepancies therefore indicate a chromophore whose absorption spectrum requires a more abrupt change in gradient somewhere around 0.6μm than can be provided by Carlson chromophore. Although this model is still an improvement on the *Crème*

Brûlée model, we are still curious to see if we can glean any information from the MUSE spectra on how a real Jovian chromophore absorption spectrum would differ from the CR16 optical constants. For this reason, we will choose to retrieve the chromophore refractive index spectrum directly from the MUSE data in section 4.6.

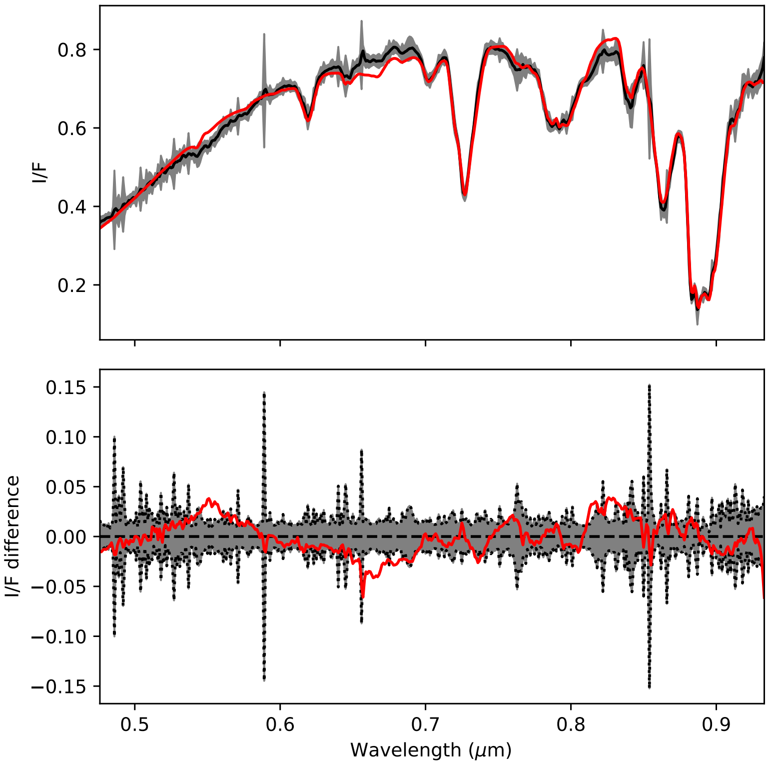

Figure 4.4.3: Best fit to the spectrum of the GRS (for the values of r_n, r_c and n_n that give the best physical fit as shown in figure 4.4.2)

4.5 Fits using other laboratory chromophores

4.5.1 Titan tholins and phosphorus chromophore

Apart from CR16, the only other available optical constants for Jovian chromophore were published by Noy et al. [1981], who produced a yellow allotrope of phosphorus in the laboratory by photolysing phosphine in the presence of hydrogen gas with UV radiation. Preliminary retrievals on OPAL data by Fry and Sromovsky [2018] showed similar promise for the Noy chromophore as for the Carlson chromophore. Unfortunately, data from Noy et al. [1981] are only available at wavelengths shortward of 0.6μm. We have therefore extrapolated these optical constants using an exponential for the rest of the wavelengths in the MUSE spectral range.

Given the scarcity of Jovian laboratory chromophore data, we have decided to also compare

Carlson chromophore with alternative non-Jovian laboratory chromophores in the literature. A great wealth of laboratory analyses and optical constant derivations of the chromophore particles (commonly known as 'tholins') that make up Titan's haze layers is available in the literature, as reviewed by Brassé et al. [2015]. This is because, unlike on Jupiter where the origin of chromophore remains elusive, the production of Titan tholins is known to be the result of photochemical reactions between N_2 and CH_4 in Titan's primarily nitrogen-based atmosphere, even if the exact reaction pathways and constituents of tholins are still subject to debate, as reviewed by Waite et al. [2009]. This is analogous to the production mechanism behind Carlson chromophore, involving reactions between NH_3 and C_2H_2, the latter compound itself a photolysis product of CH_4, in a hydrogen-based atmosphere. Although the atmospheric conditions found in Titan's upper atmosphere (which are beyond the scope of this thesis, but are reviewed in detail in Strobel et al. [2009]) that result in chromophore production are very different to those found on Jupiter, the plenitude of laboratory optical constants for Titan tholins leads to them occasionally being used to fit residuals in giant planet spectra, for instance by Sindoni et al. [2017].

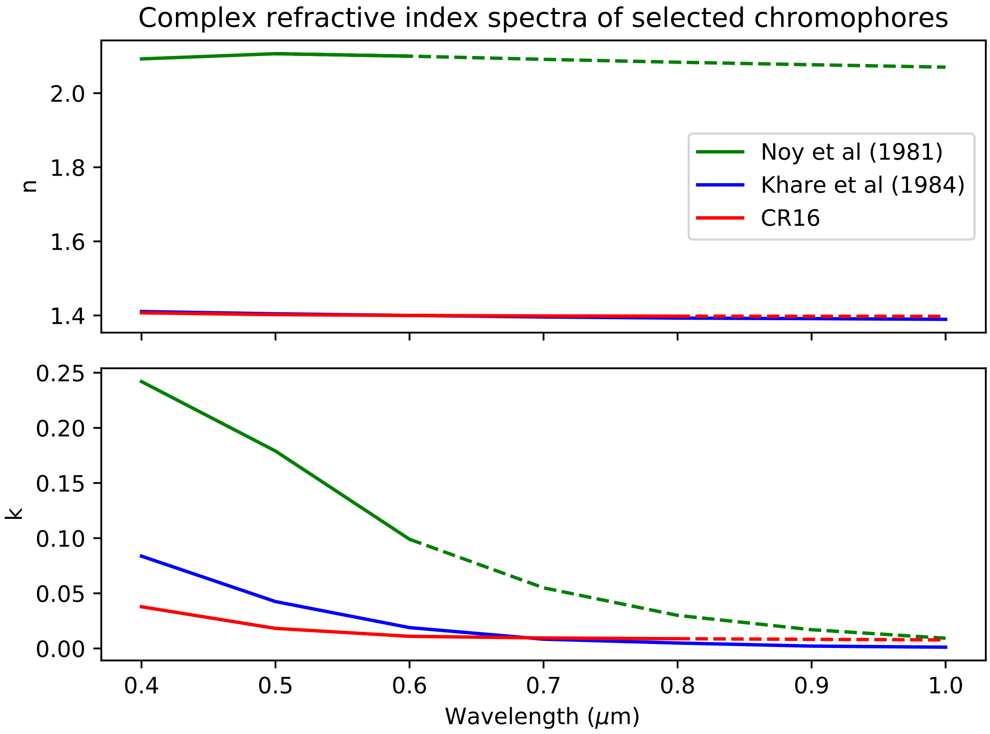

Figure 4.5.1: Optical constant spectra of different candidate chromophores, with the real part shown in the plot on top and the imaginary part in the plot on the bottom. Dashed lines indicate extrapolated values that are not present in the literature. For Noy et al. [1981], all values above 0.6μm are extrapolated, while for CR17 all values above 0.75μm are extrapolated.

Out of all the Titan tholins reviewed in Brassé et al. [2015], we tested the fit to the spectrum of the GRS using the optical constants of Khare et al. [1984], Vuitton et al. [2009] and the 2% and 5% methane analogues in Mahjoub et al. [2012]. These were chosen due to their favourable spectral range, and due to their similar smooth increase in imaginary refractive index towards short wavelengths (unlike that of Ramirez et al. [2002] which shows some decrease in absorption below 0.5µm). Of all these optical constants, we only managed to provide a comparable fit to Carlson chromophore using Khare et al. [1984], which we achieved using a value of $n_n = 1.6$, $r_n = 4.5\mu m$ and $r_c = 0.05\mu m$. We note that these optical constants were also found to provide the best fit to Juno/JIRAM spectra between 2.4 and 3.0µm of the STB white ovals according to Sindoni et al. [2017], albeit using much smaller particle sizes than in our analysis. However, the Khare et al. [1984] spectrum also provided a poor fit to wavelengths between 0.59µm and 0.68µm, which resulted in an aerosol profile where the greatest density of aerosol was perceived to be in the upper tropospheric haze, as shown in figure 4.5.3. We know this to be unphysical, as prior observations at our wavelength range in the literature have shown that a thick cloud layer must be found deeper than at least 0.7 bars (as was discussed previously in section 1.2), as we retrieve clearly with Carlson chromophore, for which the fit to the methane peak at 0.619µm is superior. We can therefore see that, even despite the many adjustments one can make to particle size distributions in order to fit an arbitrary set of chromophore optical constants to MUSE spectra, the Carlson chromophore can still provide a better fit than Titan tholins.

We obtained a fit to the GRS spectrum using the Noy chromophore very close to that of the Carlson chromophore, even despite the very large difference in real refractive index between the two compounds. This was achieved using the same values of n_n, r_n and r_c as with the optical constants of Khare et al. [1984]. However, we also obtained a similarly unphysical cloud profile with the Noy et al. [1981] optical constants to the one we obtained using the Khare et al. [1984] optical constants, partly a consequence of the lack of empirical laboratory data above 0.6µm. Since the CR16 optical constants provide better constraints on the degree of absorption up to 0.75µm, we have chosen to abandon the use of the Noy chromophore, even as a prior, for subsequent retrievals in this chapter. We will revisit the Noy chromophore when we perform retrievals of Saturn spectra in chapter 6.

4.5.2 Irradiated NH_4SH

An alternative hypothesis of the source of red colour in Jupiter's atmosphere is that of NH_4SH ice itself, which was shown first by Lebofsky and Fegley [1976] and later by Loeffler et al. [2016]

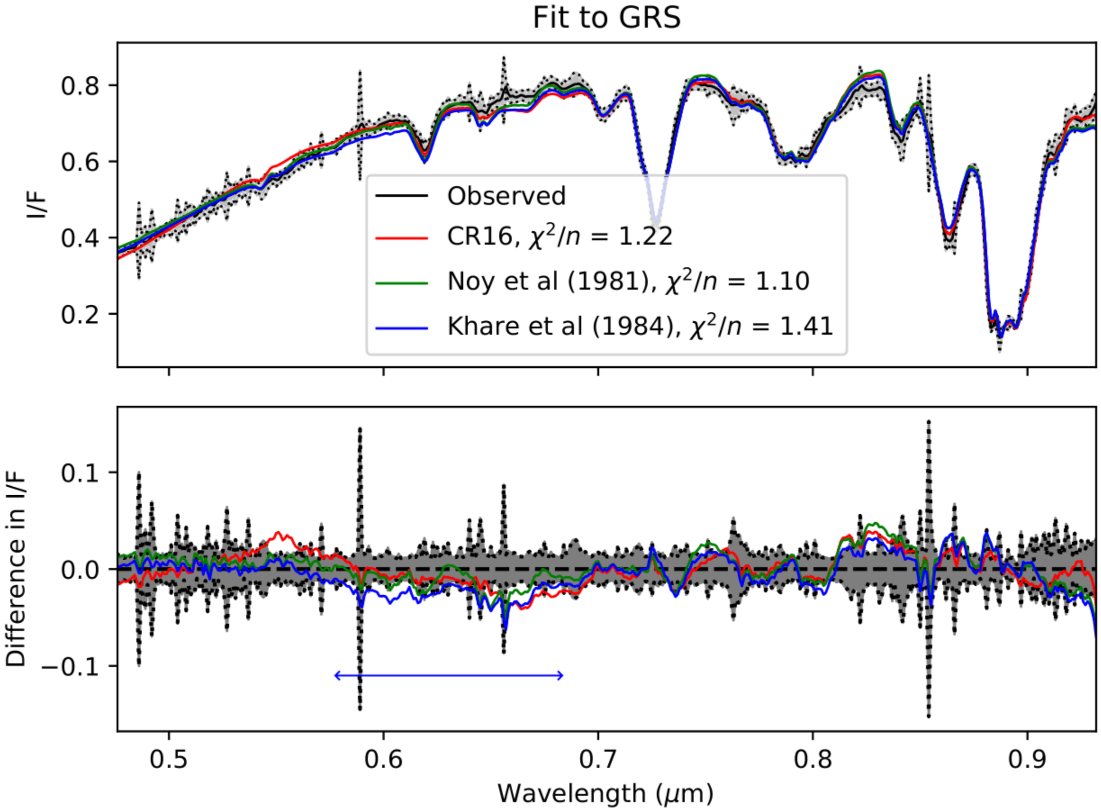

Figure 4.5.2: A comparison of the fit of Carlson chromophore to the GRS, as presented in figure 4.4.3, to the fit to the same spectrum provided by two other candidate chromophore compounds. In each case, we state the quality of convergence to the spectrum in the legend. We highlight the spectral range in which the chromophore of Khare et al. [1984] provides a poor fit to the spectrum of the GRS using the blue arrow in the bottom diagram.

and Loeffler and Hudson [2018] to dissociate into species of sulphur radicals under high-energy proton irradiation (simulating cosmic radiation) that strongly absorb shortwave radiation. This is an attractive proposition given the postulated composition of the visible cloud layers as previously explained in section 1.2, which would provide an abundant source of chromophore through this production mechanism. Additional hypotheses would therefore not need to be invoked in order to explain local elevations in the abundances of chromophore reactants such as acetylene, as would Carlson chromophore. The raised elevated real refractive index of aerosol particles found by Sato et al. [2013] in the STropZ also appears to provide some observational evidence of the presence of NH_4SH, and retrievals by Sromovsky and Fry [2010] in the near-IR even appear to suggest that NH_4SH ice could be present well into the upper tropospheric haze.

There are several issues with NH_4SH as a chromophore, however, as can be seen later in Figure 4.6.4. One is that the reflectance spectrum of irradiated NH_4SH only appears to show substantial

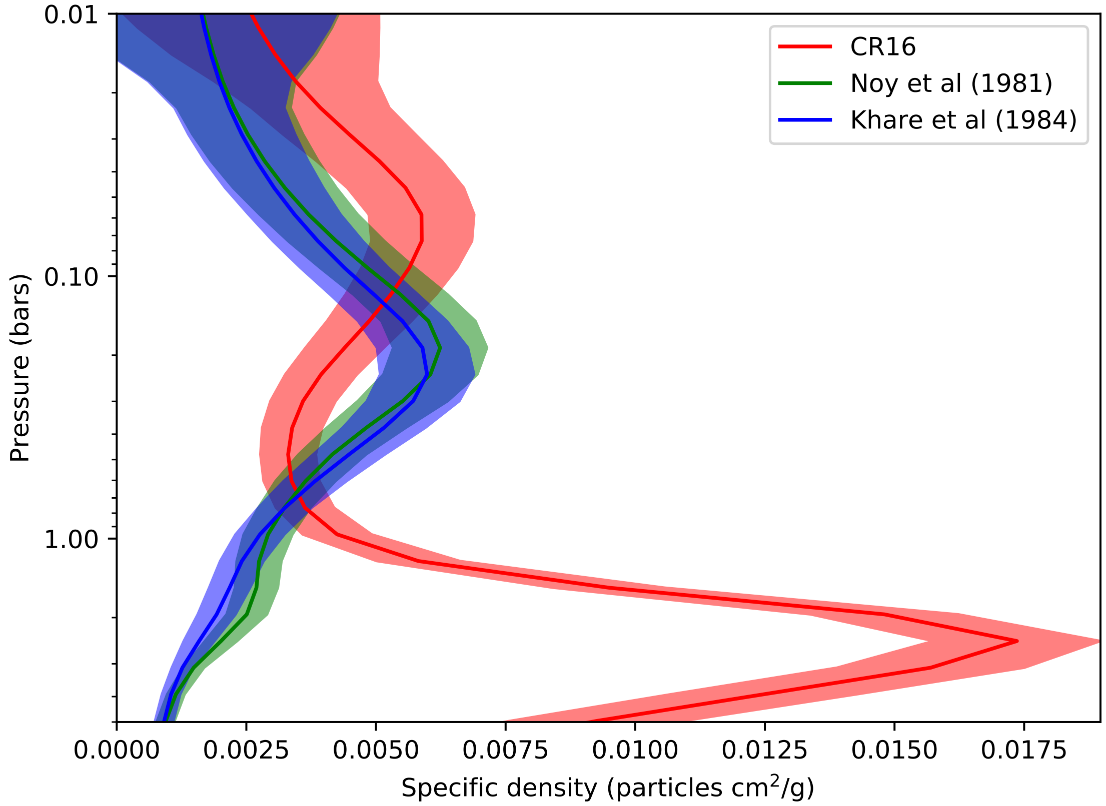

Figure 4.5.3: Retrieved cloud profiles $\tau_n(p)$ for the three different candidate chromophore compounds fit to the GRS, whose spectral fits are shown in figure 4.5.2.

absorption below 0.5µm, whereas the shortwave absorption peak in Jovian spectra extends all the way to 0.6µm. This discrepancy may be alleviated by altering the altitude of the irradiated NH_4SH particles or changing their size distribution, but this is difficult to verify currently due to the absence of NH_4SH optical constant data below 1µm. The other issue pertains to the presence of a secondary broad absorption peak at around 0.61µm due to S_3^- radicals, which is completely absent in Jovian spectra. This extra absorption peak is known to disappear under only two circumstances: a) the NH_4SH is irradiated at temperatures far below even the coldest temperatures found on Jupiter [Loeffler and Hudson, 2018], or b) the NH_4SH is irradiated at temperatures typically found in the upper troposphere, but is then reheated to temperatures one would only expect around 2 bars, substantially below the maximum visible penetration depth even in the belts [Loeffler et al., 2016]. We will therefore solely assume an organic photochemical chromophore compound unless better NH_4SH optical constants become available and a plausible hypothesis arises to explain the absence of this secondary peak in Jovian spectra.

4.6 Direct chromophore retrieval

4.6.1 Limb darkening analysis of the NEB

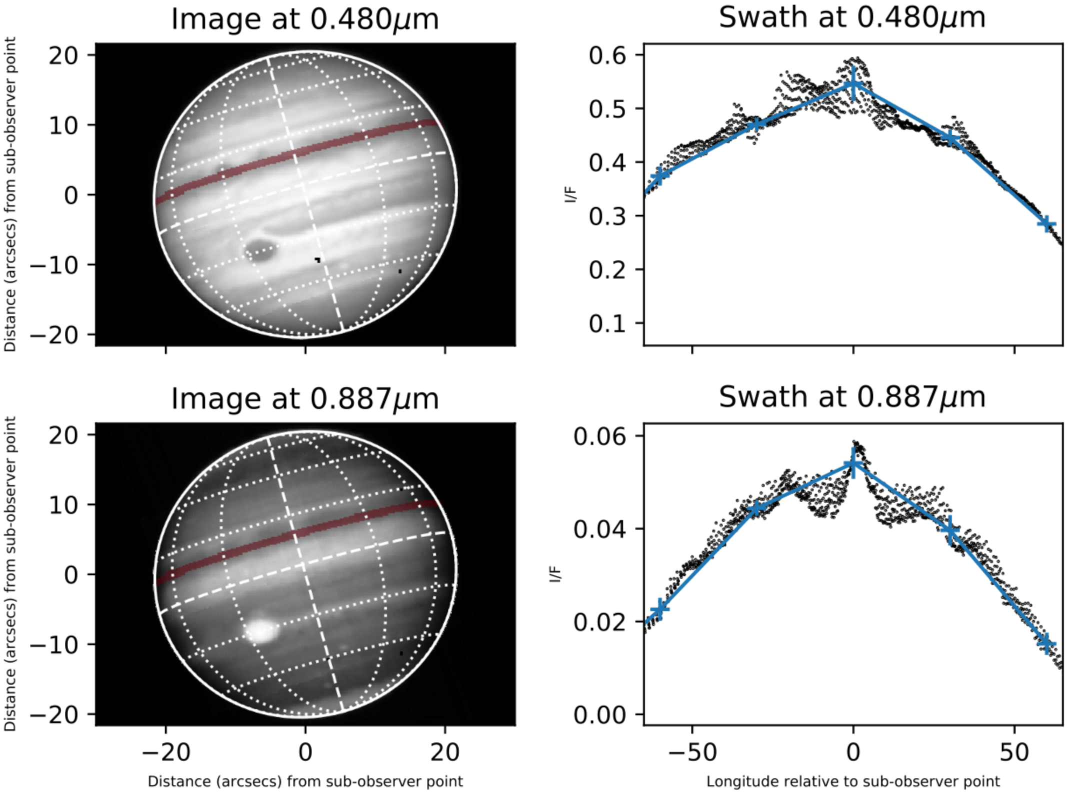

Figure 4.6.1: Plots showing the extraction of a limb darkening spectrum from the MUSE data. Plots on the left show the MUSE spectral image at two sample wavelengths: the top at a wavelength sensitive to chromophore, and the bottom at a wavelength sensitive to high-altitude haze. Dashed white lines show the equator and the sub-observer longitude, dotted lines show lines of planetocentric latitude (in increments of 20 degrees) and lines of longitude relative to the sub-observer point (in increments of 30 degrees). The thick outer white line shows the calculated terminator of Jupiter using ellipsoid limb fitting as described in section 2.4.2. The latitudinal swath extracted from the data is shown in a darker shade, bounded by 10^oN and 13^oN (planetocentric) on each side. Plots on the right show, for the same two wavelengths, all the I/F values at each spatial pixel contained within the swath in black, as a function of longitude. Points in blue then show the averaged latitudinal swath, sampled at 30 degree intervals, used for limb darkening analysis, with vertical bars showing the spectral error associated with those points. We note that the curves are not symmetric around the central meridian due to an offset between the sub-solar and sub-observer longitudes.

Seeking to improve our fit to the GRS spectrum relative to Carlson chromophore, we chose to retrieve the imaginary refractive index spectrum $k(\lambda)$ of a universal chromophore ourselves directly. A drawback of imaginary refractive index retrieval is that it takes into account any broad residuals in an observed spectrum, that may be more likely to be a result of a poor forward model than of actual chromophore absorption features. It is therefore almost completely impossible to decouple uncertainties in both aerosol size distributions and optical constants using a single spectrum alone, since any error in the shape of the spectrum caused by a bad particle size distribution would be taken into account in the shape of the imaginary refractive index spectrum. We therefore need to place an additional constraint on the particle size distributions through limb darkening analysis.

In limb darkening analysis, one assumes that a single latitudinal swath of Jupiter is spatially homogeneous over its entire longitudinal range, and measure the attenuation of spectral I/F with viewing zenith angle. This provides an additional source of information on aerosol structure to greater precision and vertical resolution than can be provided by observations of Jupiter at a single viewing geometry (so-called 'point' retrievals), as the optical path of reflected sunlight through Jupiter's atmosphere, and hence the altitude of peak sensitivity to aerosol and ammonia, increases with viewing zenith angle from nadir. Limb darkening analysis also provides greater angular constraint on the scattering phase functions of aerosols in Jupiter's atmosphere, and hence their particle size distributions and the real parts of their refractive indices. There are two major disadvantages of limb darkening, however. The first is that increasing the number of viewing geometries also increases the number of spectral points to be retrieved by the same magnitude. This makes retrievals far slower than they would otherwise be for point retrievals, especially if one makes use of geometries obtained at very high viewing zenith angles, for reasons previously explained in section 3.3. To mitigate this, we attempt to minimise the number of geometries to fit simultaneously, but over as large a viewing zenith angle range as possible. In addition, we discard 'rank 4' wavelengths in our reduced wavelength scheme (referring back to section 3.8) and only make use of wavelength ranks 3 and below. As shown in Figure 3.8.2, the difference in the retrieved profiles between using the full wavelength grid and discarding rank 4 wavelengths is not particularly noteworthy for point retrievals, and would not be substantially more noteworthy for limb darkening retrievals, given where the rank 4 wavelengths are located. The second disadvantage of limb darkening is that it is often difficult to find a latitudinal swath of Jupiter that can consistently be treated as spatially homogeneous at every single wavelength. One therefore has to choose the latitudinal range of the swath very carefully in order to avoid boundaries in the banded structure at both the level of the main cloud layer and the high-altitude haze layers. In addition, the degree of limb darkening with respect to viewing zenith angle has to be averaged over a given viewing zenith angle bin, in order to disregard anomalies in I/F due to the presence of discrete features. Nonetheless, one has to take into account that gaseous ammonia abundances vary greatly with longitude, even in the absence of discrete features, as shown by Fletcher et al. [2016].

For our representative swath, we chose the southern half of the NEB between 10^oN and 13^oN (planetographic), for a number of reasons. Firstly, it was the second reddest region of Jupiter after the GRS, as some time had already elapsed by this point since the formation of the NTBs red haze layer in late 2016 (see chapter 5). It also had low cloud and haze cover, as well as low gaseous ammonia abundances. This made extraction of a chromophore absorption spectrum more reliable, and less dependent on uncertainties in particle size distribution. Secondly, it was relatively spatially homogeneous in comparison both to the northern NEB, where a number of discrete features were present following the NTBs upheaval, and the SEB which was even more turbulent, both due to the presence of the GRS and to a large convective outbreak in the SEB in January 2017. The shape of the limb darkening curve along the swath was seen to be well-modelled if the swath was sampled at each wavelength at 30 degree longitude intervals (within a longitude range of ±60 degrees of the sub-observer longitude, in order to avoid mixing with the sky close to the outer perimeter of Jupiter's planetary disc), with each sample obtained by computing a Gaussian weighted average of all spectra within a FWHM of 3 degrees of longitude. The respective spectral errors were then found through the corresponding standard deviation of the Gaussian weighted average.

We then perform a similar χ^2/n analysis on this NEB swath as we did on the GRS in section 4.4, with only two differences. One is that the imaginary refractive index spectrum of chromophore is not fixed to Carlson chromophore at all wavelengths, but variable using the CR16 optical constants as a prior (with $\mathrm{n_c}$ fixed at 1.4). We retrieve the imaginary refractive index spectrum over a wavelength grid of 0.1µm intervals, chosen to be deliberately broad both in order to minimise the number of state vector variables to be retrieved (and hence the computational time), and so that the retrieval avoids mistaking local residuals in the spectra that may be due to other forward modelling errors as being due to chromophore absorption. The wavelength grid covers a wider range (0.4-1.0µm) than that of MUSE itself, to ensure that the imaginary refractive index spectrum fits the observed data well at the periphery of the MUSE wavelength range, given the broad spectral sampling of the imaginary refractive index grid. The other difference in our methodology from section 4.4 is that, since limb darkening retrievals have greater vertical precision than point retrievals, we have to decrease the intervals between adjacent pressure levels in the region of greatest vertical sensitivity between 0.1 and 1.5 bars, as well as increase the number of pressure levels upwards into the lower stratosphere, in order to model 0.89 micron absorption at the highest phase angles where the optical path through Jupiter's atmosphere is at its greatest.

The resulting χ^2/n values are shown in figure 4.6.2. We can see that the non-chromophore effective particle radius r_n can usually be constrained to within ±0.25µm as a function of real refractive index n_n, even with a maximum viewing zenith angle of just 60 degrees, as the value of r_n

Profile	Variable definition	Variable symbol	Fixed (F) or variable (V)?	Prior values with uncertainties
Combined cloud and haze	Specific aerosol densities of non-chromophore profile $\tau_n(P)$ (in units of aerosol particles cm^2/gram of atmosphere) as a function of a given pressure grid P (in bars)	$\tau_n(9.87)$ $\tau_n(0.45)$ $\tau_n(5.40)$ $\tau_n(0.27)$ $\tau_n(3.30)$ $\tau_n(0.16)$ $\tau_n(2.00)$ $\tau_n(0.10)$ $\tau_n(1.54)$ $\tau_n(0.06)$ $\tau_n(1.20)$ $\tau_n(0.036)$ $\tau_n(0.94)$ $\tau_n(0.02)$ $\tau_n(0.73)$ $\tau_n(0.012)$ $\tau_n(0.57)$ $\tau_n(0.001)$	V	$(1.0 \pm 0.1) \times 10^{-3} \forall P$
	Correlation length of aerosol profile	$\Lambda_{\tau n}$	F	1.5
	Effective particle radius (µm)	r_n		Found through χ^2/n analysis
	Variance of particle size distribution	σ_n		0.1
	Real refractive index at $\lambda = 0.7 \mu m$	n_n		Found through χ^2/n analysis
	Imaginary part of complex refractive index spectrum as a function of wavelength λ	$k_n(\lambda)$		$10^{-9} \forall \lambda$
	Correlation length of refractive index spectrum	Λ_{kn}		0.1
Chromophore	Aerosol density at centre of Gaussian (particles cm^2/g)	τ_c	V	$(1.0 \pm 0.2) \times 10^{-3}$
	Altitude of centre of Gaussian (bars)	P_c		1.0 ± 0.2
	Gaussian FWHM (pressure scale height)	Δ_c	F	1
	Effective particle radius (µm)	r_c		Found through χ^2/n analysis
	Variance of particle size distribution	σ_c		0.1
	Real refractive index at $\lambda = 0.7 \mu m$	n_c		1.4
	Imaginary part of complex refractive index spectrum as a function of wavelength λ	$k_c(\lambda)$	V	Carlson et al. [2016] extrapolated exponentially to wavelengths $\lambda > 0.75 \mu m$ with 10% prior uncertainty
	Correlation length of refractive index spectrum	Λ_{kc}	F	0.1
Ammonia gas	Reference pressure level (bars)	nh_3p_1	F	0.6
	Reference volume mixing ratio (VMR) at nh_3p_1 (ppv)	nh_3v_1	V	$(1.0 \pm 0.2) \times 10^{-5}$, saturation-limited
	Fractional scale height	fsh	V	0.50 ± 0.05, decreasing with height and saturation-limited

Table 4.6.1: Explanation of variables used to parametrise forward model in section 4.6, with prior values and constraints specified when applicable.

is inversely correlated with the difference in spectral I/F between low and high viewing zenith angle. However, it is still very difficult to constrain both n_n and r_n independently, even when observing a single latitude at multiple viewing geometries, while r_c can barely be constrained at all. An increase in the value of n_n can be compensated for in the fit to the spectrum simply by shifting r_n to progressively smaller values, from around 1μm when $n_n = 1.4$ to around 0.25μm when $n_n = 1.8$, while an increase in r_c can also be mitigated, to some degree, by increasing the chromophore imaginary refractive index spectrum $k_c(\lambda)$ at the shortest wavelengths. This makes an accurate retrieval of $k(\lambda)$ difficult, as r_c is the quantity for which we have the least prior knowledge. Filtering out all the solutions in our χ^2/n analysis with a χ^2/n value higher than 2.2, which corresponds roughly to the χ^2/n value below which a reasonable fit can be had to the general shape of the limb darkening curve, still leaves us with 31 possible optical constant solutions for the NEB.

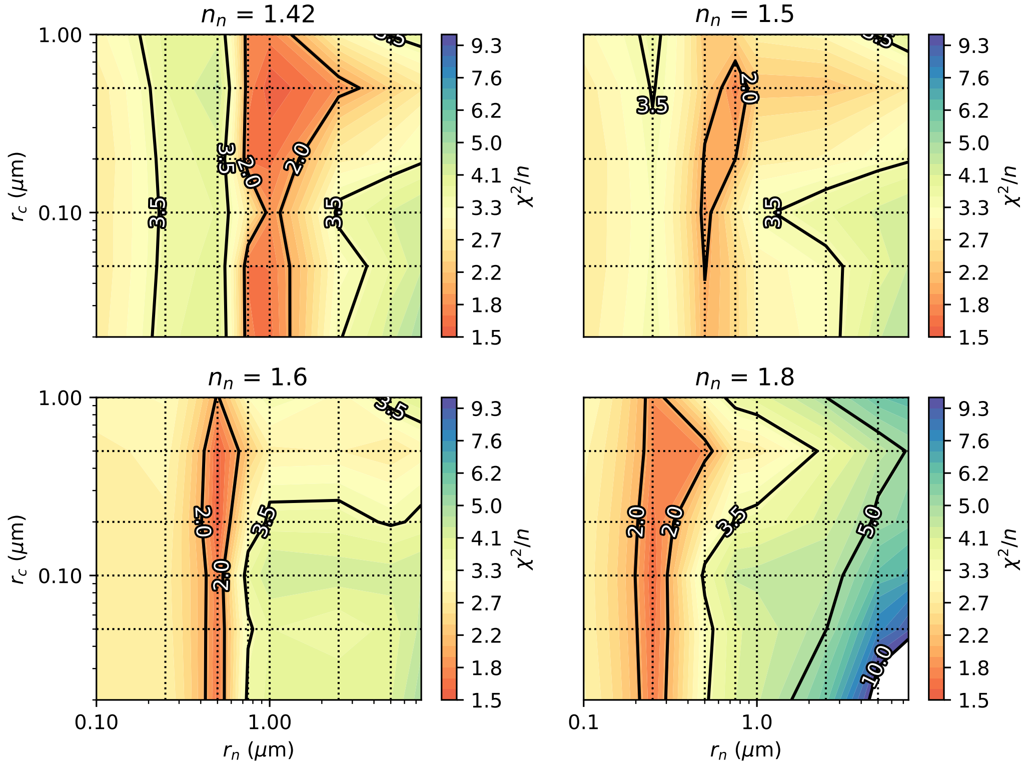

Figure 4.6.2: Results of χ^2/n analysis for a single swath of the NEB at 10^o-13^{o}N, allowing the chromophore imaginary refractive index spectrum to vary from a prior based on CR16 optical constants. Each retrieval is plotted against r_n on the x-axis and r_c on the y-axis, for a single value of n_n as given in the plot title. Intersections of dashed grid lines show the fixed r_n and r_c values of the retrievals themselves.

4.6.2 Eliminating optical constant solutions that result in unphysical aerosol profiles in the GRS

If we assume a universal chromophore, we can narrow down these degenerate optical constant solutions further by applying each one to a spectrum of the GRS and then eliminating the solutions that result in a χ^2/n value greater than 1. We use the same r_n, r_c and n_n values for each optical constant solution obtained from the NEB to fit the GRS when possible. However, if a good fit cannot be had with all of those values together, r_n is allowed to vary. If many valid solutions still remain after this process, the remaining solutions are eliminated according to more qualitative criteria. These solutions could have a) clearly unrealistic changes in aerosol density with height that do not correspond to prior observations of Jovian cloud structure (in the visible and near-infrared or otherwise), b) cloud abundances that do not match with microphysical constraints, or c) chromophore abundances that are too high given known concentrations of acetylene in the upper troposphere.

In Table 4.6.2, we tabulate retrieved maximum aerosol densities of both particle populations from the GRS using different chromophore optical constants, excluding results where $\chi^2/n > 1$. To obtain aerosol mass density values in g/l from specific aerosol densities in particles cm^2/gram, we assume that each particle (both chromophore and non-chromophore) has the same average density as ammonia ice, equal to 0.87 g/cm^3 according to Satorre et al. [2013]. If the main cloud layer is made up of NH_4SH, those values would have to be approximately tripled to account for the higher molecular mass of NH_4SH relative to NH_3. While there is substantial literature on the estimated aerosol densities of Jupiter's main cloud decks based on ECCMs and microphysical constraints, as previously discussed in section 1.2, most of these studies do not apply directly to the GRS, which is predicted to be exceptionally cloudy relative to other regions of Jupiter. Palotai et al. [2014] estimated consistent aerosol mass densities in the centre of the GRS of the order of 10^{-5} g/l over all visible altitudes using a general circulation model, while Zuchowski et al. [2009] estimated average NH_4SH cloud mass densities in the STropZ of the order of 10^{-6} g/l. By contrast, the Galileo Probe Nephelometer retrieved maximum mass densities of the order of $10^{-7} - 10^{-6}$ g/l at the PES [Ragent et al., 1998]. Recall that the PES was a hotspot region where aerosol densities are predicted to be exceptionally low by Jovian standards. Experimental constraints on the amount of chromophore that would be produced from the reaction of ammonia and acetylene in Jupiter's atmosphere is hard to come by, both because they are heavily dependent on the experimental conditions themselves, and because it is difficult to ascertain which exact endmembers of the reaction products are red in the first place. No information was given by CR16 on the yield of chromophore residue produced

<table>
<tr><th>n_n</th><th>r_n (prior, µm)</th><th>r_n (retrieved, µm)</th><th>r_c (µm)</th><th>χ^2/n</th><th>Peak cloud mass density (g/l)</th><th>Peak chromophore mass density (g/l)</th></tr>
<tr><td rowspan="7">1.42</td><td colspan="2" rowspan="4">0.75</td><td>0.02</td><td>0.86</td><td>1.11E-06</td><td>1.36E-08</td></tr>
<tr><td>0.05</td><td>0.82</td><td>1.02E-06</td><td>1.35E-08</td></tr>
<tr><td>0.2</td><td>0.77</td><td>1.60E-06</td><td>8.22E-09</td></tr>
<tr><td>0.5</td><td>0.80</td><td>2.89E-06</td><td>9.62E-09</td></tr>
<tr><td colspan="2" rowspan="2">1.0</td><td>0.05</td><td>0.96</td><td>1.67E-05</td><td>1.66E-08</td></tr>
<tr><td>0.1</td><td>0.78</td><td>1.70E-05</td><td>1.12E-08</td></tr>
<tr><td>1.0</td><td>5.63</td><td>0.2</td><td>0.57</td><td>1.02E-05</td><td>1.13E-08</td></tr>
<tr><td rowspan="4">1.5</td><td rowspan="3">0.5</td><td>1.06</td><td>0.1</td><td>0.68</td><td>2.31E-07</td><td>1.08E-08</td></tr>
<tr><td>1.30</td><td>0.05</td><td>0.75</td><td>2.18E-07</td><td>1.17E-08</td></tr>
<tr><td>1.49</td><td>0.02</td><td>0.87</td><td>2.41E-07</td><td>1.08E-08</td></tr>
<tr><td colspan="2">0.5</td><td>0.2</td><td>0.74</td><td>3.77E-07</td><td>7.92E-09</td></tr>
<tr><td rowspan="4">1.6</td><td colspan="2" rowspan="4">0.5</td><td>0.02</td><td>0.74</td><td>7.75E-07</td><td>1.92E-08</td></tr>
<tr><td>0.05</td><td>0.88</td><td>8.04E-07</td><td>1.52E-08</td></tr>
<tr><td>0.1</td><td>0.96</td><td>2.11E-06</td><td>1.15E-08</td></tr>
<tr><td>0.2</td><td>0.91</td><td>9.77E-07</td><td>9.06E-09</td></tr>
<tr><td rowspan="5">1.8</td><td colspan="2" rowspan="4">0.25</td><td>0.02</td><td>0.70</td><td>7.60E-07</td><td>1.47E-08</td></tr>
<tr><td>0.1</td><td>0.63</td><td>3.28E-07</td><td>1.07E-08</td></tr>
<tr><td>0.2</td><td>0.64</td><td>3.88E-07</td><td>7.90E-09</td></tr>
<tr><td>0.5</td><td>0.69</td><td>4.83E-07</td><td>9.76E-09</td></tr>
<tr><td>0.25</td><td>0.80</td><td>0.05</td><td>0.52</td><td>5.82E-08</td><td>2.61E-08</td></tr>
</table>

Table 4.6.2: Retrieved cloud and chromophore mass density values when chromophore optical constants obtained in limb darkening analysis (for a given r_n, r_c and n_n) are used to fit the GRS, excluding retrievals where $\chi^2/n > 1$. If fixing r_n in the retrieval does not give a superior χ^2/n than when r_n is allowed to vary, then the former retrieval is excluded in this table, otherwise the latter retrieval is excluded. The set of r_n, r_c and n_n values that will be selected for all subsequent Jupiter retrievals is highlighted in bold.

in their experiment. This makes it hard to put lower limits on Jovian chromophore abundances that would rule out retrievals with a value of τ_c that is too low, even if the acetylene production or advection rate in the upper troposphere of Jupiter is known. Keane [2017] published quantum yields of a small selection of compounds produced in the reaction of ammonia and acetylene, but none of them absorb light at visible wavelengths. Nonetheless, we can still provide a reasonable guess of an upper bound on the amount of chromophore produced in the Great Red Spot, based on the fact that the chromophore production rate cannot be greater than the acetylene flux rate. Moses et al. [2010] estimate mole fractions of acetylene of the order of 10^{-9} at 0.1 bars, which translates to approximately $10^{-10} - 10^{-9}$ g/l.

From Table 4.6.2, we can see that by far the easiest way of selecting a good set of optical constants for a given set of r_n, r_c and n_n values is by looking at retrieved maximum cloud densities, usually obtained between 1 and 2 bars of altitude. Values of n_n even slightly greater than 1.42 result in cloud abundances that are comparable to the Galileo PES or even smaller, even if NH_4SH is assumed to be the main cloud component instead of NH_3. Curiously, we begin to retrieve these low abundances even for $n_n = 1.5$, which is close to the margin of error for laboratory values of ammonia ice: although we assume a value of 1.42 to be consistent with Martonchik et al. [1984], Romanescu et al. [2010] and Satorre et al. [2013] both find values closer to 1.48. The only compound that is known to be present in Jupiter's atmosphere which is also known to have a lower refractive index than ammonia ice is water ice. Although water ice condenses out of Jupiter's atmosphere far below the level of the visible clouds, moist convection is known to be powerful enough on Jupiter to lift water ice particles to very high altitudes, particularly in regions to the northwest of the GRS [Simon-Miller et al., 2000]. It is possible that some water ice convects upwards into the visible clouds in the centre of the GRS itself, but that would require greater knowledge of microphysical processes to prove. By contrast, chromophore mass densities are consistently retrieved within a factor of 2 of 10^{-8} g/l, regardless of the chosen values of r_n, r_c or n_n. This is comparable to the amount of chromophore retrieved in the GRS by both SR17 and Baines et al. [2019], and would require acetylene abundances to be elevated by at least a factor of 10 in the GRS relative to the photochemical model of Moses et al. [2010]. Hypotheses regarding the increased abundances of acetylene in the GRS (for instance by Baines et al. [2019], who suggested lightning as a possible source) remain speculative, and are beyond the scope of this thesis. We will therefore neglect chromophore mass density values as a selection criterion for our possible chromophore solutions. Instead, we have chosen the solution in which $n_n = 1.42$ and $r_c = 0.2$µm, due to its low χ^2/n value and its high peak cloud mass density value when fit to the GRS. Although the chromophore optical constants were retrieved from the NEB using a value of $r_n = 1.0$µm, this had to be raised to 5.62µm in order to fit the GRS. Unfortunately, this means that, when we apply this chromophore optical constant solution to other regions of Jupiter, we will not be able to keep r_n constant, as previously hoped.

Figure 4.6.3 shows this optimal chromophore optical constant solution as retrieved from the NEB. We find two major deviations in the imaginary refractive index spectrum of our chromophore compared with CR16. One is the generally steeper blue-absorption gradient from 0.4 to 0.7µm that is required to fit red spectra on Jupiter. The other is a smaller secondary absorption peak at near-infrared wavelengths. This does not appear to be an artefact of a poor choice of particle size, since this feature is relatively consistent over all the prior particle sizes we chose in this analysis, nor could it be a consequence of poor airmass correction, for reasons outlined in chapter 2. Although poor modelling of CIA does overestimate the imaginary refractive index around 0.8µm, as we will show in appendix B, it cannot explain the increase at 0.9µm. It is possible that better methane or ammonia absorption data, and lesser second-order contamination, would result in these wavelengths being better fit without having to increase the imaginary refractive index. However, we also note that, in the experimental data of CR16, the absorption spectrum of their chromophore does exhibit a slight increase in absorption at the longest wavelengths they analysed, as well as a steeper blue-absorption gradient as we find, if the experiment is allowed to go on for its full 8-day duration. We clarify that the CR16 optical constants were only recorded three days into the experiment due to interference fringes in later data. This may also be one piece of evidence of a chromophore formation timescale of several weeks to months.

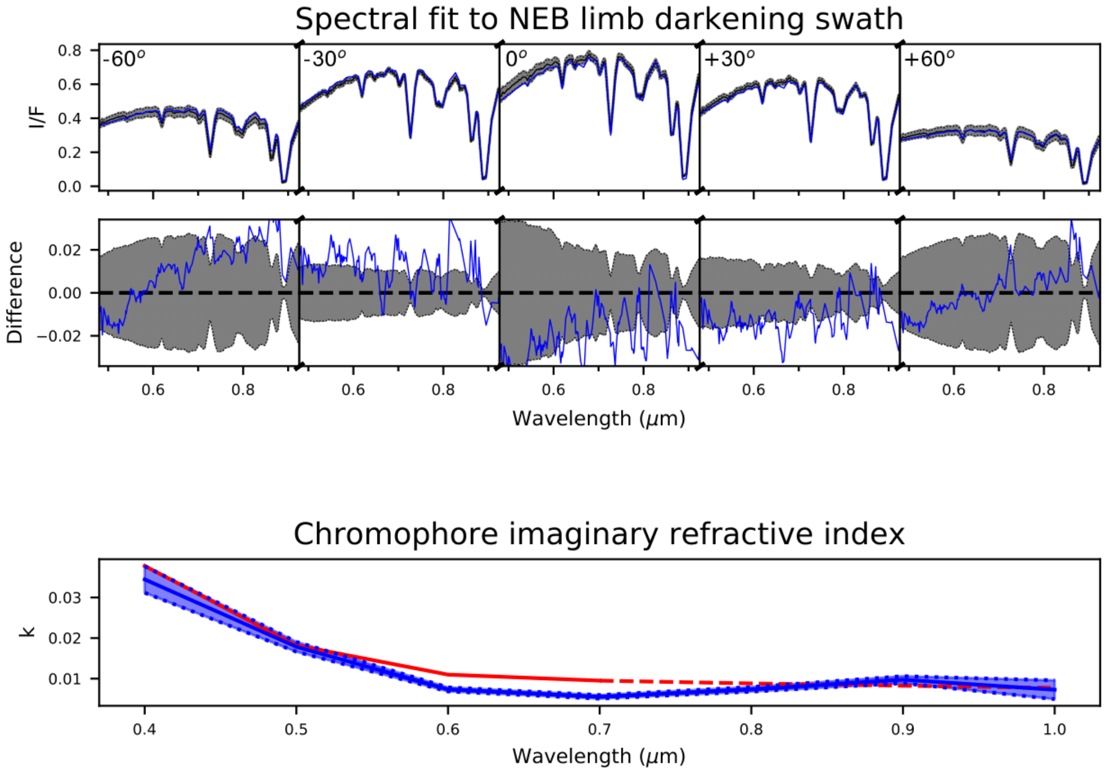

Figure 4.6.3: Results of the NEB limb darkening retrieval for which chromophore optical constants were seen to provide the best fit to the GRS. For this fit, $n_n = 1.42$, $r_n = 1.0\mu m$ and $r_c = 0.2\mu m$. Top two rows show the spectral fit (in blue) to the observed MUSE spectrum (in black, with error bounds shaded in grey) at five different angular geometries, spaced apart by 30 degrees of longitude, with the middle plot showing the difference in I/F between the fit and observed spectrum. Bottom plot shows the retrieved chromophore imaginary refractive index spectrum (in blue, with error bounds shaded) compared to the imaginary refractive index of Carlson chromophore (in red, with dashed line indicating extrapolation from CR16 values).

In figure 4.6.4 we then use this optimal chromophore solution to fit four representative MUSE spectra, with r_n varying from a prior of 1.0μm, r_c fixed at 0.2μm and the other prior variables parametrised according to table 4.4.1. Each were chosen to represent the three main spectral morphologies one typically finds on Jupiter (excluding hotspot regions): high continuum reflectivity with low blue-absorption (the EZ), low continuum reflectivity with high blue-absorption (the NEB), and high continuum reflectivity with high blue-absorption (the NTBs and GRS). Wavelengths below 0.6µm are fit well within the uncertainty boundaries for the belts and the GRS, with small deviations in the blue-absorption gradient easily explained by the uncertainty in the chromophore particle size distribution. However, although the I/F values we model for the zones lie consistently just within the error boundaries at the same wavelength, it is clear that the general shape of the fit spectral slope does not correspond with that of the observed spectrum, even when variations in particle size are accounted for. We focus on the spectral region that consistently causes the greatest perturbation to the blue-absorption slope, which is between around 0.51 and 0.54µm. Here, a slight increase in I/F is observed in the EZ and the NTBs relative to the NEB and the GRS, which is not accounted for in our retrieved chromophore absorption spectrum. The variability in I/F at these wavelengths could be due to a number of factors: a) a genuine secondary chromophore absorption feature (perhaps due to an $n \rightarrow \pi^*$ transition, as we previously explained in section 1.3) that could be characteristic of a certain molecular endmember, b) a consequence of other properties of the atmosphere that we have not properly accounted for, but which might alter the local blue-absorption gradient (such as the presence of additional aerosol or gas layers, or local changes in temperature and pressure that could alter the molecular structure of the chromophore and hence the breadth of its primary absorption feature), c) poor band data around the 0.54µm methane absorption feature, or even d) a relatively low signal-to-noise ratio. Nonetheless, our spectral fits are consistent with a chromophore that is universal, at least for regions of Jupiter that are sufficiently red. We will therefore assume the same chromophore optical constants for all regions of Jupiter, and leave the further investigation of spectral variability between 0.51 and 0.54µm to future work.

4.7 General meridional and zonal variations in cloud, haze and colour

We now apply our optimal chromophore optical constant solution to three individual meridional swaths extracted from Jupiter cube 2018-04-09T06:04:06.918, shown in figure 4.7.1. One of these swaths was selected close to the central meridian (offset west by 2^o) while two others further away from nadir were selected (offset west by 35^o and east by 40^o respectively) in order to decouple consistent meridional variations in Jovian atmospheric properties with longitudinal effects, while avoiding obvious longitudinal anomalies such as the GRS. The latter two swaths were also selected to

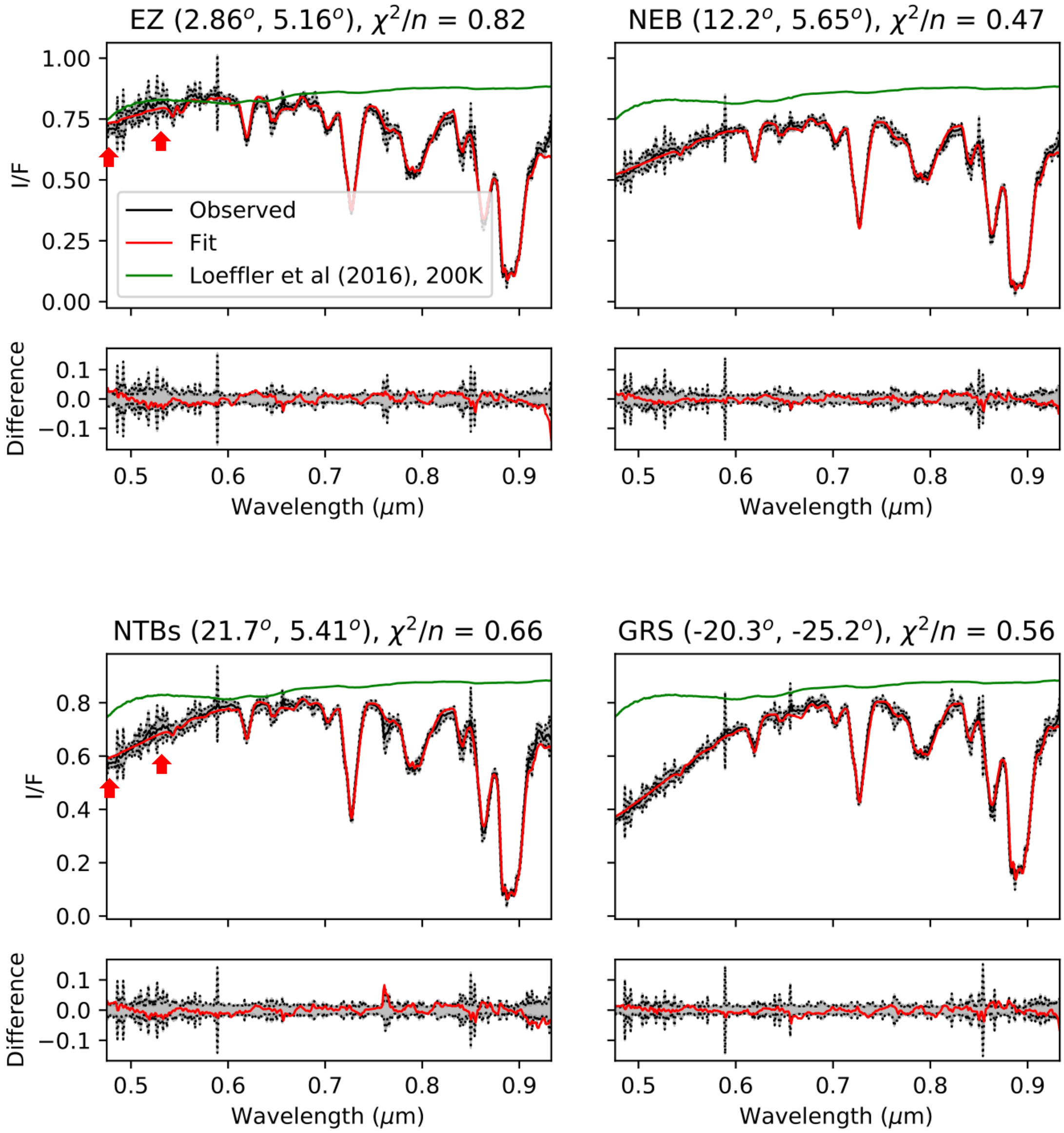

Figure 4.6.4: Fits (in red) to different representative MUSE spectra (in black, with spectral uncertainty bounds indicated by the grey dotted lines) using the chromophore imaginary refractive index spectrum retrieved in section 4.6 and displayed in figure 4.6.3. The NTBs spectrum was taken from MUSE dataset 2017-05-15T02:01:59.328, while the remaining three spectra were obtained from dataset 2018-04-09T06:04:06.918. For each of the four spectra, the given latitude values are planetocentric, while longitude values are east relative to the sub-observer. χ^2/n values of the quality of the fit of the retrieved imaginary refractive index spectrum to each MUSE spectrum are also shown. We have highlighted small deviations in the fit to the EZ and NTBs spectra at blue wavelengths with the red arrows, which we have proposed require further investigation. Poor fits above 0.91μm are mainly due to second-order contamination. For comparison, we also show the shape of the NH_4SH absorption spectrum (in green) as obtained by Loeffler et al. [2016] when reheated to 200K following proton irradiation. Reference spectra obtained at lower temperatures have a similar shape, but with a much deeper absorption feature around 0.6μm.

cover relatively similar phase angles either side of the central meridian, in order to further decouple genuine longitudinal variations from effects that simply result from the differing path length of radiation through Jupiter's atmosphere. As in the previous section, we fixed r_c at 0.2µm but we set r_n to vary from a prior of 3.0µm. We raised the prior value of r_n in this way as we believed a 'compromise value' of r_n between that required to fit the NEB and that required to fit the GRS would stabilise the retrieval of r_n. When this was implemented, however, we found that NEB spectra observed at a single geometry did not contain enough information for r_n to be constrained reliably, and so the value of r_n in the belts tends to be overestimated from the most likely value found through limb darkening. The remaining state vector variables were parametrised according to table 4.4.1. Although we will present our retrievals of gaseous ammonia here, we will leave a full discussion of temporal variations in the meridional ammonia gas profile to section 5.2. Our results for each of the three swaths are shown in figure 4.7.2.

One surprising aspect of our retrievals is the lack of the expected variations in cloud structure between the zones and the belts. We expected the zones to always be regions of thick cloud and the belts to always be regions of depleted cloud, but this does not always appear to be the case from our retrievals. We find in all three swaths that the northern NEB appears to have thicker tropospheric cloud than the EZ. This could partly be due to the thicker haze cover in the EZ, or perhaps even a possible higher-altitude cloud, which obscures much of the cloud below it. In addition, the inversion of the cloud opacities of the two regions are partly exaggerated due to temporary meteorological changes. We note that the first half of 2018 was associated with an expansion of the NTropZ southwards into the NEB, which would have led to mixing at those altitudes and hence the appearance of thicker cloud in the northern NEB than the southern NEB. The regions of relatively depleted cloud cover in the northern EZ are also associated with higher chromophore content compared to the southern EZ, marking the onset of the EZ colouration event, which will be discussed in further detail in section 5.4. We find that the STropZ has consistently the greatest tropospheric cloud opacity of all regions of Jupiter, which was also observed by Mendikoa et al. [2017] and Antuñano et al. [2018]. As expected, we also generally find thicker haze cover over the zones than the belts. The haze is thickest over the northern EZ, as it has been since the year 2000 [Lii et al., 2010]. In two of the three swaths we resolve this haze as being detached from the cloud layer below it, but this is most likely due to an attempt to fit wavelengths where second-order contamination is prominent, at the expense of wavelengths around 0.79µm where the model slightly overestimates the reflectance. We note that we do not consistently retrieve a detached haze layer in the EZ, either in figure 4.7.2 or from other Jupiter datasets.

As the belts are thought to be regions of net downwelling, we would expect the altitude of the cloud layer to be deeper here than in the zones. In addition, a lack of cloud and haze cover in the belts would allow for the observation of deeper layers than in the zones. However, we observe a relative lack of variation in the altitude of the main cloud layer, usually retrieved around 1.5 bars in both the zones and the belts. This cannot simply be explained by effects of the model, as suppressing prior cloud densities below the ammonia cloud level leads to a very poor fit both to the 0.619µm absorption feature and to continuum infrared wavelengths, regardless of particle size distribution. Even in the EZ, in which net upwelling is thought to be at its strongest, we always require a thick cloud layer deeper than 1 bar to fit our spectra. It is predicted to be too warm at these altitudes for ammonia ice to condense out of the atmosphere, and so these cloud layers cannot be made of ammonia ice. Although ECCMs usually predict an NH_4SH cloud to be located deeper than our retrieved altitude (around 2.2 bars, as previously discussed in section 1.2), the cloud could be located at a higher altitude if the H_2S mixing ratio is suppressed, or if the cloud is made of a different sulphur compound. We note that Wong et al. [2015] predicted an $(NH_4)_2S$ cloud to condense at the same altitude as where we retrieve our main cloud layer, which also happens to be the approximate altitude at which the Galileo Probe retrieved a thick cloud layer in the PES. It is also possible that the apparently missing NH_3 cloud is in fact present in the zones, but cannot be resolved either from the main 1-bar cloud layer or from the upper tropospheric hazes due to a lack of vertical resolution.

Variations in retrieved chromophore abundances between zones and belts in these two sets of retrievals are not as strong as one would generally expect, but this is partly a consequence of the NTBs upheaval and EZ colouration events, which will be discussed in further detail in chapter 5. We retrieve stronger zone-belt differences in chromophore in our 2016 data, before both these events occurred. We consistently retrieve the greatest chromophore content in the NEB than in the SEB, as was also found by Ordóñez-Etxeberria et al. [2016]. However, even in the NEB we do not retrieve sufficient chromophore content to reliably constrain its most likely altitude, as we will show in section 4.8. Nonetheless, our retrievals do suggest that chromophore in the belts cannot be located much deeper than the ammonia condensation level. We will provide further discussion on the implications of this in chapter 5.

We generally retrieve higher particle sizes in the zones than in the belts, perhaps as the zones are regions where dynamic upwelling of large cloud particles from deeper altitudes is stronger. However, the difficulty of reliably retrieving particle size values from the data is obvious, particularly if the particles are small as we will show in section 4.8. This causes unrealistic fluctuations in particle size from retrieval to retrieval, which also results in both unrealistic variations in cloud distribution and quality of fit. In order to remove the worst of these fluctuations, we have chosen to smooth over pixel-to-pixel variations in the retrieved parameters over each swath using a Gaussian. We note, however, that we are unable to have χ^2/n values consistent between the zones and the belts, even if we leave the particle size fixed.

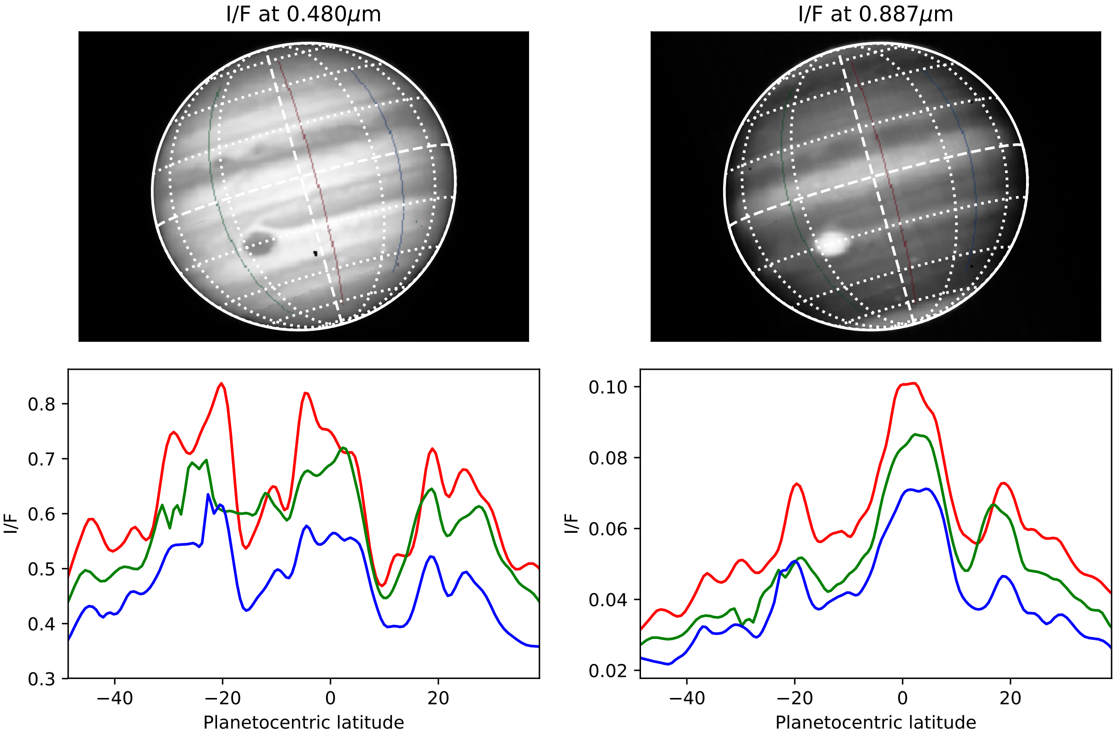

Figure 4.7.1: Top row: Images of three meridional swaths, at 0.480µm and 0.887µm, extracted from dataset 2018-04-09T06:04:06.918. These three swaths (shown as green, red and blue vertical lines) follow the -35^o, -2^o and $+40^o$ longitudes parallel respectively relative to the central meridian. The bottom row shows how the reflectivity at the same two wavelengths changes along each of the swaths, as a function of latitude.

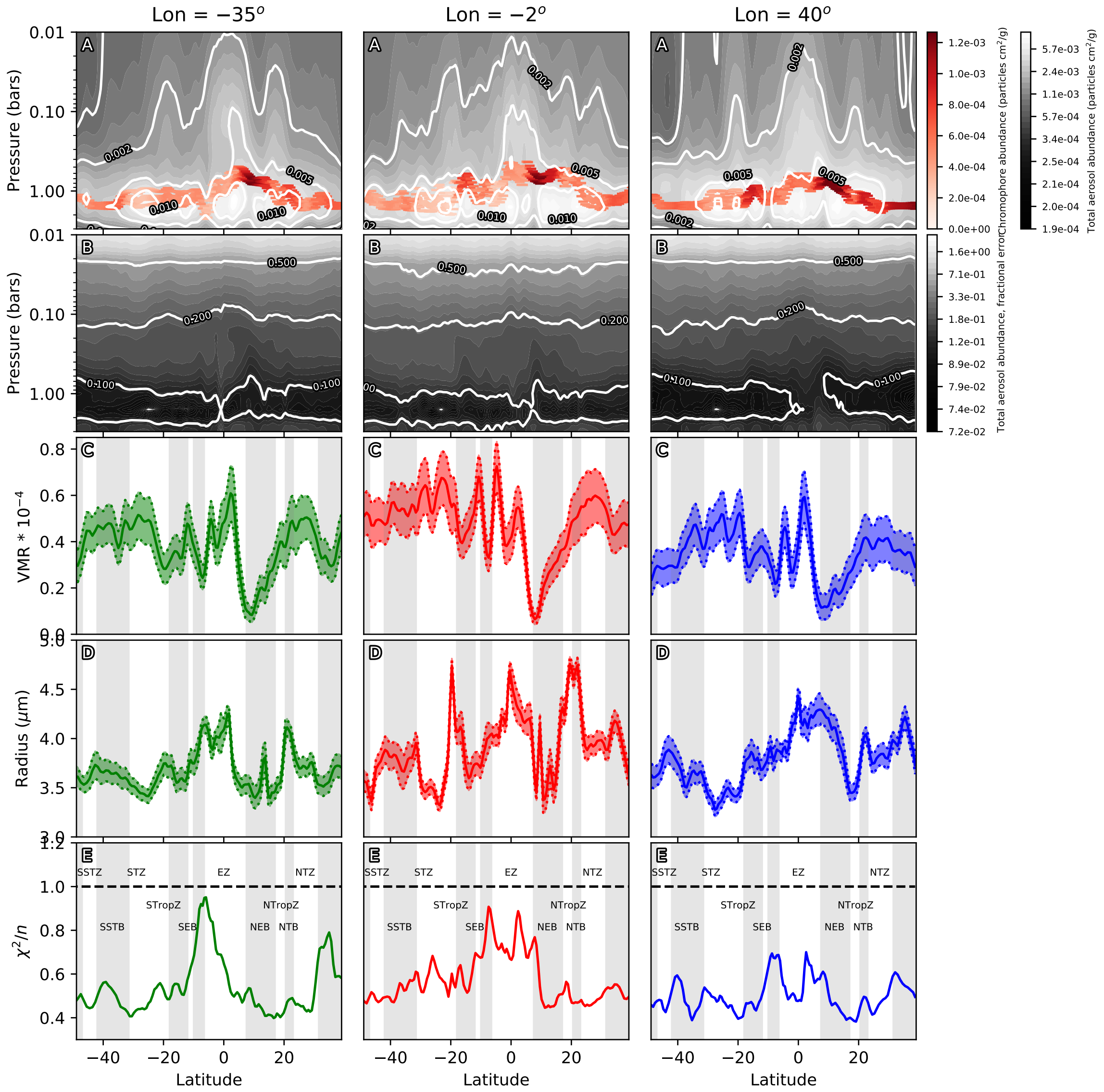

Figure 4.7.2: Results of a set of retrievals along three meridional swaths from left to right, with longitudes offset from the central meridian shown at the top, and plots C-E colour-coded according to figure 4.7.1, as a function of planetocentric latitude. Plots marked A show contour plots of aerosol abundance (chromophore and non-chromophore combined) as a function of pressure and latitude, with lighter colours indicating higher aerosol abundances. Fractional uncertainties in the retrieved aerosol abundances are given in plots marked B (the darker the colour, the lower the uncertainty). Superimposed on plot A is a plot of retrieved chromophore altitude p_c (circles, with horizontal lines indicating error bounds), with the colour of each datapoint indicating the retrieved value of τ_c. The redder the colour, the higher the value of τ_c. Plots marked C show the retrieved ammonia volume mixing ratio extrapolated down to 1.2 bars, for reasons explained in section 5.2. Plots marked D show the retrieved effective radius of the non-chromophore particle population. Plots marked E show retrieved χ^2/n values. We mark the approximate locations of each of the zones and belts on Jupiter in alternating white and light grey for plots C-E (which are labelled in plot E). We do not mark zone-belt differences for latitudes poleward of the first temperate domain (NTZ and STZ) as they are difficult to spatially resolve in the MUSE data.

4.8 Sensitivity analysis

4.8.1 Generation of synthetic spectra

In the previous section, we showed that retrievals of cloud structure and colour resulted in some unexpected meridional variations. We now have to test to what extent those variations are a result of genuine latitudinal differences, and to what extent those differences are due to shortcomings in our cloud model. The best way to test this is to randomly generate a number of state vectors according to the constraints provided by the retrievals in the previous section, then run the state vectors through a forward model to generate 'synthetic spectra', and finally attempt to retrieve the same state vector again from the synthetic spectrum using our retrieval model. One can therefore gauge the quality of the retrieval model and the amount of information one can reasonably expect to extract out of MUSE spectra by observing to what extent the randomly-generated 'input' state vector corresponds to the retrieved 'output' state vector; the greater the correspondence, the better.

To generate these input state vectors, we first create a prior state vector $\mathbf{x_0^{in}}$ whose values we wish to vary within an interval $\Delta\mathbf{x_0^{in}}$ either side of $\mathbf{x_0^{in}}$. Both of these values are constrained according to the variability we retrieved from our data in section 4.7. For profiles that are not continuous, the calculation of the input state vector $\mathbf{x_n^{in}}$ is straightforward:

$$x_{ni}^{in} = x_{0i}^{in} + R_i \left\|\Delta x_{0i}^{in}\right\|, -1 \leq R_i \leq 1 \qquad (4.8.1)$$

where R_i is a value created by a pseudo-random number generator. For continuous profiles, however, the calculation is more complicated as the correlation length of the profile Λ needs to be taken into account. We therefore simulate these continuous profiles as a set of sine waves using three randomly-generated values: an amplitude A, a length parameter l and a phase ϕ:

$$x_{ni}^{in} = x_{0i}^{in} + A \left\|\Delta x_{0i}^{in}\right\| \sin\left(\frac{2\pi i}{\Lambda l} + \phi\right) \qquad (4.8.2)$$

where $0 \leq A \leq 1$, $\frac{1}{2} \leq l \leq 20$ and $0 \leq \phi < 2\pi$.

The prior state vector $\mathbf{x_0^{in}}$ is then run through a forward model to create a synthetic spectrum $\mathbf{y}$, which is then distorted to simulate Gaussian noise according to a spectral covariance matrix $\mathbf{S_y}$ (as previously defined in section 3.7) obtained from a real MUSE spectrum, ensuring non-zero covariance between adjacent wavelengths:

$$\begin{cases} y_i' = y_i + R_{2i}\sqrt{\frac{-2S_{yi}\ln(R_{1i}^2+R_{2i}^2)}{R_{1i}^2+R_{2i}^2}} & i \mod 2 = 0 \\ y_i' = y_i + R_{1(i-1)}\sqrt{\frac{-2S_{yi}\ln(R_{1(i-1)}^2+R_{2(i-1)}^2)}{R_{1(i-1)}^2+R_{2(i-1)}^2}} & i \mod 2 = 1 \end{cases} \tag{4.8.3}$$

where $\mathbf{R_1}$ and $\mathbf{R_2}$ are both random numbers between -1 and 1.

4.8.2 Retrievals from synthetic spectra

We created 100 synthetic spectra in the manner previously described, and then retrieved our atmospheric parameters as in section 4.7, filtering out retrievals where either $\chi^2/n > 1$ or where the input ammonia gas profile was unphysical (for instance, if the abundance increased with height or was supersaturated). We present a comparison between the input and output aerosol profiles in figure 4.8.1. From these plots, it is clear to see that the profiles that most closely correspond to their true values are those where cloud abundance decreases monotonically with height from a thick cloud base (eg. panel A4), while the worst-retrieved profiles are those where the density fluctuates with height (eg. panels B4 and C3) or where the particle size is poorly retrieved (eg. panels A3 and B3). We do not obtain better retrievals of highly-fluctuating profiles even if we decrease the correlation length $\Lambda_{\tau n}$ or increase the prior uncertainties on the aerosol profile $\tau_n(p)$. This may cause issues if we wish to model detached haze layers on Jupiter, which are known to exist on Jupiter as they have been observed several times by JunoCam (Glenn Orton, personal communication). In practice, the assumption of a constant particle size distribution with height will result in an underestimate of haze particle densities anyway, regardless of whether they can be resolved from the tropospheric cloud layers or not. It also illustrates why we retrieved surprisingly low tropospheric cloud abundances in the EZ, as the thickness of the main cloud layer tends to be underestimated if substantial upper tropospheric haze is present above it. From these plots, it would therefore seem that vertical cloud profiles will be most reliably retrieved in the belts, where there is little haze cover, while cloud density around 1.5 bars will be underestimated in zones where there is more haze cover. Regardless of the haze cover, however, the cloud base appears to be reliably retrieved to within a quarter of a pressure scale height of its true altitude. The relatively consistent altitude of the main cloud base around 1.0-1.5 bars in both the zones and the belts is therefore most likely genuine.

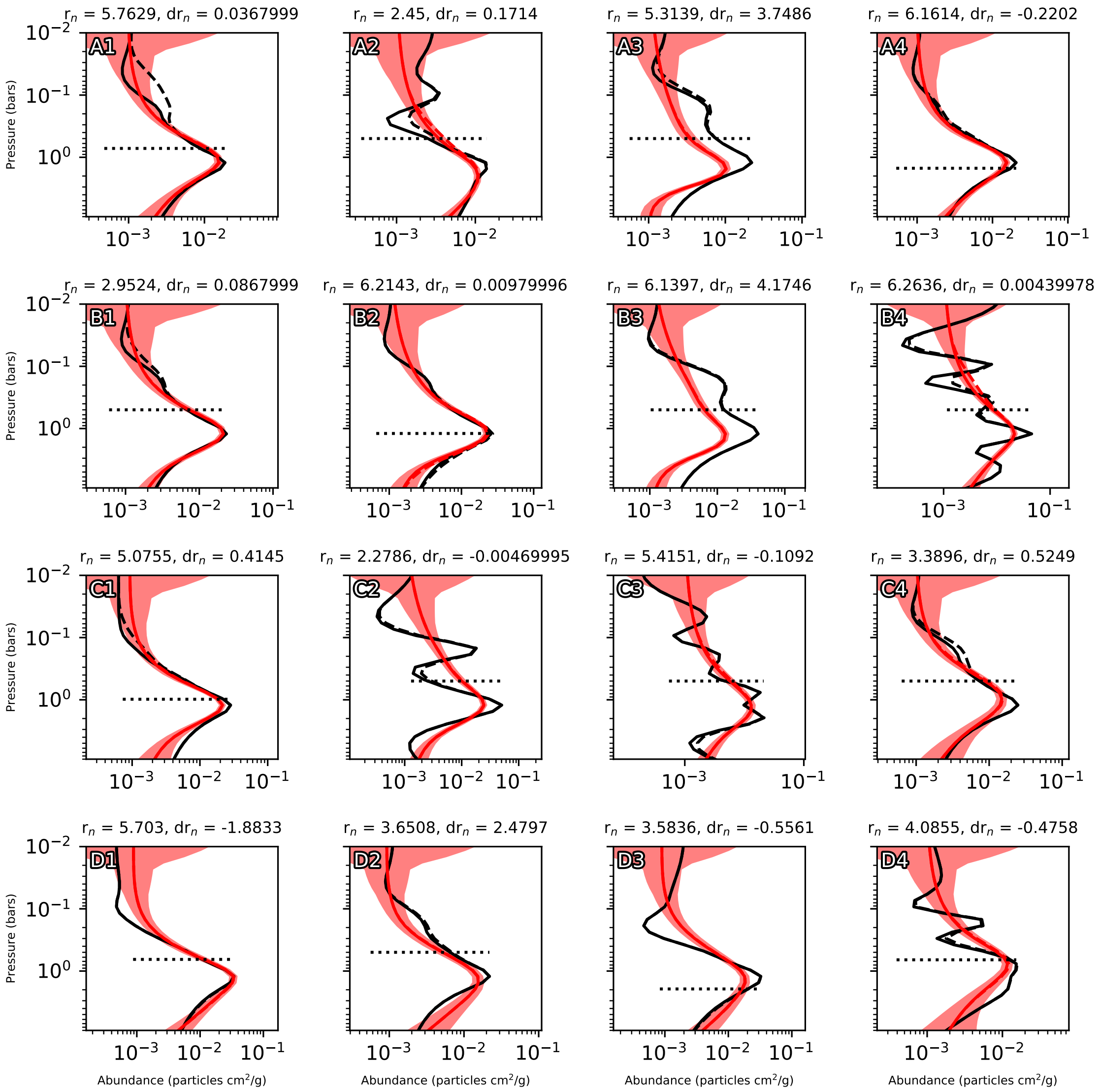

Figure 4.8.1: A comparison of a sample of randomly-generated vertical aerosol profiles (in black) used to create synthetic Jovian spectra, compared to the profiles (in red, with uncertainties shaded) later retrieved from the same spectra. The closer the correspondence between the two profiles, the better the quality of the retrieval model and the more information can be extracted on vertical cloud distribution from MUSE spectra of Jupiter. We present the conservatively-scattering non-chromophore profile as a solid line, and the cominbed chromophore and non-chromophore profile as a dashed line. Dotted horizonal black lines in each case indicate the altitude at which the input and retrieved gaseous ammonia profiles bisect each other, a proxy for the approximate altitude of peak ammonia gas sensitivity. By default we have put the line at 0.5 bars if they do not bisect each other at all, as the altitude of greatest sensitivity to ammonia would be higher than the saturation level. In the title we provide the input value of particle effective radius r_n and the extent to which the retrieved value deviates from it ($dr_n = r_n$ (output) $- r_n$ (input)).

Figure 4.8.2 then shows the modelled versus the retrieved values of the remaining parameters of this analysis. Generally, we can only reliably constrain both the chromophore opacity τ_c and pressure p_c simultaneously if peak abundances are either above 4×10^{-3} particles cm^2/gram or if the true chromophore pressure is deeper than approximately 1 bar. Retrievals of either quantity also begin to be unreliable if the chromophore pressure is less than approximately 0.15 bars. In cases where the altitude of the chromophore has been proven to be difficult to constrain, its depth tends to be overestimated. Reliable retrievals of the pressure of the chromophore are therefore only possible in the GRS, while the retrieved chromophore pressures in our meridional swaths presented in figure 4.7.2 can mostly be ignored. This is because MUSE data lacks shorter wavelength information that can constrain the higher-altitude bound of p_c in these cases through Rayleigh scattering.

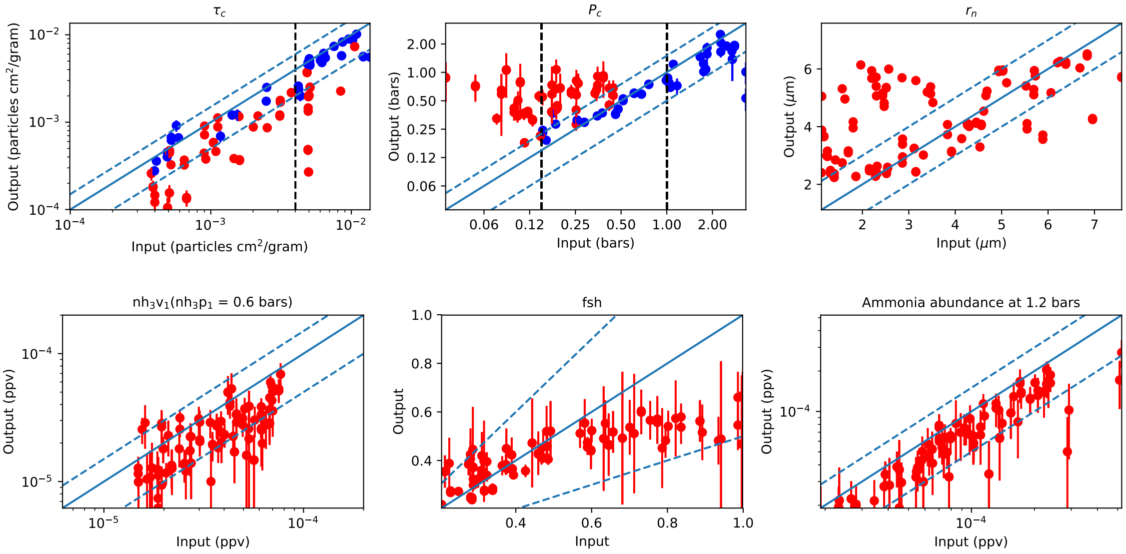

Figure 4.8.2: Sensitivity to each variable model parameter, comparing modelled input values with retrieved output values. All symbols are defined in table 4.6.1. Blue datapoints in the first two plots indicate input values in which either $\tau_c > 4 \times 10^{-3}$ particles cm^2/gram and $p_c > 0.15$ bars, or $p_c > 1$ bar, for reasons explained in the text. These values are also marked as vertical black dashed lines on the plot for clarity. In the bottom-right diagram we have extrapolated gaseous ammonia abundances down to 1.2 bars, for reasons explained in the text, based on our retrieved values of nh_3v_1 at 0.6 bars and the fractional scale height. Points on the solid blue diagonal line have identical input and output values while the dashed blue diagonal lines indicate output values within a 50% error of the input values; an ideal retrieval would have all datapoints aligned with the solid blue diagonal for each variable case.

Although we cannot retrieve either nh_3v_1 or fsh particularly reliably, we find that the correspondence between the input and retrieved ammonia abundances improves substantially if one follows the ammonia profile down to approximately 1.2 bars, equivalent to the altitude where the main cloud layer is usually retrieved. The cases where the correspondence is poor are usually due to variations in the pressure of the main cloud layer or the presence of a thick overlying haze layer. As expected, we only see a weak correlation between the modelled and retrieved values of r_n, especially if the values of r_n are small. The difficulty of retrieving particle size has particular impact on the shapes of the aerosol profiles we present in figure 4.8.1.

4.8.3 Sensitivity to calibration errors

In section 2.4 we ensured that each MUSE dataset was scaled relative to HST/WFC3 in order to ensure that the average systematic discrepancy in I/F was less 5% in each case. A 5% discrepancy in I/F can, however, have substantial detriment to retrieved atmospheric parameters. We show this in figure 4.8.3, in which we take a sample EZ spectrum of Jupiter (which was previously shown in figure 4.6.4), systematically scale its I/F values by 5% in either direction over all wavelengths, and then run NEMESIS on it. We find that the greatest impact on the scaling of I/F is at the level of the deepest visible cloud layer: the higher the I/F, the greater the opacity of the cloud at around 1 bar, although the pressure of the cloud layer itself remains relatively unchanged with respect to the scaling. Increased I/F values should also result in a systematic increase in retrieved particle sizes, due to the perceived increase in aerosol scattering cross-section, as will be clearly demonstrated in chapter 5. The chromophore and ammonia profiles, on the other hand, remain constant to within the retrieved uncertainty ranges. We must therefore be cautious of perceived changes in cloud cover over time when we analyse the full range of MUSE datasets in chapter 5, as this could be the result of small uncertainties in photometric calibration. Instead, it will be more informative to look at changes in relative latitudinal differences in cloud cover over time.

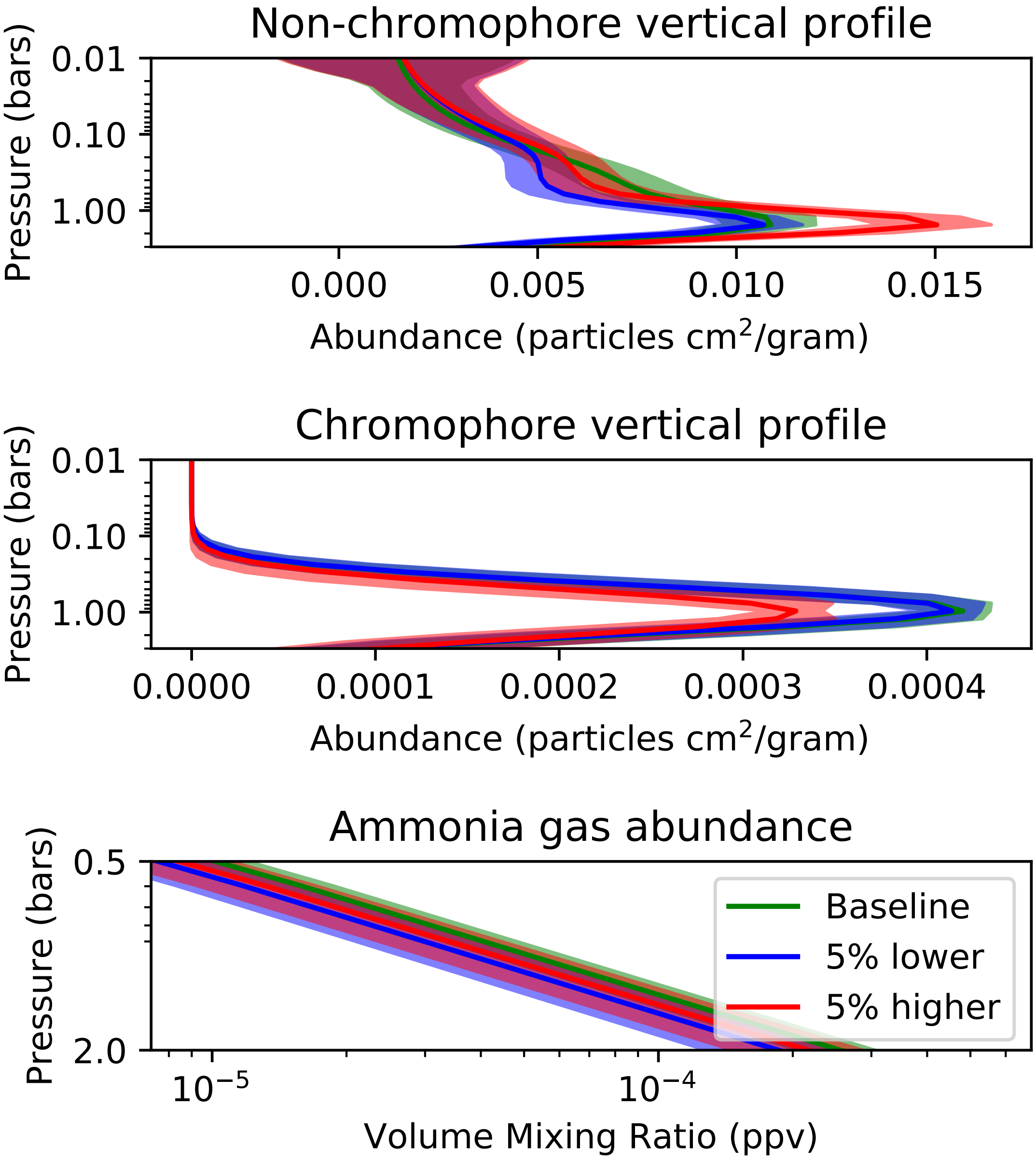

Figure 4.8.3: Change in retrieved atmospheric parameters when a sample EZ spectrum is scaled in I/F by 5% relative to the original calibrated 'baseline' values. We note that r_n has been fixed in all three retrievals, since r_n is difficult to retrieve and has a major impact on retrieved aerosol profiles by itself.

Chapter 5

Jupiter - Temporal changes in visible appearance

5.1 Overview

In the previous chapter, we explained how we refined our cloud model for Jupiter and retrieved a universal chromophore complex refractive index spectrum from a single Jupiter MUSE dataset. We now apply this model to all our Jupiter MUSE datasets in order to investigate temporal variability in the atmosphere of Jupiter between 2014 and 2018. As previously described in chapter 2, one of the main issues with this analysis is the inferior observation conditions and calibration experienced in these datasets, particularly those from 2014, compared with the 9th of April 2018 dataset analysed in chapter 4. However, if we want a full analysis of temporal variations in Jupiter's visible appearance, we cannot neglect the 2014 data, as it holds valuable information particularly of changes in the morphology of the GRS. In general, we focus mostly on changes associated with the northern tropics and temperate regions, with some discussion of the GRS and Oval BA. We will mostly leave the characterisation of concurrent changes at higher latitudes and the southern tropics to future work, as while these were indeed substantial, they tended to occur over both shorter timescales and spatial scales than could be easily resolved with our collection of MUSE data. We make no changes to the prior model parametrisation compared with section 4.7, and so an account of how much of the work presented here is my own contribution is not needed, as it is more or less identical to that of chapter 4. This of course includes the deficiencies in the modelling of CIA, for which we refer the reader to appendix B.

In section 5.2, we present meridional swaths, equivalent to those in section 4.7, from sample MUSE datasets covering the whole period between 2014 and 2018, focussing mostly on variations in cloud-top ammonia abundance, which was only discussed briefly in chapter 4. We will qualitatively compare our MUSE profiles with preliminary deep ammonia gas retrievals from Juno/MWR up to PJ9, as presented in Dr Steven Levin's (NASA/JPL) public lecture online[1] (provided in private communication). In section 5.3 we then focus on a single latitudinal region between the NEB and the NTZ, looking at changes associated with both the northward 'aborted' expansion of the NEB that occurred between 2015 and 2016, and the subsequent revival of the NTBs in late 2016 and 2017; we lump these two events together in the same section as they are most likely coupled in some fashion. In section 5.4 we then focus more broadly on the EZ to analyse the development of a local upheaval event, the first signs of which were visible in data from April 2018 and which is likely to continue well into 2019. Finally, in the last two sections (5.5 and 5.6), we attempt to analyse changes in the morphology of the GRS and Oval BA over the entire MUSE observation period; we mostly neglect any smaller discrete features as they are not well-resolved in the MUSE data.

5.2 General meridional variations in gaseous ammonia abundances

Before we examine temporal changes in specific regions of Jupiter associated with upheaval events, we first wish to examine more general temporal changes associated with Jupiter's meridional structure. Although we will present some brief discussion on changes in cloud structure and colour here, we will not focus as much on them as we did in section 4.7, as a full discussion of the changes we observe would require more analysis of upheaval events and outbreaks in the southern hemisphere, which is beyond the scope of this thesis. Instead, we wish to focus more on changes in the meridional cloud-top gaseous ammonia abundance profile, and compare them with meridional profiles obtained at other wavelengths, for which more recent literature is available than for meridional profiles in vertical cloud structure and colour. In order to use these data to constrain the composition of the main cloud layer, we would need to feed our results into a sophisticated cloud condensation model, as was done by Blain et al. [2018]. We will save such an analysis for future work.

We extracted a meridional swath from each of 10 sample MUSE datasets from February 2014 to September 2018, usually close to the central meridian but avoiding longitudinal anomalies (such as the GRS) where possible. The locations of these swaths in each case are shown in figure 5.2.1. We caution that retrieved ammonia abundances have a slight inverse correlation with particle size, the latter difficult to retrieve as previously explained in chapter 4. The latitude grid in each plot is therefore selected in order to minimise unrealistic small-scale fluctuations in ammonia abundance

---

[1] https://youtu.be/S6Joupv6f-M?t=1975 (accessed 17.01.2019)

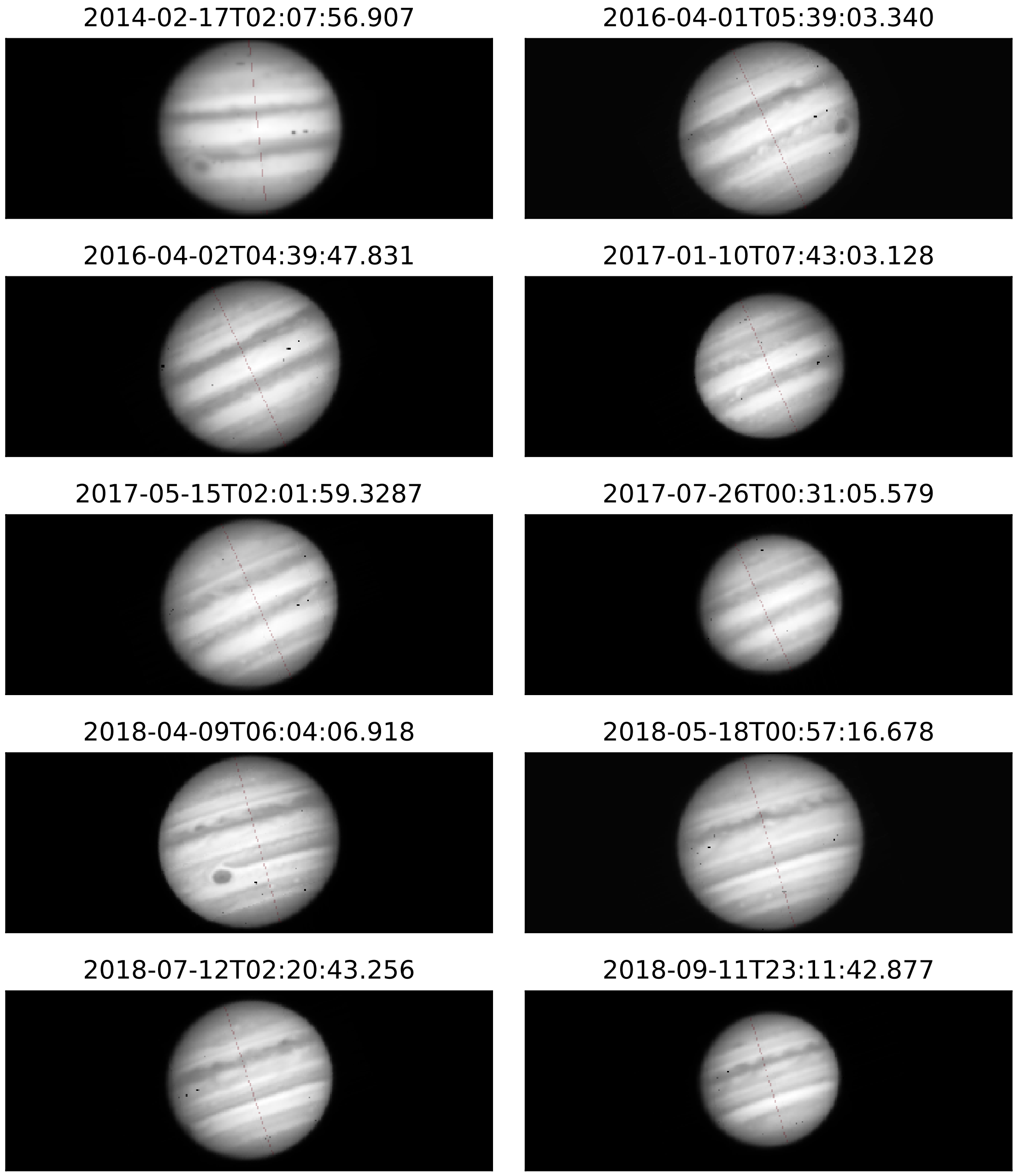

2014-02-17T02:07:56.907

2016-04-01T05:39:03.340

2016-04-02T04:39:47.831

2017-01-10T07:43:03.128

2017-05-15T02:01:59.3287

2017-07-26T00:31:05.579

2018-04-09T06:04:06.918

2018-05-18T00:57:16.678

2018-07-12T02:20:43.256

2018-09-11T23:11:42.877

Figure 5.2.1: Footprint of each of the meridional swaths described in section 5.2, shown in red on top of the respective MUSE dataset averaged between 0.485μm to 0.495μm. Each image is shown at the same spatial scale (116”x44”), in order to highlight the variation in angular diameter of Jupiter over the four-year period.

that are a result of either poor convergence due to local artefacts or of inconsistencies in the retrieval of particle size; by default we only select every second pixel along the swath to display, and then exchange pixels with local spikes in retrieved particle size with neighbouring ones. We remind the reader that we have very little sensitivity to vertical variations in ammonia abundance at these wavelengths, instead just to column abundances of ammonia gas above the deepest visible cloud layer. This means that apparently low retrieved abundances of ammonia gas are not necessarily reflective of genuine depletions; they may also be reflective of the presence of a cloud layer that is unusually opaque or elevated in altitude. For that reason, we must also take into account the altitude of the main cloud layer in our retrievals. The altitude of this cloud layer is usually retrieved between 1.2 and 1.5 bars, and so for consistency, we plot ammonia abundances extrapolated to 1.2 bars, according to the profile we specified in chapter 4. Our results are shown in figures 5.2.2 and 5.2.3, which in the former case are also compared with corresponding profiles from Juno/MWR.

As we show in Figure 5.2.2, there is a good correspondence in the general meridional profile of ammonia gas abundances between our MUSE data and MWR data between approximately 1 and 2 bars from the perijove obtained closest in time and longitude. While larger deviations in retrieved ammonia abundances are seen between MUSE dataset 2017-07-26T00:31:05.579 and the PJ7 MWR data, as well as between 2016-04-01T02:22:07.339 and the PJ1 MWR swath, they can easily be explained by longitudinal variations (we note that Juno flew directly over the GRS in PJ7). This shows that our retrievals of ammonia are generally reliable and rigorous, and can usually be decoupled from underlying cloud structure. As we consistently retrieve a relatively constant cloud base altitude, we do not generally need to worry about the influence of cloud layers on the retrievals of ammonia abundance, apart from perhaps in hotspot regions of the northern EZ or the southern NEB, where there is very low cloud cover. We also generally find a good correspondence between cloudy regions and high ammonia abundances, with only a few exceptions (among them the NTBs, which we will discuss in section 5.3). This is the opposite of what we would expect if variations in cloud altitude or thickness had a major impact on the abundances of ammonia we retrieve.

The most often-cited features of the MWR profile, namely the strong hemispherical asymmetry and the upwelling-downwelling system in the northern tropics, are much weaker in our MUSE data following the NTBs upheaval in late 2016, with similar upwelling-downwelling systems strengthening in the southern tropics that more or less correspond to the main zone-belt regions. This is also somewhat reflected at the cloud-top level in the MWR profiles. The clearest variability is in the upwelling region in the northern EZ, as we show in figure 5.2.3. The high cloud-top ammonia abundances we see in this region appear to become consistently lower in 2017 and 2018 by approximately

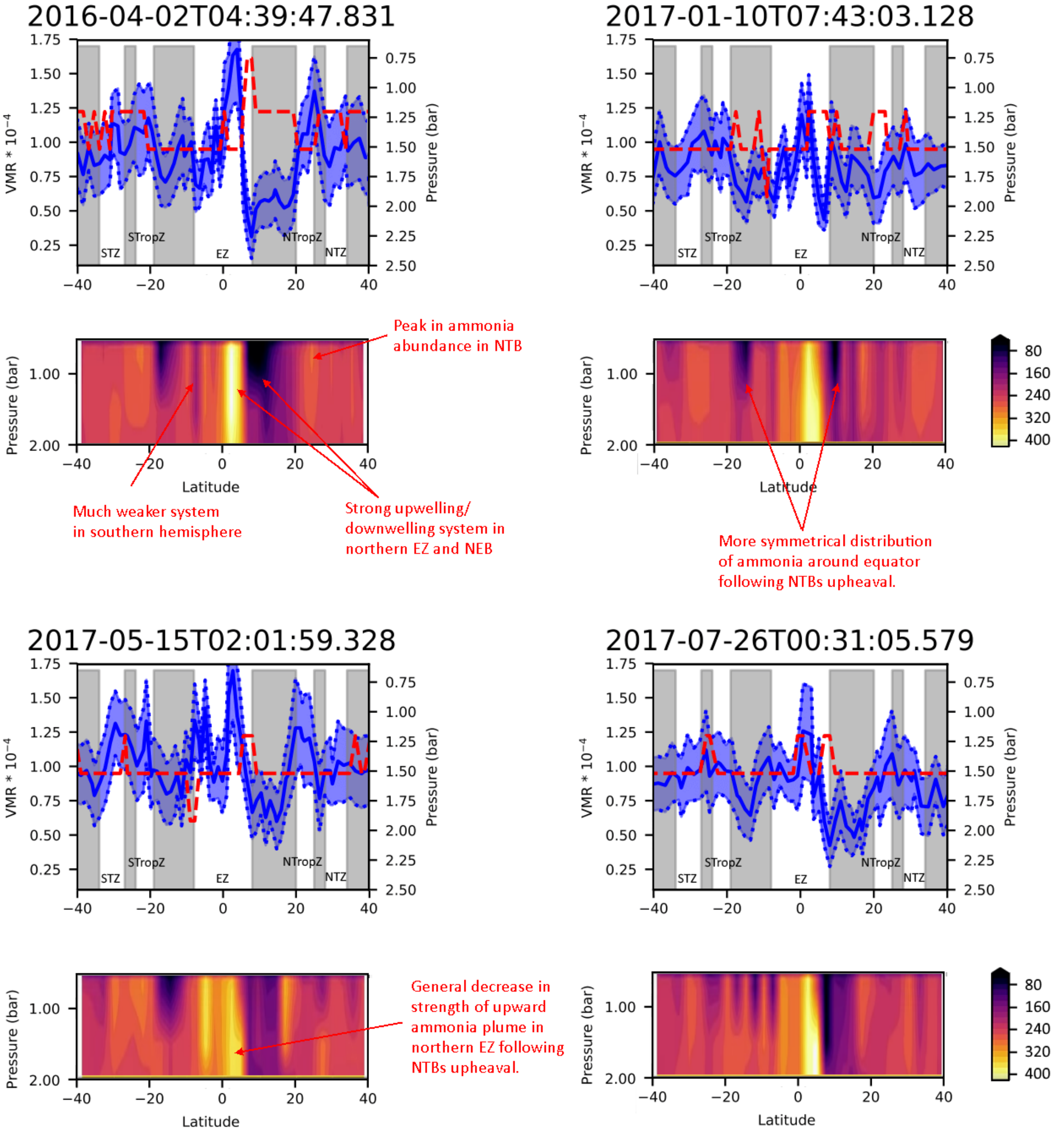
2016-04-02T04:39:47.831

2017-01-10T07:43:03.128

2017-05-15T02:01:59.328

2017-07-26T00:31:05.579

Peak in ammonia abundance in NTB

Much weaker system in southern hemisphere

Strong upwelling/ downwelling system in northern EZ and NEB

More symmetrical distribution of ammonia around equator following NTBs upheaval.

General decrease in strength of upward ammonia plume in northern EZ following NTBs upheaval.

Figure 5.2.2: In blue we show the 1.2 bar ammonia abundances retrieved from the MUSE dataset shown in the title, with the red dashed line showing the approximate altitude of the main cloud layer in bars. Below each of these graphs is a plot of the ammonia abundances retrieved from Juno/MWR by Li et al. [2018] at approximately the same altitude (we have selected the profile between 0.7 and 2.0 bars), corresponding to (clockwise from top left) PJ1 (26th of August 2016), PJ4 (2nd of February 2017), PJ7 (11th of July 2017) and PJ6 (19th of May 2017). The colour bars give the ammonia volume mixing ratios in $10^4 \times$ppmv. We have annotated the most apparent changes in the ammonia profile during this time directly on the plots. Alternating white and grey regions show approximate boundaries of individual zones and belts, with the name of each zone indicated on the plots. Latitude values are all planetocentric. Juno/MWR plots taken partially from YouTube link provided by Steven Levin in private communication, as described in section 5.1.

30% relative to their April 2016 peak. Although the complete disappearance of the northern EZ ammonia plume in the swath from 2018-04-09T06:04:06.918 is likely just a longitudinal effect, we find a secondary region of upwelling of ammonia in the southern half of the EZ, independent of longitude, that rivals that in the northern EZ. A resurgence of ammonia upwelling in the northern EZ only begins to be noticeable again in our MUSE data around the start of the EZ colouration event in July 2018, finally reaching its original 2016 levels again in September 2018.

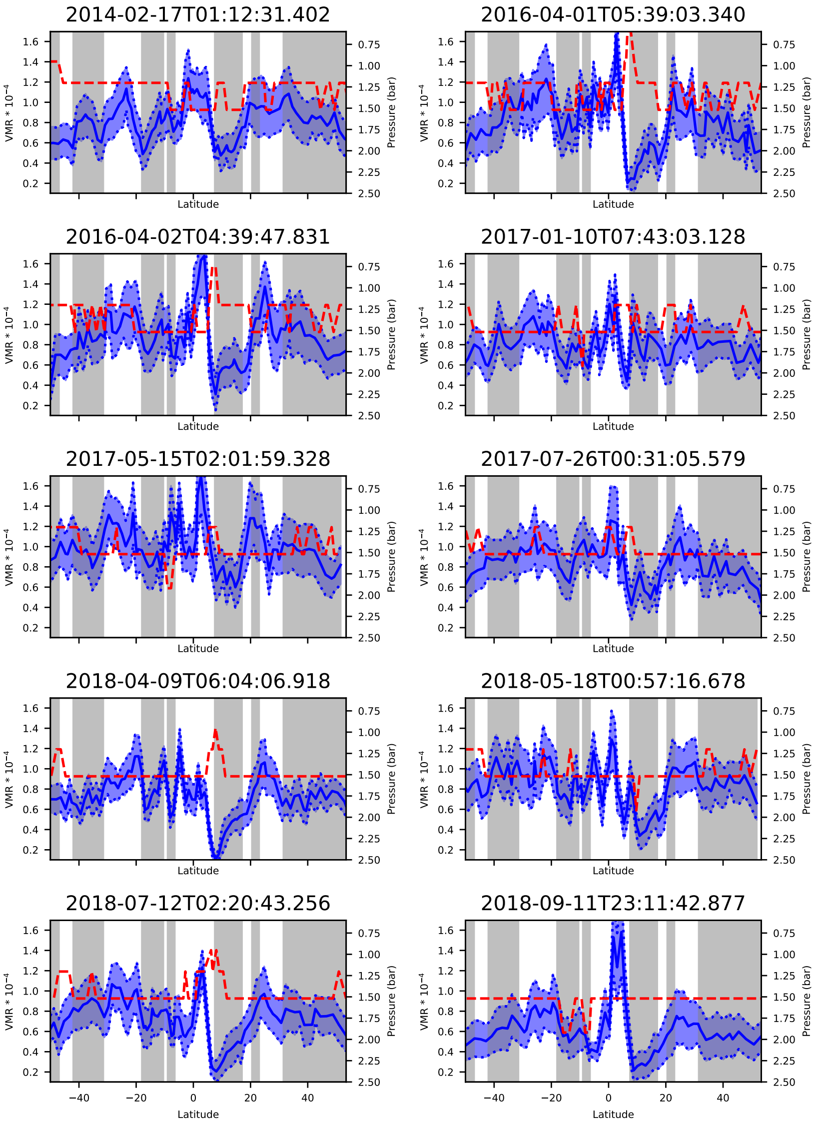

Figure 5.2.3: 1.2 bar ammonia abundances retrieved from all 10 MUSE meridional swaths. We refer to figure 5.2.2 for a detailed key.

When we examine the MWR data, it is also clear that there is some variability in ammonia abundance at the cloud-top level in the northern EZ; often the region of high ammonia abundance drops off dramatically above the altitude at which we retrieve the main cloud layer (which is what we would expect from a condensate cloud, regardless of if was made of NH_3 or NH_4SH), while at other times the main cloud layer appears to have little effect on the ammonia abundance at all. However, the variability detected in MWR does not appear to be constant or predictable, nor does it correlate with the variability that we retrieve in our MUSE profiles in this region. This is particularly clear in our 15th of May 2017 dataset, where ammonia abundances from MUSE in the northern EZ appear unusually high for this time, while conversely, retrieved abundances in the same region from PJ7 MWR data appear to be unusually low. We see no evidence for substantial changes in the cloud or haze structure in this area that could have resulted in the changes we see in our retrieved ammonia abundances from our MUSE data between 2016 and 2017, nor can we blame longitudinal variations. Alternatively, the apparently reduced ammonia abundance in the EZ could be a consequence of an underestimate of particle size, but yet again this would be reflected in thicker cloud or depleted haze in that region, for which we find no evidence either. This makes it difficult to tie temporal variations in ammonia abundance in the northern EZ conclusively with the NTBs upheaval and EZ colouration events, or indeed any other atmospheric cycles associated with equatorial regions (e.g. Simon-Miller et al. [2007]).

Unlike in the northern hemisphere, the MWR data shows that the upwelling-downwelling regions in the southern hemisphere that we retrieve in our MUSE data always appear to be confined to altitudes above which we retrieve the main cloud layer, even if the magnitudes of the upwelling and downwelling themselves are comparable with their northern counterparts at the cloud-tops. The cause of this imbalance is a mystery, and appears to imply that the main cloud layer acts as a more impenetrable barrier to sunlight in the southern hemisphere, thereby confining all meteorology to the cloud-tops, than it does in the northern tropics where the local meteorology is driven by deep convective activity. It also implies that sunlight can drive equally vigorous circulation at the cloud-tops as the heat from the interior can. However, while we do indeed generally retrieve the highest cloud abundances of any region of Jupiter beside the EZ in the STropZ, we find no evidence for consistently high cloud densities over the whole southern hemisphere relative to the northern hemisphere, nor is there any evidence of any more substantial hemispherical asymmetries in cloud structure at deeper altitudes from 5µm observations.

5.3 The NEB expansion event of 2015 and the NTBs upheaval cycle

In this section, we present retrievals of the Northern Tropical and Temperate Domains associated with two cyclical events. One is of the temporary northward expansion of the NEB into the North Tropical Zone (NTropZ), which occurs approximately every 3-5 years and was last seen in 2015-2016 [Fletcher et al., 2017c]. This is commonly known as an 'NEB expansion' event, and is illustrated in figure 5.3.1. The other is a more complex cycle of disappearance and revival of the southern NTB (NTBs) over a 5 year period, usually referred to as an 'NTBs revival' or 'NTBs upheaval' event, which is illustrated in figure 5.3.2. In this cycle, the red colour of the NTBs gradually fades over a number of years, before a dramatic set of outbreaks of convective plumes from the NTBs jet at 23.7N precedes the reappearance of the NTBs's bright red colour. NTBs outbreak events have been recorded since 1880 [Rogers, 1995], but the only ones that have been analysed in great detail were in 1975 [Rogers, 1976, Sánchez-Lavega and Quesada, 1988], 1980, 1990 [Sánchez-Lavega et al., 1991, Rogers, 1992], 2007 [Sánchez-Lavega et al., 2008, Rogers and Mettig, 2008], 2012 [Rogers and Adamoli, 2018] and, most recently, 2016 [Sánchez-Lavega et al., 2017]. On many occasions, such as in 2012, they occurred during solar conjunction and so were difficult to monitor from start to finish. The 2012 event was unusual in that the NEB expansion and NTBs revival events occurred more or less simultaneously with each other, as well as with an EZ colouration event. However, there is not usually a regular time interval between any of these events and hence it is difficult to conclude that they are related. The aforementioned citations usually describe general changes in visual appearance together with dynamical measurements of certain discrete features. Retrievals of basic cloud structure changes associated with the cycle were also made by Sánchez-Lavega et al. [2008] and Pérez-Hoyos et al. [2018] using broad-band multispectral data. However, we are not aware of any simultaneous retrievals of vertical cloud structure, colour and ammonia abundances from hyperspectral data of the NTBs prior to the writing of this thesis. Such retrievals provide a good opportunity to shed light on the possibility and origin of a universal chromophore.

To analyse the progression of the NTBs upheaval, we extracted sample slices of narrow longitudinal width (just wide enough to make small-scale longitudinal variations clear, but not too wide as to make the retrievals slow), ranging in latitude approximately from the NEB to the NTB, from each of the four datasets that follow the NTBs upheaval event. These four datasets were selected to show the rough progression of the upheaval at as many stages as possible. Although we do not have any images during the 'herring-bone' phase (see figure 5.3.2), we have one dataset from January

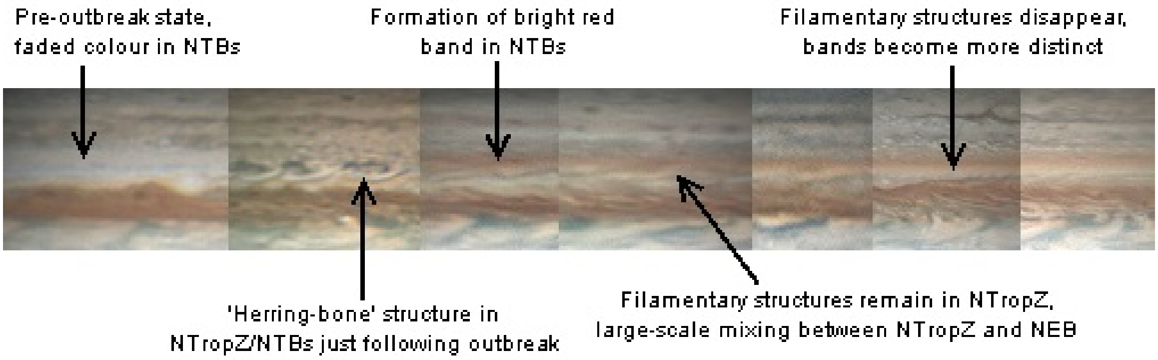

Figure 5.3.1: Progression of events in the NTropZ and NTBs, before and after the NTBs outbreak that occurred around solar conjunction in October 2016, as viewed by amateur observers. Images are projected from left to right in chronological order and cropped to between 0^o and 50^o latitude (planetographic), all were selected from the Planetary Virtual Observatory and Laboratory (PVOL) database [Hueso et al., 2010] according to clarity and seeing conditions; longitude values are therefore arbitrary. From left to right: 10th of July 2016 (Anthony Wesley), showing the pre-outbreak state of Jupiter; 2nd of November 2016 (Pic-du-Midi observatory), showing the state of the atmosphere soon after the outbreak, with 'herring-bone' structures [Rogers and Adamoli, 2018] of alternating cyclonic dark spots and anticyclonic bright filamentary arcs around the NTBs jet; 27th of November 2016 (Christopher Go), showing the appearance of the bright red haze layer around the NTBs and the dark filamentary structures in the NTropZ; 11th of December 2016 (Christopher Go); 17th of January 2017 (Paul Maxson); 26th of February 2017 (Damian Peach); 22nd of March 2017 (Christopher Go). We also refer the reader to the supplementary material of Sánchez-Lavega et al. [2017] for a more detailed view of Jupiter just after the outbreak event.

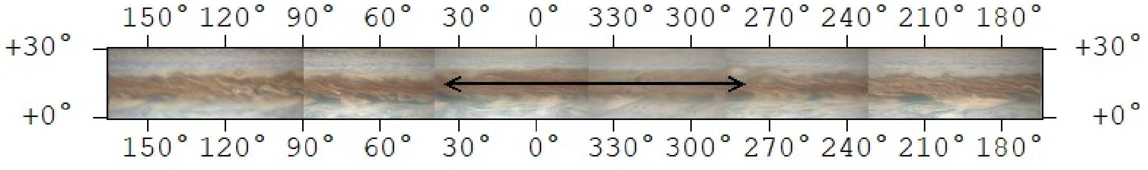

Figure 5.3.2: Illustration of the northern NEB in February 2016 during the expansion event, with the expanded region indicated by the black arrow, as viewed by amateur observers. Images are projected according to System III longitude, and cropped to between 0^o and 30^o latitude (planetographic), all were selected from the Planetary Virtual Observatory and Laboratory (PVOL) database [Hueso et al., 2010]. From left to right: 25th of February 2016 (Damian Peach); 11th of February 2016 (Christopher Go); 28th of February 2016 (Christopher Go); 18th of February 2016 (Trevor Barry); 20th of February (Christopher Go); 12th of February (Christopher Go). We refer the reader to the supplementary material of Fletcher et al. [2017c] for a more detailed view of the evolution of the NEB over time during the expansion event.

2017 when there was still substantial mixing between the NTropZ and NEB, two from May and July 2017 respectively, in which Jupiter's latitudinal structure became distinct once more but the red haze region around the NTBs remained bright, and one from April 2018 when the colour of the NTBs, while still visible, no longer overshadowed that of the other belts. These slices were obtained relatively close to the central meridian, avoiding anomalous regions where possible, in order to minimise computational time as previously explained in chapter 3. The locations of these slices in each case are shown in figure 5.3.5 and the results shown in figure 5.3.7.

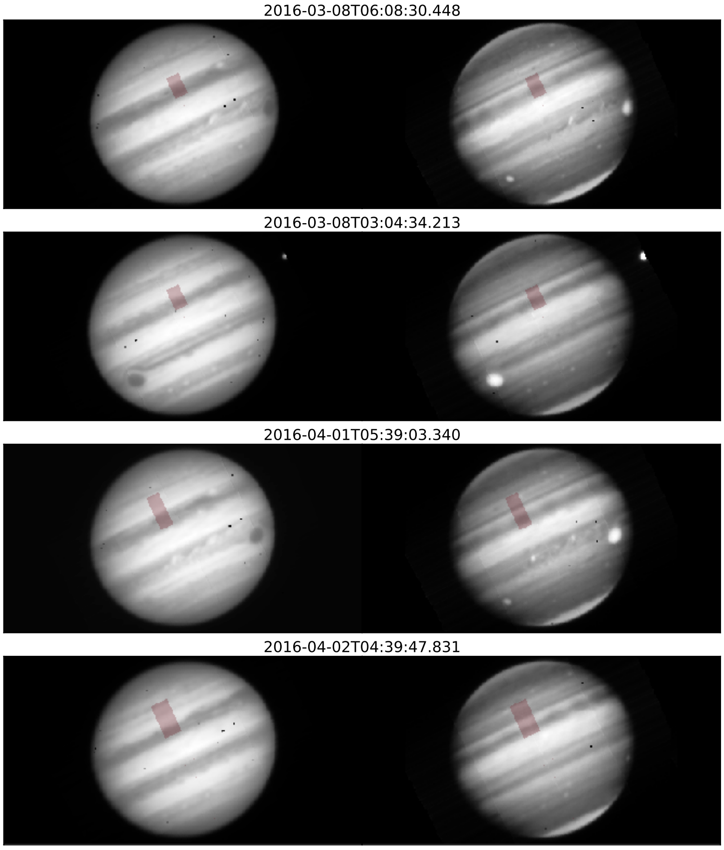

Figure 5.3.3: All the MUSE datasets described in reference to the NEB expansion event, with the image on the left an average of the spectral image cube between 0.485µm and 0.495µm, and the image on the right the corresponding image averaged between 0.885µm and 0.890µm, and the footprint of the slice in each case shown in red. In each case, we choose slices that are generally as close to the central meridian as possible, but avoiding anomalous regions. The 2016-03-08T03:04:34.213 and 2016-04-02T03:39:47.831 slices represent regions of non-expanded NEB, while the other two represent expanded NEB. Each image is shown at the same spatial scale (84"x44"). The bright circle in the second image from the top just to the right of Jupiter is the moon Io, which far outshines Jupiter at 0.89µm.

We also made use of our two global datasets from 2016 to analyse the NEB expansion, in both cases obtaining one slice from an expanded region of NEB and another from a non-expanded region of NEB, as we show in figure 5.3.3. The March 2016 dataset would ordinarily have been the most appropriate to use for this analysis, as the northern edge of the expanded region of the NEB had already begun to recede by April of that year. However, the calibration of the March 2016 datasets was sub-optimal due to the spectrum of the standard containing a number of artefacts. We therefore had to reduce the March datasets using a spectral response function that came with the calibration software, which resulted in noticeable artefacts at the shortest wavelengths as previously discussed in chapter 2. Despite the difficulties in calibrating the March 2016 data, we decided to include both 2016 datasets in our analysis of the NEB anyway. We show the results of these retrievals in figures 5.3.4.

Unfortunately, a lot of information stored in our retrieval results is somewhat obscured by the poor and unpredictable retrieval of particle size, particularly in the slices from 2016-04-02T04:39:47.831 and 2017-07-26T00:31:05.579. This results in speckling which is most visible in retrievals of high-altitude haze density, as a lower retrieved particle size results in comparatively less haze. We therefore plot our retrieval results averaged longitudinally over the slice, with errors in the retrieved profiles calculated from the standard deviation over longitude. This does not result in substantial loss of information since there is little longitudinal variation in I/F over any of the slices (except 2017-01-10T07:43:03.128 when the NTropZ was very turbulent).

The observed differences in colour between expanded and non-expanded regions of NEB are somewhat difficult to correlate with other retrieved atmospheric variables due to systematic differences in the calibration between the March and April 2016 datasets, especially with respect to the retrieval of particle size, as can be clearly seen in figure 5.3.4. However, the most consistent difference between the two regions of NEB is in the cloud structure, with the expanded region associated with cloud depletion, as well as some tentative indications of ammonia gas depletion. By contrast, we retrieve little conclusive variation in haze between the two regions. This would therefore indicate that the chromophore in this region is located not far above the cloud-tops, and we suggest that the red colour in this region could be a result of relative absence of ammonia gas that can condensate around the chromophore nuclei and mask their signature. We note that our retrieved main cloud altitude remains relatively uniform at around 1.2-1.5 bars, but as we state earlier, this is most likely made of a sulphur compound akin to NH_4SH. We still do not discount the possibility of a substantial ammonia cloud layer around 0.7 bars that is present in the zones but not the belts, but that we simply cannot resolve from the underlying NH_4SH cloud. This ammonia cloud could well prove to be the location of the chromophore. We therefore propose further investigation of a possible ammonia cloud layer in these regions for future work.

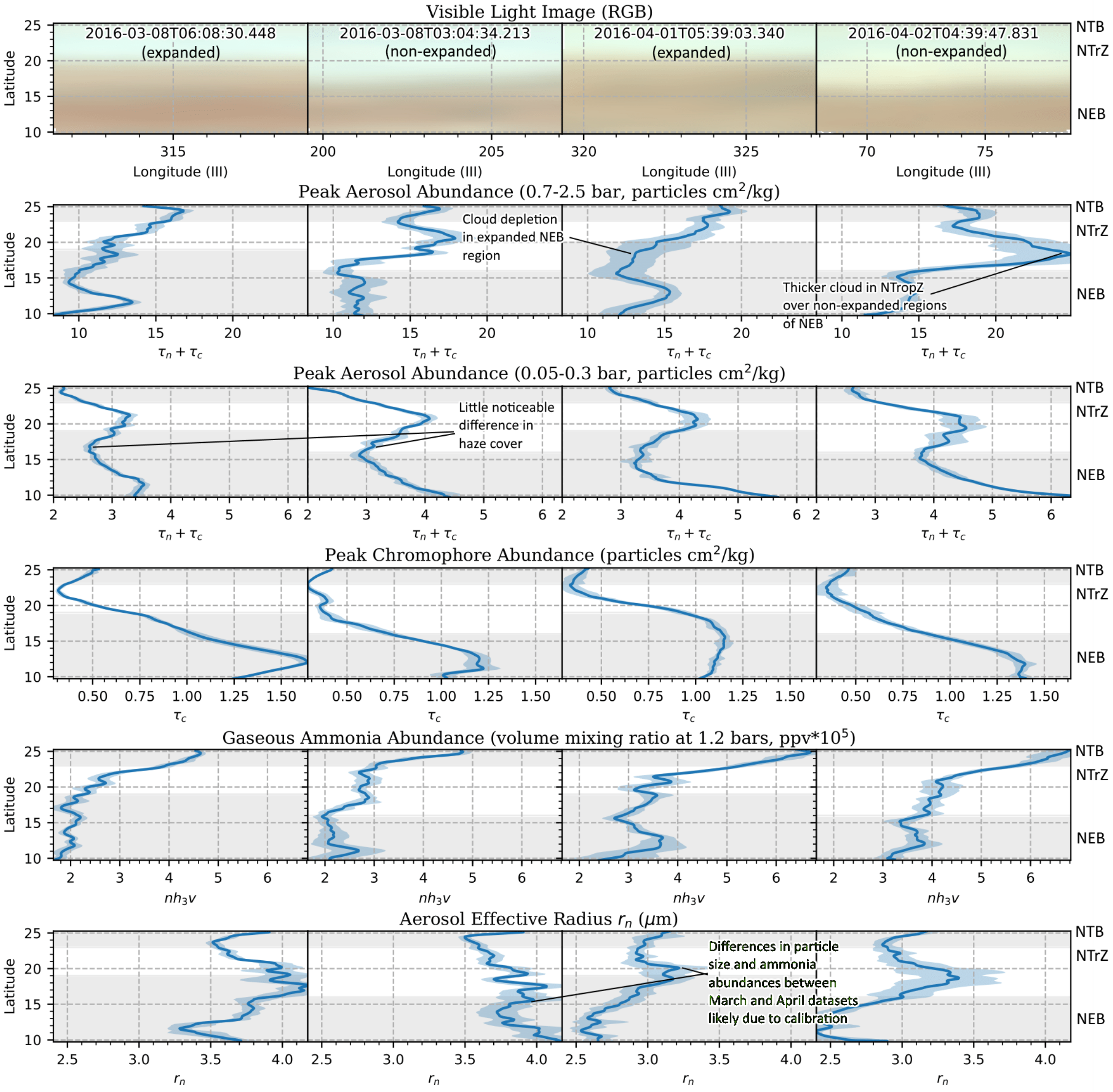

Figure 5.3.4: Results of the simultaneous retrievals of aerosol density, colour and ammonia abundance around the NEB and NTropZ, at longitudes of expansion (2016-03-08T06:08:30.448 and 2016-04-01T05:39:03.340) and non-expansion (2016-03-08T03:04:34.213 and 2016-04-02T04:39:47.831), with most notable features highlighted. The top row displays a simple RGB composite of the MUSE data, with the red component corresponding to the average I/F between 0.620µm and 0.750µm, the green component to the average I/F between 0.495µm and 0.570µm and the blue component to the average I/F between 0.475µm and 0.495µm (the wavelength ranges chosen approximately according to colours as perceived by the human eye). From top to bottom, the plots show peak aerosol abundance (chromophore + non-chromophore) in units of particles cm^2 per kg of atmosphere between 0.7 and 2.5 bars (to correspond to the main cloud layer), peak aerosol abundance between 0.1 and 0.3 bars (to correspond with high-altitude haze), peak chromophore abundance, ammonia volume mixing ratio at 1 bar (multipled by 10^5), and the effective radius of non-chromophore particles r_n, all averaged with respect to longitude and with errors calculated from the standard deviation. The main zones and belts are marked in white and light grey respectively on each graph, with the names of the zonal bands marked on the right-hand side. Latitude values are all planetographic.

In pre-outbreak data of Jupiter, we observe a dark band at 0.89µm over the NTBs in 2016, as we show in figure 5.3.6, whose brightness appears to be relatively uniform with longitude, although the northern boundary of the dark band is noticeably more distinct at longitudes of expanded NEB than at longitudes of non-expanded NEB. This same band was also seen by Simon et al. [2015] and Hueso et al. [2017] at both 0.89µm and at 0.275µm, indicating a substantial depletion in haze. We can also detect this band to a lesser extent at 0.727µm, while at 0.619µm we can only just discern a very thin dark band that separates latitudes which are 0.89µm-dark from the NTropZ. This thin dark band presumably marks the boundary between two adjacent convection cells, with greater upwelling in the southern cell (the NTropZ) than in the northern cell (the NTBs).

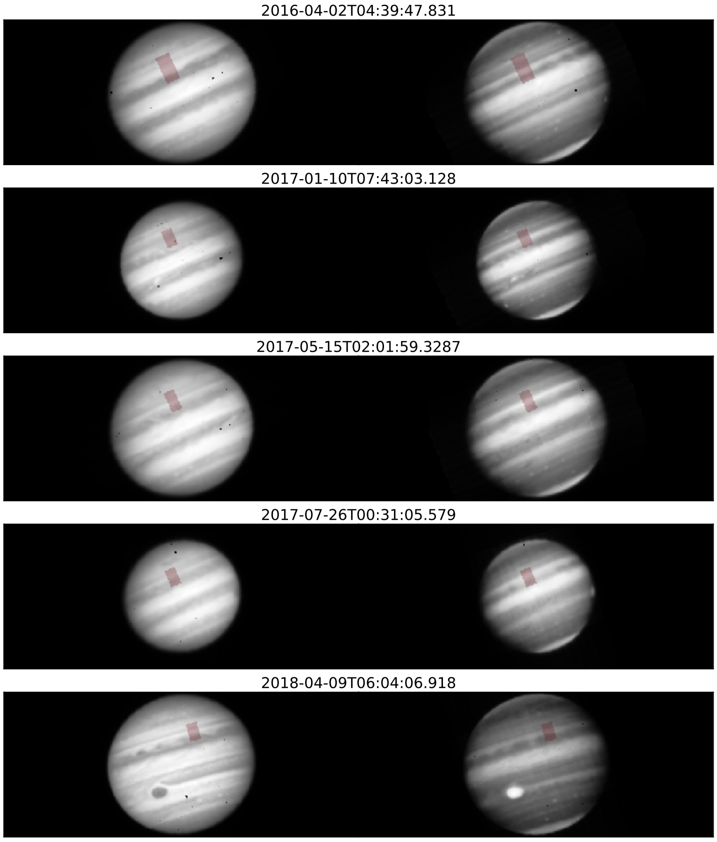
2016-04-02T04:39:47.831
2017-01-10T07:43:03.128
2017-05-15T02:01:59.3287
2017-07-26T00:31:05.579
2018-04-09T06:04:06.918

Figure 5.3.5: All MUSE datasets described in reference to the NTBs upheaval event, with the image on the left an average of the spectral image cube between 0.485µm and 0.495µm, and the image on the right the corresponding image averaged between 0.885µm and 0.890µm, and the footprint of the slice in each case shown in red. In each case, we choose slices that are generally as close to the central meridian as possible, but avoiding anomalous regions (particularly in the 2018-09-04T06:04:06.918 dataset, where a large number of discrete features can be observed in the northern EZ). It is impossible not to take longitudinal variations into account in the 10th of January 2017 dataset, and so we simply choose an arbitrary longitude close to the central meridian. The 2016-04-02T04:39:47.831 dataset takes into account a region of non-expanded NEB. Each image is shown at the same spatial scale (104"x44"), in order to highlight the variation in angular diameter of Jupiter over the four-year period.

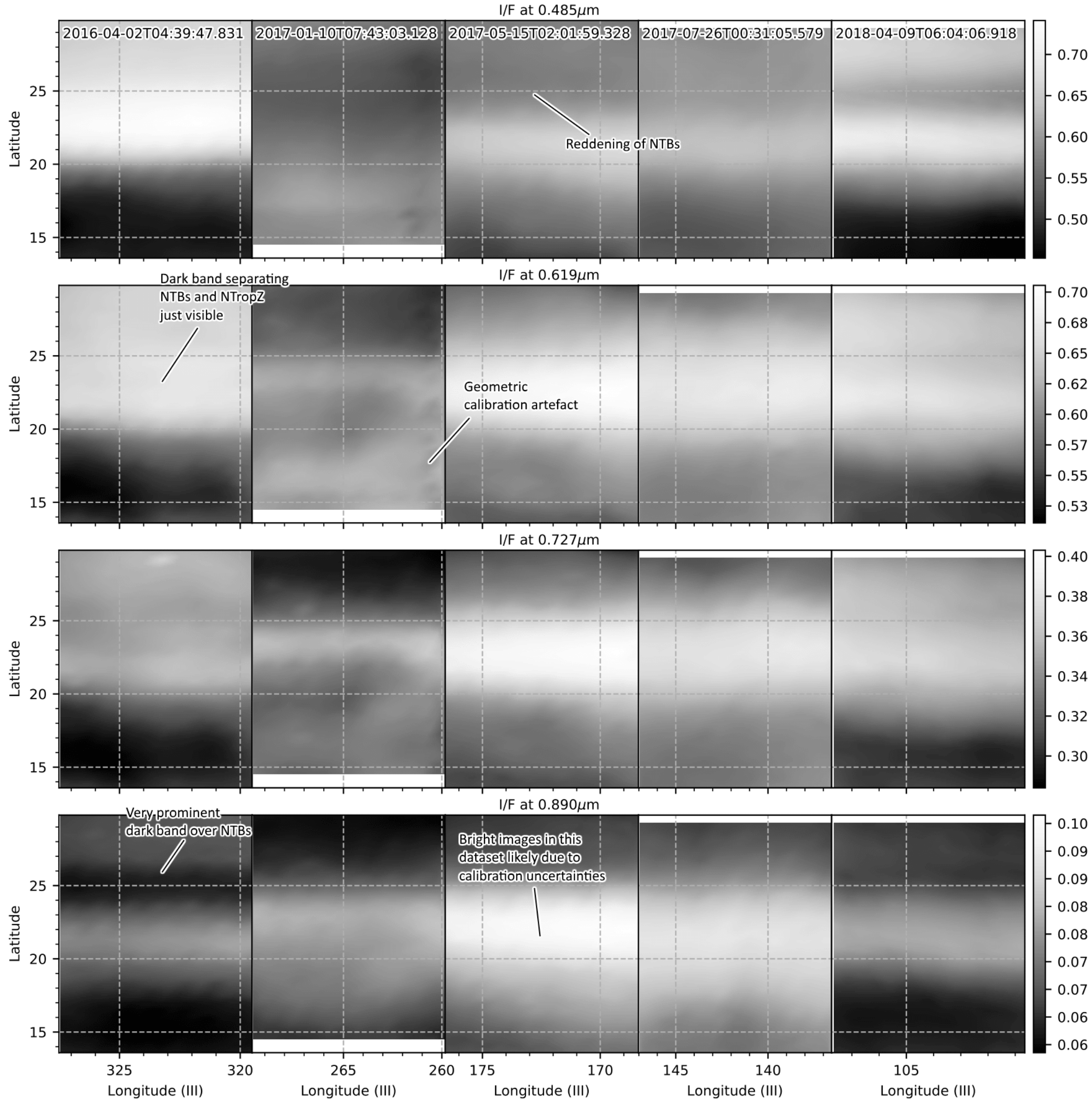

Figure 5.3.6: Average I/F values corresponding to the plots shown in figure 5.3.7, from top to bottom: average I/F between 0.480μm and 0.490μm (sensitive to chromophore), I/F at 0.619μm (sensitive to 1 bar cloud), I/F at 0.727μm (sensitive to haze between approximately 0.3-0.6 bars) and average I/F between 0.885μm and 0.895μm (sensitive to haze between approximately 0.1-0.2 bars). Latitudes values are planetographic.

MUSE retrievals from just after the outbreak in early 2017, as we show in figure 5.3.7, indicate a resurgence in both cloud and haze in the NTBs around the region that was previously dark at 0.89μm. Although our retrievals only show a gradual increase in cloud and haze cover over the NTBs over time following the upheaval, in reality this is most likely just an effect of differences in calibration and particle size retrieval. In fact, the opposite is more likely true, in that we should see a dramatic increase in cloud and haze before we see an increase in red colour. One piece of evidence for this is the apparent depletion of ammonia in the NTBs in January 2017 that is not seen in later data, most likely a consequence of unusually high cloud cover in the region. In addition, the retrieval has to increase the particle size in the NTBs in order to account simultaneously for high continuum I/F values and low I/F values at blue wavelengths, which thereby affects the retrieval of haze abundances for reasons previously explained in chapter 4. This increase in particle size is most likely genuine, and also appears to be accompanied by a small-particle region to the north, perhaps indicating a local upwelling-downwelling system.

The formation of chromophore in this region is therefore most likely a direct consequence of this dramatic upwelling. If we were to assume that Carlson chromophore is the universal chromophore on Jupiter, we could suggest that upwelling in this region is sufficient that large quantities of ammonia ice from the troposphere can react with downwelling acetylene from the stratosphere to produce chromophore directly in the tropopause. However, this would then require an explanation as to the ubiquity of chromophore closer to the level of the main cloud layer, as we found in the NEB and as we would assume by extension to also be the case in the other belt regions of Jupiter, where acetylene is not present at sufficiently high abundances to produce Carlson chromophore in situ. Conversely, if we were to assume that low-altitude chromophore in the belts was a result of sedimentation from the haze layers in which the chromophore originates, we would then have to ask why the NTBs and certain discrete features are the only regions in which we observe bright red colour associated with thick haze. For the moment, we will neglect the hypothesis of Baines et al. [2019] that lightning can raise acetylene abundances in certain regions of Jupiter sufficiently to produce tropospheric chromophore, due to its highly speculative nature. If, on the other hand, we suggest that chromophore particles act as condensation nuclei for ammonia ice (eg. Atreya et al. [2005], Kalogerakis et al. [2008]), then the particles themselves could reach sufficiently high altitudes in the NTBs (or indeed in red ovals such as the GRS) for the surrounding ammonia ice to be removed through reactions with haze constituents, leaving behind the red chromophore nuclei. This would have to be a somewhat slow reaction, as changes to high-altitude haze cover often precede colour changes in discrete features (and most likely the NTBs as well, judging by our observations) by several months. This also leaves our original question unresolved as to what the chromophore is made of and how it is formed in the first place.

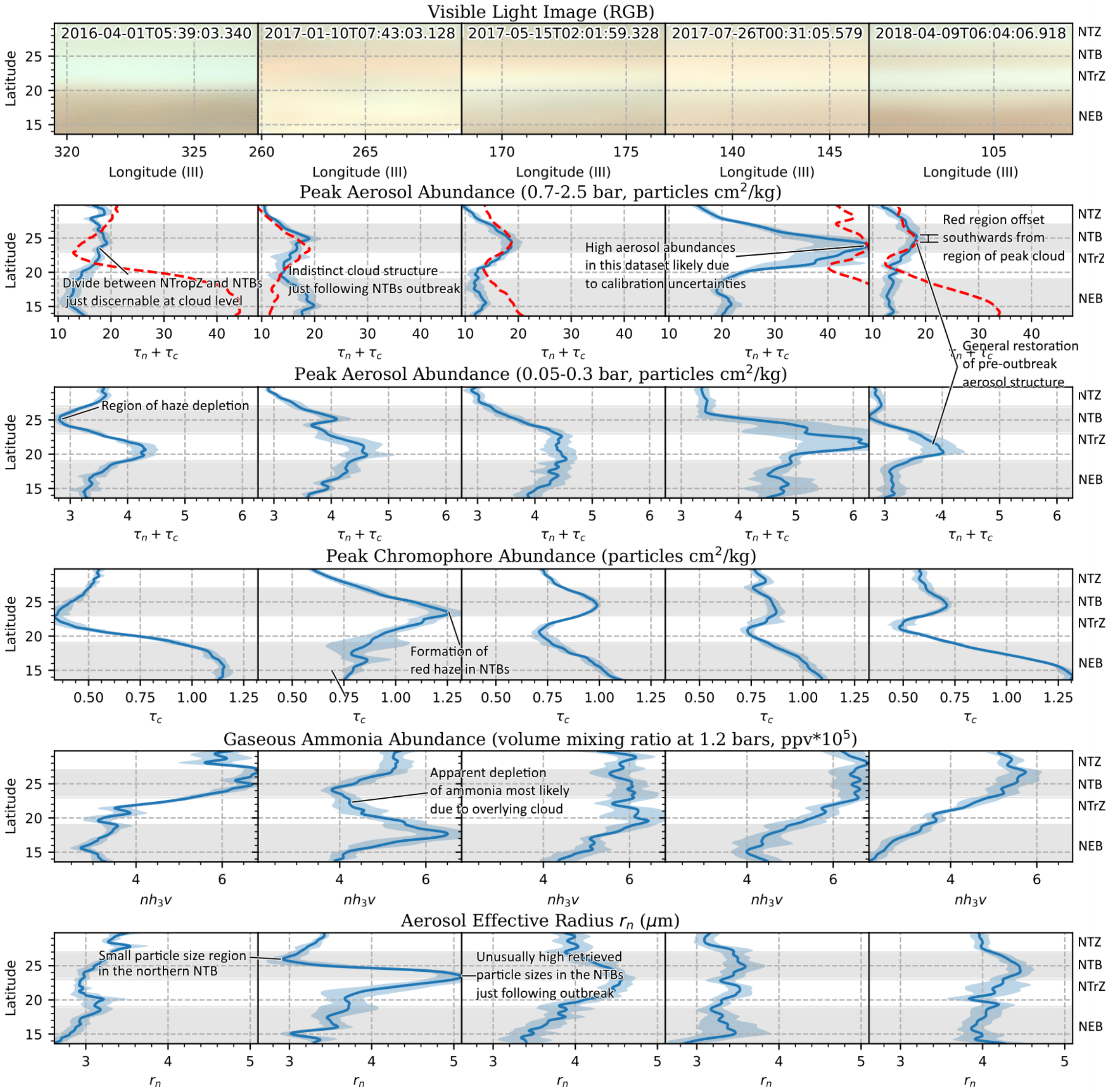

Figure 5.3.7: Results of the simultaneous retrievals of aerosol density, colour and ammonia abundance around the NTB and NTropZ, before the NTBs upheaval (2016-04-02T04:39:47.831) and after (the remaining columns). We refer the reader to figure 5.3.4 for a detailed key to each of the plots. For comparison, we also replot the zonally-averaged chromophore abundance profile in the second-plot from the top, arbitrarily scaled to the peak cloud abundance level in the NTBs, in order to show the offset in latitude between the red NTBs haze and thick cloud region.

By 2018, while the red colour of the NTBs was no longer as bright as it was a year prior, it still remained conspicuous. However, we find little match, in both our observed I/F values in figure 5.3.6 and our associated retrievals in figure 5.3.7, between the red region and local variations in aerosol structure or ammonia abundances, which revert back almost to their pre-outbreak states. The chromophore in the NTBs could therefore be located in a very stable region (perhaps near a cold trap such as the tropopause) of the atmosphere in which timescales of either chemical degradation, eddy diffusion or sedimentation are of the order of years. The NTBs only gradually loses its colour through the slow sedimentation of chromophore particles into the troposphere, where ammonia ice condenses around them and thereby masks their signature, a process that occurs in a matter of hours [Sánchez-Lavega and Gomez, 1996]. Such a hypothesis would require a detailed microphysical model to test, which we have proposed for future work.

In summary, we therefore propose that the NTBs upheaval event is associated with cyclical variations in upward convection in the NTBs, which is associated with changes in cloud and haze cover that are shortly followed by changes in colour. In order to better understand the origin of these cyclical variations, we propose further investigation of associated changes in the NTZ and NNTB for future work.

5.4 The EZ colouration event of 2018

In 2018, we saw the start of a new event in the Equatorial Zone. Starting around the time of PJ11 in February 2018, the centre of the EZ began to develop a very faint orange colour [Rogers, 2018b]. This colour then gradually became stronger over the coming months before visibly affecting the underlying cloud morphology of the EZ. Like the NTBs upheaval, this is also a quasi-regular event which last occurred in 2012 [Fletcher, 2017], but unlike the NTBs upheaval does not appear to be triggered by any particular sudden convective event. Despite a long history of colour changes in the EZ, discussion in the literature is far more sparse than for the NTBs upheaval, even when amateur work is included. The most detailed discussion of historical observations of EZ colourations is given by Antuñano et al. [2018], focussing particularly on associated observations of deep cloud at 5µm.

As in the previous section, we extracted swaths of the EZ, presented in figure 5.4.1, from four separate MUSE datasets between April and September 2018. The resulting retrievals are presented in figure 5.4.2, zonally averaged as in the previous section. Despite the relative homogeneity of the orange colour in the EZ that would indicate the presence of chromophore at high altitude, we find no conclusive evidence of changes in high-altitude haze cover over the EZ, or any kind of correlation between haze cover and colour as we saw in the NTBs. We only observe some cloud clearing in the southern half of the EZ in September 2018, several months after colour changes were first observed in the region. Even then, this apparent cloud clearing could partly be attributed to the poor calibration of the 2018-09-11T23:11:42.877 dataset instead of a real effect, although observations in the mid-IR by Antuñano et al. [2018] would appear to confirm cloud clearing in this region that is actually more pronounced and widespread than our retrievals would suggest. We find more convincing evidence of a gradual depletion of ammonia abundances in the southern EZ accompanied by a gradual increase in ammonia in the northern EZ. This could indicate some kind of cyclical atmospheric variability in the EZ as we suggested previously in section 5.2, but is difficult to link with changes in colour.

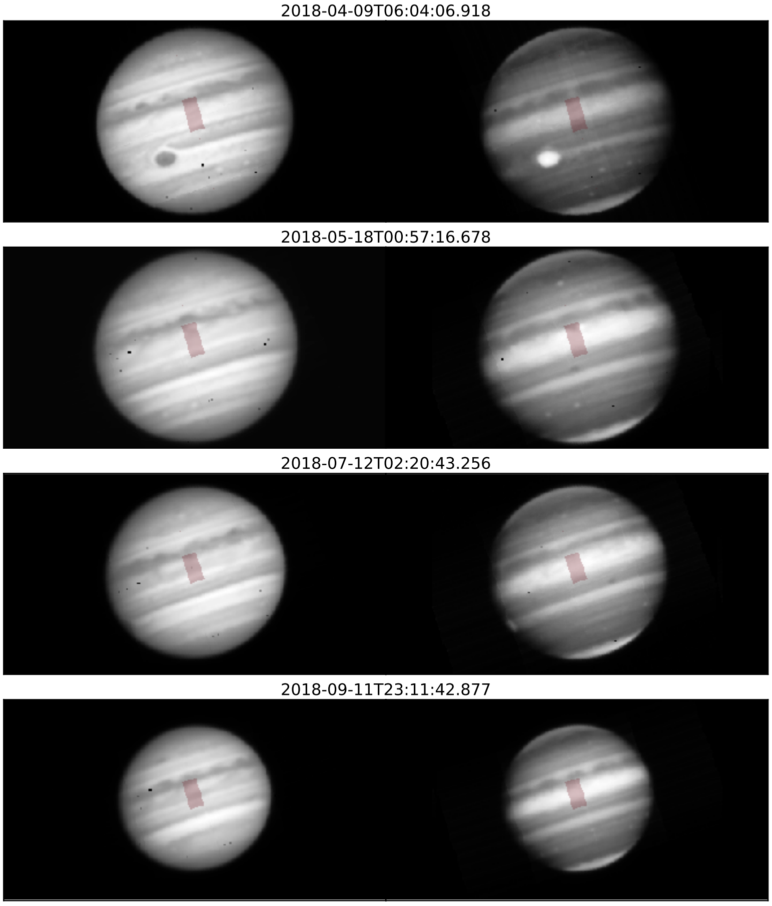

Figure 5.4.1: All MUSE datasets described in section 5.4, with footprint of the slice in each case shown in red. In each case, we choose slices that are generally as close to the central meridian as possible; the exact region is relatively arbitrary due to substantial longitudinal variations over these spatial scales. Each image is shown at the same spatial scale (84"x44"), in order to highlight the variation in angular diameter of Jupiter over the four-year period. The left image is the median of the spectral image cube over a wavelength range 0.485μm to 0.495μm, while the right image is the equivalent median between 0.885μm and 0.890μm. Note the wave structure in the northern NEB, particularly in the 2018-04-09T06:04:06.918 and 2018-09-11T23:11:42.877 images.

The fact that visible colour changes in the EZ occurred before any corresponding changes to tropospheric aerosol structure would appear to contradict the hypotheses of a universal chromophore that we laid out in the previous section. The first half of 2018 saw substantial wave activity in the NEB that was visible at 0.89μm which accompanied the southward retreat of the northern boundary of the NEB, as can be clearly seen in figure 5.4.1. It is therefore possible that the increase in chromophore in the EZ is linked with dynamics at higher altitude, but we can only speculate as to the cause of the reddening without further information on associated temperature changes in the region in 2018. In order to better understand the changes in the observed appearance of the EZ, we can only continue to perform retrievals of cloud structure and colour as the colouration event intensifies and progresses well into 2019, for which further MUSE observations have already been granted and which will hopefully be executed under better observing conditions and using better calibration.

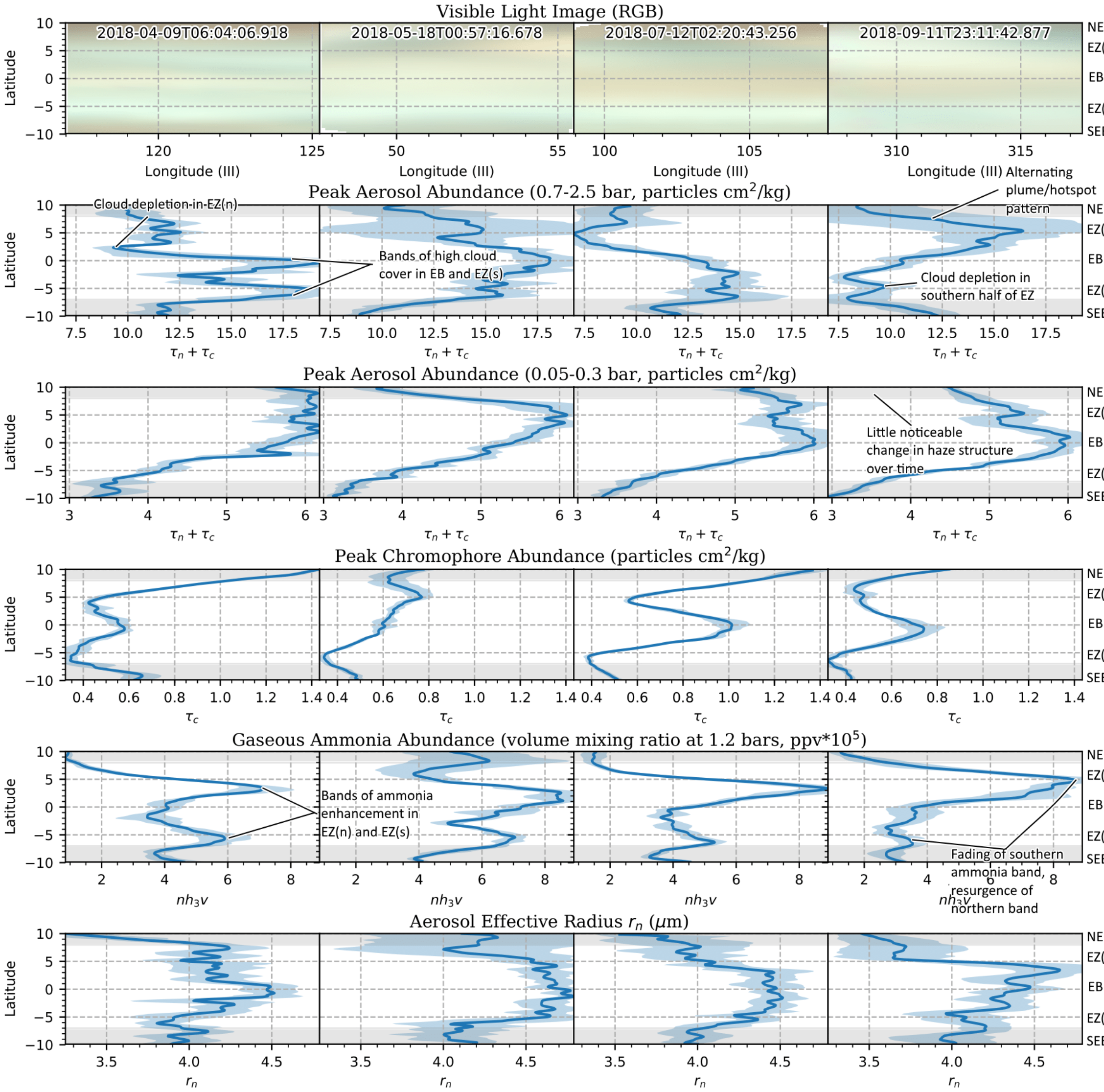

Figure 5.4.2: Results of the simultaneous retrievals of aerosol density, colour and ammonia abundance around the EZ, during the colouration event, with major features highlighted. We refer the reader to figure 5.3.4 for a detailed key to each of the plots.

5.5 Changes in cloud structure and colour of the GRS

The Great Red Spot has been extant at least since the 19th Century, and possibly even corresponded to 'Hooke's spot', a storm feature which was discovered by the eponymous astronomer 200 years earlier [Rogers, 1995]. How it has managed to survive for so long is as yet still unknown, but it is thought to be sustained by mergers with other smaller anticyclones [Vasavada and Showman, 2005]. Despite its persistence in Jupiter's atmosphere, substantial changes have been seen in the morphology of the GRS in recent years. The GRS has been observed to continually shrink in its longitudinal extent since the Voyager mission, but this shrinkage accelerated dramatically after 2014 as reported by Simon et al. [2014, 2018]. It is thought that if the shrinking continues at its current rate, the GRS will no longer be in a stable configuration and it will entirely disintegrate. The GRS is the only discrete feature on Jupiter (with the possible exception of Oval BA, as will be explained further in section 5.6) whose interior structure can be fully resolved with MUSE. We therefore wish to use our MUSE data to retrieve spatial and temporal variations in cloud structure and colour in order to shed light on both its fine structure and the origin of its shrinkage. In addition, the GRS is the only region where chromophore abundances are great enough that their altitude can be reliably retrieved using our cloud model.

While the MUSE data cover the entirety of the temporal range associated with the most dramatic shrinking of the GRS, the quality of most of our MUSE observations of the GRS are somewhat deficient. Only two observations of the GRS below a 50 degree viewing zenith angle were made before 2018: one in 2014, in which the structure of the GRS was partially obscured by striping artefacts (the effects of which were mostly, but imperfectly, corrected for as explained in section 2.4.3), and one in 2017 which was observed when Jupiter was low on the horizon and close to solar conjunction, making the fine structure of the GRS more difficult to resolve. By contrast, our observation of the GRS in April 2018 was seen to be much more reliable, taken during very good seeing conditions and at low airmass. For our retrievals, we analysed sample regions of the GRS and its environs from each of these three datasets, whose footprints are shown in figure 5.5.1. We also acquired an additional observation of the GRS close to nadir on the 25th of May 2018 (see appendix A), but we have left it out of this analysis for a number of reasons. Firstly, the boundary between two adjacent MUSE IFUs went straight through the centre of the GRS, and left a striping artefact that, while milder than those seen in the 2014 data, was still conspicuous enough to affect retrievals of cloud structure and ammonia. Aside from this artefact, preliminary retrievals showed very little difference in the fine structure of the GRS compared with our April 2018 data, apart from a few features near the inner ring of the GRS whose morphologies change over very short timescales. We therefore decided that this dataset would add little value to this particular analysis, even if the striping artefact would have been benign enough to smooth over without particular detriment to the MUSE spatial resolution. Moreover, the 25th of May 2018 observation of the GRS was obtained within half an hour of an observation in the thermal IR by VISIR (Fletcher and Donnelly, personal communication). Studying these two datasets together, one can perform retrievals of a number of different variables independently for the entirety of the GRS and its environs, as explained previously in section 3.2. This merits an entire analysis of its own, which we do not have space to cover here, and which we have therefore left to future work.

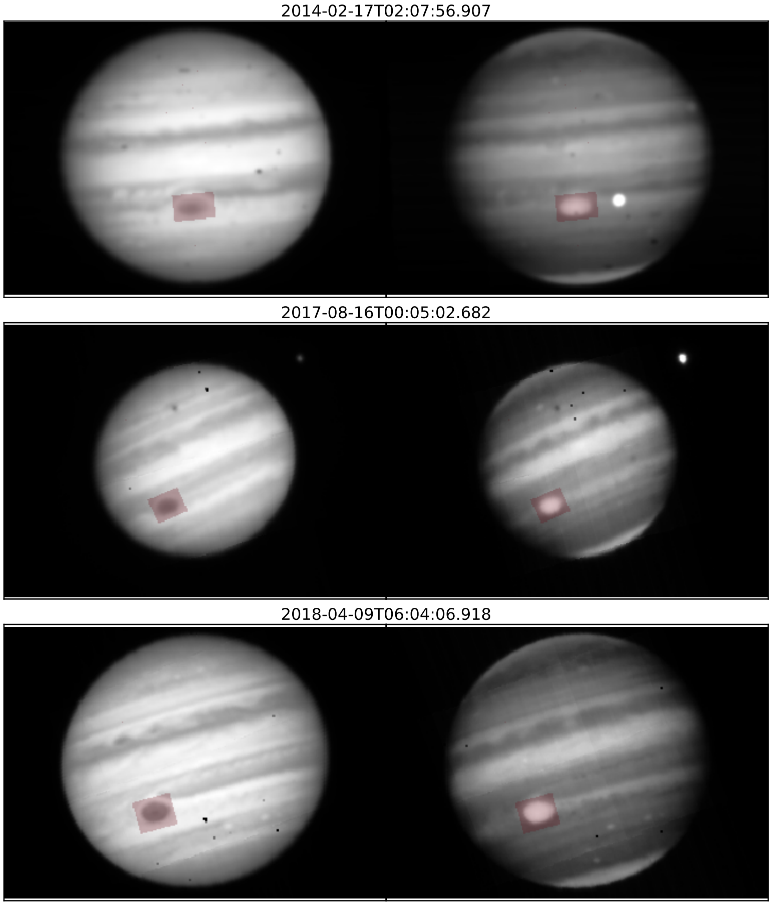

Figure 5.5.1: All MUSE datasets described in section 5.5, with footprint of the sample region in each case shown in red, taking into account the whole of the GRS and much of its environs. Each image is shown at the same spatial scale (62"x44"), in order to highlight the variation in angular diameter of Jupiter over the four-year period. The left image is the median of the spectral image cube over a wavelength range 0.485µm to 0.495µm, while the right image is the equivalent median between 0.885µm and 0.890µm. The bright circle in the top-right image to the right of the GRS is the moon Europa which far outshines Jupiter at 0.89µm. Europa is also visible to the right of Jupiter in the 16th of August 2017 images, and casts a dark shadow that is visible in the middle of the NTZ at 0.49µm.

We display the results of our retrievals in figure 5.5.2, which we smoothed using a median filter of kernel size 7x7 pixels in order to smooth over unrealistic pixel-to-pixel variations in retrieved particle size; we include an additional plot of the source I/F values in figure 5.5.3 to assure the reader that our results are consistent with our observations. The most noticeable change during the four-year period is in the cloud structure of the GRS. Like Simon et al. [2018], we find an increase in haze across the whole of the GRS, and which is less concentrated around the inner core. This also correlates with an increase in red colour across the feature, with the colour nonetheless still most intense in the central core. However, we also see an approximately fourfold increase in the density of 1 bar cloud between 2014 and 2017. The apparent increase in cloud opacity towards the central core is most likely a result of poor spatial resolution, since we can see from our April 2018 retrievals that the bulk of the aerosol density at these altitudes is contained around the centre of the GRS (a region which we will dub the 'eye wall', as per the legend in figure 5.5.2), particularly in regions of high relative vorticity (as identified by eg. Dowling and Ingersoll [1988], Choi et al. [2007], Shetty and Marcus [2010], Sánchez-Lavega et al. [2018]). Such an increase cannot be fully explained by uncertainties either in the photometric calibration or in the particle size, especially given the corresponding cloud abundances we retrieve in the surrounding 'collar'. Most likely, this is a direct consequence of vortex stretching associated with the shrinkage of the GRS and the conservation of angular momentum, as stated in Simon et al. [2018], which results in the GRS becoming taller. Our data also provides some indication of a corresponding increase in gaseous ammonia abundances in the centre of the GRS, but this is difficult to confirm definitively given the spatial resolution and the quality of the 2014 data. Despite these findings, we retrieve almost no spatial or temporal changes in the altitude of the main cloud layer.

We find a north-south asymmetry in the structure of the GRS at this altitude that is particularly clear in our retrievals of ammonia abundance and which appears constant over time. This structure is particularly well-resolved in our April 2018 retrievals, and consists of a relative elevation in cloud-top ammonia abundance in the GRS itself and the northern collar, and a relative depletion in the southern collar. This also corresponds closely to the distribution retrieved by Fletcher et al. [2010b] at around 550mbar from data obtained between 2006 and 2008, which they speculated to be a result of a southward obliquity of the GRS vortex. Asymmetries within the GRS itself are not well-reflected in cloud-top ammonia gas abundances, whose profile appears uniform over the surface of most of the GRS, but inhomogeneities are seen in the cloud structure itself within the GRS eye wall. We note in particular a relative depletion of cloud in the southwest of the GRS in 2014, and local elevations of cloud in the east and west of the GRS in 2018. These are, however, more likely to be a result of small-scale cloud clusters and vortices as identified by Sánchez-Lavega et al. [2018], which vary over short timescales. We note that the structure of the eye wall in our preliminary retrievals of GRS data from May 2018 is quite different from that in April 2018.

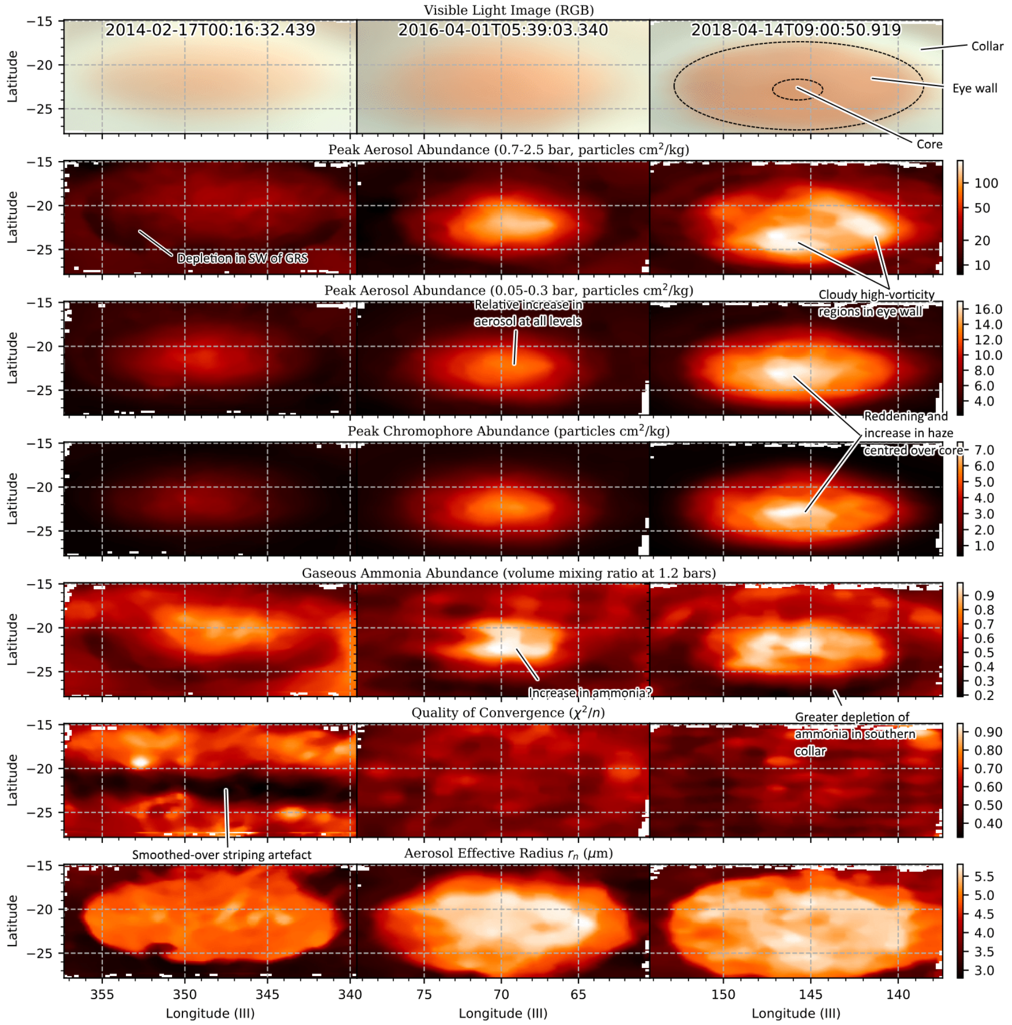

Figure 5.5.2: Results of the simultaneous retrievals of aerosol density, colour and ammonia abundance in the GRS and its surroundings, with nomenclature relating to different parts of the GRS shown in the top-right plot. The top row displays a simple RGB composite of the MUSE data, with the red component corresponding to the average I/F between 0.620µm and 0.750µm, the green component to the average I/F between 0.495µm and 0.570µm and the blue component to the average I/F between 0.475µm and 0.495µm (the wavelength ranges chosen approximately according to colours as perceived by the human eye). From top to bottom, the plots show peak aerosol abundance (chromophore + non-chromophore) in units of particles cm^2 per kg of atmosphere between 0.7 and 2.5 bars (to correspond to the main cloud layer), peak aerosol abundance between 0.1 and 0.3 bars (to correspond with high-altitude haze), peak chromophore abundance, ammonia volume mixing ratio at 1 bar (multipled by 10^4), χ^2/n, and the effective radius of non-chromophore particles r_n. Latitude values are all planetographic. The straight horizontal line that shows up in the χ^2/n plot for the 2014-02-17T02:07:56.907 dataset is a consequence of the Gaussian destriping described in section 2.4.3, while the local spikes in χ^2/n that appear in the same plot are a result of hot pixels. Noise around the edge of each plot is due to median filtering.

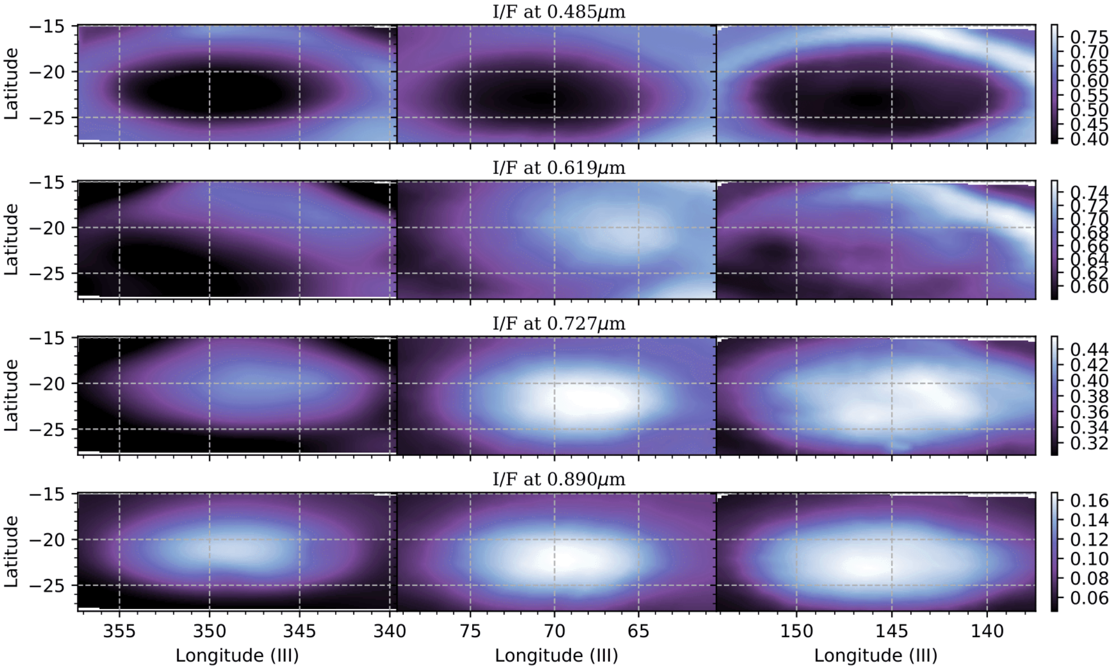

Figure 5.5.3: Average I/F values of the GRS corresponding to the plots in figure 5.5.2. We refer the reader to figure 5.3.6 for a key to each of these plots.

As we show in figure 5.5.4, we consistently retrieve the chromophore altitude in the GRS around the tropopause at 0.1 bars (for retrievals in which the retrieval of chromophore altitude is reliable), as we expect given the correlation between the region of thick haze and deep red colour. This would indicate that the chromophore, at least in the GRS, is generated or exposed in the high-altitude haze itself, as we surmise it is in the NTBs. We also note that the ammonia abundances in the centre of the GRS as retrieved by Fletcher et al. [2010b] and de Pater et al. [2019] at around 0.5 bars are not nearly as elevated relative to the surroundings as they are in our data, particularly after 2014. Even taking time variability into account, this would provide some evidence that ammonia depletes faster with altitude in the GRS than it does in the surroundings, presumably due to increased ammonia condensation or photolysis.

5.6 Characterising morphological changes in Oval BA

The second-largest discrete feature on Jupiter is Oval BA, an anticyclone that formed from the merger of three smaller white ovals in 2000 [Sánchez-Lavega et al., 2001]. While Oval BA was originally a white colour following its initial formation, it turned red over a period of a few months

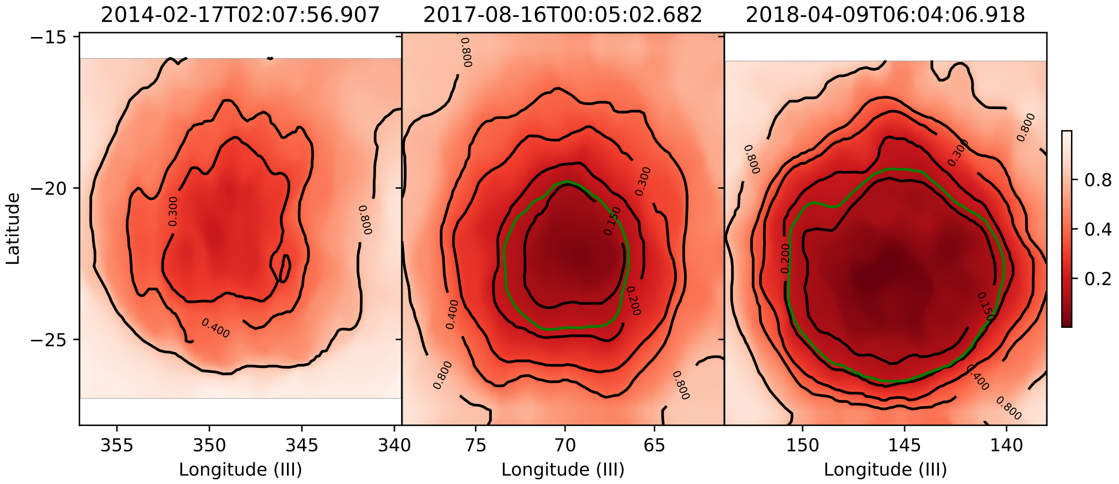

Figure 5.5.4: The temporal evolution of the retrieved 2-D chromophore altitude profile of the GRS (following median filtering as explained in the text), as exhibited by both the black contour lines and the colours (in units of bar pressure). The green contour line indicates the region within which retrieved chromophore abundances are in excess of 4 particles cm^2/kg, and hence the region in which retrieved chromophore abundance and altitude values can be reliably decoupled, as previously explained in section 4.8.

in 2006 [Naeye, 2006], despite no noticeable change in its circulation or cloud structure to trigger the colour change [Pérez-Hoyos et al., 2009, Wong et al., 2011]. More recently, this red colour has been seen to gradually fade over time, and has now almost completely disappeared as of writing in March 2019. The earliest, very tentative report of the fading colour of Oval BA that we can find appears to be Rogers [2018a], published in June 2018. However, we would argue from our own inspection of images obtained by the amateur community that the fading started becoming obvious well before this (around the end of 2017). We must note this as our latest MUSE observations of Oval BA from the 14th of April 2018 exhibit a much less red colour than our original observations from the 28th of May 2017, even when taking the different observing conditions into account.

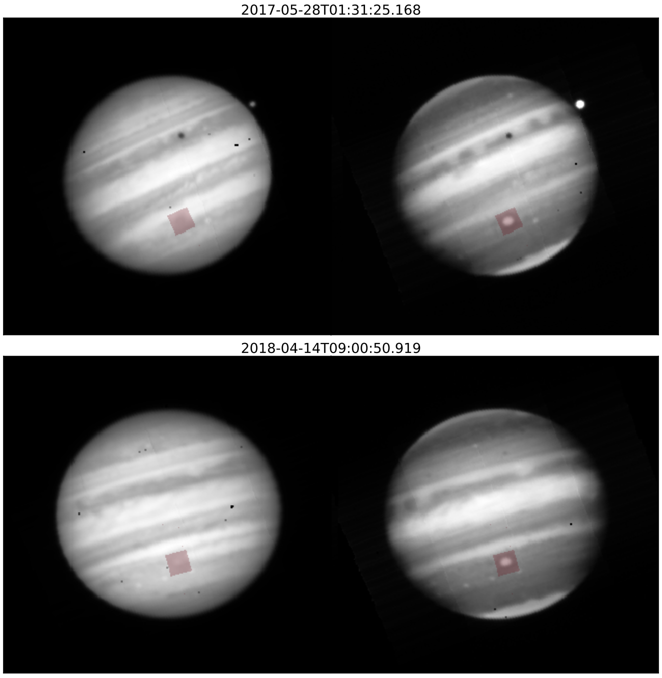

Figure 5.6.1: Both MUSE datasets described in section 5.5, taking into account the whole of Oval BA and much of its environs. Both images are shown at the same spatial scale (64"x64"). The left image is the median of the spectral image cube over a wavelength range 0.485µm to 0.495µm, while the right image is the equivalent median between 0.885µm and 0.890µm. The bright circle in the top-right image just to the right of the GRS is the moon Io which far outshines Jupiter at 0.89µm. Io also casts a noticeable dark shadow in the NEB at both wavelengths.

We extracted spectra of the region around Oval BA from these two datasets, as shown in figure 5.6.1, and performed retrievals on them, the results of which are shown in figure 5.6.2. It is difficult to compare like with like, given that the spatial resolution is far superior in the 2018 image than in the 2017 image. This is also compounded by the fact that the 2018 image of Oval BA was taken close to nadir while the 2017 image was taken at high viewing zenith angle. The clearest manifestation of this is the lack of a visible distinction between the red annulus and pale centre of the oval in the 2017 image, despite this structure being clearly visible even in concurrent amateur observations. Instead, we observe red colour concentrated in the centre of Oval BA in our MUSE data from 2017, which we know to be incorrect. By contrast, the red annulus of Oval BA is clear to see in our 2018 data and appears to be located just within the region of both increased cloud and haze, as previously observed by Asay-Davis et al. [2009]. This is consistent with the model of the vertical circulation hypothesised by de Pater et al. [2010] based on radio observations, in which the chromophore forms in a region of local downwelling, presumably due to adiabatic heating which either sublimates ammonia ice rime surrounding a chromophore condensation nucleus or elevates the reaction rate enough for chromophore to be produced in situ.

Even in the 2018 data, we find it very difficult to resolve any spatial differences in ammonia abundance that would clearly mark out Oval BA from its surroundings. However, we can clearly mark out Oval BA in both cases when we look at its cloud structure, particularly in its high-altitude haze, which, like that of the GRS, is very opaque relative to the surroundings. Curiously, as in the previous colour change in 2006, we detect little change in cloud structure associated with the whitening of Oval BA.

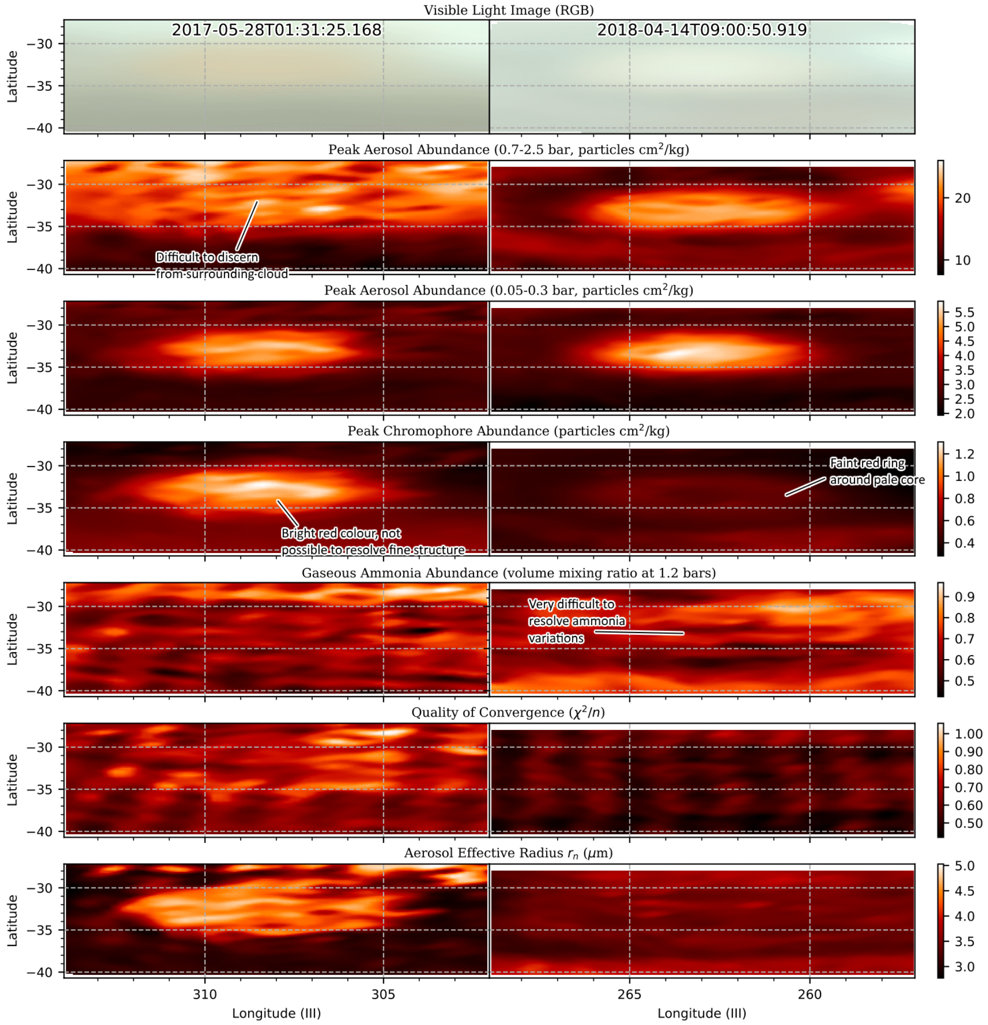

Figure 5.6.2: Results of the simultaneous retrievals of aerosol density, colour and ammonia abundance in Oval BA and its surroundings. We refer the reader to figure 5.5.2 for a detailed key to each of the plots. No median filtering was performed for these plots.

Chapter 6

Saturn - Constraining a universal chromophore and cloud model

6.1 Overview

In chapter 4, we explained how we tested and refined our retrieval model in order to maximise the amount of reliable information that could be extracted from a MUSE spectrum of Jupiter. We now apply the same methodology to refine an equivalent retrieval model for Saturn MUSE spectra in this chapter. This chapter will therefore follow a somewhat similar structure to chapter 4, and so we will avoid reiterating information that is identical in both the Jupiter and Saturn cases. The biggest difference between this work and the work presented in chapter 4 is the relative dearth of literature devoted to studies of Saturn's troposphere compared with that of Jupiter. Although several papers have been published on Saturnian cloud structure retrievals in the past, which will be described in more detail in sections 6.4 and 6.5, one has to take into account seasonal changes in cloud structure over its entire 30 year orbital period. This means that, in order to compare the current state of Saturn's atmosphere with the last northern summer solstice, one would have to refer to observations made 30 years ago with the astronomical instrumentation and computational technology that was available at the time (recall that this would predate both Cassini and HST). Literature dedicated to either the observation or laboratory synthesis of Saturnian chromophore is very sparse: any explicit mention of Saturn chromophore in the literature is usually only added as an aside (the most detailed review the writer can find is in West et al. [2009], which consists of two paragraphs of speculation and one citation to laboratory experiments of Jovian chromophore). We note the work of Guillemin et al. [2001], who found that a yellow substance could be formed through the reaction of ethene with either ammonia or phosphine under UV radiation, but these reaction products were not analysed or fit to Saturnian spectra as in CR16. This lack of prior literature comes as a blessing and a curse: on the one hand, even the most flawed and inconclusive work presented here on Saturnian chromophore is treading new scientific waters, while on the other hand, it will be much harder to constrain degenerate results with physical data as we did in section 4.6.

First, we attempt to fit the laboratory chromophores of Noy et al. [1981] and Carlson et al. [2016] to Saturn MUSE data in section 6.3, and then retrieve a universal Saturn chromophore imaginary refractive index spectrum in section 6.4. All these retrievals will be conducted on a single MUSE spectral image cube (timestamp 2017-06-18T06:04:09.111), which was the only cube to be obtained using AO. As Saturn lacks discrete features at visible wavelengths at this time, and we only have a limited set of Saturn data from 2014 and 2017, we cannot have an extended analysis of temporal changes in Saturnian cloud structure and colour that would be sufficient for a stand-alone chapter, as we did for Jupiter in chapter 5. The most obvious way of getting around this would be to study Saturn data obtained by the VIMS-V instrument between 2004 and 2017, which has received surprisingly little attention in the literature (the work of Oliva et al. [2016] being a notable exception) and onto which we could easily apply our own forward models that we refined on MUSE data. However, the standard routines provided in newer versions of the software used to calibrate VIMS-V spectra (USGS Integrated Software for Imaging and Spectrometers, better known as ISIS3) include a bug which was most likely added during a 2017 update and which, despite all our own efforts and those of the ISIS3 helpdesk, we were unable to fix. Nonetheless, we will present a brief comparison of the 2014 and 2017 MUSE datasets in section 6.5, and thereby induce possible temporal or seasonal changes in colour and cloud structure that may have occurred during that short timespan. Finally, in section 6.7 we apply a technique known as Principal Component Analysis (PCA) to the Saturn data in order to map spatial and temporal variations in ammonia abundance.

There is little to add here to describe my personal contribution to this work that has not already been stated in sections 2.1 or 4.1, since most of the NEMESIS framework that was applied to Jupiter can also be applied to Saturn. Reference atmospheres for Saturn are also given as citations, and I have little personal contribution to their creation or obtention. Although the IDL codes used to perform the PCA in the final section of this chapter were obtained directly from the IDL Astronomy User's Library (IDLAstro), courtesy of NASA/GSFC, I am solely responsible for their application to ammonia absorption features on Saturn. As with chapter 4, all the remaining analysis and conclusions presented in this chapter, where citations are not provided, are entirely my own work.

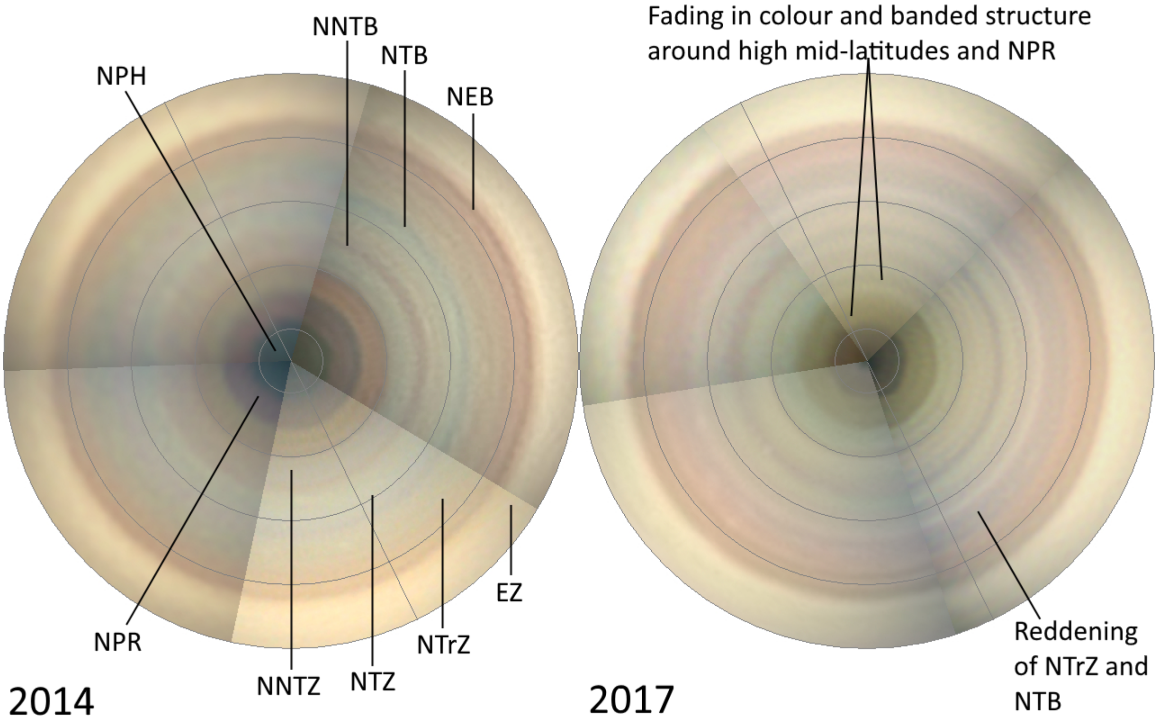

Figure 6.1.1: A comparison of polar projected amateur RGB images of Saturn (left) in 2014, with the names of the major zones and belts highlighted, and (right) in 2017 with the most distinctive changes in the visual appearance of specific latitudinal bands highlighted. We base our zone-belt nomenclature on that of Benton [2018]. Grey circular lines show lines of planetographic latitude in increments of 20^o, with the north pole in the centre and the equator at the edge (the ring shadow region is not in view as it is located just south of the equator). Images from 2014 were obtained at 2014-02-05 (Darryl Pfitzner Milika), 2014-02-16 (Darryl Pfitzner Milika), 2014-04-24 (Damian Peach) and 2014-06-02 (Christopher Go). Images from 2017 were obtained at 2017-04-03 (Clyde Foster), 2017-05-24 (Damian Peach), 2017-06-12 (Pic du Midi) and 2017-07-10 (Damian Peach).

6.2 Reference atmosphere

In this section, we detail all the aspects of the reference atmosphere that remain unchanged throughout this chapter. Many of these are also defined in Sinclair [2013] and Barstow et al. [2016]. We will not have a detailed discussion here on the sources of gas absorption and Rayleigh scattering data, as these are identical to those used in atmospheric retrievals of Jupiter as described in section 4.2. The reference atmosphere covers a pressure range from a deep limit of 4 bars (95km below the 1 bar reference level) to a high-altitude limit of 5 mbar (300km above the 1 bar level); with both altitudes lying far outside MUSE's sensitivity range. Homogeneous layer splitting is performed analogously to that for Jupiter as was illustrated in figure 4.4.1. The temperature-pressure profile from the high stratosphere down to 0.8 bars was obtained from the mean of a number of different profiles retrieved at nadir by the Cassini/CIRS instrument, as described in Fletcher et al. [2010a], and extrapolated to deeper altitudes using a dry adiabat. We neglect spatial variations in temperature, as MUSE spectra have a negligible input from Saturnian thermal emission, even though differences in temperature at the 0.1 bar level between the northern mid-latitudes and the southern EZ (regions south of which are obscured by Saturn's rings) could be up to 10K [Fletcher et al., 2010a]. All reference compositional abundance profiles are as shown in figure 1.2.2. None of these profiles will be allowed to vary, as the gases they describe are either well-mixed in the troposphere (in the case of methane), are present in very low abundances above the haze-tops (in the case of water vapour and ammonia), or do not have spectral features in the MUSE wavelength range that would allow them to be retrieved directly (in the case of every other gas). Deep volume mixing ratios of H_2, He and CH_4 (primarily isotopologue 211 as specified in the HITRAN database [Rothman et al., 2013]), which are the gases that are present at the greatest concentrations in the troposphere, are 0.88, 0.119 and 4.5×10^{-3} respectively [Conrath and Gautier, 2000, Fletcher et al., 2009]. As in chapters 4 and 5, we did not take collision-induced absorption into account properly in our retrievals, however we show in appendix B that the effect is even more minor for Saturn spectra than it is for Jupiter spectra.

6.3 Fitting Saturn chromophores with laboratory spectra

As in section 4.4, we seek a cloud model that permits conservatively-scattering haze and chromophore to be distinguished, while also allowing vertical aerosol structure to vary as freely as possible without incorporating too many degenerate variables. Once again, this involves two vertical aerosol profiles to be retrieved simultaneously: one of conservatively-scattering non-chromophore particles, whose abundances are retrieved at a set of sample altitudes and then interpolated over the whole reference atmosphere, and another of chromophore particles, whose optical constants are fixed to laboratory values, and whose vertical profile is parametrised as a Gaussian with flexible central altitude and abundance. A full list of variable parameters, together with the pressure grid over which the haze profile is retrieved, is given in table 6.3.1. We also perform our homogeneous layer splitting in such a way so that the number of layers between each pressure value in the haze profile grid is roughly equal, with 39 layers in total as for Jupiter. However, once again we face the issue of a lack of prior knowledge of both particle size distributions r_n and r_c, as well as the real refractive index of the non-chromophore haze particles n_n (this last parameter being even more problematic than on Jupiter, since we do not know the composition of the upper tropospheric haze). Roman et al. [2013] suggest from simple considerations of Stoke's law that, for particles to remain suspended in the upper tropospheric haze for sufficient time, they must have an effective radius of around 1µm at the equator, where the gravity is lowest, with the effective radius increasing with latitude. However, we should also take into consideration a possible contribution to the spectrum from the deeper ammonia cloud layer, where particle sizes are predicted to be even larger (although exact sizes are very difficult to constrain observationally). On the other end of the scale, polar stratospheric haze particles could be as small as 0.1µm [Muñoz et al., 2004, Karkoschka and Tomasko, 2005, Pérez-Hoyos et al., 2005]. Of course, we have even less theoretical and observational constraint when it comes to the values of r_c and n_n. We therefore perform a χ^2/n analysis on the data using the same prior values of r_n, r_c and n_n as for Jupiter. The spectrum we choose for our retrievals is located at 21.47^o planetographic latitude and 9.90^o longitude relative to the sub-observer point, a location that was observed to be relatively depleted in haze but rich in colour.

In Figure 6.3.1a we show the results of the χ^2/n analysis when the chromophore optical constants are fixed to those of the Noy chromophore. A somewhat wide range of values for r_n and n_n give reasonable fits to the data with $\chi^2/n < 2$, provided that $r_c < 0.1\mu m$, although the values for r_n are not within the range one would predict for the upper tropospheric haze at this latitude. When we take the best fits to the observed MUSE spectra as shown in figure 6.3.2, we find very similar discrepancy patterns in spectral fit for all values of r_n, r_c and n_n that give reasonable values of χ^2/n. At wavelengths below 0.55µm, the Noy chromophore fits the MUSE spectrum almost consistently within an error of 1%, but at longer wavelengths the discrepancies are more obvious, and in many ways resemble the fit to the GRS using the Carlson chromophore optical constants as previously shown in section 4.4. Our exponential extrapolation of the Noy optical constants results in both an overestimation in depth of the 0.619µm methane absorption feature and an overestimation of continuum I/F at near-infrared wavelengths. This results in an upper tropospheric haze layer with a deeper retrieved altitude than it would be in reality. Although the very good fit of the Noy chromophore to blue wavelengths shows promise, it is clear that, if we are to assume a phosphorus chromophore with such a high real refractive index as the Noy chromophore, we must retrieve the imaginary refractive index spectrum directly from the MUSE data, and not simply rely on laboratory constants.

When we fix the chromophore optical constants to those of the Carlson chromophore, by contrast, the resulting χ^2/n map looks superficially similar to both that found using the Noy chromophore optical constants, and to that retrieved from the NEB on Jupiter in figure 4.4.2. However, the χ^2/n values themselves are substantially higher; the lowest χ^2/n value we could retrieve using the CR16 optical constants was 2.6, compared with 1.2 using the Noy optical constants. The reason for this is that the shape of the blue-absorption gradient of a Saturn NEB spectrum is different to that of a

Profile	**Variable definition**	**Variable symbol**		**Fixed (F) or variable (V)?**	**Prior values with uncertainties**
Haze	Specific aerosol densities of non-chromophore profile $\tau_n(P)$ (in units of aerosol particles cm^2/gram of atmosphere) as a function of a given pressure grid P (in bars)	$\tau_n(3.95)$	$\tau_n(0.074)$	V	$(1.0 \pm 0.3) \times 10^{-3} \forall P$
		$\tau_n(1.20)$	$\tau_n(0.044)$		
		$\tau_n(0.80)$	$\tau_n(0.027)$		
		$\tau_n(0.50)$	$\tau_n(0.017)$		
		$\tau_n(0.32)$	$\tau_n(0.01)$		
		$\tau_n(0.20)$	$\tau_n(0.004)$		
		$\tau_n(0.12)$	$\tau_n(0.0005)$		
	Correlation length of aerosol profile	$\Lambda_{\tau n}$		F	1.5
	Effective particle radius (μm)	r_n			Found through χ^2/n analysis
	Variance of particle size distribution	σ_n			0.1
	Real refractive index at $\lambda = 0.7\mu m$	n_n			Found through χ^2/n analysis
	Imaginary part of complex refractive index spectrum as a function of wavelength λ	$k_n(\lambda)$			$10^{-9} \forall \lambda$
	Correlation length of refractive index spectrum	Λ_{kn}			0.1
Chromophore	Aerosol density at centre of Gaussian (particles cm^2/g)	τ_c		V	$(1.0 \pm 0.5) \times 10^{-3}$
	Altitude of centre of Gaussian (bars)	P_c			1.0 ± 0.5
	Gaussian FWHM (pressure scale height)	Δ_c		F	1
	Effective particle radius (μm)	r_c			Found through χ^2/n analysis
	Variance of particle size distribution	σ_c			0.1
	Real refractive index at $\lambda = 0.7\mu m$	n_c			2.1 [Noy et al., 1981] or 1.4 [Carlson et al., 2016]
	Imaginary part of complex refractive index spectrum as a function of wavelength λ	$k_c(\lambda)$			Noy et al. [1981] extrapolated exponentially to wavelengths $\lambda > 0.6\mu m$, or Carlson et al. [2016] extrapolated exponentially to wavelengths $\lambda > 0.75\mu m$.
	Correlation length of refractive index spectrum	Λ_{kc}			0.1

Table 6.3.1: Explanation of all the variables used to parametrise the forward model in section 6.3, with prior values and constraints specified when applicable.

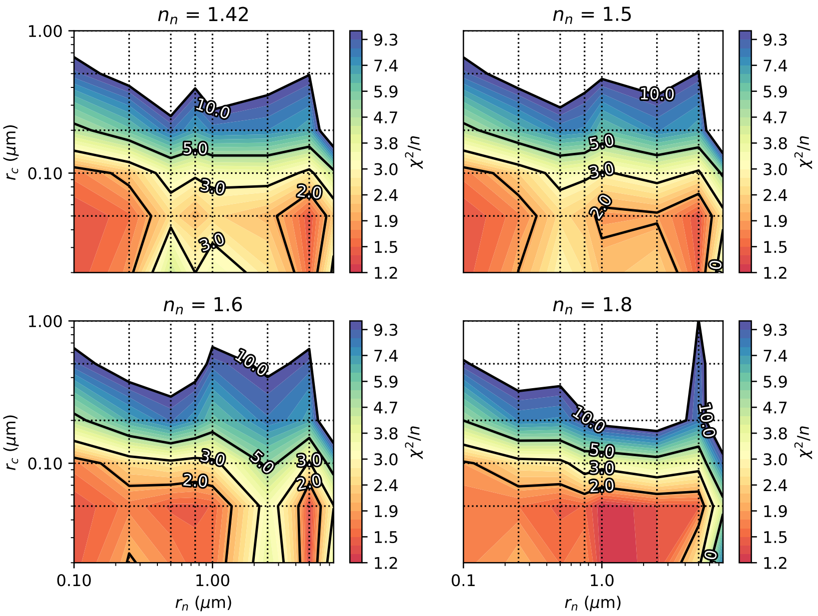

(a) Noy et al. [1981]

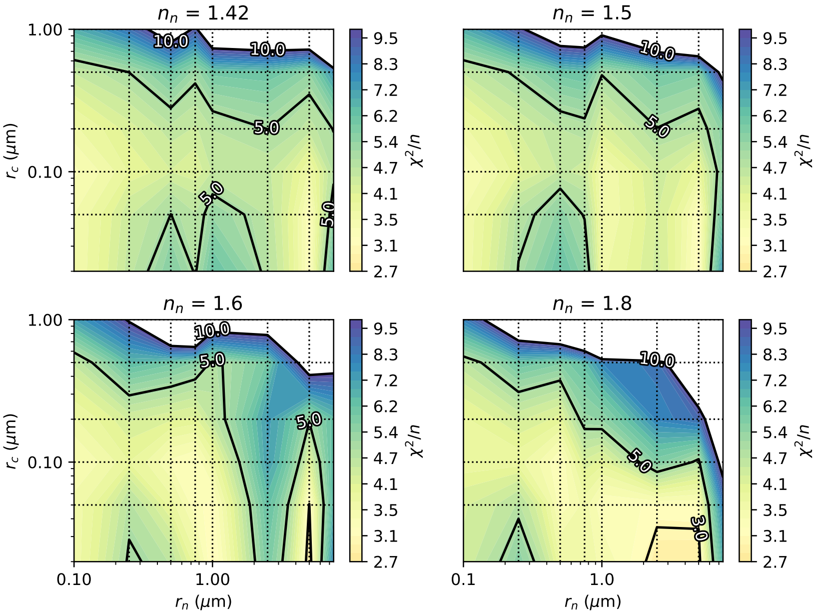

(b) Carlson et al. [2016]

Figure 6.3.1: Results of χ^2/n analysis on a single pixel in Saturn's NEB, when plotted against r_n, r_c and n_n. Image (a) shows the case where the chromophore optical constants are fixed to the Noy chromophore values, while image (b) shows the case where they are fixed to the Carlson chromophore values, extracted exponentially to wavelengths where they are not tabulated as explained in the text. Redder colours show values of r_n, r_c and n_n with the best convergence, with retrievals where $\chi^2/n > 10$ masked in white. Intersections of dashed grid lines show the fixed r_n and r_c values of the retrievals themselves.

Jupiter NEB spectrum: while the shape of a red Jupiter spectrum below 0.6µm can be approximated to first order by an exponential with increasing gradient towards shorter wavelengths, the shape of a corresponding Saturn NEB spectrum within the same wavelength range appears much more linear, with even a slight decrease in gradient towards shorter wavelengths. This could be an indication of the presence of a bathochrome in Saturnian chromophore that is absent in Jovian chromophore. Indeed, disc-averaged observations of Jupiter and Saturn in the near-UV by eg. Karkoschka [1994, 1998] show that the central absorption feature in Saturn spectra is around 0.38µm, while in Jupiter spectra it is closer to 0.32µm, depending on whether one is looking at a zone or a belt.

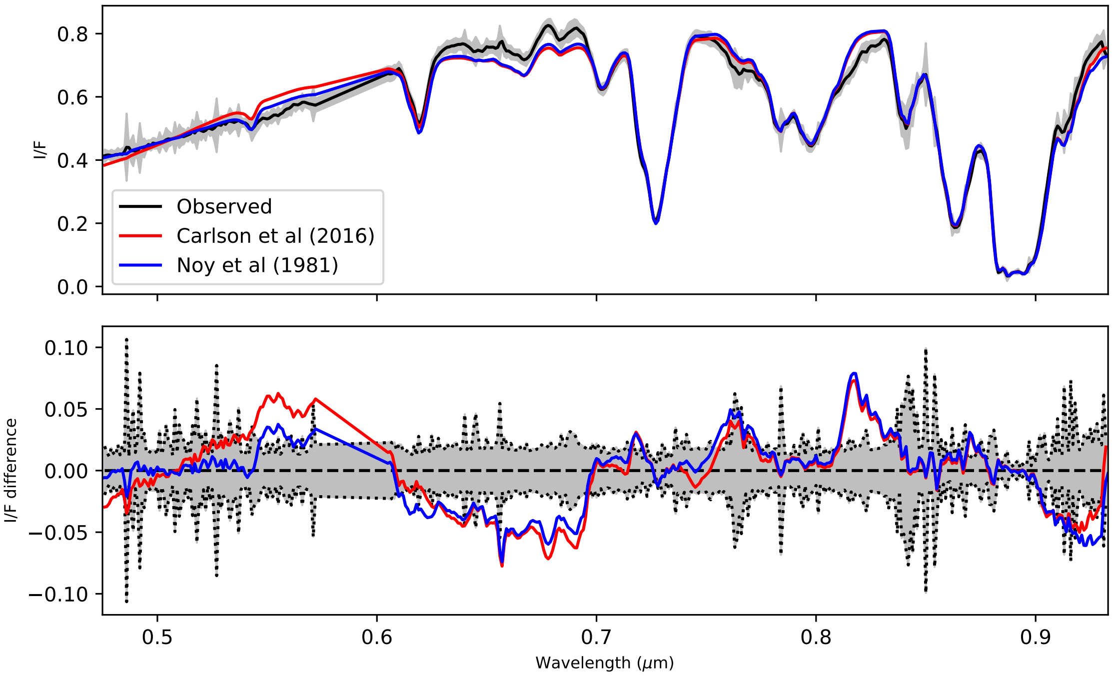

Figure 6.3.2: Fit to observed NEB spectrum of Saturn, where the complex refractive index spectrum is fixed to two different values as shown in the legend. Plot on the bottom shows the difference between the fit and the observed spectra (fit-observed). In both cases, $r_n = 5.0\mu m$, $r_c = 0.02\mu m$ and $n_n = 1.6$.

6.4 Direct chromophore retrieval using limb darkening analysis

As we did in section 4.6 for Jupiter, we now attempt to retrieve a chromophore imaginary refractive index spectrum directly by performing limb darkening analysis on a single latitude swath of Saturn, taking into account variations in particle size and real refractive index through χ^2/n analysis. This is more challenging for Saturn than it is for Jupiter, as individual latitudinal bands are narrower and less distinct, making it more difficult to find a band that can be treated as completely homogeneous across its entire latitude and longitude range. For our analysis, we chose a swath between 19^{o}N and 24^{o}N (planetographic), where the haze was seen to be thinnest and where the colour reddest, and which we sampled at each wavelength at 35 degree longitude intervals (within a longitude range of -35 to +70 degrees of the sub-observer longitude, in order to avoid mixing with the sky close to the outer perimeter of Saturn's planetary disc; the geometry at -70 degrees had to be discarded as its I/F values appeared to be anomalously high across all wavelengths), with each sample obtained by computing a Gaussian weighted average of all spectra within a FWHM of 3 degrees of longitude. The respective spectral errors were then found through the corresponding standard deviation of the Gaussian weighted average. However, since the latitude swath has a narrow pixel width, this value is much smaller than it would be for a Jupiter swath, even though the spectral uncertainties on the Saturn swath are likely to be proportionally much larger due to the difficulty of selecting a swath that is completely homogeneous. The spectral errors are therefore underestimated using this method, and this is reflected in even the best χ^2/n values we retrieve in our analysis. As with Jupiter, we discard 'rank 4' wavelengths from our reduced wavelength scheme in our analysis, as well as all wavelengths between 0.573µm and 0.604µm taken up by the laser guide star. This results in a total of 184 wavelengths per geometry to be retrieved, over four geometries in total.

Again, we retrieve the chromophore imaginary refractive index spectrum directly, in the first case using the Noy optical constants as a prior ($n_c = 2.1$), and in the second using the CR16 optical constants as a prior ($n_c = 1.4$). We also increase both the vertical resolution and the vertical range over which we retrieve the non-chromophore aerosol profile in order to account for the increased precision and accuracy of limb darkening retrievals relative to retrievals at a single point geometry. A table of all the fixed and free parameters is given in table 6.4.1. Unlike with Jupiter, we do not just increase the resolution at altitudes above MUSE peak sensitivity (to take into account the larger optical path at high viewing zenith angles), but also at altitudes below MUSE peak sensitivity, in order to confirm that an ammonia cloud layer is not needed to fit the MUSE data, in spite of its frequent inclusion in cloud models using observations at this wavelength range (eg. Ortiz et al. [1996], Acarreta and Sánchez-Lavega [1999], Muñoz et al. [2004], Roman et al. [2013]). In addition, we retrieve our imaginary refractive index spectrum at 0.1µm intervals between 0.45µm and 0.95µm, as the previous grid between 0.4µm and 1.0µm was seen to produce edge effects in the retrieved imaginary refractive index spectra that fit point retrievals poorly. The resulting χ^2/n map is shown in figure 6.4.2. As expected, we retrieve best-fit values of r_n that are somewhat larger than on Jupiter, presumably due to the lower gravity on Saturn that allows for larger particles to be present

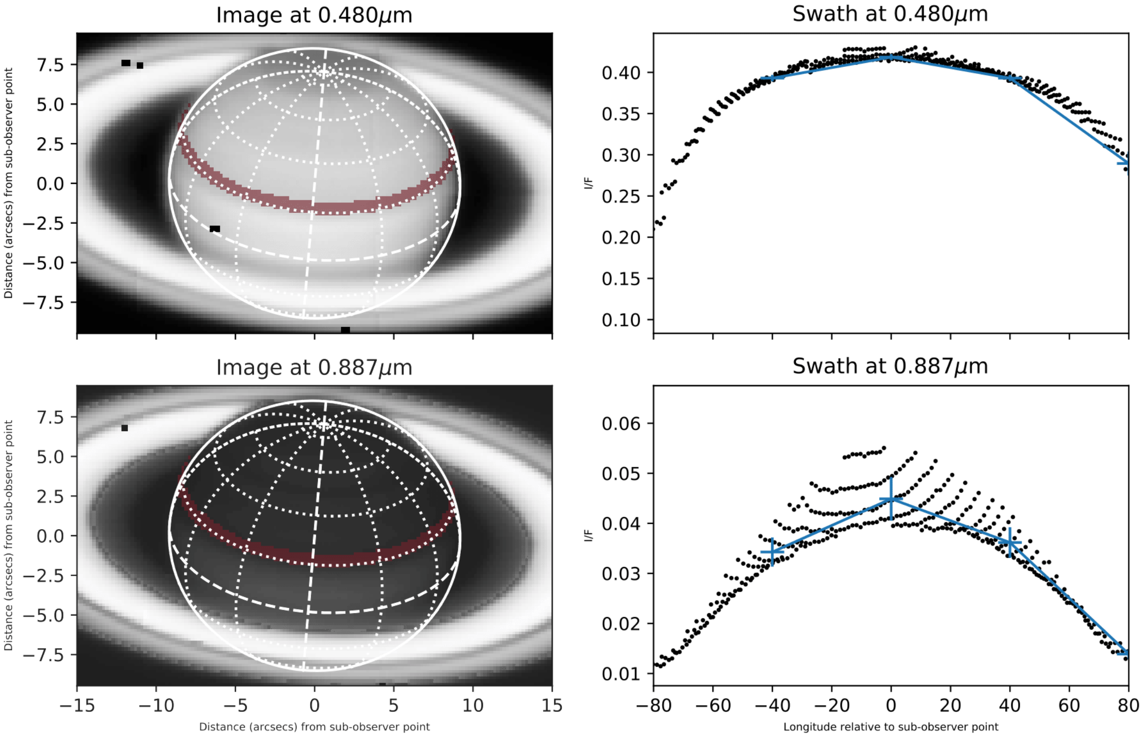

Figure 6.4.1: Plots showing the extraction of a limb darkening spectrum from Saturn MUSE data. Plots on the left show the MUSE spectral image at two sample wavelengths: the top at a wavelength sensitive to chromophore, and the bottom at a wavelength sensitive to high-altitude haze (mostly in the lower stratosphere). At this time, we are observing Saturn close to northern solstice and at solar opposition, with the sub-observer point located at 31.3 degrees north (planetographic). Dashed white lines show the equator and the sub-observer longitude, dotted lines show lines of planetographic latitude (in increments of 20 degrees, although lines south of the equator are in practice obscured by Saturn's rings) and lines of longitude relative to the sub-observer point (in increments of 30 degrees). The thick outer white line shows the calculated perimeter of Saturn's planetary disc (excluding the rings) using ellipsoid limb fitting as described in section 2.4.2. The latitudinal swath extracted from the data is shown in red, bounded by 19 and 24 degrees north (planetographic) on each side. Plots on the right show, for the same two wavelengths, all the I/F values at each spatial pixel contained within the swath in black, as a function of longitude. Points in blue then show the averaged latitudinal swath, sampled at 35 degree intervals (with the average at -70 degrees discarded as explained in the text), used for limb darkening analysis, with vertical bars showing the spectral error associated with those points. We have increased the overall brightness of the bottom-left image and decreased the relative brightness of the rings in order to bring out the contrast in 0.89μm brightness with respect to latitude that would otherwise not be visible in the print version of this thesis; we note in particular the increased brightness in the region bounded by the equator and our selected swath due to stratospheric haze cover. In reality, the rings far outshine Saturn at these wavelengths, particularly close to solar opposition when the rings brighten due to the Seeliger effect.

at higher altitudes than on Jupiter. For lower values of n_n, we retrieve best-fit values of r_n around 2.5μm, which is in line with the particle effective radii of upper tropospheric haze particles given microphysical constraints as estimated by Roman et al. [2013]. However, as with Jupiter, we are still unable to completely constrain r_c and n_n using this method, although our results do suggest that the chromophore particles cannot have an effective radius much larger than $0.1\mu m$ if we were to assume $n_c = 2.1$, and microphysical constraints suggest that the sizes of r_n we would need to model the limb darkening spectra when $n_n = 1.8$ are too small given where we retrieve the altitude of maximum haze opacity. We retrieve similar χ^2/n maps in both the $n_c = 2.1$ and $n_c = 1.4$ cases, albeit with larger r_c values permitted in the latter case, and for a given set of n_n, r_n and r_c the two prior solutions result in almost identical haze and chromophore profiles. MUSE spectra on their own are therefore insufficient to discriminate between an organic and a phosphorus chromophore.

In the Noy case, our χ^2/n analysis leaves us with 17 solutions that provide a reasonable fit to the limb darkening spectrum (approximately where $\chi^2/n < 1.61$). While this is half the number of solutions that could reasonably fit the equivalent Jupiter limb-darkening spectrum as previously discussed in section 4.6, it will be much more difficult to select one representative 'best' solution as the degree of spatial variation in blue-absorption is less than on Jupiter (even if the shape of the blue-absorption gradient does vary, as we will show in section 6.5). One alternative method is to use basic microphysical constraints to filter out unphysical solutions. From HST and Cassini/ISS observations made just after the last southern summer solstice, both Karkoschka and Tomasko [2005] and Roman et al. [2013] retrieved particle sizes around 1μm in the EZ which then increased twofold as one moved away from the EZ. This was shown by Roman et al. [2013] to be a consequence of lower gravity at the equator and hence slower sedimentation times. One gauge of the quality of the limb darkening solution would therefore be to observe if a high quality of fit is possible, given the same imaginary refractive index spectrum as well as r_c and n_n, using a value of $r_n = 2.5\mu m$ in the NEB but using a value of $r_n \approx 1\mu m$ in the EZ. This would, of course, mean discarding any of the solutions where $r_n \neq 2.5\mu m$, which may be an unfair assumption given that the model of Roman et al. [2013] did not take into account several factors that would have affected particle sedimentation rates such as coagulation or non-spherical particle shapes. In addition, there is some uncertainty with respect to the timescales of visible changes in the upper tropospheric haze, usually anything from months to years for given latitudinal regions [Pérez-Hoyos et al., 2005], which would also affect how long a haze particle of a given size would stay in the troposphere. Nonetheless, for the sake of simplifying our model, we will take this assumption of $r_n = 2.5\mu m$ in the NEB as given.

Of the 17 best solutions from the limb darkening χ^2/n analysis, a total of six solutions had a

Profile	**Variable definition**	**Variable symbol**		**Fixed (F) or variable (V)?**	**Prior values with uncertainties**
Haze	Specific aerosol densities of non-chromophore profile $\tau_n(P)$ (in units of aerosol particles cm^2/gram of atmosphere) as a function of a given pressure grid P (in bars)	$\tau_n(3.95)$	$\tau_n(0.12)$	V	$(1.0 \pm 0.1) \times 10^{-3} \forall P$
		$\tau_n(2.00)$	$\tau_n(0.074)$		
		$\tau_n(1.20)$	$\tau_n(0.044)$		
		$\tau_n(0.80)$	$\tau_n(0.027)$		
		$\tau_n(0.63)$	$\tau_n(0.017)$		
		$\tau_n(0.50)$	$\tau_n(0.01)$		
		$\tau_n(0.38)$	$\tau_n(0.006)$		
		$\tau_n(0.32)$	$\tau_n(0.004)$		
		$\tau_n(0.25)$	$\tau_n(0.0015)$		
		$\tau_n(0.20)$	$\tau_n(0.0005)$		
		$\tau_n(0.15)$			
	Correlation length of aerosol profile	$\Lambda_{\tau n}$		F	1.5
	Effective particle radius (µm)	r_n			Found through χ^2/n analysis
	Variance of particle size distribution	σ_n			0.1
	Real refractive index at $\lambda = 0.7\mu m$	n_n			Found through χ^2/n analysis
	Imaginary part of complex refractive index spectrum as a function of wavelength λ	$k_n(\lambda)$			$10^{-9} \forall \lambda$
	Correlation length of refractive index spectrum	Λ_{kn}			0.1
Chromophore	Aerosol density at centre of Gaussian (particles cm^2/g)	τ_c		V	$(1.0 \pm 0.2) \times 10^{-3}$
	Altitude of centre of Gaussian (bars)	P_c			1.0 ± 0.2
	Gaussian FWHM (pressure scale height)	Δ_c		F	1
	Effective particle radius (µm)	r_c			Found through χ^2/n analysis
	Variance of particle size distribution	σ_c			0.1
	Real refractive index at $\lambda = 0.7\mu m$	n_c			2.1
	Imaginary part of complex refractive index spectrum as a function of wavelength λ	$k_c(\lambda)$		V	Noy et al. [1981] extrapolated exponentially to wavelengths $\lambda > 0.6\mu m$. Prior uncertainties of 10%.
	Correlation length of refractive index spectrum	Λ_{kc}		F	0.1

Table 6.4.1: Explanation of variables used to parametrise forward model in section 6.4, with prior values and constraints specified when applicable.

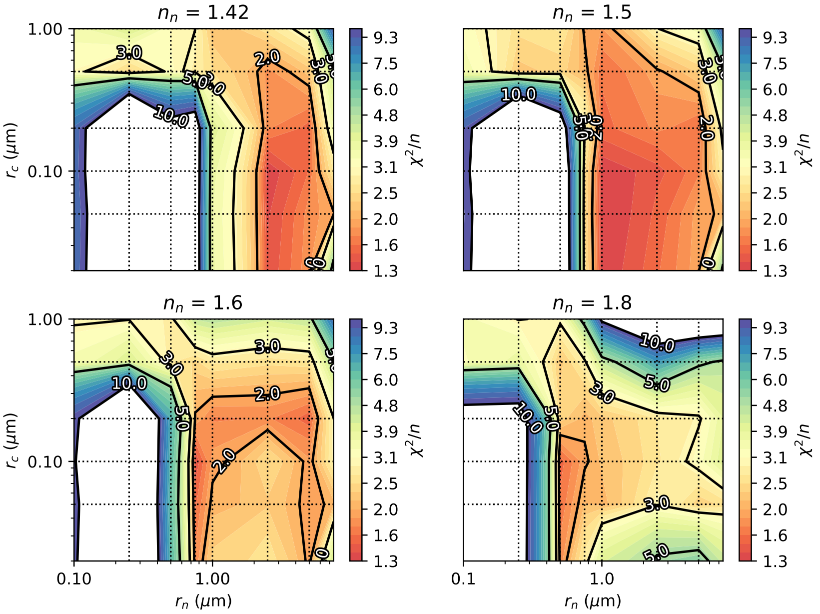

(a) Noy et al. [1981]

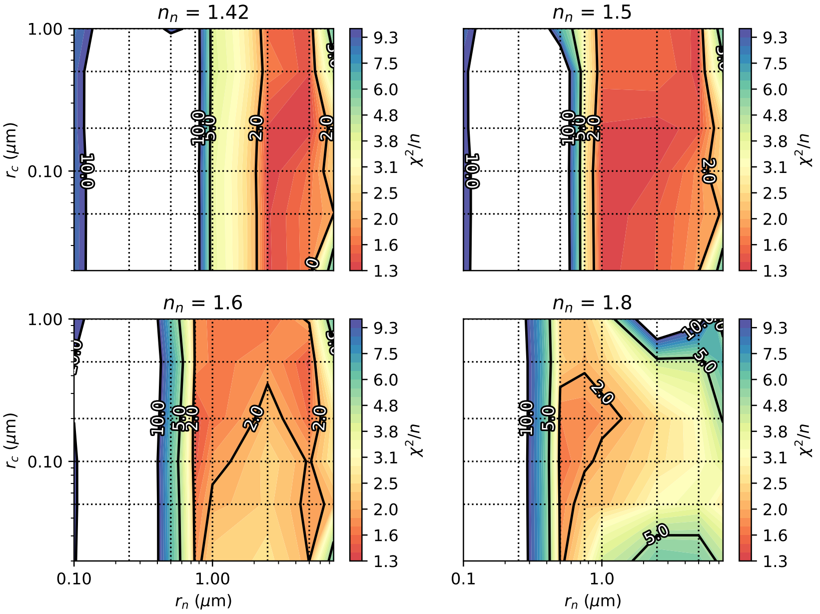

(b) Carlson et al. [2016]

Figure 6.4.2: Results of χ^2/n analysis applied to a limb-darkening spectrum of the NEB, where the complex refractive index spectrum is allowed to vary from a prior spectrum (equal to the optical constants of Noy et al. [1981] in case (a) and Carlson et al. [2016] in case (b). In effect, the two plots show the difference in convergence between (a) a chromophore of real refractive index $n_c = 2.1$ and (b) one of $n_c = 1.4$. Retrievals where $\chi^2/n > 10$ have been masked in white.

n_c	n_n	r_n (retrieved, µm)	r_c (µm)	χ^2/n	Level of peak haze density (bars)	Peak haze mass density (g/l)	Level of peak chromophore density (bars)	Peak chromophore mass density (g/l)
2.1 [Noy et al., 1981]	**1.42**	**0.93**	**0.02**	**0.66**	**0.35**	**3.44E-07**	**0.18**	**1.93E-09**
		1.80	0.05	1.08	0.31	4.46E-07	0.31	3.08E-09
		1.87	0.1	0.78	0.31	3.79E-07	0.31	1.76E-09
	1.5	1.17	0.02	0.79	0.40	2.15E-07	0.45	4.59E-09
		1.18	0.05	0.71	0.40	1.91E-07	0.40	3.73E-09
		1.24	0.1	0.66	0.40	1.48E-07	0.58	2.79E-09
1.4 [Carlson et al., 2016]	1.42	1.50	0.02	1.19	0.35	4.52E-07	0.31	9.62E-09
		1.80	0.05	0.97	0.31	4.86E-07	0.27	1.03E-08
		1.71	0.1	0.94	0.31	3.79E-07	0.27	8.71E-09
		1.82	0.2	0.85	0.31	3.56E-07	0.31	7.03E-09
	1.5	1.29	0.1	0.75	0.35	1.70E-07	0.45	1.27E-08
		1.32	0.2	0.72	0.35	1.44E-07	0.51	9.56E-09

Table 6.4.2: Retrieved cloud and chromophore mass density values when chromophore optical constants obtained in NEB limb darkening analysis (for a given r_n, r_c and n_n) are used to fit the EZ (lat, lon = 5.86^o, 25.55^o), in each case letting the value of r_n vary from a prior value of 1µm. In this table we have excluded solutions obtained from NEB limb darkening analysis where $r_n < 1\mu m$ or $r_n > 2.5\mu m$. The set of r_n, r_c and n_n values that will be selected for all subsequent Saturn retrievals is highlighted in bold.

value of $r_n = 2.5\mu m$. We then applied these six chromophore imaginary refractive index solutions to a point spectrum of the EZ, in one case keeping the value of r_n the same, and in the other allowing the value of r_n to vary from a prior value of $(1.0 \pm 0.1)\mu m$. All these solutions were seen to have very similar fits to point retrievals of the NEB. In two cases ($n_n = 1.42$, $r_c = 0.05\mu m$ and $n_n = 1.42$, $r_c = 0.1\mu m$), the EZ retrieval attempted to raise the value of r_n back towards 2µm. These two solutions were therefore discarded. In another ($n_n = 1.5$, $r_c = 0.1\mu m$), the altitude of peak chromophore opacity was retrieved almost half a pressure scale height below the altitude of peak haze opacity, which seems unlikely to be physical given that the upper tropospheric haze is almost completely opaque in the MUSE wavelength range. Of the remaining three solutions, the only one where a substantially better fit to continuum near-infrared wavelengths was seen in the $r_n = 1\mu m$ case compared to the $r_n = 2.5\mu m$ case was the one where $n_n = 1.4$ and $r_c = 0.02\mu m$ (although we note that in all cases the imaginary refractive index spectra failed to model the shortest wavelengths of the EZ spectra correctly). This is important, since we explained in previous chapters that the retrieval of particle size from MUSE spectra is somewhat unreliable, and so if we are to allow r_n to vary for a retrieval of a meridional swath of Saturn, we must be sure that physical particle sizes give better solutions than non-physical particle sizes. By contrast, we were unable to obtain a similar solution from limb darkening analysis using the Carlson chromophore as a prior.

In all cases, our retrievals indicate a chromophore that is located either within or just above the upper tropospheric haze, akin to the *Crème Brûlée* model for Jupiter described in section 4.3. With such small chromophore particle sizes retrieved, it is unlikely that they would be a result of chromophore sedimenting down from the stratosphere. Instead, the chromophore is most likely created in situ in the tropospheric haze, perhaps through the reaction of organic haze particles with a phosphorus compound that results in a very thin coating of chromophore around the haze particles. It seems unlikely that Saturnian chromophore would be formed as a result of the reaction mechanism detailed by Guillemin et al. [2001], since ethene is present at even lower abundances at these altitudes than acetylene is [Moses et al., 2000, Moses and Greathouse, 2005], but it is possible that a similar chromophore reaction mechanism could occur with ethene substituted by a different unsaturated organic compound present in the haze. Spectral constraints place the amount of phosphine at these altitudes at the order of a few parts per million (eg. Noll and Larson [1991], Fletcher et al. [2007]), which is approximately two orders of magnitude greater than the amounts of chromophore we retrieve. This would make the prospect of a phosphorus-based chromophore seem plausible, although more definite constraints are not currently possible due to the lack of reaction rate data for phosphine photolysis [White et al., 2016]. A chromophore more similar to the Carlson chromophore (that is, with $n_c = 1.4$), which we assume as a proxy for a chromophore in which phosphine photochemistry does not play a major role, would require abundances larger than that of the Noy-based chromophore ($n_c = 2.1$) by a factor of 10, and so an $n_c = 1.4$ chromophore would require the presence of much greater abundances of ammonia in the upper troposphere than an $n_c = 2.1$ chromophore. Given the scarcity of ammonia at these altitudes, we would either have to favour an $n_c = 2.1$ chromophore, or assume that a Carlson-type chromophore is convected upwards from below the tropospheric haze. We will assume the former in the rest of this chapter.

The resulting 'best' chromophore imaginary refractive index spectrum is shown in figure 6.4.3. Just as when we retrieved Jovian chromophore from a Carlson chromophore prior, we find that we need a steeper blue-absorption slope to fit Saturn spectra than the Noy chromophore can provide. We also require a secondary absorption peak around 0.85µm (even if we properly take CIA into account, as we show in appendix B), although this could be due to poor methane band data.

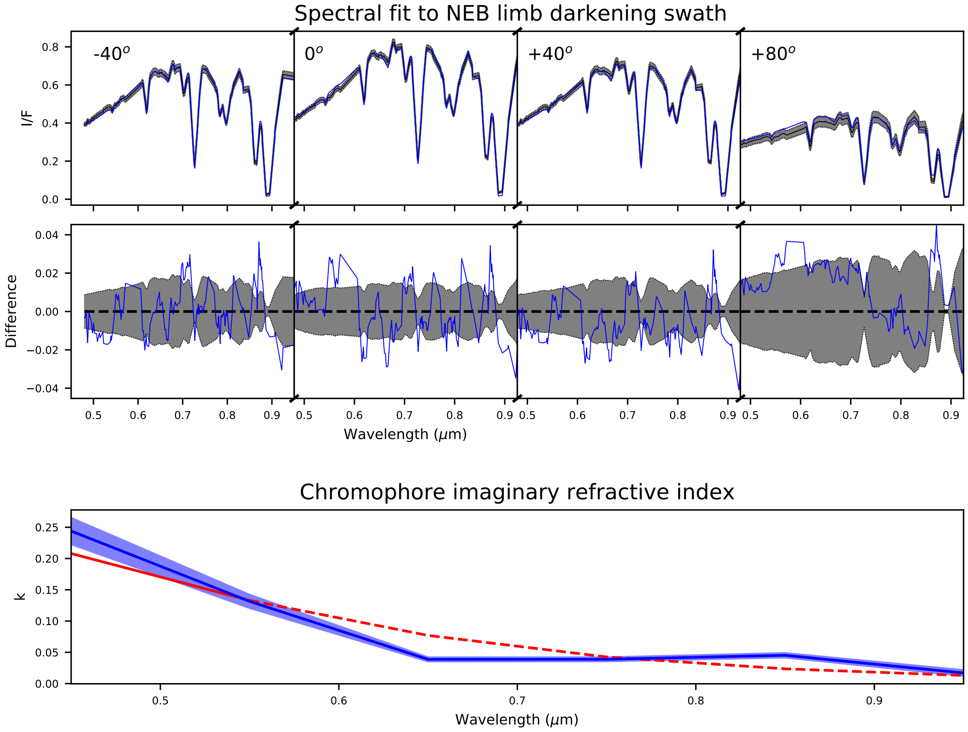

Figure 6.4.3: Results of the NEB limb darkening retrieval for which chromophore optical constants were seen to provide a good fit, and for which a physical haze and chromophore profile was found to be possible in the EZ. For this fit, $n_n = 1.42$, $n_c = 2.1$, $r_n = 2.5\mu m$ and $r_c = 0.02\mu m$. Top two rows show the spectral fit (in blue) to the observed MUSE spectrum (in black, with error bounds shaded in grey) at four different angular geometries (with the longitudes relative to the sub-observer point marked on the plot), with the middle plot showing the difference in I/F between the fit and observed spectrum. Bottom plot shows the retrieved chromophore imaginary refractive index spectrum (in blue, with error bounds shaded) compared to the imaginary refractive index of the Noy chromophore (in red, with dashed line indicating extrapolation from the Noy et al. [1981] values).

6.5 General variations in chromophore and haze structure

We now apply our chromophore optical constant solution to a single individual meridional swath extracted from each of our three Saturn MUSE data cubes, to observe how haze structure and chromophore abundances vary over latitude, according to our model, and to see if we can discern any temporal variation between 2014 and 2017. As we do not expect major temporal variation to occur in the three months that elapsed between the obtention of the two 2017 datasets, we will assume that any observed differences between the two 2017 retrievals are either to do with longitudinal variations or deficiencies in the model. The AO dataset from June 2017 was obtained close to opposition, which would cause the rings to appear exceptionally bright compared to the non-AO dataset from April 2017 due to the Seeliger effect, but this should not have any impact on observations of Saturn's atmosphere. A key to the zone-belt nomenclature is provided in figure 6.1.1.

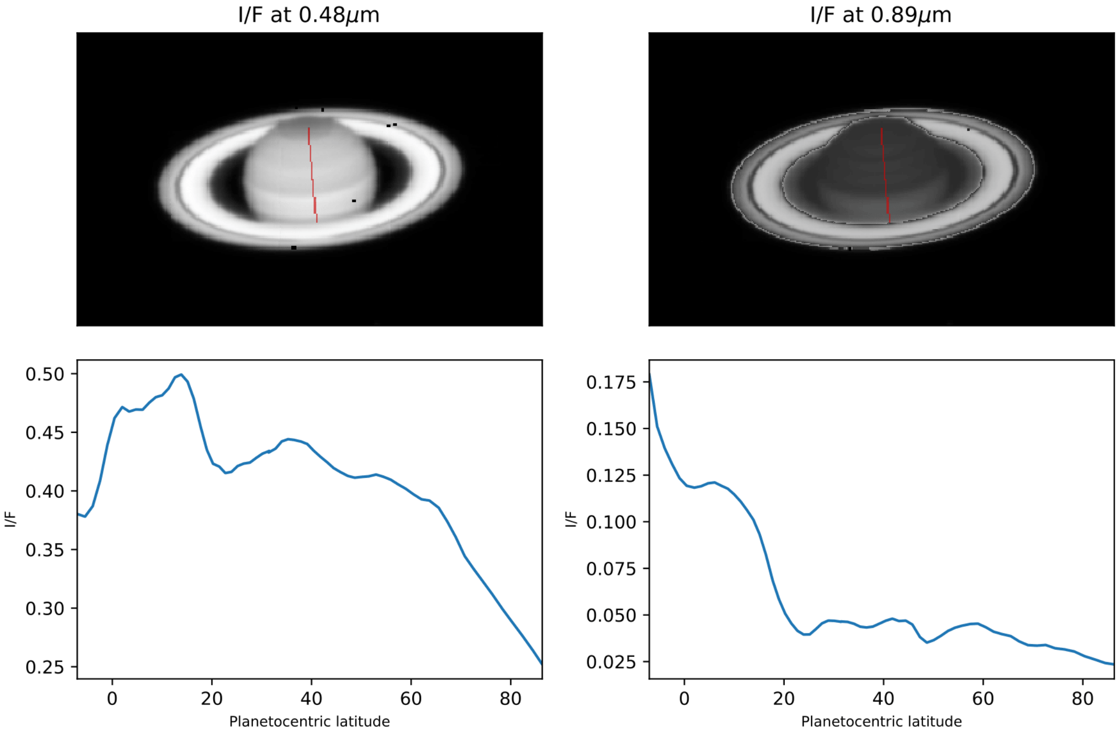

Figure 6.5.1: Top row: Images of a meridional swath, at 0.48µm and 0.89µm, extracted from MUSE dataset 2017-06-18T06:04:09.111, shown as a red diagonal line through the middle of Saturn, avoiding Saturn's rings where possible. The bottom row shows how the reflectivity at the same two wavelengths changes along the swath, as a function of latitude. This observation was obtained when Saturn was at opposition, resulting in the rings appearing unusually bright due to the Seeliger effect. We have therefore lowered the brightness of the rings and increased the brightness of Saturn itself in the top-right image (hence the artefacts around the edges of the rings) in order to make the latitudinal structure clearer.

In our swaths we excluded any latitudes that were either completely obscured by Saturn's thick A and B rings or where the contribution of the A and B rings to the spectra was obvious enough to make them scientifically useless to discern local haze structure. However, we included Saturn's ring shadow for reference, despite it often being partly obscured by the thin inner C ring. As in the previous section, we fixed r_c to 0.02µm but we set r_n to vary from a prior of 2.0µm. The remaining state vector variables were parametrised according to table 6.3.1. Although we included ammonia gas absorption k-tables in our model, we did not allow the ammonia gas profile to vary in any way, as we found very little sensitivity to haze-top ammonia abundances in preliminary retrievals. We provide a more qualitative analysis of ammonia variations in section 6.7.

When we compare the spectral fits of our chromophore to different latitudinal regions of Saturn in figure 6.5.2, we generally find that the further one moves away from the NEB and the mid-latitudes, the less the shape of the observed Saturn spectrum below 0.55µm resembles that of the chromophore spectrum we retrieved in section 6.4. While at the poles and the equator, the spectral slope increases with decreasing wavelength below 0.6µm, at the NEB we observe the opposite, perhaps indicating a central wavelength of the chromophore absorption feature only just outside the MUSE wavelength range. Such a dramatic change in shape of the blue-absorption feature between the NEB and elsewhere is difficult to model using a single 'universal' chromophore absorption spectrum as we have done in this work. Like on Jupiter, we also see substantial variability in the shape of the spectrum between approximately 0.51µm and 0.54µm. We suggest that Saturnian spectra are in fact influenced by two different chromophore compounds: one formed in the high-altitude haze layers themselves, which most closely resembles the chromophore we retrieved in section 6.4, and one formed deeper in Saturn's atmosphere, which more closely resembles Jovian chromophore. In regions of high upwelling, such as the EZ, chromophore formed at deeper layers could be convected to higher altitudes where it can be seen above Saturn's thick haze layers. Conversely, at the poles, the tropospheric haze could be thin enough that deeper chromophore colour becomes visible. In addition, the polar haze layers are likely to be more dominated by aromatic hydrocarbons than the haze layers at lower latitudes [Kim et al., 2019], which would also inevitably alter the chromophore absorption spectrum. The NEB may occupy a 'sweet spot' where the tropospheric haze is thick enough to obscure deeper structure, but where upwelling is not sufficient for deep tropospheric components to be advected to visible altitudes. Such a hypothesis may also require that the so-called 'deep chromophore' is formed deeper in Saturn's atmosphere than it would be on Jupiter, where we mostly retrieve it above the main visible cloud layer. This is not an unreasonable assumption given Saturn's lower temperatures and hence deeper cloud levels. Our results could, however, be explained by alternative hypotheses: perhaps a unique chromophore formation process is present in the NEB and in mid-latitudes that is absent in the rest of Saturn, or perhaps there is indeed a universal Saturnian chromophore, but there is some alternative scattering process that modulates the NEB spectrum which we have not accounted for in our model, as we suggested for Jupiter. We suggest further study of limb darkening in other latitudinal bands (particularly the EZ), as well as the extension of our analysis to shorter wavelengths, for future work, in order to completely rule out the possibility of a universal Saturnian chromophore.

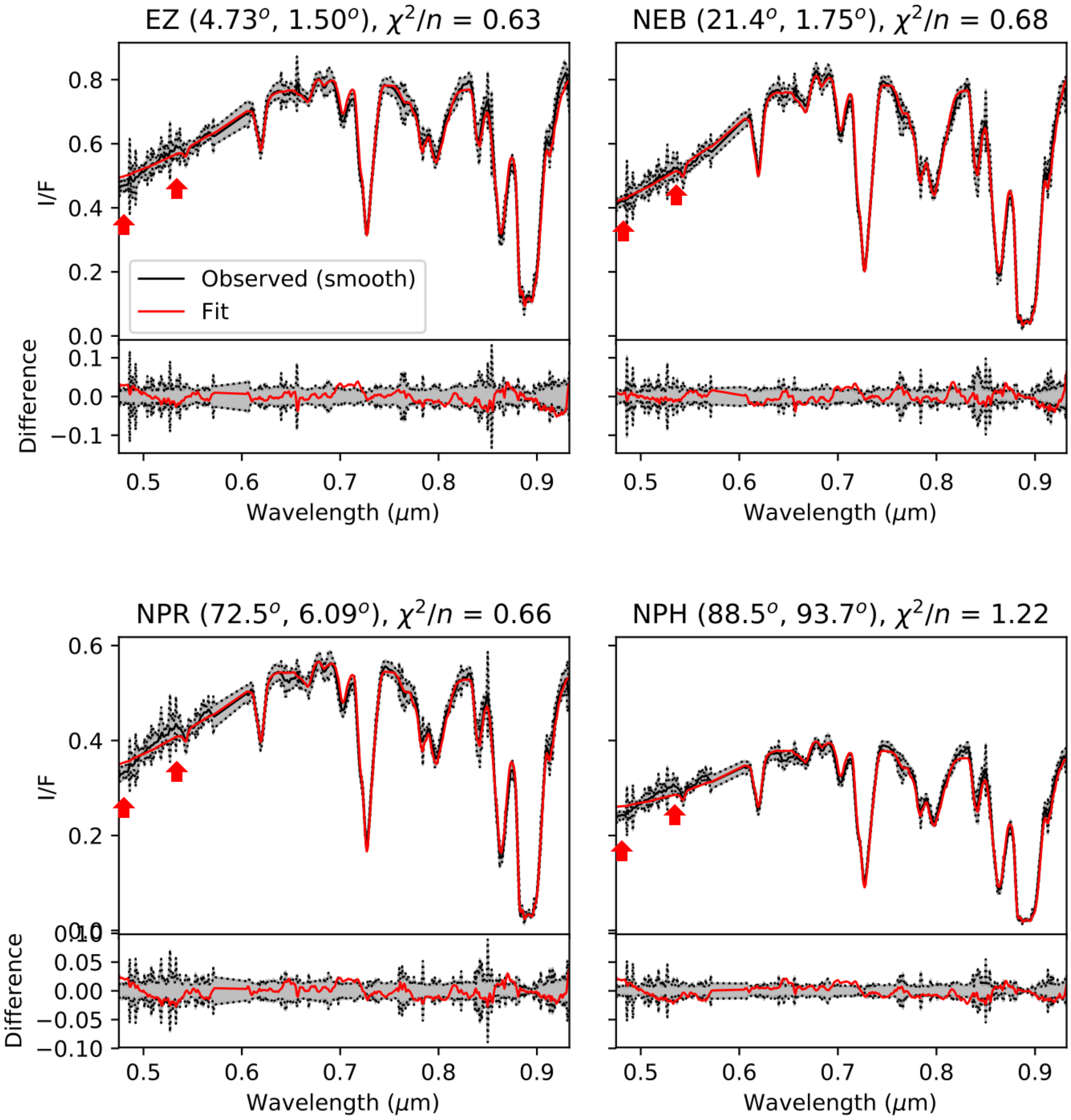

Figure 6.5.2: Fits (in red) to representative MUSE spectra (in black, with spectral uncertainty bounds shaded in grey and bounded by grey dotted lines) along a single north-south swath obtained from Saturn MUSE dataset 2017-06-18T06:04:09.111, using the chromophore refractive index spectrum retrieved in section 6.4 and displayed in figure 6.4.3. For each of the spectra, we give the locations on the surface of Saturn in terms of planetographic latitude and east longitude relative to the sub-observer, as well as the retrieved χ^2/n value which quantifies the quality of fit in each case. Red arrows highlight regions where the fit is most noticeably deficient in each case.

Outside the ring shadow, where haze retrievals may be affected by Saturn's translucent C ring, we consistently observe the stratospheric haze layer to be highest and thickest in the EZ as expected, where it is located around 0.03 bars. We retrieve the stratospheric haze in the EZ as being detached from the underlying tropospheric haze layer by a layer of low haze opacity around the tropopause.

This is in agreement with previous studies of Saturn's haze structure, most definitively by Stam et al. [2001]. We also retrieve elevated haze in the NTZ and the NNTZ; it is possible that the haze layers in both of these regions extend well above the tropopause level, but we are not able to resolve them as being detached from the deeper tropospheric haze like in the EZ. Unlike on Jupiter, we retrieve some substantial variation in the altitude of the tropospheric haze layer, peaking at around 0.3 bars in the southern EZ and then moving down to around 0.5-0.6 bars in the northern EZ and southern NEB. This also corresponds somewhat to past studies of Saturnian cloud structure in the southern hemisphere (eg. Pérez-Hoyos et al. [2005], Roman et al. [2013]). In those studies, however, the decrease in altitude is more gradual with southern latitude, whereas we retrieve a more dramatic decrease between around 10-20 degrees northern latitude. Curiously, this was also found in the northern hemisphere by Karkoschka and Tomasko [2005], and was observed to be relatively invariant over season. This is perhaps indicative of an intrinsic hemispheric asymmetry in haze structure on Saturn. From our retrievals it would appear that the region of thick haze in the northern EZ is a region of substantial upward convection, akin to the NTBs region on Jupiter as previously discussed, which for some reason is absent in the southern hemisphere. Contrary to past studies, we also observe a gradual increase in the altitude of the tropospheric haze as one moves northward from the NEB. This cannot purely be an effect of changes in the optical path with latitude, as otherwise we would observe a similar and even more dramatic effect in our retrievals of Jupiter, which we do not. As expected, we find no evidence of being able to detect variations in tropospheric cloud structure deeper than 1 bar, even in regions where the fractional error in retrieved aerosol abundance around 1 bar (particularly in the NEB and NTB) is comparable to uncertainties in higher-altitude haze retrievals in the EZ.

Temporal changes in haze structure between 2014 and 2017 are very difficult to discern from the data, partly due to the often imperfect fits to the spectra in regions where visual changes were greatest (most notably around the poles), by the unreliable retrieval of particle size (particularly in the NTB), and by clear systematic offsets in chromophore density and altitude from observation to observation due to imperfect calibration. We observe some signs of an increase in tropospheric haze in the southern EZ close to the ring-shadow region, but this may be more due to a lack of spatial resolution in the 2014 data than a real effect. On the other hand, the apparent increase in haze around the NPH is more likely to be a real phenomenon, as we would expect a build-up of haze around the poles during the summer solstice as it heats up [Edgington et al., 2012]. Seasonal changes in chromophore abundance are equally difficult to determine, especially away from the NEB where the spectral fit at blue wavelengths deteriorates, although we note that latitudes of high chromophore usually correlate with latitudes of high haze cover (which is generally the opposite of what we observe on Jupiter). The dramatic decrease in chromophore opacity and altitude over the northern EZ after 2014 is also curious and difficult to explain given the observations. We find some evidence in our retrievals of a change in colour between 2014 and 2017, as could be seen in contemporaneous amateur observations (figure 6.1.1), but this appears to manifest itself in our retrievals as an increase in the *altitude* of the chromophore rather than its density. It is therefore clear that a thorough analysis of temporal changes in Saturn's colour and haze structure will require better modelling of latitudinal changes in the chromophore absorption spectrum that perhaps takes into account more than one chromophore.

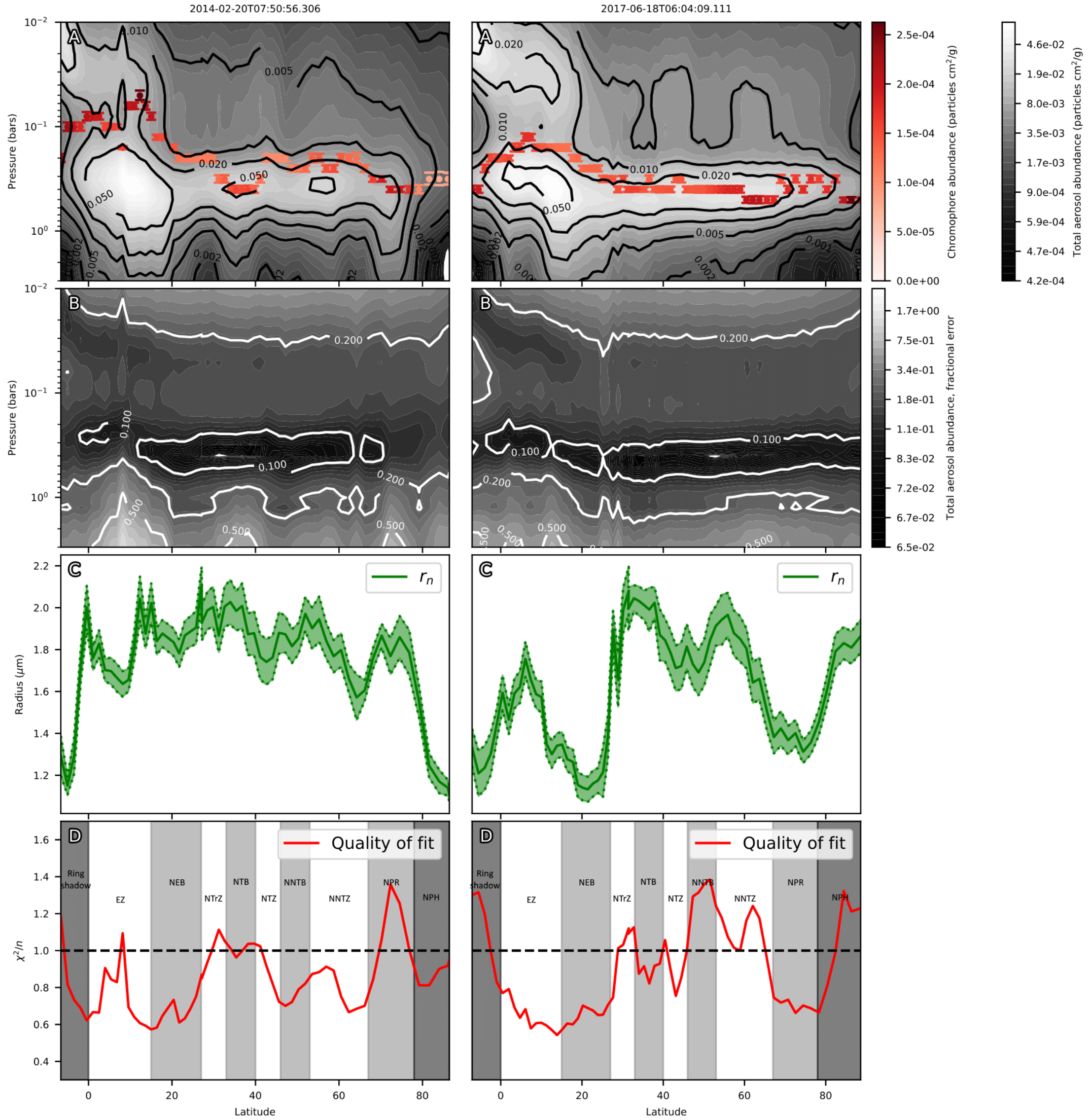

Figure 6.5.3: Results of the retrievals of a single north-south swath from (left) 2014-02-20T07:50:56.306 and (right) 2017-06-18T06:04:09.111, analysing general changes between 2014 and 2017. (A): Combined haze and chromophore abundance profile, with fractional error shown in (B). (C): Retrieved effective radius r_n of non-chromophore particles. (D): χ^2/n, with rough boundaries of zone and belt regions marked (although fine zone-belt structure between NNTZ and NPR is included as part of the NNTZ). Latitude values are planetographic.

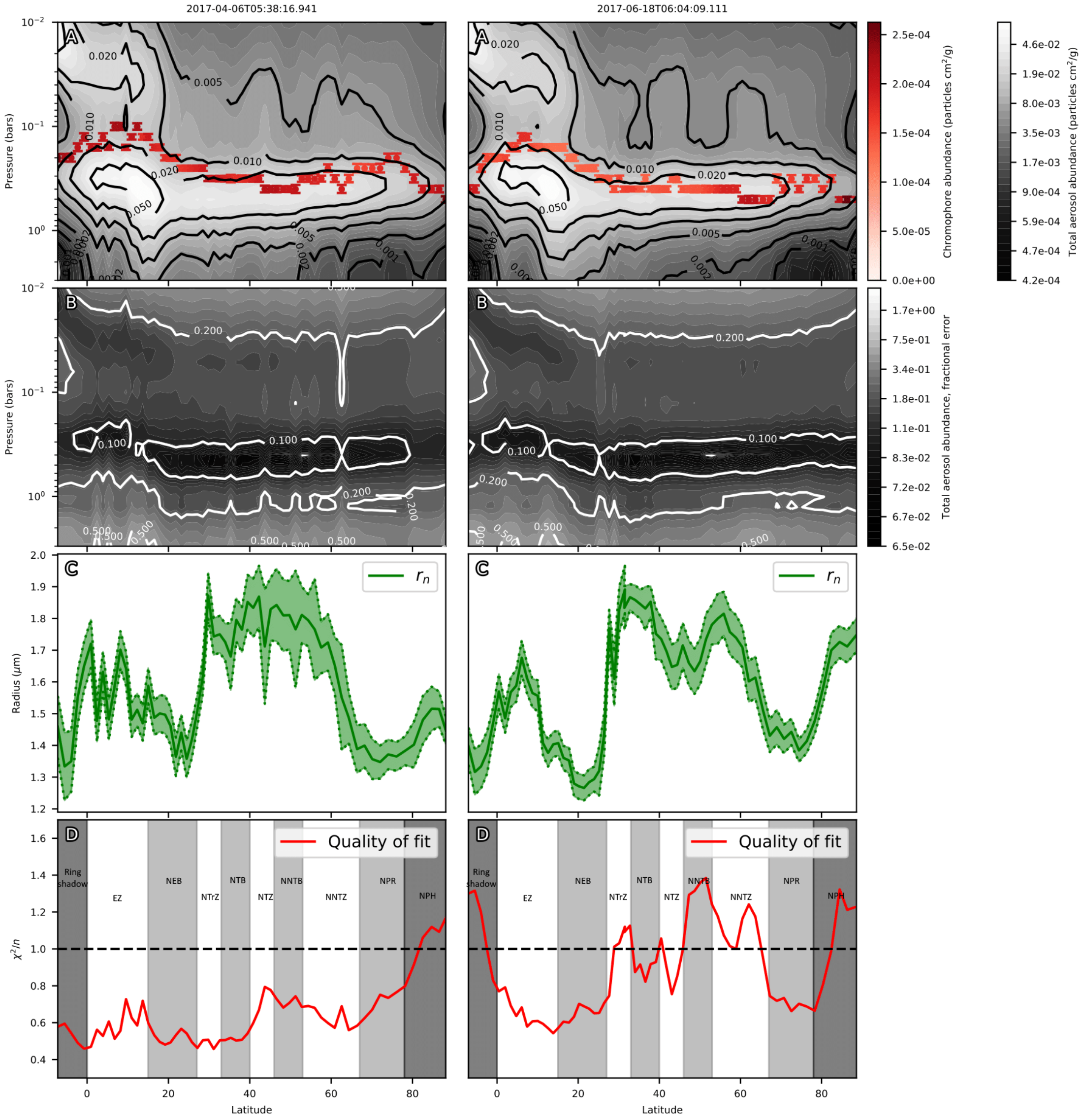

Figure 6.5.4: Results of the retrievals of a single north-south swath from (left) 2017-04-06T05:38:16.941 and (right) 2017-06-18T06:04:09.111, looking at differences between the cubes obtained with and without the use of adaptive optics. Key to individual plots is as in figure 6.5.3.

6.6 Sensitivity analysis

As in section 4.8, we now analyse to what extent the variations in haze and chromophore that we retrieve from Saturn are due to genuine variation, and to what extent they are due to deficiencies in our forward model. We also wish to see whether it would be possible to retrieve any kind of tropospheric cloud layer from the MUSE spectra. To this end, we generate 50 synthetic spectra according to the methodology presented in section 4.8, but this time according to the constraints of our Saturn retrievals in section 6.5. Unlike for Jupiter, we also have to take into account uncertainties in prior methane abundances due to the lack of in situ constraints on Saturn. This is displayed in figure 6.6.1, where we performed three retrievals of haze and chromophore on the same spectrum, each using a different scaling of the prior methane profile of Fletcher et al. [2009] across all altitudes. From our results, it appears that variations in haze specific density are approximately linear with respect to methane abundances over all altitudes, while a doubling of the methane abundance results in an upward shift in altitude of each haze layer by approximately half a pressure scale height. The most reliable and accurate deep volume mixing ratio values retrieved from Cassini/CIRS spectra are those of Flasar et al. [2005] and Fletcher et al. [2009], the former to within an uncertainty of ±20% and the latter to within ±5%. If we believe the measurements of Fletcher et al. [2009], we can therefore assume similar systematic uncertainties on our retrieved aerosol densities of just 5%. Even if we were to fall back on the uncertainties of Flasar et al. [2005], however, we would find that the resulting uncertainties in the altitudes of the haze layers would be insignificant given the vertical resolution of the MUSE spectra. In addition, we should note that these retrievals were made without properly taking CIA into account; errors in the methane abundance profile should be reflected in the fit to wavelengths between 0.81μm and 0.83μm, as we show in appendix B.

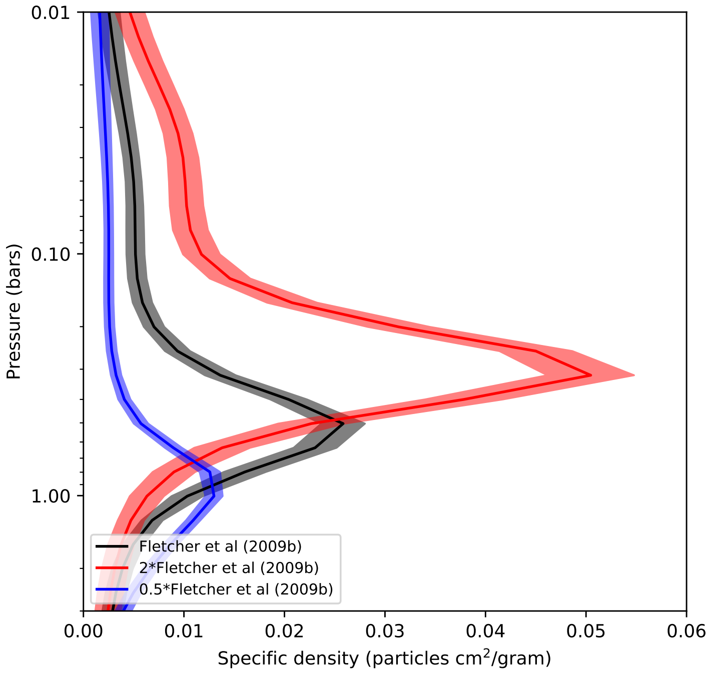

Figure 6.6.1: Results of a retrieval of a single spectrum of the NEB when the prior methane profile (assumed to correspond to Fletcher et al. [2009]) is either doubled (in red) or halved (in blue). The plot corresponds to a vertical profile of haze and chromophore combined.

In Figure 6.6.2, we present a comparison between the input and output aerosol profiles. As with Jupiter, it is clear to see that the profiles that most closely correspond to their true values are those where cloud abundance decreases monotonically with height from a thick cloud base, while the worst-retrieved profiles are those where the density fluctuates rapidly with height, or where the particle effective radius is retrieved poorly.

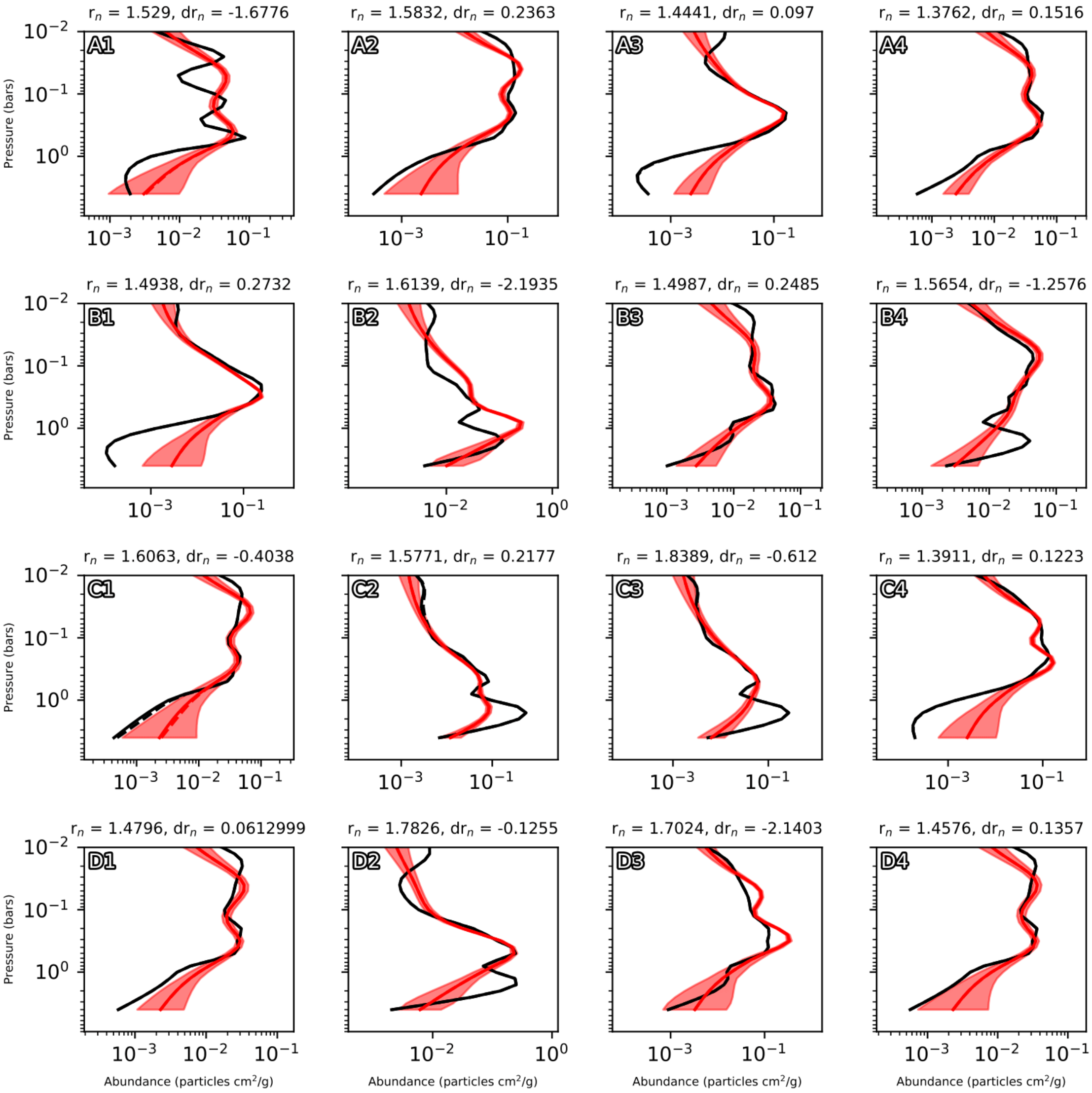

Figure 6.6.2: A comparison of a sample of modelled vertical aerosol profiles (in black) used to create synthetic Saturn spectra, with chromophore and non-chromophore abundances combined, compared to the profiles (in red, with uncertainties shaded) retrieved from the same spectra. The closer the correspondence between the two profiles, the better the quality of the retrieval model and the more information can be extracted on vertical haze distribution from MUSE spectra of Saturn.

The model can usually both resolve stratospheric and tropospheric haze layers from each other, and retrieve their densities independently. However, if there is thick stratospheric haze above an altitude of approximately 0.02 bars, as is often predicted (eg. Pérez-Hoyos et al. [2005]), the model will underestimate the altitude of both the main stratospheric haze layer and the gas layer separating it from the tropospheric haze, due to the lack of vertical sensitivity to haze at the highest altitudes, which can only be detected tentatively at 0.89µm. As expected, we find that the tropospheric cloud layer is almost universally impossible to retrieve from MUSE spectra, even if there is little overlying haze, and so it makes little sense to include a discrete cloud layer there as many have done (referring back to the citations in section 6.4), with the possible exception of around the NPH (provided it is observed close to nadir).

Figure 6.6.3 then shows the modelled versus the retrieved values of the remaining parameters of this analysis. We find that chromophore abundances and altitudes are generally retrieved reliably to within half a pressure scale height of the true altitude, provided that chromophore abundances are above approximately 10^{-4} particles cm^2/gram and that the chromophore layer is not located in the stratosphere at pressures less than 0.07 bars. These are values that are comfortably satisfied in all our Saturn retrievals, apart from in 2014 where we retrieve unusually high chromophore altitudes around the equator. Concerningly, there appears to be almost no correlation between modelled and retrieved r_n values, even though we generally retrieve the variations in r_n that we expect from our actual Saturn data. Our retrieved particle size variations in section 6.5 are therefore most likely due to variations in tropospheric haze density, with which they are degenerate.

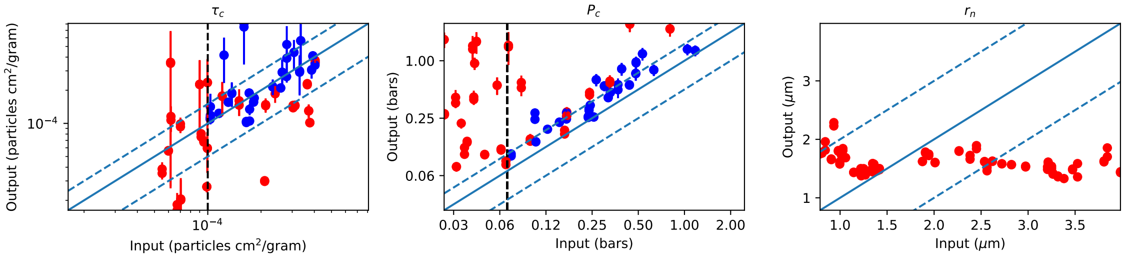

Figure 6.6.3: Sensitivity to peak abundance and altitude of chromophore, and to the effective radius of the non-chromophore particle population, comparing modelled input values with retrieved output values. Dark blue datapoints in the first two plots indicate input values in which both $\tau_c > 10^{-4}$ particles cm^2/gram and $p_c > 0.07$ bars are simultaneously satisfied, which are seen to be the most reliable retrievals as outlined in the text. These values are also marked as vertical black dashed lines on the plots for clarity. Points on the solid blue diagonal line have identical input and output values while the dashed blue diagonal lines indicate output values within a 50% error of the input values; an ideal retrieval would have all datapoints aligned with the solid blue diagonal for each variable case.

6.7 Observing variations in gaseous ammonia abundances through Principal Component Analysis

6.7.1 Motivation and theory

In preliminary retrievals, we attempted to retrieve gaseous ammonia abundances simultaneously with haze structure and chromophore from Saturn spectra as with Jupiter spectra. However, the ammonia absorption features were usually small enough to lie within observed spectral uncertainty constraints, and so we found that we were unable to reliably retrieve haze-top ammonia abundances from Saturn spectra. Nonetheless, the ammonia absorption features in Saturn MUSE spectra, particularly at 0.648µm, are still large enough in Saturn MUSE spectra that we should be able to extract some scientific information from them through other more qualitative means. Observing I/F variations of Saturn at 0.648µm alone will give some indication of this, but we caution that these may be as much a result of haze variations as ammonia variations. We therefore wish to use a different technique to decouple gaseous ammonia variations from variations in vertical haze structure as much as possible. One that is commonly used to extract scientific information from data that is either noisy or lacks spectral accuracy is known as Principal Component Analysis (PCA) (eg. Ready and Wintz [1973], Murtagh and Heck [2012]). In this subsection, we explain the theory behind PCA, which mostly paraphrases Murtagh and Heck [2012], while in the following subsections we apply this technique to MUSE data of Jupiter and Saturn to map spatial variations in ammonia.

In PCA, multidimensional data is linearly transformed by deducing the perpendicular axes over which the variation in the data is strongest. The data is then reprojected onto those axes by solving an eigenvalue problem, which is illustrated graphically in figure 6.7.1. The orthogonal axes of strongest variation (ie. the eigenvectors) are known as the *principal components* of the data, while the associated eigenvalues quantify the extent of the variation along each given axis, in terms of how many of the original variables are required to explain the same amount of variance. Each principal component should, in theory, account for variation due to a single atmospheric variable. If we therefore optimise our PCA correctly, the data projected onto one principal component should account for most of the spatial variation in cloud structure on Saturn, while data projected onto a different principal component should account for equivalent variations in ammonia. This technique has already been applied to map equivalent variations of H_2S on Neptune by Irwin et al. [2019b], for which spectral signals were weak in the observed wavelength range. In practice, it is not always very straightforward to decouple two variables using this technique: principal components can often be difficult to interpret physically, and wavelength ranges often have to be manipulated very carefully to yield principal components that each correspond to single atmospheric variables, as opposed to linear combinations of several variables. It therefore makes very little sense to extract scientific information

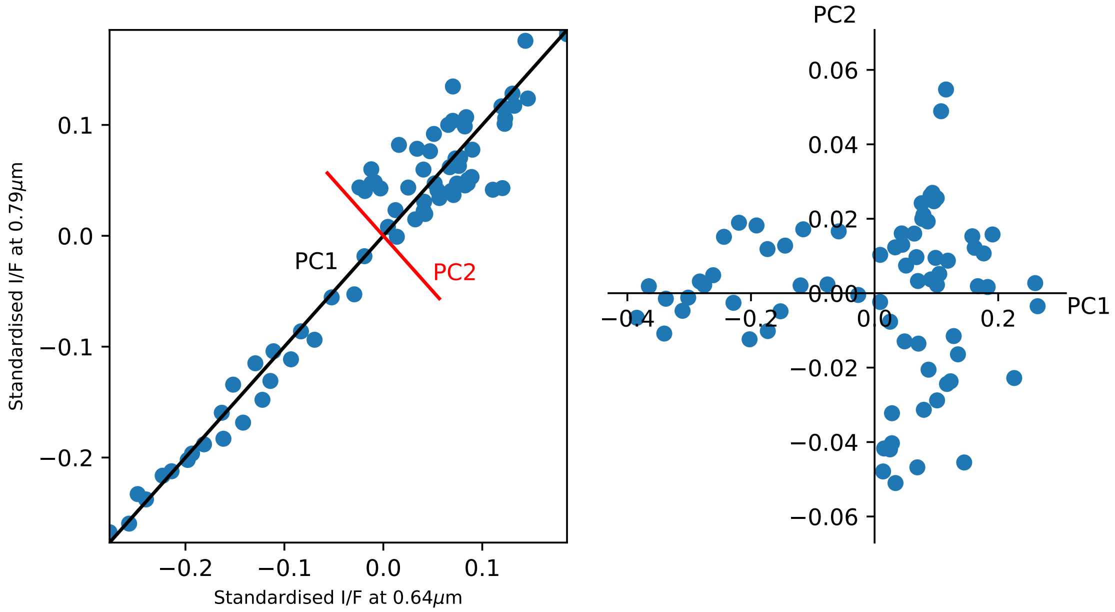

Figure 6.7.1: A visual demonstration of PCA on example MUSE data, analysing the correlation in I/F between two separate wavelengths. On the left is a scatter plot of I/F, standardised as in equation 6.7.1, obtained over a range of spatial pixels. Here, we wish to find the two perpendicular principal components that encompass the axes of the most variation in the data. Using PCA, we find that the greatest variation in the data is along the first principal component (PC1), shown by the black line, however there is also another axis with secondary variation in the data, which is given by the second principal component (PC2), shown in red. The scatter plot on the right shows the same data projected against the two principal components, with the range of the data along each axis encoded by the eigenvalue of the principal component. In this case, PC2 could probably be dismissed as simply encoding noise. Hence, principal component analysis can also prove a useful tool to reduce the number of dimensions of multidimensional data. Although in this case one could also have derived the same axes through linear regression, if more wavelengths are included in the analysis (as we do in this section), the number of wavelengths one would have to plot against (and hence the number of dimensions in the plot) would increase to the point that linear regression becomes impractical. In addition, the greater the number of dimensions, the greater number of principal components that are likely to encode useful information about the data.

from spectral data using PCA if the signal to noise ratio is low enough, and the spectral resolution high enough, that the same information can be extracted more accurately and quantitatively using spectral retrievals directly. We therefore present the application of PCA on MUSE observations of Jupiter in this chapter not in order to derive scientific information on variations in gaseous ammonia abundances on Jupiter per se, for which we already have spectrally retrieved abundance values as presented in section 5.2, but simply in order to determine the quality of PCA when applied to observations of Saturn, for which we do not have the required signal-to-noise ratio at wavelengths of significant ammonia absorption to retrieve ammonia abundance variations using NEMESIS.

Consider elements M_{ij} of a matrix $\mathbf{M}$ of size $n_i \times n_j$, representing the I/F values in a single spectral image cube of Saturn within a given spectral range, where i represents the spatial dimension (the ordering of each spatial pixel in the matrix does not matter) and j the spectral dimension. In PCA, we do not care about the magnitudes of each of the I/F values per se. Instead, we only wish to know how far each of the values are from each other, so that the axes of variation encompasses the maximum distances between points. This requires the data matrix to be standardised, which involves centring it around the spectral mean and normalising it to unit standard deviation:

$$\bar{M}_{ij} = \frac{M_{ij} - \frac{\sum_i M_{ij}}{n_i}}{\sqrt{\sum_i \left(M_{ij} - \frac{\sum_i M_{ij}}{n_i}\right)^2}} \tag{6.7.1}$$

which is then converted into a correlation matrix $\mathbf{C}$, a symmetric matrix with dimensions $n_j \times n_j$, as follows:

$$C_{xy} = \sum_i \bar{M}_{ix}\bar{M}_{iy} \tag{6.7.2}$$

It can be shown, eg. in Murtagh and Heck [2012], that the correlation between two points is directly proportional to the Euclidean distance between them, and hence the correlation matrix can be used as a proxy for distances between points. Occasionally, a covariance matrix can be used instead of a correlation matrix for PCA for similar reasons, but it is more common to use a correlation matrix, as we do here. We now wish to find a set of axes $\mathbf{u}_k$ for which the sum of the distances between the chosen set of axes and all the points is minimised. This is done by solving a Lagrangian, which can be simplified down to a regular eigenvalue problem for $\mathbf{C}$:

$$\mathbf{C}\mathbf{u}_k = \alpha_k \mathbf{u}_k \tag{6.7.3}$$

Each of these principal components will then be sorted in order of descending eigenvalue α_k, so that the first principal component is responsible for the greatest variation in the spectrum while higher-order principal components can be neglected as pure noise. Finally, we project the original data onto each eigenvector $\mathbf{u}_k$ to give a vector $\mathbf{m}_k^{proj}$:

$$m_{ik}^{proj} = \sum_j \bar{M}_{ij} u_{jk}$$

If the PCA is successful, and if the wavelengths to analyse are chosen carefully, one $\mathbf{m}^{proj}$ vector should correspond to a map of cloud structure variations on Saturn, while another should correspond to a map of ammonia variations. The principal component that is responsible for ammonia variations should look as similar as possible to an ammonia absorption spectrum, and would have as large an eigenvalue as possible (preferably greater than 1, as a lower eigenvalue would imply that the variation in gaseous ammonia abundance could be explained better by observing I/F variations at single wavelengths instead of through PCA).

6.7.2 Refining PCA on Jovian ammonia retrievals

To optimise the PCA to obtain the most accurate possible ammonia maps of Saturn, we need to know how to manipulate the wavelength ranges of the PCA so that differences in ammonia abundance account for as much of the variation in the MUSE spectra as possible. In addition, we need to understand to what extent the output of the PCA corresponds to genuine variations in ammonia abundance on Saturn. To do this, we first apply PCA onto the meridional north-south swath of Jupiter presented in section 4.7, for which we could constrain gaseous ammonia abundances much better than from equivalent Saturn data, and observe the extent to which the data projected onto the ammonia principal component correlates with the retrieved meridional ammonia profile. We show the results for this meridional swath in figure 6.7.2, as well as the whole of Jupiter for context in figure 6.7.3.

In both cases, we found that we were able to produce the best results by performing PCA on the wavelength ranges with the three strongest ammonia absorption bands simultaneously: 0.640-0.655µm, 0.780-0.800µm and 0.921-0.933µm, encompassing 50 individual wavelengths in total. Of these three bands, the one around 0.79µm was seen to be the most important, despite being sensitive to ammonia absorption at slightly higher altitudes on Jupiter than the other two, and so should exhibit smaller variation in depth over Jupiter. Nonetheless, by far the most variation in the data (more than 99%) was due to almost entirely linear correlations in I/F. This variation, encompassed by PC1, is most likely due to general aerosol structure variations (mostly from the uppermost visible cloud layer), and the data projected onto this component resemble regular zone-belt variations in cloud structure. PC2 appears to account for the majority of spatial variations in gaseous ammonia abundance, and the data projected onto this principal component match closely with ammonia abundance variations that were retrieved in section 4.7. PC3 accounts mostly for second-order contamination, as very clearly illustrated in the third row in figure 6.7.3. This component should not arise in our Saturn data where the effect of second-order contamination is much smaller, as we previously described in section 2.4.3. Although principal components from PC4 onwards account for much less variation than any of the previous three components, PC4 does appear to account for some additional small variation in ammonia abundance that is not encompassed in PC2, perhaps a result of very small sensitivities to altitudinal differences in ammonia abundance.

Our results show that PCA is able to separate out variations in ammonia abundance and cloud structure well for Jupiter MUSE data. However, the fact that even PC2 has an eigenvalue much less than 1 is concerning, and implies that the observation of I/F values at a single wavelength (or perhaps the difference in I/F between two single wavelengths) would provide a better measurement of ammonia abundance variations than PCA. Nonetheless, this may not necessarily be the case for Saturn, where zone-belt variations in visible aerosol structure are much more subdued and where I/F difference measurements would have a lower signal to noise ratio, although this could be further mitigated by the fact that the ammonia absorption features will be smaller on Saturn and so would encompass less variation in I/F.

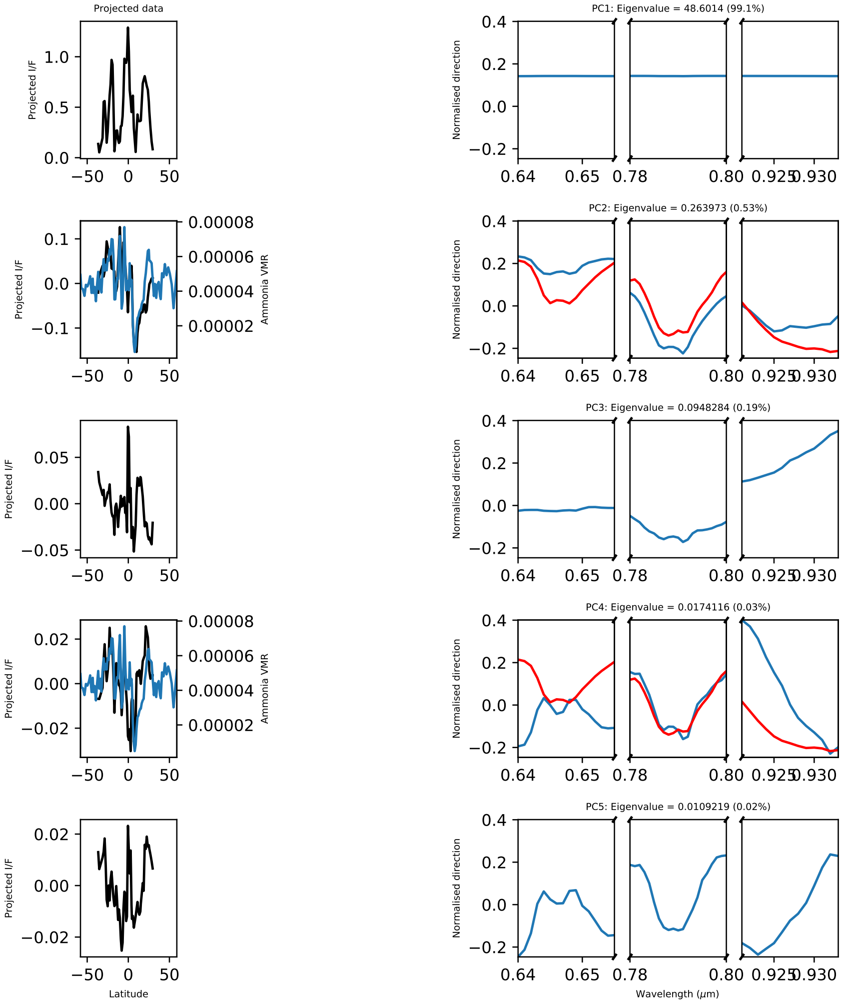

Figure 6.7.2: Results of PCA on the meridional north-south swath of Jupiter, shown in figure 4.7.1, for which atmospheric retrievals were performed in section 4.7. Each row corresponds to a single principal component, with the associated eigenvalue shown in the title, together with the percentage of the total variation in the data that the principal component encompasses. The right column shows the normalised directions of the principal components over all the wavelengths analysed, with an example of a modelled gaseous ammonia spectrum shown in red superimposed on the second and fourth principal components for comparison. In the left column, we show the original I/F data projected onto each principal component following standardisation, with the retrieved gaseous ammonia abundances from figure 4.7.2 shown in blue in the second and fourth rows for comparison.

6.7.3 Application of PCA to Saturn

We now apply the same methodology to I/F observations of Saturn from 2017-06-18T06:04:09.111, cropping out latitudes below -5^o S (planetographic) where the effects of Saturn's rings are visible, to see if PCA can successfully sift out spatial variations in ammonia absorption band depths on Saturn. Our results are shown in figure 6.7.4. As for Jupiter, the bulk of the variation in the data is due to

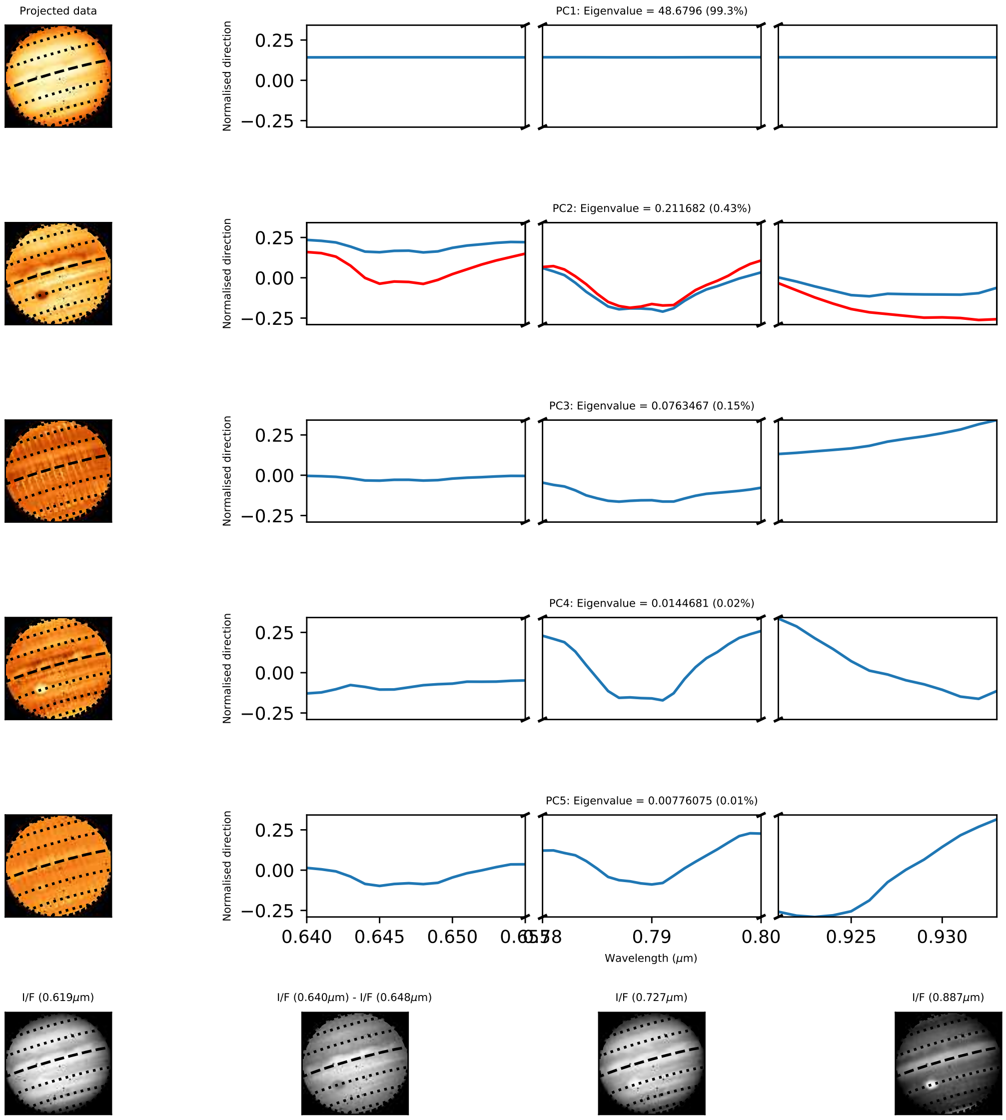

Figure 6.7.3: Results of PCA for the whole of Jupiter, as obtained from the 2018-04-09T06:04:06.918 dataset. The first 5 rows correspond to each of the first 5 principal components, with the associated eigenvalue shown in the title, together with the percentage of the total variation in the data that the principal component encompasses. The right column shows the normalised directions of the principal components over all the wavelengths analysed, with an example of a modelled gaseous ammonia spectrum shown in red superimposed on the second principal component for comparison. In the left column we show the original I/F data projected onto each principal component following standardisation. The images in the bottom row show images of Jupiter (in terms of unstandardised I/F) at four different wavelengths: one at 0.619μm (sensitive to the main cloud layer), one at 0.648μm subtracted from one at 0.640μm (a rough proxy for gaseous ammonia abundances at the cloud-tops), and two images at 0.727μm and 0.889μm (higher haze structure). Black horizontal dotted lines show lines of latitude in increments of 20^o (planetocentric), with the equator shown as a thick dashed line for reference.

linear correlations in I/F, mostly a result of differences in haze cover between the poles, equator and mid-latitudes. The ammonia absorption feature around 0.79µm once again appears to be the most important of the three features. However, it is clear that the subtlety of the ammonia absorption features in the Saturn spectra make finding variations in their depth more difficult than for Jupiter, even with PCA. It is not entirely clear from the shapes of the eigenvectors whether PC2 or PC3 takes into account most of the ammonia absorption variations. The shape of the PC2 eigenvector around 0.78-0.80µm does appear to bear some resemblance to the ammonia absorption spectrum in this wavelength range, but it also bears resemblance to the observed variation in the methane absorption band in the same wavelength region, which is asymmetric around 0.79µm. By contrast, the shape of the PC3 eigenvector in the same wavelength range is more symmetrical around 0.79µm, but the effect is more subtle. The single unprojected I/F image of Saturn that provides the closest approximation of ammonia abundance - that of 0.640µm minus 0.648µm - appears to bear the most resemblance to the data projected onto PC2, particularly of the apparently PC2-depleted region around 20N. It is therefore likely that PC2 takes into account both ammonia and cloud structure variations. PC3 mostly appears to be the inverse of PC2, with the greatest difference between the two around 20N (although there is also a very subtle instrumental artefact around this region which may have interfered with the principal component) and in the NPR. We also note that variations in absorption at 0.92-0.93µm have a greater contribution to PC3 than to PC2, which indicates that variations in tropospheric haze cover contribute to PC3, as well as some very subtle second-order contamination effects. Disconcertingly, all our eigenvalues (apart from that of PC1) are substantially lower than 1, which means that there is likely a spectral image of Saturn that would encapsulate spatial ammonia variations better than any of our obtained principal components could, though it is unclear which wavelength that would be. It is also strange how little the effect of spectral variation at 0.640-0.648µm has on either PC2 and PC3, given that we can see very obvious spatial variation in that ammonia absorption feature in figure 6.5.2.

Physically, PC2 would make the most sense in representing variations in observed ammonia abundances. The region around the equator appears to be analogous to the ammonia profile retrieved from Jupiter in the upper troposphere [Achterberg et al., 2006]: a large upwelling system of ammonia just north of the equator, for which we find similar evidence in our haze structure retrievals, followed by a large downwelling system of ammonia in the NEB. Apparent raised abundances in the poles could be due to the relative lack of haze cover in the region associated with northern summer that would otherwise mask ammonia gas signatures in MUSE spectra. All these phenomena could, however, be explained equally well by accounting for a combination of stratospheric and upper tropospheric haze variations. Likewise, the apparent lack of ammonia around the EZ compared with the mid-latitudes in PC3 could be explained by increased stratospheric haze cover, while depletions in the poles may be explained by downwelling. Retrievals of 0.6 bar ammonia abundances from far-infrared Cassini/CIRS data obtained during southern summer [Hurley et al., 2012] show a meridional profile in the southern hemisphere somewhat similar to what we observe in PC3 in the northern hemisphere: depletion around the equator and the poles, but elevation in the mid-latitudes. Such a profile could be further modulated by the overlying haze layers to accentuate differences between the equator and the mid-latitudes as we see in our analysis.

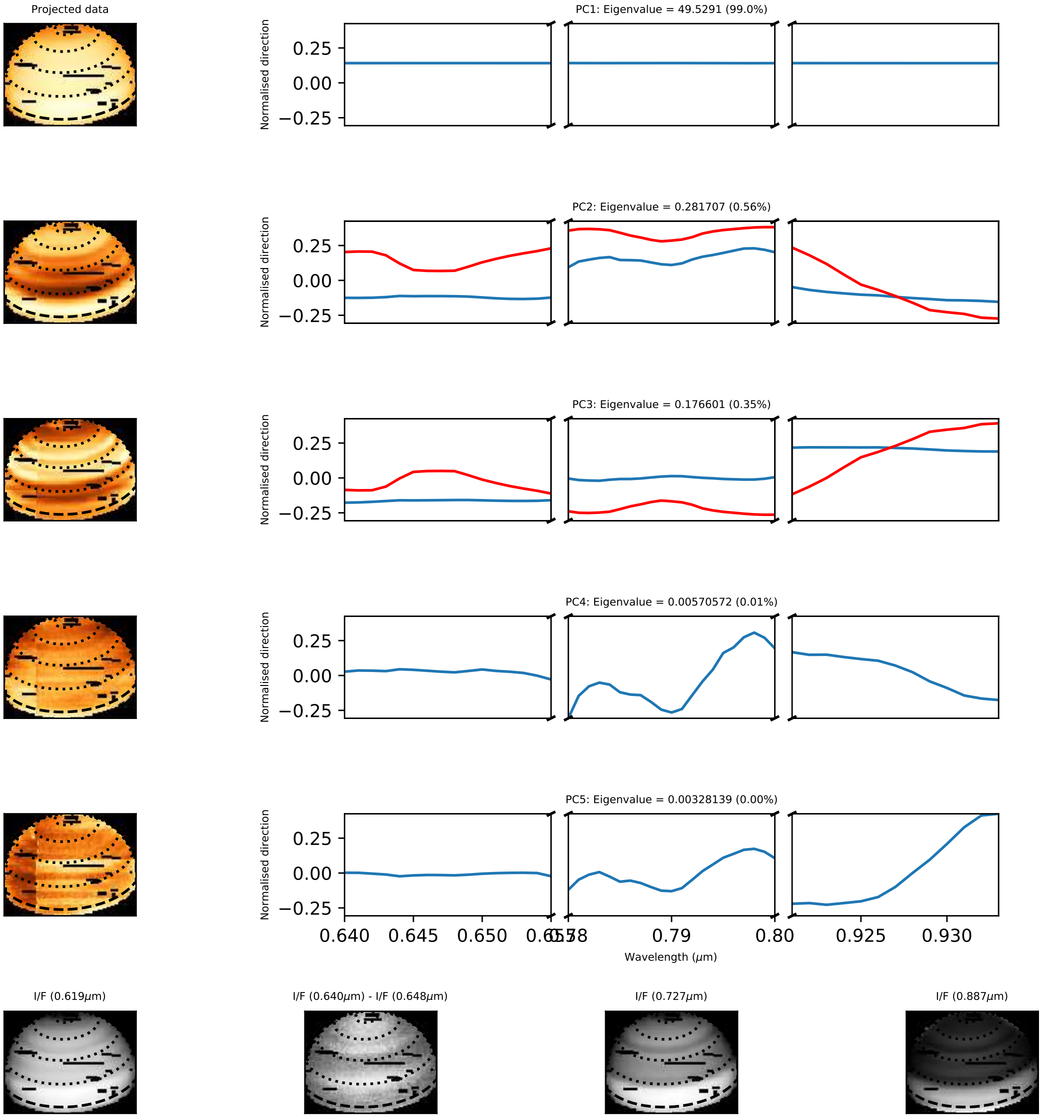

Figure 6.7.4: Results of PCA for the whole of Saturn's northern hemisphere, as obtained from the 2017-06-18T06:04:09.111 dataset. The key to each plot is as in figure 6.7.3, although the modelled absorption spectrum is also shown here for PC3 reflected in the x-axis.

Chapter 7

Conclusions and Future Work

7.1 Overview and summary

This thesis has described the calibration and analysis of multiple spectral datasets of Jupiter and Saturn obtained from the VLT/MUSE instrument between 2014 and 2018, the former as part of the wider ground-based support for NASA's Juno mission currently in orbit around Jupiter. These data, spanning a wavelength range of between 0.48µm and 0.93µm at 0.001µm resolution, contained unprecedented information on spatial and temporal variations of chromophore, tropospheric cloud and haze structure and gaseous ammonia abundance over the visible hemispheres of Jupiter and Saturn. The information on chromophore was particularly valuable, as no other instrument since Cassini/VIMS (bar NAIC, which we mentioned briefly in section 2.2), either on board Juno itself or as part of its ground-based support, has been able to measure this effectively due to their lack of spectral resolution at visible and near-infrared wavelengths.

In chapter 2, we explained how we first calibrated and reduced the raw MUSE datasets using the standard pipeline, and then corrected for systematic errors in photometric calibration and for instrumental artefacts in post-processing. The Jupiter dataset that was seen to have the best calibration - 2018-04-09T06:04:06.918 - was then selected for further analysis in chapter 4. We tested various cloud models and laboratory chromophore spectra on the data using NEMESIS, and then extracted our own 'universal' chromophore imaginary refractive index spectrum directly from the data using our optimal cloud model. This was done by performing limb darkening retrievals on a single latitudinal region of the NEB using a wide range of prior variables, and then ruling out unphysical solutions from both theoretical and in situ observational data on cloud structure, as well as ruling out non-universal chromophore imaginary refractive indices that would not provide a good fit to a spectrum of the Great Red Spot. Using our new chromophore imaginary refractive index solution, we then expanded our analysis to all our remaining Jupiter datasets in Chapter 5, in order to retrieve temporal changes in colour, cloud structure and gaseous ammonia abundances associated in particular with three 'upheavals' (namely the NEB expansion, the NTBs upheaval and the EZ colouration events), as well as with the Great Red Spot and Oval BA. We then applied a similar method in Chapter 6 to extract a universal chromophore spectrum from MUSE data of Saturn, and applied that chromophore spectrum to retrievals of rudimentary temporal changes in latitudinal variations of colour and haze. Finally, we applied the method of Principal Component Analysis to Jupiter and Saturn data in order to qualitatively determine variations in gaseous ammonia abundances just above Saturn's thick upper tropospheric haze layer, as the ammonia signatures present in Saturn MUSE spectra were too small to be retrieved directly using NEMESIS.

In section 7.2, we summarise the main outcomes of our analysis that resulted from the method we have just described, and relate them to our original scientific aims that we outlined at the beginning of this thesis. In each case, we highlight important, conclusive outcomes of this thesis in bold. Finally, in section 7.3 we outline some suggestions for future work (in no particular chronological order) with our MUSE data that we did not have either the time or the space to describe in this thesis itself.

7.2 Conclusions

At the beginning of Chapter 1 of this thesis, we asked the following questions that we will now address as fully as possible based on the results presented here:

1) To what extent can aerosol density be decoupled from particle size and real refractive index, and to what extent can these degeneracies be neglected to retrieve reliable cloud and chromophore profiles?

Throughout chapters 4 to 6, we used a cloud model that consisted of two particle populations: one of chromophore and one of conservatively-scattering aerosols (non-chromophore), with the latter particle population serving as a proxy for both tropospheric cloud and high-altitude haze simultaneously. In both cases, we assumed a constant particle size distribution with height, an assumption we know not to be true. Retrievals at a single viewing geometry constrain particle size distributions very poorly, and yet continuous profiles of aerosol are very dependent on particle size especially at higher altitudes: a low particle size generally results in a profile with a very thick high-altitude haze relative to the 1 bar cloud in the case of Jupiter. However, limb-darkening retrievals over an entire latitudinal swath provide a reasonable constraint on the non-chromophore particle size distribution even using a relatively small phase angle range, provided that the real refractive index of the non-chromophore particles is known *a priori*. In the case of Jupiter, the effective radius of the non-chromophore particles most likely corresponds to that of the tops of the deepest visible cloud layer, while on Saturn it most likely corresponds to the opaque, ubiquitous upper tropospheric haze. Although one cannot distinguish the effective radius of the non-chromophore particles from their real refractive index even from limb-darkening alone, one can deduce the most likely real refractive index value by examining its effect on retrieved cloud abundances. In the case of Jupiter, this means that we were able to provide a good constraint on both particle size and real refractive index simultaneously from limb-darkening in section 4.6, as we had both in situ data of aerosol density from the Galileo probe and a wealth of literature pertaining to theoretical constraints on the particle densities of the tropospheric cloud layers. **We concluded that the effective radius of the cloud particles in the NEB was around 1µm, with a real refractive index of approximately 1.42. This is difficult to reconcile with a cloud made out of pure NH_4SH ice**. By contrast, decoupling these two quantities was much more difficult from Saturn data in section 6.4, due to the lack of in situ data and microphysical constraints on the tropospheric haze. Constraining the particle size and real refractive index for Saturn simultaneously therefore required a greater element of guesswork and circular reasoning. From basic microphysical constraints, we had to assume that the particle size was around 1µm at the EZ and more than 2µm at higher latitudes, with a real refractive index of 1.42. For point retrievals in both Jupiter and Saturn, we had to allow the non-chromophore particle size to be variable in order to be able to fit the GRS spectrum on Jupiter, for which a small particle size provided a poor fit, and to fit realistic latitudinal variations in particle size on Saturn. However, most spectra obtained at single geometries do not contain sufficient information for particle size to be properly retrieved by NEMESIS. This had adverse impact on most of our retrievals, particularly in chapter 5 and in section 6.5.

Constraining the same two quantities for the chromophore particle population, on the other hand, was very difficult due to the complete lack of prior information. In the case of Jupiter, we did not even make an attempt at retrieving the chromophore real refractive index, which we just assumed to be 1.4 to correspond with that of the organic chromophore of Carlson et al. [2016] (which we have usually referred to as CR16). We also found it difficult to constrain both the chromophore particle size and its *imaginary* refractive index spectrum simultaneously, even with limb-darkening and neglecting degeneracies in real refractive index. The only way in which we were able to provide some constraint on the chromophore particle size was to apply the solution that was retrieved from the NEB to the GRS, for which we had to assume that spatial chromophore particle sizes were completely invariant over the surface of Jupiter. We found that a chromophore particle size of 0.2µm was sufficient to provide a good fit to all red regions of Jupiter. For Saturn, the only way in which we were able to constrain particle size was to find a solution where the chromophore was located above the upper tropospheric haze layer. The only possible solution was a very low particle size of 0.02µm, with a real refractive index of 2.1, akin to the phosphorus chromophore of Noy et al. [1981].

2) Are hypothetical chromophore spectra obtained under laboratory conditions compatible with observed MUSE spectra of the giant planets? If not, can a reliable chromophore spectrum be retrieved directly from the MUSE data?

There are two main reasons as to why the composition of giant planet chromophore is so difficult to discern. One is the relative lack of distinct absorption signatures in giant planet spectra that would allow the discernment of individual compounds, other than a broad absorption feature shortward of 0.6µm to which one could fit a whole number of different compounds. The second reason is the relative lack of laboratory analyses of giant planet chromophore. Where those analyses do exist, their absorption spectra are often tabulated over a restricted set of wavelengths. In addition, they usually fail to replicate the exact mixtures of red compounds present in the atmospheres of the giant planets, or the blue-absorption seen in giant planet spectra, due to sometimes very minute assumptions and errors in the experimental methodology. Fitting laboratory chromophores to giant planet spectra is made even more difficult by the lack of prior knowledge of aerosol particle sizes, which can change the shape of the blue-absorption dramatically.

Having said that, in section 4.5 we showed that we were able to provide a fit to Jovian spectra using the CR16 chromophore that was superior to any other laboratory chromophore that we could find. Unlike Sromovsky et al. [2017], we did require some modification to the imaginary refractive index spectrum tabulated by CR16, due to the large spectral slope present in MUSE spectra of the GRS that was not present in equivalent spectra from the Cassini/VIMS-V instrument obtained before the recent reddening of the GRS. **Regardless of particle size, we consistently required a Jovian chromophore with a steeper gradient in absorption below 0.6µm than CR16. This was, however, still compatible with the general results of CR16**, since they tabulated their chromophore optical constants before their experiment was complete; **chromophore absorp-**

tion spectra obtained later in the CR16 experiment more closely resembled our own retrieved chromophore spectrum.

In section 6.3, by contrast, we found that **the shape of Saturn spectra from the NEB below 0.6μm most closely resembled the absorption curve of the chromophore of Noy et al. [1981]**. Even then, we did have to make similar adjustments to the chromophore absorption in section 6.4 as we did for our Jovian spectrum, namely **we required a greater slope in the spectral absorption below 0.6μm and a secondary absorption peak in the near-infrared**.

3) Can spatial variations in colour on Jupiter and Saturn be explained by one single chromophore compound (a 'universal chromophore'), or is more than one chromophore compound necessary?

We showed in section 4.6 that, if one adjusts particle sizes accordingly, the same chromophore optical constants can fit the shape of the spectral slope found in all 'red' Jupiter spectra, with few major discrepancies in the fit. This includes the major belt regions of Jupiter, as well as the NTBs red haze, the GRS and Oval BA. Thus, from a purely spectral standpoint and neglecting all prior theoretical constraints, **there is no need for a different chromophore to explain the colour of the belts and of the GRS and so we can safely assume a universal Jovian chromophore. Instead, the differences in colour morphology between the belts and the GRS can be more easily explained by differences in underlying cloud cover**. We suggest the following hypothesis for the presence of the same chromophore in all red regions of Jupiter: in most regions of Jupiter, the chromophore is located around the altitude at which one would expect an ammonia cloud layer (which from most equilibrium cloud condensation models is located around 0.7-0.8 bars). As the zones are colder and more rich in ammonia than the belts, the chromophores act as condensation nuclei for ammonia ice, which thereby mask the signature of the chromophore. By contrast, in the warmer belts, ammonia ice sublimates, leaving behind the red chromophore nuclei. In the NTBs and in discrete features such as the GRS, upwelling is sufficient for the cloud particles to reach high altitudes, where the surrounding ammonia ice could be removed through reactions with substances in the haze to leave behind chromophore. The only observed colouration that defies this hypothesis is the reddening of the EZ that began in mid-2018, as described in section 5.4, which requires further investigation. In addition, this still begs the question as to the origin and composition of the chromophore in the first place. **The regions of Jupiter for which our**

universal chromophore provided the most imperfect fit were the zones, due to spectral variability between 0.51μm and 0.54μm. This could be explained by a number of factors: imperfect modelling of particle scattering properties, imperfect methane and ammonia band data, or the presence of a compound in the zones that is either entirely absent in the rest of Jupiter or that is masked by chromophore. We recommend further study of variability in this spectral region in particular.

Surprisingly, **it is more difficult to assume a universal chromophore on Saturn**, despite the apparent uniformity of Saturn's appearance compared with Jupiter. We found in section 6.5 that **the chromophore optical constants we retrieved from the NEB appeared to be unique to the NEB, while the spectral slope of the EZ and the poles at blue wavelengths appeared to more closely resemble that found in Jupiter spectra. In those regions, we also found similar spectral variability between 0.51μm and 0.54μm that we found in the zones of Jupiter**. **We propose that the spectral variations with latitude on Saturn could be a result of two different chromophores**: one formed in the tropospheric haze layers itself (and which is unique to Saturn), and one that is convected into the haze from deeper altitudes (which could be similar to the one we retrieved in the atmosphere of Jupiter). We recommend further investigation of these variations.

4) Can the most likely altitude of the chromophore be reliably constrained?

In the case of Jupiter, mostly not. In section 4.8 we showed that the altitude of chromophore could only be reliably retrieved on Jupiter if the peak chromophore abundance was either above approximately 4 particles cm^2 per kg of atmosphere, a value we were only able to retrieve in the Great Red Spot, or if the chromophore was located deeper than 1 bar. In section 5.5 we found that **the chromophore altitude in the GRS was retrieved around the tropopause at 0.1 bars**, a value that corresponds with a chromophore that is either formed or exposed in the high-altitude haze layers. For other regions of Jupiter with much lower retrieved chromophore abundances (particularly the zones), the chromophore altitude tended to be retrieved deeper in the atmosphere, just above the visible cloud layers, than its most likely location. Instead, we had to gauge the approximate location of the chromophore by more indirect means, namely through correlations with cloud and haze structure. On the other hand, we showed in section 6.6 that the chromophore altitude on Saturn could be more reliably retrieved, provided that the chromophore was not located too high in the stratosphere (although in practice, the retrieved altitude of the chromophore on Saturn should also be somewhat degenerate with particle size, especially given the lower constraints from prior data). In section 6.5 we showed that **generally, chromophore on Saturn tended to be retrieved just above the tropospheric haze layer**, with the exception of the EZ where the chromophore was often retrieved close to the base of the stratospheric haze layer, although this may simply have been a consequence of the different spectral shape of the EZ relative to the chromophore absorption spectrum.

5) What is the source of the discrepancy in the most likely altitudes of the thick cloud layers on Jupiter between those predicted by Equilibrium Cloud Condensation Models (ECCMs) and observations made at different wavelengths? Hence, can the most likely composition of the uppermost cloud layer be deduced?

In section 1.2 we explained how there was a discrepancy in the uppermost detectable cloud layer between previous observations in the visible and near-infrared, where the cloud was observed to be located around 0.7 bars, corresponding to a pure ammonia ice cloud, and observations in the thermal infrared, where a thick cloud was required somewhere between 1.0 and 1.5 bars. As shown in section 4.7 onwards, we consistently agree with previous observations in the thermal infrared (and with the Galileo probe), in that **we almost always retrieve a thick cloud layer somewhere between 1.2 and 1.5 bars**. We were unable to fit any Jupiter spectra without a cloud layer deeper than 1 bar, although we do not discount the possibility of the presence of an additional cloud layer where we predict pure ammonia to condense which we cannot resolve from the cloud layer below using the MUSE data alone. We note that the principal works in which the main cloud layer was retrieved at 0.7 bars, namely Banfield et al. [1998b] and Simon-Miller et al. [2001a], made use of only a small number of discrete wavelength filters, as opposed to hyperspectral data as we have. They would therefore have lacked data at 0.619µm which would have allowed for a better constraint of the altitude of the cloud layer (although we should note that in our own trial retrievals using similar multispectral data we also required a cloud deeper than 1 bar). Curiously, **we observe almost no resolvable spatial variation in the altitude of this cloud layer**, just in its opacity. As for its likely composition, it cannot be ammonia ice, as it would sublimate at these altitudes. The reaction between NH_3 and H_2S is very poorly-constrained, but it is most likely that this cloud layer is made primarily of a product of such a reaction, such as $(NH_4)_2S$. More detailed constraints on the composition of the observed cloud layers would require both better knowledge of the reaction between NH_3 and H_2S, and a detailed microphysical model for which we could use the ammonia abundances retrieved in section 5.2 as an input.

6) How does the concentration of ammonia gas vary with latitude and time on Jupiter, and to what extent does it match with deep observations of ammonia gas by Juno/MWR?

In section 5.2, we presented retrievals of cloud-top ammonia abundance over a single representative latitudinal swath obtained from 10 of our Jupiter MUSE datasets from 2014 to 2018. We found that **the northern EZ exhibited substantial and often predictable temporal variability in gaseous ammonia abundances**, decreasing in 2017 following the NTBs upheaval and then increasing again in 2018 to coincide with the EZ colouration event. This temporal variability, however, is not as well-reflected by MWR observations, where changes in ammonia abundances in the northern EZ appear less predictable. We therefore recommend further study of global and temporal variations in ammonia abundance in this region. Nonetheless, we generally find a good correspondence between our ammonia abundance retrievals and the profile at the surface level obtained by Li et al. [2017, 2018] from the MWR up to PJ9. Where differences arise between the MUSE and MWR data, they can usually be easily explained by temporal and longitudinal variability. The substantial hemispherical asymmetry between the depths of the upwelling-downwelling systems of ammonia appear to be undetectable at the visible cloud layers, either in our MUSE data or in the MWR data.

7) Can reliable latitudinal variations in ammonia abundance be obtained from MUSE observations of Saturn?

In section 6.7, we attempted to extract qualitative information about variations in gaseous ammonia abundances at the level of Saturn's tropospheric haze layers through Principal Component Analysis (PCA), since the ammonia absorption signatures present in Saturn spectra were too small, and the signal-to-noise ratio too low, for ammonia abundances to be directly retrieved from the spectra using NEMESIS. We found that we were able to account for at least some of the spatial variation in the ammonia absorption feature at 0.79µm to correspond with genuine variations in ammonia abundance. **These variations provided tentative indications of either relative elevations in ammonia abundance in the EZ and around the poles, and relative depletions in ammonia abundance in the mid-latitudes, or the reverse**. However, we were unable to discern from the PCA which of the two possibilities was the case, nor were we able to deduce to what extent those variations could also have been influenced by variations in haze. Previous work on Saturn combined with analogous work with Jupiter could have justified either possibility. Nonetheless, our results appeared promising, and we would be able to detect variations more conclusively if even minor improvements were made to the signal-to-noise ratio around 0.79µm.

8) Can the NTBs and EZ revival events, the shrinking and reddening of the Great Red Spot (GRS), and the change in colour of Oval BA be related to changes in cloud structure and ammonia gas?

In section 5.3, we showed that the NTBs revival itself was associated with elevated aerosol abundances over all altitudes detected by MUSE, as well as an apparent local suppression of ammonia gas, presumably due to the formation of cloud. These were all indications of substantial upwelling that preceded the reformation of the bright red band around the NTBs. What was most curious however, was that **the bright red haze band was still detectable in the NTBs more than a year after the upheaval, but was not discernable in any way in the associated cloud structure or ammonia abundance profile, which had long since reverted back almost to its pre-upheaval state**. This may have been an indication of the presence of a chromophore layer in a stable region of the atmosphere (presumably close to the tropopause) which takes of the order of years to either chemically decompose or sediment down towards the cloud layers below. Likewise, we also observed that the shrinking of the GRS coincided with both its reddening and increased aerosol density over all measurable altitudes, particularly in the 'eye wall' of the GRS, as was also observed by Simon et al. [2018]. However, **we observed no discernable change in either cloud structure or ammonia abundance associated with Oval BA's colour change from red to white**, similar to what was observed in Oval BA's previous colour change in 2006. We can therefore only assume that Oval BA's colour change must be a result of local temperature variations that could sublimate ammonia ice around chromophore nuclei. Retrievals of the EZ upheaval event appear to suggest little initial correlation between cloud structure and colour, but this could change as the event progresses and more reliable MUSE data is obtained.

7.3 Future work

Analysis of upheavals in Jupiter's southern hemisphere

In this thesis, we focussed mostly on retrieving cloud structure and colour relating to upheavals and outbreaks in Jupiter's northern tropics. However, there is also a wealth of information contained in the MUSE data on similar upheavals in the southern tropics that we did not have the time or space to cover here. We would like to highlight several events in particular for which MUSE retrievals could prove enlightening:

- Multiple outbreaks in the mid-SEB occurred at the end of December 2016 going on to January 2017 [Rogers, 2016, Mizumoto, 2017]. Several of these are clearly seen to interact in our first 2017 dataset (2017-01-10T07:43:03.128). The outbreaks resulted in substantial turbulence and disruption to the structure of the northern SEB that was visible throughout 2017. We note that this region often provides some of the poorest fits to our MUSE spectra using the cloud model we perfected in chapter 4 (as can be seen particularly in the 2017-05-15T02:01:59.328 dataset), and therefore deserves further investigation.
- An interaction between Oval BA and the GRS in mid-2017 led to a change in the latitudinal structure of the STropZ, and in February 2018 a feature formed in the STropZ (the 'STropZ disturbance') which interacted with the GRS around the time we acquired MUSE dataset 2018-04-09T06:04:06.918. In most of our 2018 MUSE datasets, we find the northern STropZ to be unusually bright at wavelengths sensitive to both tropospheric cloud and high-altitude haze.
- In early 2019 we observed the first signs of a fading in colour of the northern SEB. This usually marks the start of a major upheaval cycle known as an 'SEB revival' event, which has received by far the most study out of all of Jupiter's major upheavals, particularly the events in 1972-75 [Orton et al., 1981], 1989-1990 [Satoh and Kawabata, 1992, Kuehn and Beebe, 1993, Satoh and Kawabata, 1994], 1992-93 [Sánchez-Lavega and Gomez, 1996, Moreno et al., 1997] and 2009-2011 [Fletcher et al., 2011b, Pérez-Hoyos et al., 2012, Fletcher et al., 2017b]. We have been granted four hours of MUSE observation time of Jupiter between April and September

2019, including observations to coincide with each of the four Juno perijoves (PJ19-22) as well as a set of global observations at solar opposition in June 2019. This will present a perfect time series in order to study the temporal evolution of the SEB revival.

Analysis of mid-latitudes and of White Spot Z

White Spot Z (WSZ) was, until the NTBs upheaval, one of the most distinct discrete features on Jupiter after the GRS and Oval BA. Although originally white following its inception in 1997, it turned red in 2013, then back to white a few years later, and then went through multiple colour changes after the NTBs upheaval. These were also accompanied by changes in brightness at 0.89µm. We already have an observation of WSZ during its first red phase (2014-02-17T00:16:32.439), as well as another observation when it first turned white again (2016-04-01T05:39:03.340), and preliminary retrievals of WSZ from these observations show great promise, even despite the lack of spatial resolution. WSZ is more difficult to make out in more recent observations (such as 2017-01-10T07:43:03.128 and 2018-04-14T09:00:50.919), but it could become more distinct again in the future. In addition, a number of other red spots formed in the NEB and NTropZ following the NTBs upheaval that could merit study. We have proposed a trial observation of Jupiter in 2019 using adaptive optics, which will hopefully allow us to resolve the fine structure of smaller, less distinct discrete features than we were able to using previous MUSE observations. This could include the series of anticyclonic white ovals present in the STB, whose individual properties and structure were found by Sindoni et al. [2017] to vary considerably from oval to oval.

Although the polar regions of Jupiter are very difficult to resolve with MUSE, and retrievals of spectra from these latitudes are slow for reasons previously explained in section 3.3, it is still possible to glean information about the mid-latitudes of Jupiter which have been almost completely neglected in this thesis. One aspect in particular that was neglected was the disturbances in the NNTB that were associated with the NTBs upheaval, with activity in the two regions often observed to have been coupled in previous revival events, as well as cyclical darkenings of regions of the NTZ (the 'North Temperate Disturbance') which usually occur a year or two after an NTBs upheaval, as it did in 2018.

Spatial differences in the spectral shape at short wavelengths

In our retrievals of the chromophore imaginary refractive index spectrum of both Jupiter and Saturn, we found that there was some spatial variability in the shape of spectra between around 0.51µm and 0.54µm. This could have been due to a number of factors as previously discussed, in terms of either genuine absorption features that are present in some regions and not in others, or in terms of our scattering and gas absorption models themselves. Although preliminary retrievals on Jupiter using a rudimentary model with changes in particle size with height were not seen to improve the fit to spectra substantially compared to a model with a constant particle size with height, there could be other factors at play which we have neglected, such as a poor size distribution around the effective radius, or assumptions about the shapes of the particles that resulted in erroneous scattering phase functions. These factors need to be fully ruled out before we can definitively say that variability at these wavelengths is due to a unique absorption feature. In the case of Saturn, spatial differences in the spectral shape at these wavelengths are more extreme, and span a wider range of wavelengths. This may require the use of a model with more than one chromophore.

Extension of chromophore absorption spectrum to a wider wavelength range

We have been granted a single trial observation each of Jupiter and Saturn in 2019 using MUSE's extended wavelength range (0.46-0.93µm), as opposed to all previous observations which were obtained using MUSE's nominal wavelength range (listed as 0.48-0.93µm, though in practice it is closer to 0.476-0.933µm and we assume a similar discrepancy in our favour to be the case with the extended wavelength range). This will allow us to see to what extent the shape of our chromophore absorption spectra can be extrapolated into the blue, as well as provide a better constraint on the altitude of the chromophore layer (particularly on its upper bound). A major disadvantage with using MUSE's extended wavelength range is the presence of greater second-order contamination over a wider wavelength range than in our previous data obtained using MUSE's nominal wavelength range, as stated in the MUSE user manual which we provided a link to in section 2.1. Although we are not fully aware of the detriment of second-order contamination to observations of Saturn using the extended wavelength range, we demonstrated in section 2.4.3 that the effect on observations of Jupiter at wavelengths above approximately 0.905µm was substantial, even using MUSE's nominal wavelength range. We predict that the effect would dominate observations of Jupiter at 0.89µm, making reliable retrievals of high-altitude haze impossible. Analysis of the extended wavelength range would therefore require either some sort of correction in post-processing (eg. Stanishev [2007]), the exclusive use of limb darkening so that small-scale variations in I/F can be averaged over viewing zenith angle, or the exclusion of the most affected wavelengths entirely.

We have also attempted to extend our analysis ourselves to a wavelength range of 0.4µm to 1.0µm by using Cassini/VIMS-V data, but sadly we are unable to calibrate the VIMS-V spectra using available versions of the calibration software. However, VIMS-V spectra of Jupiter and Saturn are being successfully analysed by other research groups currently [Sromovsky et al., 2017, Fry and Sromovsky, 2018], due to their use of an older, functioning edition of the calibration software that we are unable to access. The chromophore imaginary refractive index spectra we have retrieved in this thesis can therefore be extended to a wider wavelength range in the VIMS-V spectra either through close collaboration or through a future update in the calibration software. There is also the potential to make use of HST/WFC3 data from the OPAL program (as previously described in Chapter 2), for which additional observations at blue and near-UV wavelengths exist (particularly in wavelength filters F343N, F395N and F467M), in order to extend our analysis shortward to the required wavelength range, albeit at much lower spectral resolution than would be possible using VIMS-V.

Joint visible, near-infrared and thermal infrared analysis of the GRS

Within an hour of our MUSE dataset from 2018-05-25T04:22:34.417, a series of observations of the GRS were also made using the VLT/VISIR instrument (Fletcher and Donnelly, personal communication). We stress that the proximity in time of the MUSE and VISIR observations was entirely unplanned and coincidental on both our parts, our MUSE observations being conducted entirely in service mode and therefore planned by on-site observers according to their own timetabling concerns. These VISIR observations consisted of a number of individual images of Jupiter obtained at single wavelength filters ranging from 5µm to 19.5µm, sensitive to both 2-3 bar cloud and upper tropospheric haze, as well as upper tropospheric ammonia abundances and temperature profiles, and stratospheric methane abundances. In addition, they also have substantially greater spatial resolution than MUSE. However, these VISIR observations do not have the same constraint on the actual altitudes at which these aerosol densities occur that our MUSE observations do, and they also contain no information about ammonia abundances near the cloud layers themselves (and it goes without saying that they contain no information about chromophore either). Our MUSE data and their VISIR images can therefore complement each other to provide a more precise vertical constraint on spatial variations in tropospheric cloud structure and gaseous ammonia abundances across the surface of the GRS, together with both temperature and chromophore, without having to take significant temporal variability into account. This could therefore provide a better constraint on the origin of chromophore in the GRS and the altitude at which it is either formed or exposed, by looking at the extent to which ammonia is depleted with height. In addition, it could also get rid of particle size degeneracies that affect the haze aerosol densities that we retrieve from MUSE alone.

Theoretical constraints using a microphysical model

One of the major issues in the constraint of vertical aerosol distribution is the lack of observational constraints on particle size distribution, particularly that of chromophore. This prevents us from providing a physically consistent hypothesis as to why a universal chromophore would exist in red regions of Jupiter, but not in the zones. We suggest feeding the results that we have obtained in this thesis into a microphysical model that has already been developed for ice giant atmospheres by Toledo and Irwin [2017]. This will provide theoretical constraints on a) the particle size distribution of the upper tropospheric haze, in order to better constrain our retrieved vertical aerosol profiles; b) the altitude in the atmosphere at which a chromophore layer of the particle size that we have retrieved in this thesis would remain stable (particularly in the NTBs), and hence validate our hypothesis as to the presence of a universal chromophore in all the regions we observe it; c) whether chromophore particles can act as cloud condensation nuclei in the zones, and what degree of ammonia depletion would be required to mask their presence relative to the belts; and d) the composition of the deepest visible cloud layer given the ammonia gas abundances we have retrieved in this analysis.

Bibliography

J. R. Acarreta and A. Sánchez-Lavega. Vertical Cloud Structure in Saturn's 1990 Equatorial Storm. *Icarus*, 137:24–33, 1999. doi: 10.1006/icar.1998.6034.

R. K. Achterberg, B. J. Conrath, and P. J. Gierasch. Cassini CIRS Retrievals of Ammonia in Jupiter's Upper Troposphere. *Icarus*, 182:169–180, 2006. doi: 10.1016/j.icarus.2005.12.020.

A. Adriani, A. Coradini, G. Filacchione, J. I. Lunine, A. Bini, C. Pasqui, L. Calamai, B. M. Colosimo, F.and Dinelli, D. Grassi, et al. JIRAM, the Image Spectrometer in the Near Infrared On Board the Juno Mission to Jupiter. *Astrobiology*, 8:613–622, 2008. doi: 10.1089/ast.2007.0167.

D. G. Andrews. *An Introduction to Atmospheric Physics.* Cambridge University Press, 2010.

A. Antuñano, L. N. Fletcher, G. S. Orton, H. Melin, J. H. Rogers, J. Harrington, P. T. Donnelly, N. Rowe-Gurney, and J. S. D. Blake. Infrared Characterisation of Jupiter's Equatorial Disturbance Cycle. *Geophysical Research Letters*, 45:10, 2018. doi: 10.1029/2018GL080382.

R. Arsenault, P.-Y. Madec, N. Hubin, S. Stroebele, J. Paufique, E. Vernet, W. Hackenberg, J.-F. Pirard, L. Jochum, A. Glindemann, A. Jost, R. Conzelmann, et al. Manufacturing of the ESO Adaptive Optics Facility. In *Adaptive Optics Systems II*, volume 7736, page 77360L, 2010.

X. S. Asay-Davis, P. S. Marcus, M. H. Wong, and I. de Pater. Jupiter's Shrinking Great Red Spot and Steady Oval BA: Velocity Measurements with the 'Advection Corrected Correlation Image Velocimetry' Automated Cloud-Tracking Method. *Icarus*, 203:164–188, 2009. doi: 10.1016/j.icarus.2009.05.001.

S. W. Asmar, S. J. Bolton, D. R. Buccino, T. P. Cornish, W. M. Folkner, R. Formaro, L. Iess, A. P. Jongeling, D. K. Lewis, A. P. Mittskus, R. Mukai, and L. Simone. The Juno Gravity Science Instrument. *Space Science Reviews*, 213:205–218, 2017. doi: 10.1007/s11214-017-0428-7.

S. K. Atreya and P. N. Romani. Photochemistry and Clouds of Jupiter, Saturn and Uranus. *Recent Advances in Planetary Meteorology*, 17:68, 1985.

S. K. Atreya, M. H. Wong, T. C. Owen, P. R. Mahaffy, H. B. Niemann, I. De Pater, P. Drossart, and T. Encrenaz. A Comparison of the Atmospheres of Jupiter and Saturn: Deep Atmospheric Composition, Cloud Structure, Vertical Mixing, and Origin. *Planetary and Space Science*, 47: 1243–1262, 1999.

S. K. Atreya, A. S. Wong, K. H. Baines, M. H. Wong, and T. C. Owen. Jupiter's Ammonia Clouds - Localized or Ubiquitous? *Planetary and Space Science*, 53:498–507, 2005. doi: 10.1016/j.pss.2004.04.002.

R. Bacon, M. Accardo, L. Adjali, H. Anwand, S. Bauer, I. Biswas, J. Blaizot, D. Boudon, S. Brau-Nogue, J. Brinchmann, et al. The MUSE Second-Generation VLT Instrument. In *Ground-based and Airborne Instrumentation for Astronomy III*, volume 7735 of *Proc. SPIE*, page 773508, 2010. doi: 10.1117/12.856027.

F. Bagenal, T. E. Dowling, and W. B. McKinnon. *Jupiter: The Planet, Satellites and Magnetosphere*, volume 1. Cambridge University Press, 2007.

K. H. Baines, R. W. Carlson, and L. W. Kamp. Fresh Ammonia Ice Clouds in Jupiter: I. Spectroscopic Identification, Spatial Distribution, and Dynamical Implications. *Icarus*, 159:74–94, 2002. doi: 10.1006/icar.2002.6901.

K. H. Baines, L. A. Sromovsky, R. W. Carlson, T. W. Momary, and P. M. Fry. The Visual Spectrum of Jupiter's Great Red Spot Accurately Modeled with Aerosols Produced by Photolyzed Ammonia Reacting with Acetylene. *Icarus*, 330:217–229, 2019. doi: 10.1016/j.icarus.2019.04.008.

P. Ballester, K. Banse, S. Castro, R. Hanuschik, R. N. Hook, C. Izzo, Y. Jung, A. Kaufer, J. M. Larsen, T. Licha, et al. Data Reduction Pipelines for the Very Large Telescope. In *SPIE Astronomical Telescopes+ Instrumentation*, volume 6270, page 62700T. International Society for Optics and Photonics, 2006.

D. Banfield, B. J. Conrath, P. J. Gierasch, P. D. Nicholson, and K. Matthews. Near-IR Spectrophotometry of Jovian Aerosols - Meridional and Vertical Distributions. *Icarus*, 134:11–23, 1998a. doi: 10.1006/icar.1998.5942.

D. Banfield, P. J. Gierasch, M. Bell, E. Ustinov, A. P. Ingersoll, A. R. Vasavada, Robert A. West, and M. J. S. Belton. Jupiter's Cloud Structure from Galileo Imaging Data. *Icarus*, 135:230–250, 1998b. doi: 10.1006/icar.1998.5985.

J. K. Barstow. *Global Cloud Properties on Venus from Orbital Infrared Spectroscopy.* DPhil Thesis, University of Oxford, 2012.

J. K. Barstow, Patrick G. J. Irwin, L. N. Fletcher, R. S. Giles, and C. Merlet. Probing Saturn's Tropospheric Cloud with Cassini/VIMS. *Icarus*, 271:400–417, 2016. doi: 10.1016/j.icarus.2016.01.013.

M. J. S. Belton and H. Spinrad. H_2 Pressure-Induced Lines in the Spectra of the Major Planets. *Astrophysical Journal*, 185:363–372, 1973. doi: 10.1086/152424.

J. Benton. ALPO Observations of Saturn During the 2013 - 2014 Apparition. *Journal of the Association of Lunar and Planetary Observers, the Strolling Astronomer*, 60(4):74–92, 2018.

G. L. Berge and S. Gulkis. Earth-Based Observations of Jupiter: Millimeter to Meter Wavelengths. In *Jupiter*, pages 621–692, 1976.

D. Blain, T. Fouchet, T. Greathouse, T. Encrenaz, B. Charnay, B. Bézard, C. Li, E. Lellouch, G. Orton, L. N. Fletcher, and P. Drossart. Mapping of Jupiter's Tropospheric NH_3 Abundance Using Ground-Based IRTF/TEXES Observations at 5 μm. *Icarus*, 314:106–120, 2018. doi: 10.1016/j.icarus.2018.06.002.

S. J. Bolton, J. Lunine, D. Stevenson, J. E.P. Connerney, S. Levin, T. C. Owen, F. Bagenal, D. Gautier, A. P. Ingersoll, G. S. Orton, et al. The Juno Mission. *Space Science Reviews*, 213:5–37, 2017. doi: 10.1007/s11214-017-0429-6.

A. Borysow and L. Frommhold. Collision-Induced Infrared Spectra of H_2 - He Pairs at Temperatures from 18 to 7000 K. II - Overtone and Hot Bands. *Astrophysical Journal*, 341:549–555, 1989. doi: 10.1086/167515.

A. Borysow, J. Borysow, and Y. Fu. Semi-Empirical Model of Collision-Induced Absorption Spectra of H_2 - H_2 Complexes in the Second Overtone Band of Hydrogen at Temperatures from 50 to 500 K. *Icarus*, 145:601–608, 2000. doi: 10.1006/icar.2000.6384.

N. E. Bowles. *Infrared Spectroscopy to Support Measurement of the Atmosphere of the Planet Jupiter.* DPhil Thesis, University of Oxford, 2003.

N. E. Bowles, S. Calcutt, P. Irwin, and J. Temple. Band Parameters for Self-Broadened Ammonia Gas in the Range 0.74 to 5.24 μm to Support Measurements of the Atmosphere of the Planet Jupiter. *Icarus*, 196:612–624, 2008. doi: 10.1016/j.icarus.2007.12.029.

C. Brassé, O. Muñoz, P. Coll, and F. Raulin. Optical Constants of Titan Aerosols and Their Tholin Analogs: Experimental Results and Modeling/Observational Data. *Planetary and Space Science*, 109:159–174, 2015. doi: 10.1016/j.pss.2015.02.012.

T. Y. Brooke, R. F. Knacke, T. Encrenaz, P. Drossart, and D. Crisp. Models of the ISO 3-μm Reflectance Spectrum of Jupiter. *Icarus*, 136:1–13, 1998. doi: 10.1006/icar.1998.6013.

R. H. Brown, K. H. Baines, G. Bellucci, J.-P. Bibring, B. J. Buratti, F. Capaccioni, P. Cerroni, R. N. Clark, A. Coradini, D. P. Cruikshank, et al. The Cassini Visual and Infrared Mapping Spectrometer (VIMS) Investigation. *Space Science Reviews*, 115:111–168, 2004. doi: 10.1007/s11214-004-1453-x.

S. Brown, M. Janssen, V. Adumitroaie, S. Atreya, S. Bolton, S. Gulkis, A. Ingersoll, S. Levin, C. Li, and L. Li. Prevalent Lightning Sferics at 600 Megahertz near Jupiter's Poles. *Nature*, 558:87–90, 2018. doi: 10.1038/s41586-018-0156-5.

B. E. Carlson, W. B. Rossow, and G. S. Orton. Cloud Microphysics of the Giant Planets. *Journal of the Atmospheric Sciences*, 45:2066–2081, 1988.

R. Carlson, W. Smythe, K. Baines, E. Barbinis, K. Becker, R. Burns, S. Calcutt, W. Calvin, R. Clark, G. Danielson, A. Davies, P. Drossart, T. Encrenaz, et al. Near-Infrared Spectroscopy and Spectral Mapping of Jupiter and the Galilean Satellites: Results from Galileo's Initial Orbit. *Science*, 274: 385–388, 1996. doi: 10.1126/science.274.5286.385.

R. W. Carlson, K. H. Baines, M. S. Anderson, G. Filacchione, and A. A. Simon. Chromophores from Photolyzed Ammonia Reacting with Acetylene: Application to Jupiter's Great Red Spot. *Icarus*, 274:106–115, 2016. doi: 10.1016/j.icarus.2016.03.008.

K. Chance and R. L. Kurucz. An Improved High-Resolution Solar Reference Spectrum for Earth's Atmosphere Measurements [sic] in the Ultraviolet, Visible, and Near Infrared. *Journal of Quantitative Spectroscopy and Radiative Transfer*, 111(9):1289–1295, 2010. doi: 10.1016/j.jqsrt.2010.01.036.

D. S. Choi, D. Banfield, P. Gierasch, and A. P. Showman. Velocity and Vorticity Measurements of Jupiter's Great Red Spot Using Automated Cloud Feature Tracking. *Icarus*, 188:35–46, 2007. doi: 10.1016/j.icarus.2006.10.037.

P. A. Coles, R. I. Ovsyannikov, O. L. Polyansky, S. N. Yurchenko, and J. Tennyson. Improved Potential Energy Surface and Spectral Assignments for Ammonia in the Near-Infrared Region. *Journal of Quantitative Spectroscopy and Radiative Transfer*, 219:199–212, 2018. doi: 10.1016/j.jqsrt.2018.07.022.

J. E. P. Connerney, M. Benn, J. B. Bjarno, T. Denver, J. Espley, J. L. Jorgensen, P. S. Jorgensen, P. Lawton, A. Malinnikova, J. M. Merayo, et al. The Juno Magnetic Field Investigation. *Space Science Reviews*, 213:39–138, 2017. doi: 10.1007/s11214-017-0334-z.

B. J. Conrath and D. Gautier. Saturn Helium Abundance: A Reanalysis of Voyager Measurements. *Icarus*, 144:124–134, 2000. doi: 10.1006/icar.1999.6265.

E. Dahl, N. J. Chanover, D. Voelz, D. Kuehn, R. Hull, P. D. Strycker, and K. H. Baines. Preliminary Radiative Transfer Analysis of Hyperspectral Image Cubes of Jupiter Acquired During Juno's 13th Perijove Pass. In *AAS/Division for Planetary Sciences Meeting Abstracts*, volume 50, page 214.17, 2018.

J. V. Dave. *Subroutines for Computing the Parameters of the Electromagnetic Radiation Scattered by a Sphere*. IBM Palo Alto Scientific Center, 1968.

I. de Pater, M. H. Wong, P. Marcus, S. Luszcz-Cook, M. Ádámkovics, A. Conrad, X. Asay-Davis, and C. Go. Persistent Rings In and Around Jupiter's Anticyclones - Observations and Theory. *Icarus*, 210:742–762, 2010. doi: 10.1016/j.icarus.2010.07.027.

I. de Pater, R. J. Sault, M. H. Wong, L. N. Fletcher, D. DeBoer, and B. Butler. Jupiter's Ammonia Distribution Derived from VLA maps at 3-37 GHz. *Icarus*, 322:168–191, 2019. doi: 10.1016/j.icarus.2018.11.024.

T. E. Dowling and A. P. Ingersoll. Potential Vorticity and Layer Thickness Variations in the Flow Around Jupiter's Great Red Spot and White Oval BC. *Journal of Atmospheric Sciences*, 45:1380–1396, 1988.

P. Drossart, M. Roos-Serote, T. Encrenaz, E. Lellouch, R. W. Carlson, K. H. Baines, L. Kamp, G. S. Orton, S. Calcutt, and P. Irwin. The Solar Reflected Component in Jupiter's 5-μ Spectra from NIMS/Galileo Observations. *Journal of Geophysical Research*, 103:23043–23050, 1998. doi: 10.1029/98JE01899.

S. G. Edgington, S. K. Atreya, L. M. Trafton, J. J. Caldwell, R. F. Beebe, A. A. Simon, R. A. West, and C. Barnet. On the Latitude Variation of Ammonia, Acetylene, and Phosphine Altitude

Profiles on Jupiter from HST Faint Object Spectrograph Observations. *Icarus*, 133:192–209, 1998. doi: 10.1006/icar.1998.5925.

S. G. Edgington, S. K. Atreya, L. M. Trafton, J. J. Caldwell, R. F. Beebe, A. A. Simon, and R. A. West. Ammonia and Eddy Mixing Variations in the Upper Troposphere of Jupiter from HST Faint Object Spectrograph Observations. *Icarus*, 142:342–356, 1999. doi: 10.1006/icar.1999.6228.

S. G. Edgington, S. K. Atreya, E. H. Wilson, R. A. West, K. H. Baines, G. L. Bjoraker, L. N. Fletcher, and T. Momary. Photochemistry in Saturn's Ring Shadowed Atmosphere: Production Rates of Key Atmospheric Molecules and Preliminary Analysis of Observations. In *AGU Fall Meeting Abstracts*, 2012.

F. Feroz and M. P. Hobson. Multimodal Nested Sampling: An Efficient and Robust Alternative to Markov Chain Monte Carlo Methods for Astronomical Data Analyses. *Monthly Notices of the Royal Astronomical Society*, 384:449–463, 2008. doi: 10.1111/j.1365-2966.2007.12353.x.

J. P. Ferris and Y. Ishikawa. HCN and Chromophore Formation on Jupiter. *Nature*, 326:777, 1987. doi: 10.1038/326777a0.

J. P. Ferris and Y. Ishikawa. Formation of Hydrogen Cyanide and Acetylene Oligomers by Photolysis of Ammonia in the Presence of Acetylene: Applications to the Atmospheric Chemistry of Jupiter. *Journal of the American Chemical Society*, 110(13):4306–4312, 1988. doi: 10.1021/ja00221a033.

R. O. Fimmel. Pioneer Odyssey. *NASA STI/Recon Technical Report N*, 77, 1977.

F. M. Flasar, R. K. Achterberg, B. J. Conrath, J. C. Pearl, G. L. Bjoraker, D. E. Jennings, P. N. Romani, A. A. Simon-Miller, V. G. Kunde, C. A. Nixon, et al. Temperatures, Winds, and Composition in the Saturnian System. *Science*, 307:1247–1251, 2005. doi: 10.1126/science.1105806.

L. N. Fletcher. Cycles of Activity in the Jovian Atmosphere. *Geophysical Research Letters*, 44: 4725–4729, 2017. doi: 10.1002/2017GL073806.

L. N. Fletcher, P. G. J. Irwin, N. A. Teanby, G. S. Orton, P. D. Parrish, S. B. Calcutt, N. Bowles, R. de Kok, C. Howett, and F. W. Taylor. The Meridional Phosphine Distribution in Saturn's Upper Troposphere from Cassini/CIRS Observations. *Icarus*, 188:72–88, 2007. doi: 10.1016/j.icarus.2006.10.029.

L. N. Fletcher, G. S. Orton, N. A. Teanby, and P. G. J. Irwin. Phosphine on Jupiter and Saturn from Cassini/CIRS. *Icarus*, 202:543–564, 2009. doi: 10.1016/j.icarus.2009.03.023.

L. N. Fletcher, G. S. Orton, N. A. Teanby, P. G. J. Irwin, and G. L. Bjoraker. Methane and its Isotopologues on Saturn from Cassini/CIRS Observations. *Icarus*, 199:351–367, 2009. doi: 10.1016/j.icarus.2008.09.019.

L. N. Fletcher, R. K. Achterberg, T. K. Greathouse, G. S. Orton, B. J. Conrath, A. A. Simon-Miller, N. Teanby, S. Guerlet, P. G. J. Irwin, and F. M. Flasar. Seasonal Change on Saturn from Cassini/CIRS Observations, 2004–2009. *Icarus*, 208:337–352, 2010a. doi: 10.1016/j.icarus.2010.01.022.

L. N. Fletcher, G. S. Orton, O. Mousis, P. Yanamandra-Fisher, P. D. Parrish, P. G. J. Irwin, B. M. Fisher, L. Vanzi, T. Fujiyoshi, T. Fuse, et al. Thermal Structure and Composition of Jupiter's Great Red Spot from High-Resolution Thermal Imaging. *Icarus*, 208:306–328, 2010b. doi: 10.1016/j.icarus.2010.01.005.

L. N. Fletcher, K. H. Baines, T. W. Momary, A. P. Showman, P. G. J. Irwin, G. S. Orton, M. Roos-Serote, and C. Merlet. Saturn's Tropospheric Composition and Clouds from Cassini/VIMS 4.6–5.1 μm Nightside Spectroscopy. *Icarus*, 214:510–533, 2011a. doi: 10.1016/j.icarus.2011.06.006.

L. N. Fletcher, G. S. Orton, J. H. Rogers, A. A. Simon-Miller, I. de Pater, M. H. Wong, O. Mousis, P. G. J. Irwin, M. Jacquesson, and P. A. Yanamandra-Fisher. Jovian Temperature and Cloud Variability During the 2009-2010 Fade of the South Equatorial Belt. *Icarus*, 213:564–580, 2011b. doi: 10.1016/j.icarus.2011.03.007.

L. N. Fletcher, T. K. Greathouse, J. I. Moses, S. Guerlet, and R. A. West. Saturn's Seasonally Changing Atmosphere: Thermal Structure, Composition and Aerosols. In *Saturn in the 21st Century*. Cambridge University Press, 2015.

L. N. Fletcher, T. K. Greathouse, G. S. Orton, J. A. Sinclair, R. S. Giles, P. G. J. Irwin, and T. Encrenaz. Mid-Infrared Mapping of Jupiter's Temperatures, Aerosol Opacity and Chemical Distributions with IRTF/TEXES. *Icarus*, 278:128–161, 2016. doi: 10.1016/j.icarus.2016.06.008.

L. N. Fletcher, S. Guerlet, G. S. Orton, R. G. Cosentino, T. Fouchet, P. G. J. Irwin, L. Li, F. M. Flasar, N. Gorius, and R. Morales-Juberías. Disruption of Saturn's Quasi-Periodic Equatorial Oscillation by the Great Northern Storm. *Nature Astronomy*, 1:765, 2017a. doi: 10.1038/s41550-017-0271-5.

L. N. Fletcher, G. S. Orton, J. H. Rogers, R. S. Giles, A. V. Payne, P. G. J. Irwin, and M. Vedovato.

Moist Convection and the 2010-2011 Revival of Jupiter's South Equatorial Belt. *Icarus*, 286: 94–117, 2017b. doi: 10.1016/j.icarus.2017.01.001.

L. N. Fletcher, G. S. Orton, J. A. Sinclair, P. Donnelly, H. Melin, J. H. Rogers, T. K. Greathouse, Y. Kasaba, T. Fujiyoshi, T. M. Sato, et al. Jupiter's North Equatorial Belt Expansion and Thermal Wave Activity Ahead of Juno's Arrival. *Geophysical Research Letters*, 44:7140–7148, 2017c. doi: 10.1002/2017GL073383.

J. Fortney. A Deeper Look at Jupiter. *Nature*, 555:168–169, 2018. doi: 10.1038/d41586-018-02612-y.

T. Fouchet, J. I. Moses, and B. J. Conrath. Saturn: Composition and Chemistry. In Michele Dougherty, Larry Esposito, and Stamatios Krimigis, editors, *Saturn from Cassini-Huygens*. Springer Science & Business Media, 2009.

A. J. Friedson, A.-S. Wong, and Y. L. Yung. Models for Polar Haze Formation in Jupiter's Stratosphere. *Icarus*, 158:389–400, 2002. doi: 10.1006/icar.2002.6885.

P. M. Fry and L. Sromovsky. Using HST Bandpass Filter Images from the OPAL Program to Test the Ability of Candidate Chromophores to Model Spatial and Temporal Variations on Jupiter. In *AAS/Division for Planetary Sciences Meeting Abstracts*, volume 50, page 119.13, 2018.

R. Garland and P. G. J. Irwin. Effectively Calculating Gaseous Absorption in Radiative Transfer Models of Exoplanetary and Brown Dwarf Atmospheres. *arXiv e-prints*, 2019.

T. Gehrels. The Results of the Imaging Photopolarimeter on Pioneers 10 and 11. In *IAU Colloq. 30: Jupiter: Studies of the Interior, Atmosphere, Magnetosphere and Satellites*, pages 531–563, 1976.

S. Geman, E. Bienenstock, and R. Doursat. Neural Networks and the Bias/Variance Dilemma. *Neural Computation*, 4(1):1–58, 1992. doi: 10.1162/neco.1992.4.1.1.

P. J. Gierasch, B. J. Conrath, J. A. Magalha, et al. Zonal Mean Properties of Jupiter's Upper Troposphere from Voyager Infrared Observations. *Icarus*, 67:456–483, 1986. doi: 10.1016/0019-1035(86) 90125-9.

R. S. Giles. *Jupiter's Tropospheric Composition and Cloud Structure from 5μm Spectroscopy.* DPhil Thesis, University of Oxford, 2016.

R. S. Giles, L. N. Fletcher, and P. G. J. Irwin. Cloud Structure and Composition of Jupiter's Troposphere from 5-μm Cassini VIMS Spectroscopy. *Icarus*, 257:457–470, 2015. doi: 10.1016/j.icarus.2015.05.030.

F. C. Gillett, F. J. Low, and W. A. Stein. The 2.8-14 micron Spectrum of Jupiter. *The Astrophysical Journal*, 157:925, 1969. doi: 10.1086/150124.

L. P. Giver. Intensity Measurements of the CH_4 Bands in the Region 4350 Å to 10,600 Å. *Journal of Quantitative Spectroscopy and Radiative Transfer*, 19(3):311–322, 1978.

G. R. Gladstone, S. Persyn, J. Eterno, D. C. Slater, M. W. Davis, M. H. Versteeg, K. B. Persson, O. H. Siegmund, B. Marquet, J. Gerard, and D. C. Grodent. The Ultraviolet Spectrograph (UVS) on Juno. *AGU Fall Meeting Abstracts*, pages SM41B–1678, 2008.

R. Goody, R. West, L. Chen, and D. Crisp. The Correlated-K Method for Radiation Calculations in Nonhomogeneous Atmospheres. *Journal of Quantitative Spectroscopy and Radiative Transfer*, 42(6):539–550, 1989. doi: 10.1016/0022-4073(89)90044-7.

R. M. Goody and Y. L. Yung. *Atmospheric Radiation: Theoretical Basis*. Oxford University Press, 1995.

J.-C. Guillemin, S. El Chaouch, A. Bouayad, and T. Janati. Partial Pressures and Nature of Products. Application to the Photolysis of PH_3 and NH_3 in the Atmosphere of Jupiter and Saturn. *Advances in Space Research*, 27:245–253, 2001. doi: 10.1016/S0273-1177(01)00054-0.

T. Guillot, D. J. Stevenson, W. B. Hubbard, and D. Saumon. The Interior of Jupiter. *Jupiter: The Planet, Satellites and Magnetosphere*, pages 35–57, 2004.

R. A. Hanel, B. J. Conrath, D. E. Jennings, and R. E. Samuelson. *Exploration of the Solar System by Infrared Remote Sensing*. Cambridge University Press, 2003.

C. J. Hansen, M. A. Caplinger, A. Ingersoll, M. A. Ravine, E. Jensen, S. Bolton, and G. Orton. JunoCam: Juno's Outreach Camera. *Space Science Reviews*, pages 1–32, 2014. doi: 10.1007/s11214-014-0079-x.

J. E. Hansen. Multiple Scattering of Polarized Light in Planetary Atmospheres Part II. Sunlight Reflected by Terrestrial Water Clouds. *Journal of the Atmospheric Sciences*, 28:1400–1426, 1971.

J. E. Hansen and L. D. Travis. Light Scattering in Planetary Atmospheres. *Space Science Reviews*, 16:527–610, 1974. doi: 10.1007/BF00168069.

L. G. Henyey and J. L. Greenstein. Diffuse Radiation in the Galaxy. *The Astrophysical Journal*, 93: 70–83, 1941. doi: 10.1086/144246.

G. Herzberg. *Infrared and Raman Spectra of Polyatomic Molecules.* D. Van Nostrand Company.; New York, 1945.

C. W. Hord, R. A. West, K. E. Simmons, D. L. Coffeen, M. Sato, A. L. Lane, and J. T. Bergstralh. Photometric Observations of Jupiter at 2400 Angstroms. *Science*, 206:956–959, 1979. doi: 10.1126/science.206.4421.956.

C. J. A. Howett, R. W. Carlson, P. G. J. Irwin, and S. B. Calcutt. Optical Constants of Ammonium Hydrosulfide Ice and Ammonia Ice. *Journal of the Optical Society of America B*, 24(1):126–136, 2007. doi: 10.1364/JOSAB.24.000126.

R. Hueso, J. Legarreta, S. Pérez-Hoyos, J. F. Rojas, A. Sánchez-Lavega, and A. Morgado. The International Outer Planets Watch Atmospheres Node Database of Giant-Planet Images. *Planetary and Space Science*, 58:1152–1159, 2010. doi: 10.1016/j.pss.2010.04.006.

R. Hueso, A. Sánchez-Lavega, P. Iñurrigarro, J. F. Rojas, S. Pérez-Hoyos, I. Mendikoa, J. M. Gómez-Forrellad, C. Go, D. Peach, F. Colas, et al. Jupiter Cloud Morphology and Zonal Winds from Ground-Based Observations Before and During Juno's First Perijove. *Geophysical Research Letters*, 2017. doi: 10.1002/2017GL073444.

J. Hurley, L. N. Fletcher, P. G. J. Irwin, S. B. Calcutt, J. A. Sinclair, and C. Merlet. Latitudinal Variation of Upper Tropospheric NH_3 on Saturn Derived from Cassini/CIRS Far-Infrared Measurements. *Planetary and Space Science*, 73:347–363, 2012. doi: 10.1016/j.pss.2012.08.003.

A. P. Ingersoll, T. E. Dowling, P. J. Gierasch, G. S. Orton, P. L. Read, A. Sánchez-Lavega, A. P. Showman, A. A. Simon-Miller, and A. R. Vasavada. Dynamics of Jupiter's Atmosphere. *Jupiter: The Planet, Satellites and Magnetosphere*, 105, 2004.

P. G. J. Irwin. *Giant Planets of Our Solar System: Atmospheres, Composition, and Structure.* Springer-Verlag, 2nd edition, 2008.

P. G. J. Irwin, A. L. Weir, S. E. Smith, F. W. Taylor, A. L. Lambert, S. B. Calcutt, P. J. Cameron-Smith, R. W. Carlson, K. Baines, G. S. Orton, et al. Cloud Structure and Atmospheric Composition of Jupiter Retrieved from Galileo Near-Infrared Mapping Spectrometer Real-Time Spectra. *Journal of Geophysical Research: Planets*, 103:23001–23021, 1998. doi: 10.1029/98JE00948.

P. G. J. Irwin, A. L. Weir, F. W. Taylor, S. B. Calcutt, and R. W. Carlson. The Origin of Belt/Zone Contrasts in the Atmosphere of Jupiter and their Correlation with 5-μm Opacity. *Icarus*, 149: 397–415, 2001. doi: 10.1006/icar.2000.6542.

P. G. J. Irwin, N. A. Teanby, R. De Kok, L. N. Fletcher, C. J. A. Howett, C. C. C. Tsang, C. F. Wilson, S. B. Calcutt, C. A. Nixon, and P. D. Parrish. The NEMESIS Planetary Atmosphere Radiative Transfer and Retrieval Tool. *Journal of Quantitative Spectroscopy and Radiative Transfer*, 109(6):1136–1150, 2008. doi: 10.1016/j.jqsrt.2007.11.006.

P. G. J. Irwin, D. S. Tice, L. N. Fletcher, J. K. Barstow, N. A. Teanby, G. S. Orton, and G. R. Davis. Reanalysis of Uranus' Cloud Scattering Properties from IRTF/SpeX Observations Using a Self-Consistent Scattering Cloud Retrieval Scheme. *Icarus*, 250:462–476, 2015. doi: 10.1016/j.icarus.2014.12.020.

P. G. J. Irwin, N. Bowles, A. S. Braude, R. Garland, and S. Calcutt. Analysis of Gaseous Ammonia (NH_3) Absorption in the Visible Spectrum of Jupiter. *Icarus*, 302:426–436, 2018. doi: 10.1016/j.icarus.2017.11.031.

P. G. J. Irwin, N. Bowles, A. S. Braude, R. Garland, S. Calcutt, P. A. Coles, S. N. Yurchenko, and J. Tennyson. Analysis of Gaseous Ammonia (NH_3) Absorption in the Visible Spectrum of Jupiter - Update. *Icarus*, 321:572–582, 2019a. doi: 10.1016/j.icarus.2018.12.008.

P. G. J. Irwin, D. Toledo, R. Garland, N. A. Teanby, L. N. Fletcher, G. S. Orton, and B. Bézard. Probable Detection of Hydrogen Sulphide (H_2S) in Neptune's Atmosphere. *Icarus*, 321:550–563, 2019b. doi: 10.1016/j.icarus.2018.12.014.

M. A. Janssen, S. T. Brown, J. E. Oswald, and A. Kitiyakara. Juno at Jupiter: The Juno Microwave Radiometer (MWR). In *2014 39th International Conference on Infrared, Millimeter, and Terahertz waves (IRMMW-THz)*, pages 1–3. IEEE, 2014.

K. S. Kalogerakis, J. Marschall, A. U. Oza, P. A. Engel, R. T. Meharchand, and M. H. Wong. The Coating Hypothesis for Ammonia Ice Particles in Jupiter: Laboratory Experiments and Optical Modeling. *Icarus*, 196:202–215, 2008. doi: 10.1016/j.icarus.2008.03.001.

E. Karkoschka. Spectrophotometry of the Jovian Planets and Titan at 300-to 1000-nm Wavelength [sic]: The Methane Spectrum. *Icarus*, 111:174–192, 1994. doi: 10.1006/icar.1994.1139.

E. Karkoschka. Methane, Ammonia, and Temperature Measurements of the Jovian Planets and Titan from CCD–Spectrophotometry. *Icarus*, 133:134–146, 1998. doi: 10.1006/icar.1998.5913.

E. Karkoschka and M. Tomasko. Saturn's Vertical and Latitudinal Cloud Structure 1991–2004 from HST Imaging in 30 Filters. *Icarus*, 179:195–221, 2005. doi: 10.1016/j.icarus.2005.05.016.

E. Karkoschka and M. G. Tomasko. Methane Absorption Coefficients for the Jovian Planets from Laboratory, Huygens, and HST Data. *Icarus*, 205:674–694, 2010. doi: 10.1016/j.icarus.2009.07.044.

J. A. Kaye and D. F. Strobel. HCN Formation on Jupiter: The Coupled Photochemistry of Ammonia and Acetylene. *Icarus*, 54:417–433, 1983. doi: 10.1016/0019-1035(83)90238-5.

J. A. Kaye and D. F. Strobel. Phosphine Photochemistry in the Atmosphere of Saturn. *Icarus*, 59: 314–335, 1984. doi: 10.1016/0019-1035(84)90105-2.

T. C. Keane. Mechanism for the Coupled Photochemistry of Ammonia and Acetylene: Implications for Giant Planets, Comets and Interstellar Organic Synthesis. *Origins of Life and Evolution of the Biosphere*, 47:223–248, 2017. doi: 10.1007/s11084-017-9545-2.

B. N. Khare, C. Sagan, E. T. Arakawa, F. Suits, T. A. Callcott, and M. W. Williams. Optical Constants of Organic Tholins Produced in a Simulated Titanian Atmosphere: From Soft X-ray to Microwave Frequencies. *Icarus*, 60:127–137, 1984. doi: 10.1016/0019-1035(84)90142-8.

S. J. Kim, C. K. Sim, T. S. Stallard, and R. Courtin. Spectral Characteristics and Formation of High-Altitude Haze in the South-Polar Regions of Saturn. *Icarus*, 321:436–444, 2019. doi: 10.1016/j.icarus.2018.12.004.

D. M. Kuehn and R. F. Beebe. A Study of the Time Variability of Jupiter's Atmospheric Structure. *Icarus*, 101:282–292, 1993. doi: 10.1006/icar.1993.1025.

W. S. Kurth, G. B. Hospodarsky, D. L. Kirchner, B. T. Mokrzycki, T. F. Averkamp, W. T. Robison, C. W. Piker, M. Sampl, and P. Zarka. The Juno Waves Investigation. *Space Science Reviews*, 213:347–392, 2017. doi: 10.1007/s11214-017-0396-y.

A. A. Lacis and V. Oinas. A Description of the Correlated K Distribution Method for Modeling Nongray Gaseous Absorption, Thermal Emission, and Multiple Scattering in Vertically Inhomogeneous Atmospheres. *Journal of Geophysical Research: Atmospheres*, 96:9027–9063, 1991. doi: 10.1029/90JD01945.

L. A. Lebofsky and M. B. Fegley. Laboratory Reflection Spectra for the Determination of Chemical Composition of Icy Bodies. *Icarus*, 28:379–387, 1976. doi: 10.1016/0019-1035(76)90151-2.

C. B. Leovy, A. J. Friedson, and G. S. Orton. The Quasiquadrennial Oscillation of Jupiter's Equatorial Stratosphere. *Nature*, 354:380–382, 1991. doi: 10.1038/354380a0.

J. S. Lewis. The Clouds of Jupiter and the NH_3-H_2O and NH_3-H_2S Systems. *Icarus*, 10:365–378, 1969. doi: 10.1016/0019-1035(69)90091-8.

J. S. Lewis and M. B. Fegley. Vertical Distribution of Disequilibrium Species in Jupiter's Troposphere. *Space Science Reviews*, 39:163–192, 1984. doi: 10.1007/BF00173673.

J. S. Lewis and R. G. Prinn. Jupiter's Clouds: Structure and Composition. *Science*, 169:472–473, 1970. doi: 10.1126/science.169.3944.472.

C. Li, A. Ingersoll, M. Janssen, S. Levin, S. Bolton, V. Adumitroaie, M. Allison, J. Arballo, A. Bellotti, S. Brown, et al. The Distribution of Ammonia on Jupiter from a Preliminary Inversion of Juno Microwave Radiometer Data. *Geophysical Research Letters*, 44:5317–5325, 2017. doi: 10.1002/2017GL073159.

C. Li, F. A. Oyafuso, S. T. Brown, V. Adumitroaie, A. Bellotti, J. K. Arballo, Y. S. Aglyamov, M. Allison, et al. Microwave Observations of Jupiter's Atmosphere from 1 bar to 200 bars. AGU Fall Meeting 2018, Results from the Investigation of Jupiter's Atmosphere by Juno and a Supporting Campaign of Earth-Based Observations, December 2018.

P. S. Lii, M. H. Wong, and I. de Pater. Temporal Variation of the Tropospheric Cloud and Haze in the Jovian Equatorial Zone. *Icarus*, 209:591–601, 2010.

M. J. Loeffler and R. L. Hudson. Coloring Jupiter's Clouds: Radiolysis of Ammonium Hydrosulfide (NH_4SH). *Icarus*, 302:418–425, 2018. doi: 10.1016/j.icarus.2017.10.041.

M. J. Loeffler, R. L. Hudson, N. J. Chanover, and A. A. Simon. Giant-Planet Chemistry: Ammonium Hydrosulfide (NH_4SH), its IR spectra and Thermal and Radiolytic Stabilities. *Icarus*, 258:181–191, 2015. doi: 10.1016/j.icarus.2015.06.015.

M. J. Loeffler, R. L. Hudson, N. J. Chanover, and A. A. Simon. The Spectrum of Jupiter's Great Red Spot: The Case for Ammonium Hydrosulfide (NH_4SH). *Icarus*, 271:265–268, 2016. doi: 10.1016/j.icarus.2016.02.010.

A. Lucchesini and S. Gozzini. Diode Laser Spectroscopy of Ammonia at 760 nm. *Optics Communications*, 282:3493–3498, 2009. doi: 10.1016/j.optcom.2009.05.049.

W. Macy. Inhomogeneous Models of the Atmosphere of Saturn. *Icarus*, 32:328–347, 1977. doi: 10.1016/0019-1035(77)90006-9.

A. Mahjoub, N. Carrasco, P.-R. Dahoo, T. Gautier, C. Szopa, and G. Cernogora. Influence of Methane Concentration on the Optical Indices of Titan's Aerosols Analogues. *Icarus*, 221:670–677, 2012. doi: 10.1016/j.icarus.2012.08.015.

J. V. Martonchik, G. S. Orton, and J. F. Appleby. Optical Properties of NH_3 Ice from the Far Infrared to the Near Ultraviolet. *Applied Optics*, 23:541–547, 1984. doi: 10.1364/AO.23.000541.

K. I. Matcheva, B. J. Conrath, P. J. Gierasch, and F. M. Flasar. The Cloud Structure of the Jovian Atmosphere As Seen by the Cassini/CIRS Experiment. *Icarus*, 179:432–448, 2005. doi: 10.1016/j.icarus.2005.06.020.

S. Matousek. The Juno New Frontiers Mission. *Acta Astronautica*, 61:932–939, 2007. doi: 10.1016/j.actaastro.2006.12.013.

C. N. Matthews. Dark Matter in the Solar System: Hydrogen Cyanide Polymers. *Origins of Life and Evolution of the Biosphere*, 21:421–434, 1991. doi: 10.1007/BF01808312.

B. H. Mauk, D. K. Haggerty, S. E. Jaskulek, C. E. Schlemm, L. E. Brown, S. A. Cooper, R. S. Gurnee, C. M. Hammock, J. R. Hayes, G. C. Ho, et al. The Jupiter Energetic Particle Detector Instrument (JEDI) Investigation for the Juno Mission. *Space Science Reviews*, 213:289–346, 2017. doi: 10.1007/s11214-013-0025-3.

J. O. P. McBride and R. W. Nicholls. The Vibration-Rotation Spectrum of Ammonia Gas. I. *Journal of Physics B: Atomic and Molecular Physics*, 5(2):408, 1972. doi: 10.1088/0022-3700/5/2/038.

W. McLean, D. M. Stam, S. Bagnulo, G. Borisov, M. Devogèle, A. Cellino, J. P. Rivet, P. Bendjoya, D. Vernet, G. Paolini, et al. A Polarimetric Investigation of Jupiter: Disk-Resolved Imaging Polarimetry and Spectropolarimetry. *Astronomy & Astrophysics*, 601:A142, 2017. doi: 10.1051/0004-6361/201629314.

I. Mendikoa, A. Sánchez-Lavega, S. Pérez-Hoyos, R. Hueso, J. F. Rojas, J. Aceituno, F. Aceituno, G. Murga, L. De Bilbao, and E. García-Melendo. PlanetCam UPV/EHU: A Two-Channel Lucky Imaging Camera for Solar System Studies in the Spectral Range 0.38–1.7 μm. *Publications of the Astronomical Society of the Pacific*, 128(961):035002, 2016. doi: 10.1088/1538-3873/128/961/035002.

I. Mendikoa, A. Sánchez-Lavega, S. Pérez-Hoyos, R. Hueso, J. F. Rojas, and J. López-Santiago. Temporal and Spatial Variations of the Absolute Reflectivity of Jupiter and Saturn from 0.38 to

1.7 μm with PlanetCam-UPV/EHU. *Astronomy & Astrophysics*, 607:A72, 2017. doi: 10.1051/0004-6361/201731109.

S. Mizumoto. 2016-2017 Mid-SEB Outbreak Final Report. ALPO-Japan, August 2017. URL `http://alpo-j.asahikawa-med.ac.jp/kk17/j170923s.htm`.

F. Moreno, A. Molina, and J. L. Ortiz. The 1993 South Equatorial Belt Revival and Other Features in the Jovian Atmosphere: An Observational Perspective. *Astronomy and Astrophysics*, 327:1253–1261, 1997.

J. I. Moses and T. K. Greathouse. Latitudinal and Seasonal Models of Stratospheric Photochemistry on Saturn: Comparison with Infrared Data from IRTF/TEXES. *Journal of Geophysical Research: Planets*, 110:E09007, 2005. doi: 10.1029/2005JE002450.

J. I. Moses, B. Bézard, E. Lellouch, G. R. Gladstone, H. Feuchtgruber, and M. Allen. Photochemistry of Saturn's Atmosphere: I. Hydrocarbon Chemistry and Comparisons with ISO Observations. *Icarus*, 143:244–298, 2000. doi: 10.1006/icar.1999.6270.

J. I. Moses, T. Fouchet, R. V. Yelle, A. J. Friedson, G. S. Orton, B. Bézard, P. Drossart, G. R. Gladstone, T. Kostiuk, and T. A. Livengood. The Stratosphere of Jupiter. *Jupiter: Planet, Satellites and Magnetosphere*, pages 129–157, 2004.

J. I. Moses, C. Visscher, T. C. Keane, and A. Sperier. On the Abundance of Non-Cometary HCN on Jupiter. *Faraday discussions*, 147:103–136, 2010. doi: 10.1039/c003954c.

O. Muñoz, F. Moreno, A. Molina, D. Grodent, J.-C. Gérard, and V. Dols. Study of the Vertical Structure of Saturn's Atmosphere using HST/WFPC2 Images. *Icarus*, 169:413–428, 2004. doi: 10.1016/j.icarus.2003.12.018.

F. Murtagh and A. Heck. *Multivariate Data Analysis*, volume 131. Springer Science & Business Media, 2012.

R. Naeye. A New Red Spot. *Sky and Telescope*, 111(6):18, 2006.

K. Nassau. *The Physics and Chemistry of Color: The Fifteen Causes of Color*. Wiley series in pure and applied optics. Wiley, 1983. ISBN 0-471-86776-4.

H. B. Niemann, S. K. Atreya, G. R. Carignan, T. M. Donahue, J. A. Haberman, D. N. Harpold, R. E. Hartle, D. M. Hunten, W. T. Kasprzak, P. R. Mahaffy, et al. The Composition of the Jovian

Atmosphere As Determined by the Galileo Probe Mass Spectrometer. *Journal of Geophysical Research: Planets*, 103:22831–22846, 1998. doi: 10.1029/98JE01050.

K. S. Noll and H. P. Larson. The Spectrum of Saturn from 1990 to 2230 cm^{-1}: Abundances of AsH_3, CH_3D, CO, GeH_4, NH_3, and PH_3. *Icarus*, 89:168–189, 1991. doi: 10.1016/0019-1035(91)90096-C.

N. Noy, M. Podolak, and A. Bar-Nun. Photochemistry of Phosphine and Jupiter's Great Red Spot. *Journal of Geophysical Research: Oceans*, 86:11985–11988, 1981. doi: 10.1029/JC086iC12p11985.

F. Oliva, A. Adriani, M. L. Moriconi, G. L. Liberti, E. D'Aversa, and G. Filacchione. Clouds and Hazes Vertical Structure of a Saturn's Giant Vortex [sic] from Cassini/VIMS-V Data Analysis. *Icarus*, 278:215–237, 2016. doi: 10.1016/j.icarus.2016.06.021.

I. Ordóñez-Etxeberria, R. Hueso, A. Sánchez-Lavega, and S. Pérez-Hoyos. Spatial Distribution of Jovian Clouds, Hazes and Colors from Cassini ISS Multi-Spectral Images. *Icarus*, 267:34–50, 2016. doi: 10.1016/j.icarus.2015.12.008.

J. L. Ortiz, F. Moreno, and A. Molina. Saturn 1991–1993: Clouds and Hazes. *Icarus*, 119:53–66, 1996. doi: 10.1006/icar.1996.0002.

G. S. Orton, A. P. Ingersoll, R. J. Terrile, and S. R. Walton. Images of Jupiter from the Pioneer 10 and Pioneer 11 Infrared Radiometers - A Comparison with Visible and 5-Micron Images. *Icarus*, 47:145–158, 1981. doi: 10.1016/0019-1035(81)90162-7.

T. Owen and R. J. Terrile. Colors on Jupiter. *Journal of Geophysical Research: Space Physics*, 86: 8797–8814, 1981. doi: 10.1029/JA086iA10p08797.

C. Palotai, T. E. Dowling, and L. N. Fletcher. 3D Modeling of Interactions Between Jupiter's Ammonia Clouds and Large Anticyclones. *Icarus*, 232:141–156, 2014. doi: 10.1016/j.icarus.2014.01.005.

S. Pérez-Hoyos, A. Sánchez-Lavega, R.G. French, and J.F. Rojas. Saturn's Cloud Structure and Temporal Evolution from Ten Years of Hubble Space Telescope Images (1994–2003). *Icarus*, 176: 155–174, 2005. doi: 10.1016/j.icarus.2005.01.014.

S. Pérez-Hoyos, A. Sánchez-Lavega, and R. G. French. Short-Term Changes in the Belt/Zone Structure of Saturn's Southern Hemisphere (1996–2004). *Astronomy & Astrophysics*, 460:641–645, 2006. doi: 10.1051/0004-6361:20065972.

S. Pérez-Hoyos, A. Sánchez-Lavega, R. Hueso, E. Garcia-Melendo, and J. Legarreta. The Jovian Anticyclone BA: III. Aerosol Properties and Color Change. *Icarus*, 203:516–530, 2009. doi: 10.1016/j.icarus.2009.06.024.

S. Pérez-Hoyos, J. F. Sanz-Requena, N. Barrado-Izagirre, J. F. Rojas, A. Sánchez-Lavega, and IOPW Team. The 2009-2010 Fade of Jupiter's South Equatorial Belt: Vertical Cloud Structure Models and Zonal Winds from Visible Imaging. *Icarus*, 217:256–271, 2012. doi: 10.1016/j.icarus.2011.11.008.

S. Pérez-Hoyos, A. Sanchez-Lavega, J. F. Sanz-Requena, R. Hueso, J. F. Rojas, I. Mendikoa, P. Irwin, N. Barrado-Izagirre, O. Carrión-Gonzalez, and A. Anguiano. Changes in the Upper Clouds and Hazes of Jupiter Following a North Temperate Belt Disturbance. In *AAS/Division for Planetary Sciences Meeting Abstracts*, volume 50, page 503.06, 2018.

G. N. Plass, G. W. Kattawar, and F. E. Catchings. Matrix Operator Theory of Radiative Transfer. 1: Rayleigh Scattering. *Applied Optics*, 12:314–329, 1973. doi: 10.1364/AO.12.000314.

C. C. Porco, R. A. West, A. McEwen, A. D. Del Genio, A. P. Ingersoll, P. Thomas, S. Squyres, L. Dones, C. D. Murray, T. V. Johnson, et al. Cassini Imaging of Jupiter's Atmosphere, Satellites, and Rings. *Science*, 299:1541–1547, 2003. doi: 10.1126/science.1079462.

R. G. Prinn and T. Owen. Chemistry and Spectroscopy of the Jovian Atmosphere. In *IAU Colloq. 30: Jupiter: Studies of the Interior, Atmosphere, Magnetosphere and Satellites*, pages 319–371, 1976.

B. Ragent, D. S. Colburn, K. A. Rages, T. C. D. Knight, P. Avrin, G. S. Orton, P. A. Yanamandra-Fisher, and G. W. Grams. The Clouds of Jupiter: Results of the Galileo Jupiter Mission Probe Nephelometer Experiment. *Journal of Geophysical Research: Planets*, 103:22891–22909, 1998. doi: 10.1029/98JE00353.

S. I. Ramirez, P. Coll, A. Da Silva, R. Navarro-Gonzalez, J. Lafait, and F. Raulin. Complex Refractive Index of Titan's Aerosol Analogues in the 200–900nm Domain. *Icarus*, 156:515–529, 2002. doi: 10.1006/icar.2001.6783.

J. T. Rayner, D. W. Toomey, P. M. Onaka, A. J. Denault, W. E. Stahlberger, W. D. Vacca, M. C. Cushing, and S. Wang. SpeX: A Medium-Resolution 0.8-5.5 Micron Spectrograph and Imager for the NASA Infrared Telescope Facility. *Publications of the Astronomical Society of the Pacific*, 115:362, 2003. doi: 10.1086/367745.

P. Ready and P. Wintz. Information Extraction, SNR Improvement, and Data Compression in Multispectral Imagery. *IEEE Transactions on communications*, 21(10):1123–1131, 1973.

C. D. Rodgers. Information Content and Optimization of High-Spectral-Resolution Measurements. In *SPIE's 1996 International Symposium on Optical Science, Engineering, and Instrumentation*, pages 136–147. International Society for Optics and Photonics, 1996.

C. D. Rodgers. *Inverse Methods for Atmospheric Sounding: Theory and Practice*, volume 2. World Scientific, 2000.

D. M. Roessler. Kramers-Kronig Analysis of Reflection Data. *British Journal of Applied Physics*, 16(8), 1965. doi: 10.1088/0508-3443/16/8/310.

J. H. Rogers. A High-Velocity Outbreak on the North Temperate Belt. *Journal of the British Astronomical Association*, 86:401–408, 1976.

J. H. Rogers. Jupiter in 1989-90. *Journal of the British Astronomical Association*, 102:135–150, 1992.

J. H. Rogers. *The Giant Planet Jupiter*. Cambridge University Press, 1995.

J. H. Rogers. Jupiter in 2016-17, Report no.17: Summary of the Mid-SEB Outbreak. British Astronomical Association, 2016. URL `https://britastro.org/node/16772`.

J. H. Rogers. Jupiter in 2018: Report no. 5 (2018 June 17), 2018a. URL `https://www.britastro.org/node/14405`.

J. H. Rogers. JunoCam at Perijove-11 (2018 Feb.7): What the Pictures Show. British Astronomical Association, February 2018b. URL `https://britastro.org/node/12580`.

J. H. Rogers and G. Adamoli. Jupiter's North Equatorial Belt and Jet: III, The 'Great Northern Upheaval' in 2012. *arXiv e-prints*, 2018.

J. H. Rogers and H.-J. Mettig. Jupiter in 2007: Final Numerical Report, 2008. URL `http://www.britastro.org/jupiter/2007report20.htm`.

M. T. Roman, D. Banfield, and P. J. Gierasch. Saturn's Cloud Structure Inferred from Cassini ISS. *Icarus*, 225:93–110, 2013. doi: 10.1016/j.icarus.2013.03.015.

C. Romanescu, J. Marschall, D. Kim, A. Khatiwada, and K. S. Kalogerakis. Refractive Index Measurements of Ammonia and Hydrocarbon Ices at 632.8 nm. *Icarus*, 205:695–701, 2010. doi: 10.1016/j.icarus.2009.08.016.

W. B. Rossow. Cloud Microphysics: Analysis of the Clouds of Earth, Venus, Mars and Jupiter. *Icarus*, 36:1–50, 1978. doi: 10.1016/0019-1035(78)90072-6.

L. S. Rothman, I. E. Gordon, Y. Babikov, A. Barbe, D. C. Benner, P. F. Bernath, M. Birk, L. Bizzocchi, V. Boudon, L. R. Brown, et al. The HITRAN2012 Molecular Spectroscopic Database. *Journal of Quantitative Spectroscopy and Radiative Transfer*, 130:4–50, 2013. doi: 10.1016/j.jqsrt.2013.07.002.

A. Sánchez-Lavega and J. M. Gomez. The South Equatorial Belt of Jupiter, I: Its Life Cycle. *Icarus*, 121:1–17, 1996. doi: 10.1006/icar.1996.0067.

A. Sánchez-Lavega and J. A. Quesada. Ground-Based Imaging of Jovian Cloud Morphologies and Motions: II. The Northern Hemisphere from 1975 to 1985. *Icarus*, 76:533–557, 1988. doi: 10.1016/0019-1035(88)90020-6.

A. Sánchez-Lavega, I. Miyazaki, D. Parker, P. Laques, and J. Lecacheux. A Disturbance in Jupiter's High-Speed North Temperate Jet during 1990. *Icarus*, 94:92–97, 1991. doi: 10.1016/0019-1035(91)90142-G.

A. Sánchez-Lavega, G. S. Orton, R. Morales, J. Lecacheux, F. Colas, B. Fisher, P. Fukumura-Sawada, W. Golisch, D. Griep, C. Kaminski, et al. The Merger of Two Giant Anticyclones in the Atmosphere of Jupiter. *Icarus*, 149:491–495, 2001. doi: 10.1006/icar.2000.6548.

A. Sánchez-Lavega, G. S. Orton, R. Hueso, E. García-Melendo, S. Pérez-Hoyos, A. Simon-Miller, J. F. Rojas, J. M. Gómez, P. Yanamandra-Fisher, L. Fletcher, et al. Depth of a Strong Jovian Jet from a Planetary-Scale Disturbance Driven by Storms. *Nature*, 451:437–440, 2008. doi: 10.1038/nature06533.

A. Sánchez-Lavega, J. Legarreta, E. García-Melendo, R. Hueso, S. Pérez-Hoyos, J. M. Gómez-Forrellad, L. N. Fletcher, G. S. Orton, A. Simon-Miller, N. Chanover, et al. Colors of Jupiter's Large Anticyclones and the Interaction of a Tropical Red Oval with the Great Red Spot in 2008. *Journal of Geophysical Research: Planets*, 118:2537–2557, 2013. doi: 10.1002/2013JE004371.

A. Sánchez-Lavega, G. Fischer, L. N. Fletcher, E. García-Melendo, B. Hesman, S. Pérez-Hoyos, K. M. Sayanagi, and L. A. Sromovsky. The Great Saturn Storm of 2010-2011. In *Saturn in the 21st Century*. Cambridge University Press, 2016.

A. Sánchez-Lavega, J. H. Rogers, G. S. Orton, E. García-Melendo, J. Legarreta, F. Colas, J. L. Dauvergne, R. Hueso, J. F. Rojas, S. Pérez-Hoyos, et al. A Planetary-Scale Disturbance in the

Most Intense Jovian Atmospheric Jet from JunoCam and Ground-Based Observations. *Geophysical Research Letters*, 44:4679–4686, 2017. doi: 10.1002/2017GL073421.

A. Sánchez-Lavega, R. Hueso, G. Eichstädt, G. Orton, J. Rogers, C. J. Hansen, T. Momary, F. Tabataba-Vakili, and S. Bolton. The Rich Dynamics of Jupiter's Great Red Spot from JunoCam: Juno Images. *Astronomical Journal*, 156:162, 2018. doi: 10.3847/1538-3881/aada81.

T. M. Sato, T. Satoh, and Y. Kasaba. Retrieval of Jovian Cloud Structure from the Cassini ISS Limb-Darkening Data: I. Continuum Scattering Phase Functions for Cloud and Haze in the South Tropical Zone. *Icarus*, 222:100–121, 2013. doi: 10.1016/j.icarus.2012.09.035.

T. Satoh and K. Kawabata. Methane Band Photometry of the Faded South Equatorial Belt of Jupiter. *Astrophysical Journal*, 384:298–304, 1992. doi: 10.1086/170873.

T. Satoh and K. Kawabata. A Change of Upper Cloud Structure in Jupiter's South Equatorial Belt During the 1989-1990 event. *Journal of Geophysical Research*, 99:8425–8440, 1994. doi: 10.1029/94JE00215.

M. A. Satorre, J. Leliwa-Kopystynski, C. Santonja, and R. Luna. Refractive Index and Density of Ammonia Ice at Different Temperatures of Deposition. *Icarus*, 225:703–708, 2013. doi: 10.1016/j.icarus.2013.04.023.

G. J. Scherer, K. K. Lehmann, and W. Klemperer. The High-Resolution Visible Overtone Spectrum of CH_4 and CD_3H at 77 K. *The Journal of Chemical Physics*, 81(12):5319–5325, 1984. doi: 10.1063/1.447674.

M. Sheik-Bahae. Nonlinear Optics Basics. Kramers-Kronig Relations in Nonlinear Optics. *Encyclopedia of Modern Optics. RD Guenther, editor. Academic Press, Amsterdam*, 2005.

S. Shetty and P. S. Marcus. Changes in Jupiter's Great Red Spot (1979-2006) and Oval BA (2000-2006). *Icarus*, 210:182–201, 2010. doi: 10.1016/j.icarus.2010.06.026.

A. P. Showman and I. de Pater. Dynamical Implications of Jupiter's Tropospheric Ammonia Abundance. *Icarus*, 174:192–204, 2005. doi: 10.1016/j.icarus.2004.10.004.

G. T. Sill. The Chemistry of the Jovian Cloud Colors. In *IAU Colloq. 30: Jupiter: Studies of the Interior, Atmosphere, Magnetosphere and Satellites*, pages 372–383, 1976.

A. A. Simon, M. H. Wong, J. H. Rogers, G. S. Orton, I. De Pater, X. Asay-Davis, R. W. Carlson, and P. S. Marcus. Dramatic Change in Jupiter's Great Red Spot from Spacecraft Observations. *The Astrophysical Journal Letters*, 797:L31, 2014. doi: 10.1088/2041-8205/797/2/L31.

A. A. Simon, M. H. Wong, and G. S. Orton. First Results from the Hubble OPAL Program: Jupiter in 2015. *The Astrophysical Journal*, 812:55, 2015. doi: 10.1088/0004-637X/812/1/55.

A. A. Simon, F. Tabataba-Vakili, R. Cosentino, R. F. Beebe, M. H. Wong, and G. S. Orton. Historical and Contemporary Trends in the Size, Drift, and Color of Jupiter's Great Red Spot. *The Astronomical Journal*, 155:151, 2018. doi: 10.3847/1538-3881/aaae01.

A. A. Simon-Miller, B. Conrath, P. J. Gierasch, and R. F. Beebe. A Detection of Water Ice on Jupiter with Voyager IRIS. *Icarus*, 145:454–461, 2000. doi: 10.1006/icar.2000.6359.

A. A. Simon-Miller, D. Banfield, and P. J. Gierasch. Color and the Vertical Structure in Jupiter's Belts, Zones, and Weather Systems. *Icarus*, 154:459–474, 2001a. doi: 10.1006/icar.2001.6742.

A. A. Simon-Miller, D. Banfield, and P. J. Gierasch. An HST Study of Jovian Chromophores. *Icarus*, 149:94–106, 2001b. doi: 10.1006/icar.2001.6473.

A. A. Simon-Miller, B. W. Poston, G. S. Orton, and B. Fisher. Wind Variations in Jupiter's Equatorial Atmosphere: A QQO Counterpart? *Icarus*, 186:192–203, 2007. doi: 10.1016/j.icarus.2006.08.009.

J. Sinclair. *Seasonal and Interannual Variability in Saturn's Stratosphere*. DPhil Thesis, University of Oxford, 2013.

G. Sindoni, D. l. Grassi, A. Adriani, A. Mura, M. L. Moriconi, B. M. Dinelli, G. Filacchione, F. Tosi, G. Piccioni, A. Migliorini, et al. Characterization of the White Ovals on Jupiter's Southern Hemisphere Using the First Data by the Juno/JIRAM Instrument. *Geophysical Research Letters*, 44:4660–4668, 2017. doi: 10.1002/2017GL072940.

B. A. Smith, L. Soderblom, R. Batson, P. Bridges, J. Inge, H. Masursky, E. Shoemaker, R. Beebe, J. Boyce, G. Briggs, et al. A New Look at the Saturn System: The Voyager 2 Images. *Science*, 215:504–537, 1982. doi: 10.1126/science.215.4532.504.

J. R. Spencer, R. W. Carlson, T. L. Becker, and J. S. Blue. Maps and Spectra of Jupiter and the Galilean Satellites. In F. Bagenal, T. E. Dowling, and W. B. McKinnon, editors, *Jupiter: The Planet, Satellites, and Magnetosphere*, page 689. Cambridge University Press, 2004.

S. Squyres. Vision and Voyages for Planetary Science in the Decade 2013–2022. *National Research Council Publications*, 2011.

L. A. Sromovsky and P. M. Fry. The Source of 3-μm Absorption in Jupiter's Clouds: Reanalysis of ISO Observations Using New NH_3 Absorption Models. *Icarus*, 210:211–229, 2010. doi: 10.1016/j.icarus.2010.06.040.

L. A. Sromovsky and P. M. Fry. Composition and Structure of Fresh Ammonia Clouds on Jupiter Based on Quantitative Analysis of Galileo/NIMS and New Horizons/LEISA Spectra. *Icarus*, 307:347–370, 2018. doi: 10.1016/j.icarus.2017.10.037.

L. A. Sromovsky, K. H. Baines, and P. M. Fry. Saturn's Great Storm of 2010-2011: Evidence for Ammonia and Water Ices from Analysis of VIMS Spectra. *Icarus*, 226:402–418, 2013. doi: 10.1016/j.icarus.2013.05.043.

L. A. Sromovsky, K. H. Baines, P. M. Fry, and R. W. Carlson. A Possibly Universal Red Chromophore for Modeling Color Variations on Jupiter. *Icarus*, 291:232–244, 2017. doi: 10.1016/j.icarus.2016.12.014.

D. M. Stam, D. Banfield, P. J. Gierasch, P. D. Nicholson, and K. Matthews. Near-IR Spectrophotometry of Saturnian Aerosols - Meridional and Vertical Distribution. *Icarus*, 152:407–422, 2001. doi: 10.1006/icar.2001.6641.

V. Stanishev. Correcting Second-Order Contamination in Low-Resolution Spectra. *Astronomische Nachrichten*, 328:948, 2007. doi: 10.1002/asna.200710779.

C. P. Stoll. *Polarimetry of Jupiter at Large Phase Angles.* PhD thesis, Arizona Univ., Tucson., 1980.

B. P. Straughan. *Spectroscopy*, volume 2. Chapman and Hall, 1976.

D. F. Strobel, S. K. Atreya, B. Bézard, F. Ferri, F. M. Flasar, M. Fulchignoni, E. Lellouch, and I. Müller-Wodarg. Atmospheric Structure and Composition. In *Titan from Cassini-Huygens*, pages 235–257. Springer, 2009.

S. Ströbele, P. La Penna, R. Arsenault, R. D. Conzelmann, B. Delabre, M. Duchateau, R. Dorn, E. Fedrigo, N. Hubin, J. Quentin, et al. GALACSI System Design and Analysis. In *Adaptive Optics Systems III*, volume 8447, page 844737. International Society for Optics and Photonics, 2012.

P. D. Strycker, N. J. Chanover, A. A. Simon-Miller, D. Banfield, and P. J. Gierasch. Jovian Chromophore Characteristics from Multispectral HST Images. *Icarus*, 215:552–583, 2011. doi: 10.1016/j.icarus.2011.08.004.

W. R. Thompson. Global Four-Band Spectral Classification of Jupiter's Clouds: Color/Albedo Units and Trends. *The International Journal of Supercomputing Applications*, 4:48–65, 1990. doi: 10.1177/109434209000400205.

A. T. Tokunaga, R. F. Knacke, and S. T. Ridgway. High Spatial and Spectral Resolution 10-μm Observations of Jupiter. *Icarus*, 44:93–101, 1980. doi: 10.1016/0019-1035(80)90058-5.

D. Toledo and P. G. J. Irwin. Modelling Cloud Microphysics on Uranus. *European Planetary Science Congress*, 11:EPSC2017-246, 2017.

M. G. Tomasko, R. A. West, G. S. Orton, and V. G. Teifel. *Saturn*, chapter Clouds and Aerosols in Saturn's Atmosphere, pages 150–194. University of Arizona Press, 1984.

A. R. Vasavada and A. P. Showman. Jovian Atmospheric Dynamics: An Update After Galileo and Cassini. *Reports on Progress in Physics*, 68(8):1935–1996, 2005. doi: 10.1088/0034-4885/68/8/R06.

L. Ventress and A. Dudhia. Improving the Selection of IASI Channels for Use in Numerical Weather Prediction. *Quarterly Journal of the Royal Meteorological Society*, 140(684):2111–2118, 2014. doi: 10.1002/qj.2280.

U. von Zahn, D. M. Hunten, and G. Lehmacher. Helium in Jupiter's Atmosphere: Results from the Galileo Probe Helium Interferometer Experiment. *Journal of Geophysical Research: Planets*, 103: 22815–22830, 1998. doi: 10.1029/98JE00695.

V. Vuitton, B. N. Tran, P. D. Persans, and J. P. Ferris. Determination of the Complex Refractive Indices of Titan Haze Analogs Using Photothermal Deflection Spectroscopy. *Icarus*, 203:663–671, 2009. doi: 10.1016/j.icarus.2009.04.016.

G. Wahba and S. Wold. A Completely Automatic French Curve: Fitting Spline Functions by Cross Validation. *Communications in Statistics-Theory and Methods*, 4(1):1–17, 1975. doi: 10.1080/03610927508827223.

J. H. Waite, D. T. Young, J. H. Westlake, J. I. Lunine, C. P. McKay, and W. S. Lewis. High-Altitude Production of Titan's Aerosols. In *Titan from Cassini-Huygens*, pages 201–214. Springer, 2009.

S. J. Weidenschilling and J. S. Lewis. Atmospheric and Cloud Structures of the Jovian Planets. *Icarus*, 20:465–476, 1973. doi: 10.1016/0019-1035(73)90019-5.

E. W. Weisstein and E. Serabyn. Submillimeter Line Search in Jupiter and Saturn. *Icarus*, 123: 23–36, 1996. doi: 10.1006/icar.1996.0139.

R. A. West, K. H. Baines, A. J. Friedson, D. Banfield, B. Ragent, and F. W. Taylor. Jovian Clouds and Haze. In *Jupiter: The Planet, Satellites, and Magnetosphere*. Cambridge University Press, 2004.

R. A. West, K. H. Baines, E. Karkoschka, and A. Sanchez-Lavega. Clouds and Aerosols in Saturn's Atmosphere. In Michele Dougherty, Larry Esposito, and Stamatios Krimigis, editors, *Saturn from Cassini-Huygens*. Springer Science & Business Media, 2009.

J. D. White, Y. Liu, D. Matsiev, and R. Robertson. Laboratory Studies of Phosphine Chemistry Relevant to the Jovian and Saturnian Atmospheres. *AGU Fall Meeting Abstracts*, art. P33B-2139, 2016.

F. Woeller and C. Ponnamperuma. Organic Synthesis in a Simulated Jovian Atmosphere. *Icarus*, 10:386–392, 1969. doi: 10.1016/0019-1035(69)90093-1.

M. H. Wong, I. de Pater, X. Asay-Davis, P. S. Marcus, and C. Y. Go. Vertical Structure of Jupiter's Oval BA Before and After It Reddened: What Changed? *Icarus*, 215:211–225, 2011. doi: 10.1016/j.icarus.2011.06.032.

M. H. Wong, S. K. Atreya, W. R. Kuhn, P. N. Romani, and K. M. Mihalka. Fresh Clouds: A Parameterized Updraft Method for Calculating Cloud Densities in One-Dimensional Models. *Icarus*, 245:273–281, 2015. doi: 10.1016/j.icarus.2014.09.042.

X. Zhang, R. A. West, D. Banfield, and Y. L. Yung. Stratospheric Aerosols on Jupiter from Cassini Observations. *Icarus*, 226:159–171, 2013. doi: 10.1016/j.icarus.2013.05.020.

L. C. Zuchowski, Y. H. Yamazaki, and P. L. Read. Modeling Jupiter's Cloud Bands and Decks. 2. Distribution and Motion of Condensates. *Icarus*, 200:563–573, 2009. doi: 10.1016/j.icarus.2008.11.015.

Appendix A

List of MUSE observations

Jupiter 2014 (commissioning data, prevalent striping artefacts. Solar opposition occurred on the 5th of January 2014)					
Observation ID	Seeing (arcsec)	Airmass (science)	Airmass (standard)	Sub-observer longitude (III)	Notes
2014-02-17T00:16:32.439	0.49	1.625	1.16	311.6	WSZ at nadir.
2014-02-17T01:12:31.402	0.83	1.503	1.33	345.4	
2014-02-17T02:07:56.907	0.64	1.500	1.37	18.92	GRS at nadir.

Jupiter 2016 (global observations, pre-Juno approach. Solar opposition occurred on the 8th of March 2016)					
Observation ID	Seeing (arcsec)	Airmass (science)	Airmass (standard)	Sub-observer longitude (III)	Notes
2016-03-08T03:04:34.213	0.62	1.322	-	208.0	Non-expanded region of NEB. GRS close to limb. Poor observatory standard, reduced science using spectral response function that came with ESOREX pipeline.
2016-03-08T06:08:30.448	0.65	1.226	-	319.3	WSZ, GRS and Oval BA in view, although GRS close to limb. Expanded region of NEB. Poor observatory standard, reduced science using spectral response function that came with ESOREX pipeline.
2016-03-09T05:33:45.913	0.93	1.183	1.11	88.99	
2016-03-31T02:56:48.559	1.15	1.179	1.06	68.20	Poor observing conditions, not photometric.
2016-04-01T02:22:07.339	1.00	1.204	1.37	197.8	GRS close to limb.
2016-04-01T05:39:03.340	0.83	1.497	1.37	316.9	WSZ in view, but GRS and Oval BA close to limb. Expanded region of NEB. Original observatory standard rejected due to large airmass.
2016-04-02T04:39:47.831	0.88	1.288	1.17	71.68	Non-expanded region of NEB.

Jupiter 2017 (observations to coincide with originally-scheduled Juno perijoves and to image GRS. Solar opposition occurred on the 7th of April 2017)					
Observation ID	Seeing (arcsec)	Airmass (science)	Airmass (standard)	Sub-observer longitude (III)	Notes
2017-01-10T07:43:03.128	0.48	1.458	1.59	263.1	3 weeks before PJ4, just after NTBs outbreak, NTropZ and NTBs difficult to distinguish. WSZ in view but very difficult to discern.
2017-03-25T05:46:26.490	0.49	1.053	1.29	178.9	2 days before PJ5. Very poor geometric calibration.
2017-05-15T02:01:59.328	1.10	1.067	1.46	165.5	4 days before PJ6. Default observation used for bright NTBs haze.
2017-05-28T01:31:25.168	0.65	1.073	1.31	304.0	Oval BA close to nadir.
2017-07-20T00:39:35.489	1.03	1.423	1.12	325.1	9 days after PJ7. Poor observing conditions.
2017-07-26T00:31:05.579	1.04	1.492	1.04	142.0	GRS at terminator.
2017-08-16T00:05:02.682	0.84	1.861	1.05	43.03	GRS close to nadir.

Jupiter 2018 (observations to coincide with Juno perijoves and to image GRS, Oval BA and WSZ close to nadir. Solar opposition occurred on the 9th of May 2018)

Observation ID	Seeing (arcsec)	Airmass (science)	Airmass (standard)	Sub-observer longitude (III)	Notes
2018-04-09T06:04:06.918	0.36	1.028	1.03	121.14	8 days after PJ12, GRS close to nadir, a number of red ovals visible in NEBn. Best of all the MUSE observations in terms of seeing and airmass.
2018-04-14T07:37:31.919	0.59	1.050	1.04	210.98	
2018-04-14T09:00:50.919	0.49	1.240	1.04	261.37	Oval BA close to nadir, WSZ in view but difficult to discern.
2018-05-18T00:57:16.678	0.82	1.377	1.48	51.78	6 days before PJ13.
2018-05-25T04:22:34.417	0.59	1.039	1.14	150.3	GRS close to nadir, but bisected by an instrumental artefact. Observation made within half an hour of another observation of Jupiter obtained by the VLT/VISIR instrument.
2018-07-12T02:20:43.256	0.70	1.190	1.85	103.06	4 days before PJ14. EZ colouration event starts to become very clear.
2018-09-11T23:11:42.877	0.66	1.301	-	312.0	4 days after PJ15. EZ still red. Very poor observatory standard, reduced science using spectral response function that came with ESOREX pipeline.

Saturn

Observation ID	Seeing (arcsec)	Airmass (science)	Airmass (standard)	Sub-observer longitude (III)	Notes
2014-02-20T07:50:56.306	0.81	1.189	1.47	72.49	Presence of striping artefacts.
2017-04-06T05:38:16.941	0.55	1.683	1.28	235.88	
2017-06-18T06:04:09.111	AO	1.076	1.08	45.31	Obtained at opposition, rings unusually bright due to Seeliger effect.

Appendix B

Systematic errors due to poor modelling of collision-induced absorption (CIA)

Shortly before submission of this thesis, it was discovered that the CIA look-up table used to produce all the results presented in chapters 4-6 was faulty and had absorption data missing in the required wavelength range. The effect of CIA on giant planet spectra in this wavelength range is substantial enough that it cannot be ignored entirely, but the fault in our CIA table was found at too short notice to redo all the models and retrievals in this thesis with the correct absorption data. Fortunately, the wavelength region that is affected most by CIA generally has relatively little information content, containing telluric water vapour absorption lines and only minor methane absorption from the giant planet atmospheres themselves (although there is some small overlap with the ammonia absorption feature at 0.79µm). It was for this reason that the fault took so long to spot: the effect of CIA on gas giant spectra in this wavelength range was initially assumed to be as negligible as pure quadrupole H_2 absorption (as previously described in section 3.4), while the resulting deficiencies in fit were assumed to be a result of poor methane absorption data and the presence of telluric absorption. We have therefore used this appendix to present all the effects that the inclusion of CIA would have on our results, and thereby reassure the reader that the effects are minor and do not invalidate any of our conclusions presented in chapter 7.

Using the correct CIA table, we re-retrieved a chromophore imaginary refractive index spectrum for Jupiter and Saturn from the same limb darkening spectra as in sections 4.6 and 6.4 respectively. In both cases, we fixed the values of r_n, r_c, n_n and n_c according to the most physical values that we found in the same analyses (that is $r_n = 1.0$, $r_c = 0.2$, $n_n = 1.42$ and $n_c = 1.4$ for Jupiter, and $r_n = 2.5$, $r_c = 0.02$, $n_n = 1.42$ and $n_c = 2.1$ for Saturn). The resulting atmospheric profiles for

Jupiter are shown in figure B.0.1. The greatest effect of the inclusion of CIA on our model is of a reduction in the imaginary refractive index around 0.8µm. This is because, as is clearly illustrated in figure B.0.4, CIA contributes to substantial absorption around continuum wavelengths at 0.81µm, and so our original model had to compensate for the lack of CIA parametrisation by increasing the chromophore imaginary refractive index in the same region. A consequence of this lack of a chromophore absorption feature at 0.8µm is a small reduction in retrieved chromophore opacity when CIA is included in the model. Surprisingly, we see little change in the retrieved ammonia gas profile, even though the region of CIA overlaps with a major ammonia absorption feature around 0.79µm. For Saturn, the effect of CIA is even less dramatic as can be seen in figures B.0.3 and B.0.4, presumably due to the colder temperatures and the presence of haze which obscures CIA at deeper altitudes on Saturn. However, we observe a greater net contribution of H_2-He CIA on Saturn relative to Jupiter where it is almost completely negligible compared with H_2-H_2 CIA, despite the fact that the ratio of hydrogen to helium is greater on Saturn than it is on Jupiter. In addition, we still observe a small net increase in absorption around 0.85µm, as we do on Jupiter around 0.9µm, although this could well be to do with poor methane band modelling in that region or an overconstrained vertical aerosol parametrisation. The effect of CIA on Saturn spectra is, however, strong enough to provide some simultaneous constraint of aerosol structure and methane abundance that is not possible without CIA, as we show in figure B.0.2.

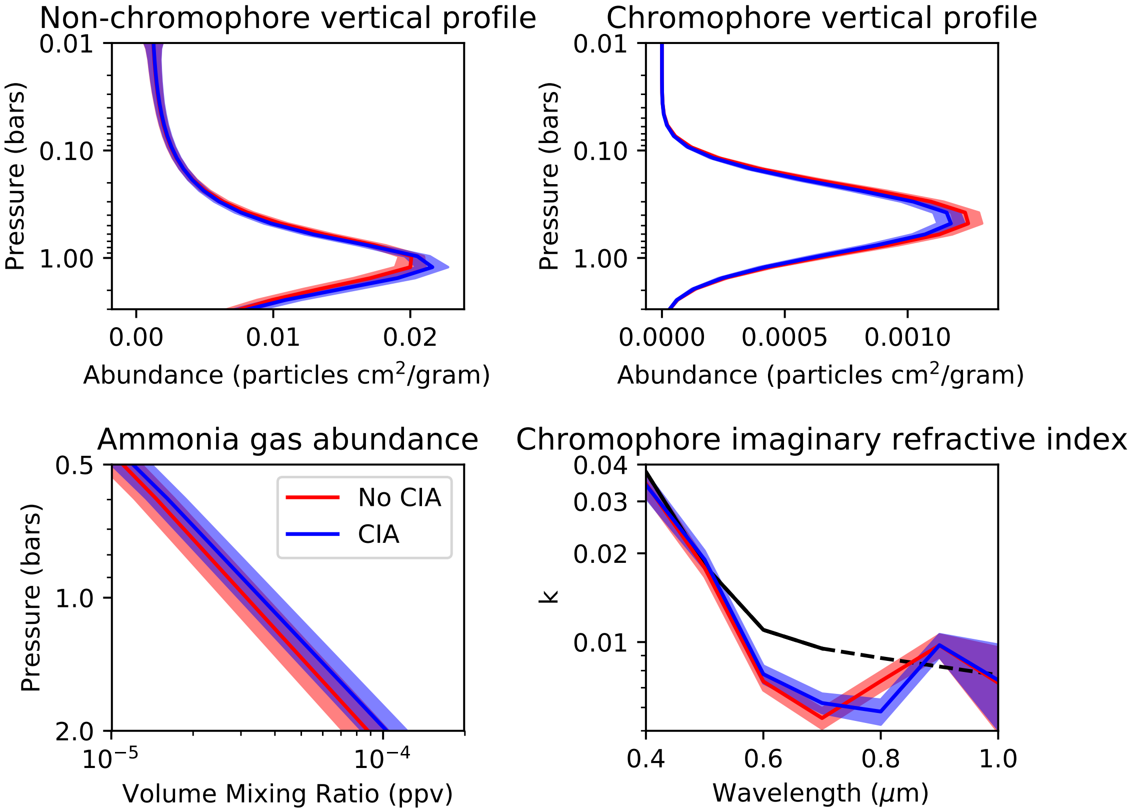

Figure B.0.1: Retrieved atmospheric parameters through limb darkening analysis of Jupiter's NEB according to the parametrisation in table 4.4.1, with our original analysis shown in red and with the proper inclusion of collision-induced absorption (H_2-H_2 and H_2-He combined) shown in blue. The optical constants of the chromophore of Carlson et al. [2016] are shown in black in the bottom-right diagram, with the dashed region showing extrapolated values.

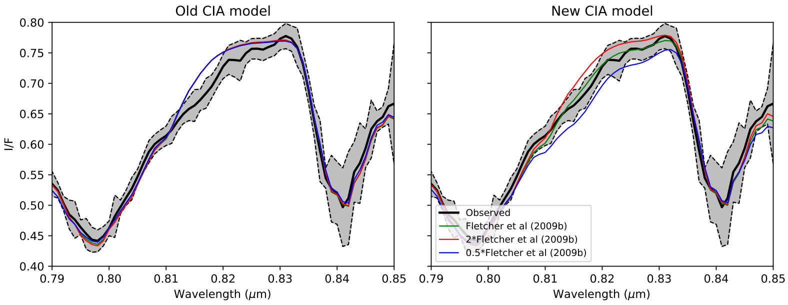

Figure B.0.2: Effect on the fit to Saturn spectra between 0.81μm and 0.83μm (left) with the old CIA model and (right) using the new, correct CIA model, when varying the prior methane abundance profile from that of Fletcher et al. [2009] as we did in section 6.6. Note in the plot on the right that, while the fit to the spectrum here is best using the methane abundances of Fletcher et al. [2009], the actual shape of the spectral fit suggests that the abundances from Fletcher et al. [2009] could be a slight overestimate. We can therefore use these wavelengths to constrain Saturnian methane abundances to first order, which we cannot without CIA, as can be seen clearly in the plot on the left.

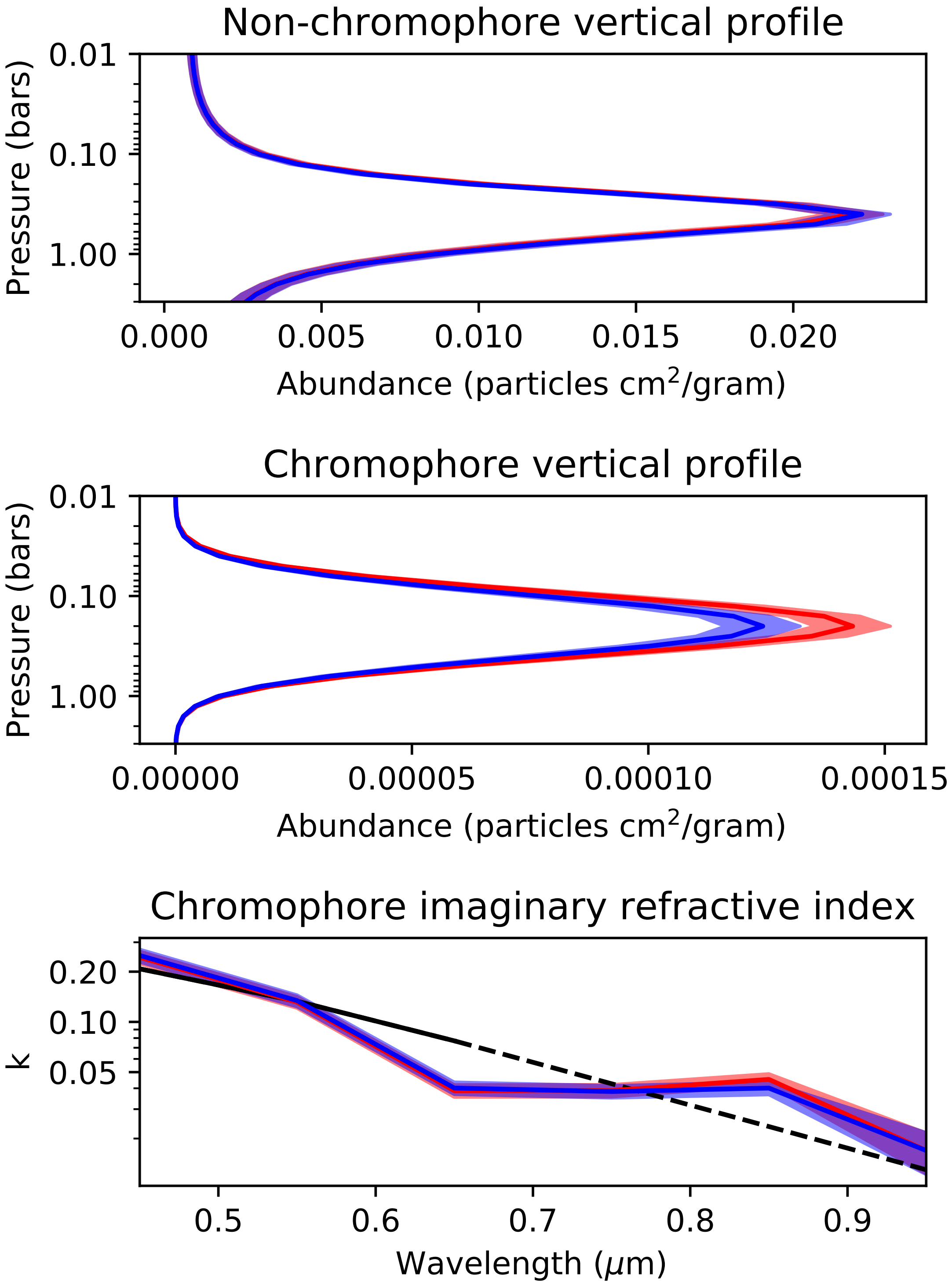
Non-chromophore vertical profile

Chromophore vertical profile

Chromophore imaginary refractive index

Figure B.0.3: Retrieved atmospheric parameters through limb darkening analysis of Saturn's NEB according to the parametrisation in table 6.4.1, with our original analysis shown in red and with the proper inclusion of collision-induced absorption (H_2-H_2 and H_2-He combined) shown in blue. The optical constants of the chromophore of Noy et al. [1981] are shown in black in the bottom diagram, with the dashed region showing extrapolated values.

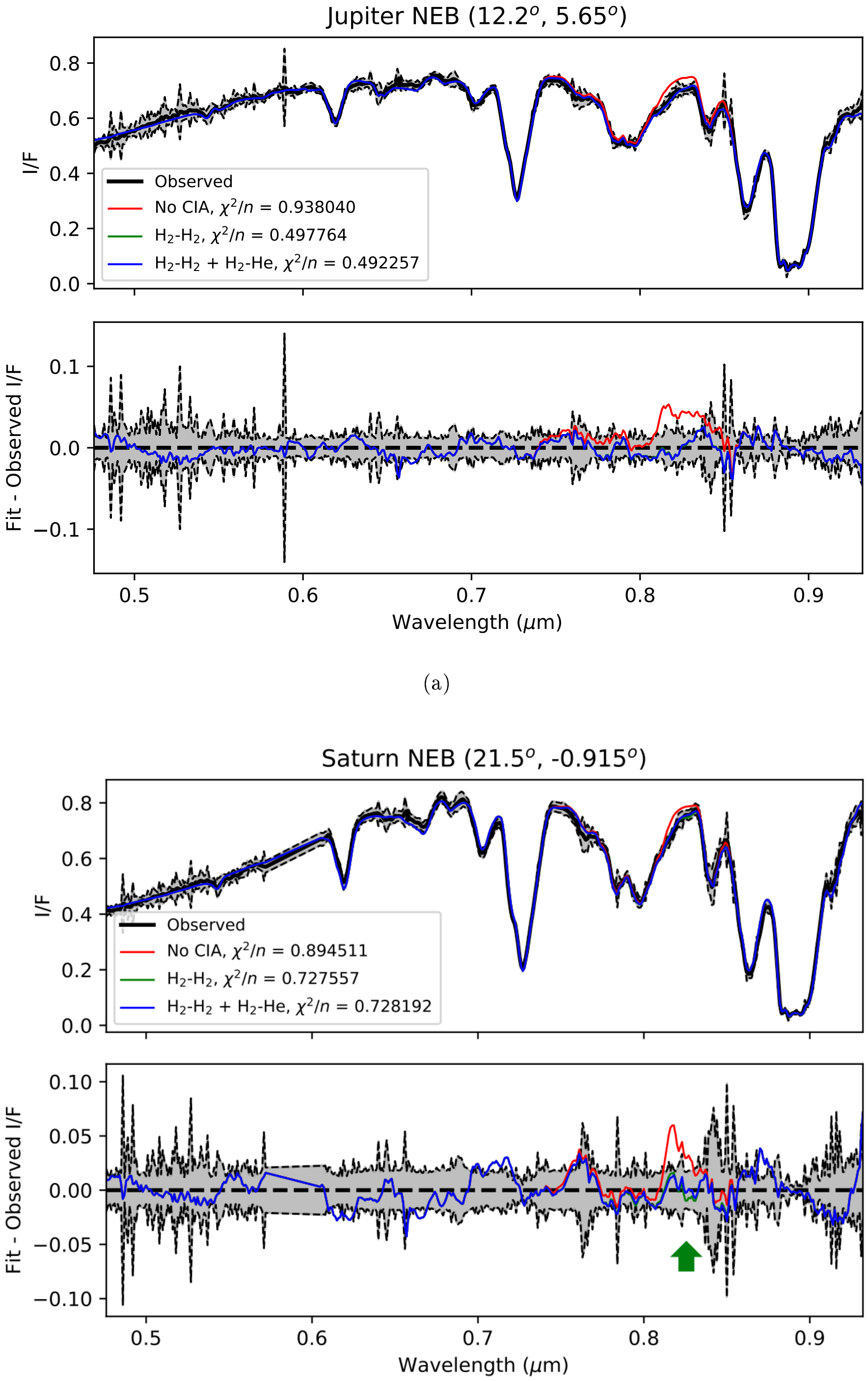

(a)

(b)

Figure B.0.4: Application of the imaginary refractive index spectrum retrieved through limb darkening analysis to a single NEB point spectrum of (a) Jupiter and (b) Saturn. In red we show the fit to the spectrum with the complete absence of CIA, as in our models presented in the body of this thesis (we note that we get better fits in chapters 4 and 6 than we do here despite the lack of CIA due to the retrieved increase of imaginary refractive index at 0.8μm to compensate). In green we show the fit to the spectrum when just H_2-H_2 CIA is included, while in blue we show the fit with the inclusion of H_2-H_2 and H_2-He CIA combined, with the region of greatest discrepancy between the two highlighted by the green arrow. In both cases, the former effect dominates overwhelmingly over the latter.